



**UNIVERSIDAD NACIONAL AUTÓNOMA DE MÉXICO**  
PROGRAMA DE POSGRADO EN ASTROFÍSICA  
Instituto de Astronomía, Ciudad Universitaria.

**ESTUDIO DE EMISIONES ÓPTICAS TEMPRANAS Y  
TARDÍAS DE GRBS CON EL TELESCOPIO ROBÓTICO  
COATLI**

TESIS

**QUE PARA OPTAR POR EL GRADO DE:  
DOCTOR EN CIENCIAS (ASTROFÍSICA)**

PRESENTA:

**ROSA LETICIA BECERRA GODÍNEZ**

TUTORES PRINCIPALES

**DR. ALAN MORGAN WATSON FORSTER,**

Instituto de Astronomía, Ciudad Universitaria.

**DR. WILLIAM HENRY LEE ALARDÍN,**

Instituto de Astronomía, Ciudad Universitaria.

MÉXICO, CDMX, MAYO 2019



Universidad Nacional  
Autónoma de México



**UNAM – Dirección General de Bibliotecas**  
**Tesis Digitales**  
**Restricciones de uso**

**DERECHOS RESERVADOS ©**  
**PROHIBIDA SU REPRODUCCIÓN TOTAL O PARCIAL**

Todo el material contenido en esta tesis esta protegido por la Ley Federal del Derecho de Autor (LFDA) de los Estados Unidos Mexicanos (México).

El uso de imágenes, fragmentos de videos, y demás material que sea objeto de protección de los derechos de autor, será exclusivamente para fines educativos e informativos y deberá citar la fuente donde la obtuvo mencionando el autor o autores. Cualquier uso distinto como el lucro, reproducción, edición o modificación, será perseguido y sancionado por el respectivo titular de los Derechos de Autor.







# Resumen

Los destellos de rayos gamma (GRBs) son eventos transitorios con duraciones que van desde una fracción de segundo hasta varios segundos, con algunos que llegan a durar minutos. Son producidos por el colapso de una estrella masiva cuya masa supera las  $8M_{\odot}$  o por la colisión de dos objetos compactos como estrellas de neutrones. Hasta el día de hoy, son los eventos más brillantes que conocemos en el universo. Sin embargo, a pesar de que se descubrieron en la década de los 60s, el entendimiento de estos fenómenos continua siendo incompleto en muchos aspectos, principalmente en su fase temprana debido a la dificultad que se presenta al momento de su observación por la corta duración de los GRBs y el tiempo de respuesta de los telescopios.

Ésta es la motivación para el tema de esta tesis: las pocas observaciones fotométricas a tiempos tempranos de los destellos de rayos gamma en el pasado por los telescopios terrestres existentes y por lo tanto, la escasa cantidad de información que se tiene de esta etapa. En ese sentido, con la finalidad de mejorar las observaciones en el óptico de objetos transientes desde su fase pronta, la llegada de un telescopio robótico como *COATLI*, instalado en el 2016 en el OAN-SPM y que a partir de mayo del 2017 entró en operaciones, se han aportado resultados científicos en este campo. Así, al complementarlo con el instrumento *RATIR*, colocado en el telescopio de 1.5 metros también en el OAN-SPM, permiten tener una amplia cobertura temporal de los destellos de rayos gamma desde sus fases tempranas hasta tardías.

El principal objetivo del trabajo fue aportar observaciones e interpretación de diversos destellos de rayos gamma, por lo tanto, este trabajo presenta el estudio de las emisiones prontas y tardías de destellos de rayos gamma utilizando datos de los telescopios robóticos *COATLI* y *RATIR*.

En los últimos años, se han detectado numerosos eventos; sin embargo, se destaca el GRB 130427A, el cual ha sido estudiado desde diversos enfoques debido a la energía emitida, convirtiéndolo en un transiente de gran interés en el campo de estudio de altas energías. Este GRB fue observado por *RATIR*, el cual proporcionó la mejor fotometría en óptico/cercano infrarrojo de la fase tardía al

paso de días y meses posteriores al evento.

Por otro lado, COATLI tuvo su primer conjunto de datos astronómicos al detectar el GRB 180205A 6 segundos después de la alerta emitida por el satélite espacial *SWIFT*, varios segundos antes que otros telescopios terrestres. Esto permitió registrar datos en óptico al mismo tiempo que para rayos X y por lo tanto, observar el *flare* que aparece después de 200 segundos del destello. El análisis del GRB 180205A permitió estudiar y entender la actividad del motor central. La fotometría de este evento fue complementado en noches posteriores por RATIR.

Finalmente, el GRB 180418A, candidato a destello de rayos gamma corto, observado por la colaboración *TAROT* tan solo 28 segundos después del estallido y más tarde por *RATIR*, también cuenta con observaciones tempranas en las bandas ópticas presentando una componente reversa típica en muchos choques.

En este trabajo se incluye una introducción a los destellos de rayos gamma en el primer capítulo; en el segundo capítulo se presenta un panorama general de los telescopios enfocados en la observación de GRBs tanto espaciales como terrestres. El tercer capítulo describe las características y funcionamiento del telescopio robótico *COATLI*. En el cuarto capítulo se encuentran las publicaciones como primer autor realizadas durante este proyecto de doctorado: la descripción y el análisis de los datos obtenidos con *COATLI* del GRB 180205A; la confirmación fotométrica con datos del instrumento *RATIR* de la asociación de una supernova al GRB 130427A así como sus principales características; y el estudio a tiempos tempranos del posible SGRB 180418A. Finalmente, en el quinto capítulo se encuentran las conclusiones de este trabajo.

# Abstract

Gamma-ray bursts (GRBs) are transient events with a duration of few seconds produced by the collapse of a massive star ( $M > 8M_{\odot}$ ) or by the coalescence of two compact objects. To this day, GRBs are the brightest events known in the universe. However, in spite of their discovery in the decade of the 60s, our understanding of these phenomena is still incomplete in many ways, especially in the prompt phase due to the short duration of GRBs and the response time of telescopes.

This is the motivation for this thesis: to significantly increase the number of photometric observations at early times of GRBs and thus, have a better sample of these events in these phases. In this way, in order to improve the optical observations of transient objects, the arrival of the robotic telescope *COATLI*, installed in 2016 at OAN-SPM and working from May 2017, has contributed with scientific results in the field. *COATLI* together with the *RATIR* instrument mounted on 1.5 meter telescope Harold L. Johnson also at OAN-SPM, allows to have a large temporal coverage of gamma-ray bursts from early epoch to late times.

The main goal was to contribute with observations and interpretations of several GRBs and therefore, this work presents the study of prompt and early emissions of gamma-ray burst using the data set provided by the *COATLI* telescope and the *RATIR* instrument.

In last few years, there have been detected numerous events; however, GRB 130427A stands out, which has been studied from different approaches due to the energy emitted, which means that GRB 130427A, is a transient of great interest in the field of high energy astrophysics. This GRB was observed by *RATIR*, which provided the best photometry in optical/near-infrared of the late phase to the passage of days and months after the event.

On the other hand, *COATLI* had its first set of astronomical data when detecting GRB 180205A 6 seconds after the alert sent by the *BAT-SWIFT* instrument, several seconds before other terrestrial telescopes and that allowed registering a flare after 200 seconds of the flash. The analysis of

GRB 180205A allowed a better understand the central engine. The photometry of this event was supplemented on subsequent nights by RATIR.

Finally, GRB 180418A, candidate for short gamma-ray burst, was observed by the *TAROT* collaboration only 28 seconds after the alert and later by the *RATIR* instrument, and also has early observations in the optical bands presenting a typical reverse component observed previously in many shocks, but the first recorded for a short GRB.

This work includes an introduction to the gamma-ray bursts in the first chapter; in the second chapter we present an overview of telescopes focused on the observation of GRBs, both spatial and terrestrial. The third chapter describes the characteristics and operation of the *COATLI* robotic telescope. In the fourth chapter we include publications as first author made during this doctoral project: the description and analysis of the data obtained with *COATLI* from GRB 180205A; photometric confirmation with data from the *RATIR* instrument of the association of a supernova with GRB 130427A as well as its main characteristics; and the study at early times of the possible SGRB 180418A. Finally, we give our conclusions.

# List of publications

- Becerra, R. L., Dichiara, S., Watson, A. M., et al. 2019, **Reverse shock emission revealed in early photometry in the short GRB 180418A**, ApJ, (submitted).
- Fraija, N., Dichiara, S., Veres P. et al. 2019, **Analysis of the LAT component in the most powerful GRBs**, ApJ, (submitted).
- Fraija, N., Dichiara, S., Galván-Gómez, A. et al. 2019, **Very high energy photons from GRB 190114C**, ApJ, (submitted).
- Becerra, R. L., Watson, A. M., Fraija, N., et al. 2019, **Late Central-engine Activity in GRB 180205A**, ApJ, 872, 118.
- Perley, D. A., Mazzali, P. A., Yan, L., et al. 2019, **The fast, luminous ultraviolet transient AT2018cow: extreme supernova, or disruption of a star by an intermediate-mass black hole?**, MNRAS, 484, 1031.
- Fraija, N., Veres, P., Zhang, B. B., et al. 2017, **Theoretical Description Of GRB 160625B with Wind-to-ISM Transition and Implications for a Magnetized Outflow**, ApJ, 848, 15.
- Becerra, R. L., Watson, A. M., Lee, W. H., et al. 2017, **Photometric Observations of Supernova 2013cq Associated with GRB 130427A**, ApJ, 837, 116.

# Contents

<b>Resumen</b>	<b>iii</b>
<b>Abstract</b>	<b>v</b>
<b>1 Introduction</b>	<b>5</b>
1.1 General . . . . .	5
1.1.1 Spectrum . . . . .	5
1.1.2 Relativistic motion . . . . .	7
1.1.3 Classification . . . . .	7
1.2 Fireball model . . . . .	13
1.2.1 Central engine . . . . .	14
1.2.2 Prompt emission: Internal shocks . . . . .	15
1.2.3 Afterglow: External shock . . . . .	18
1.2.4 Synchrotron emission . . . . .	20
<b>2 Previous observations and current optical ground telescopes</b>	<b>27</b>
2.1 Space observatories . . . . .	27
2.1.1 SWIFT . . . . .	27
2.1.2 FERMI . . . . .	29
2.2 Ground telescopes . . . . .	29
2.2.1 <i>MASTER</i> . . . . .	30
2.2.2 <i>BOOTES</i> . . . . .	30
2.2.3 <i>TAROT</i> . . . . .	30
2.2.4 <i>RAPTOR</i> . . . . .	30
2.3 GCN published . . . . .	32
<b>3 COATLI telescope</b>	<b>33</b>
3.1 Description . . . . .	33
3.2 Extinction correction . . . . .	36
3.3 Interim system . . . . .	36

---

3.4	Measurements Signal-to-Noise . . . . .	37
3.5	Response time . . . . .	37
3.6	Transformation of $w$ to PANSTARRS filters . . . . .	37
3.7	First Results . . . . .	41
<b>4</b>	<b>Observations and publications</b>	<b>43</b>
4.1	Late Central Engine Activity in GRB 180205A . . . . .	43
4.2	Reverse shock emission in GRB 180418A . . . . .	56
4.3	Photometric Observations of Supernova 2013cq Associated with GRB 130427A . . . . .	72
<b>5</b>	<b>Conclusions</b>	<b>97</b>
	<b>References</b>	<b>101</b>





# Chapter 1

## Introduction

### 1.1 General

GRBs are sudden intense flashes of  $\gamma$ -rays. They were discovered in the late 1960s by the military Vela satellites. Their isotropic energies can reach  $10^{54}$  erg (Gehrels et al. 2009).

GRBs are produced at cosmological distances, and they are distributed isotropically (Gehrels et al. 2009). The *BeppoSAX* mission obtained, in collaboration with the *Keck* telescope, the first measurement of the distance for a GRB in 1997 using  $[FeII]$  and  $[MgII]$  absorption lines. The determination of the redshift associated to the GRB 970598 of 0.835 was the first demonstration that GRBs occur at a cosmological distances. Figure 1.1 shows the redshift distribution of GRBs detected by *Swift* mission and available in its catalogue <https://swift.gsfc.nasa.gov/results/batgrbcats/>. The *Swift* mission is described in §4.

#### 1.1.1 Spectrum

The spectrum of a GRB is non-thermal, and the energy flux peak is around 200 keV, and in some cases up to MeV (Figure 1.2). There is a phenomenological fit for their spectrum called the *Band function* (Band et al. 1993) which consist in two power-laws:

$$N(\nu) = N_0 \begin{cases} (h\nu)^\alpha \exp\left(\frac{-h\nu}{E_0}\right) & \text{for } h\nu < (\alpha - \beta)E_0 \\ [(\alpha - \beta)E_0]^{\alpha - \beta} (h\nu)^\beta \exp(\beta - \alpha) & \text{for } h\nu > (\alpha - \beta)E_0, \end{cases} \quad (1.1)$$

where  $E_0$ ,  $\nu$ ,  $\alpha$  and  $\beta$  parameters are the characteristic energy, the frequency, and the temporal index (typically about  $-1 \pm 1$ ) and spectral index (typically about  $-2_{-2}^{+1}$ ) respectively. Here, it is important to remark the empirical sense of this function because, up to today, there is not a

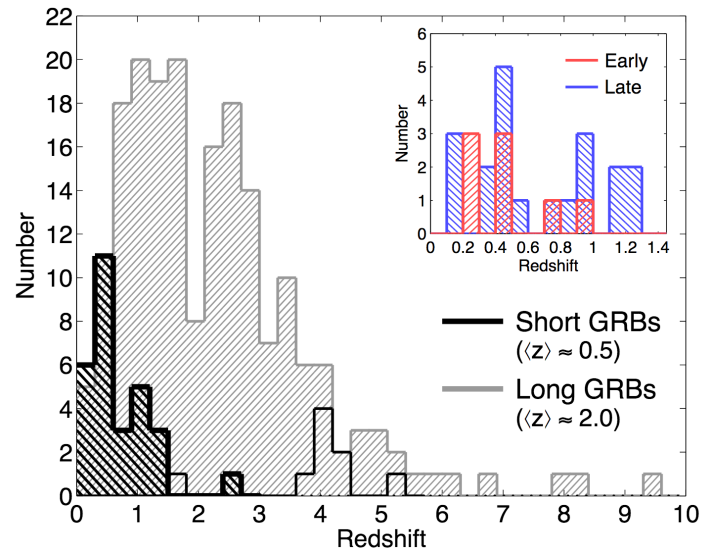


Figure 1.1: The redshift distribution of short GRBs (black) and long GRBs (gray). The open histogram marks redshift upper limits based on the lack of a Lyman- $\alpha$  break in afterglow and/or host galaxy optical detections. The inset shows the redshift distribution of short GRBs separated by host galaxy type, which exhibits no discernible difference between early-type (red) and late-type (blue) hosts. Credits: Berger (2014).

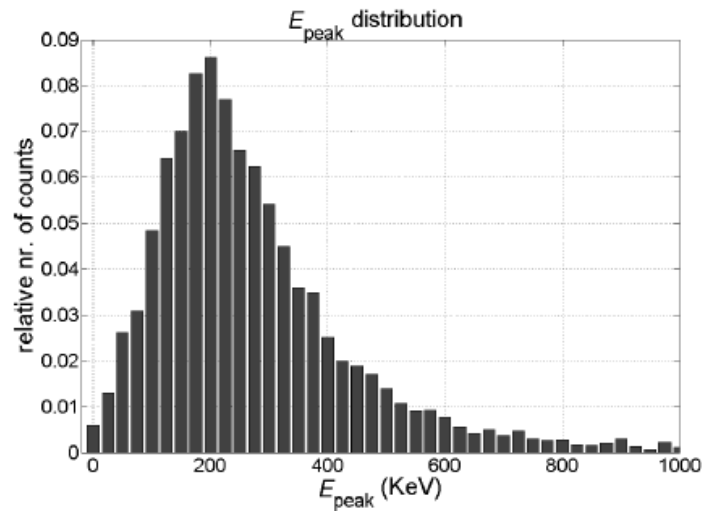


Figure 1.2:  $E_{peak}$  histogram. Credits: Gehrels et al. (2009).

well-defined physical model to reproduce the spectrum of GRB. Even so, the Band function fits a great number of observed spectrum of GRBs.

### 1.1.2 Relativistic motion

As it was mention in previous section, GRBs have a non-thermal spectrum but show a variability in the light curve with a timescale of  $\delta t$ . This implies an emission region size of  $c\delta t$  for the source, where  $c$  is the speed of light. For a GRB, using the observed flux  $F$ , its duration  $t$  and, the distance  $d$  to the observator, it is possible calculates the energy  $E$ . Therefore, the photon density associated  $\approx 4\pi d^2 F / E_\gamma c^3 \delta t^2$  where  $E_\gamma$  is the typical energy of the photon. The process of pair production (to produce  $e^+e^-$ ) occurs if the energy in the center of mass frame is larger than  $2m_e c^2$ . Then, the optical depth for the pair creation is:

$$\tau_{\gamma\gamma} \approx \frac{f_e^\pm \sigma_T 4\pi d^2 F}{E_\gamma c^2 \delta t}, \quad (1.2)$$

where  $f_e^\pm$  is the probability of collision between two photons for a pair creation. The typical values obtained for the equation 1.2 is  $\tau_{\gamma\gamma} \sim 10^{15}$ , which is inconsistent with the observations.

The way to solve this apparent problem, about to observe the GRB in a region with an optical depth  $\tau \gg 1$ , is assuming a relativistic motion toward the observer with a Lorentz factor  $\Gamma$ . Thus, there are two corrections to the previous calculations. First, the size of the source would be  $c\delta t\Gamma^2$ . Second, the energy in the source frame is lower by a factor  $\Gamma$ . The first effect modifies the density by a factor of  $\Gamma^{-4}$  and therefore is the optical depth as  $\Gamma^{-2}$ . The second effect changes the probability of collision  $f_e^\pm$  by a factor of  $\Gamma^{-2\alpha}$ , with  $\alpha$  the value of the spectral index mentioned in the previous section. The Lorentz factor  $\Gamma$  for GRBs is typically about  $10^2 - 10^3$  (Gehrels et al. 2009).

### 1.1.3 Classification

The first study of the temporal properties for the GRBs was done with the catalog produced by the *BATSE* mission. The data obtained shows a bimodal distribution in a histogram for the  $T_{90}$  parameter, which is defined as the time during which 90% of the counts above background are measured (Figure 1.3).

The peaks of the histogram show in Figure 1.3 are at  $T_{90}$  about 0.3 and 20 seconds with a minimum at 2 seconds. Then, it is possible to identify two groups of GRBs using  $T_{90} = 2$  seconds as the

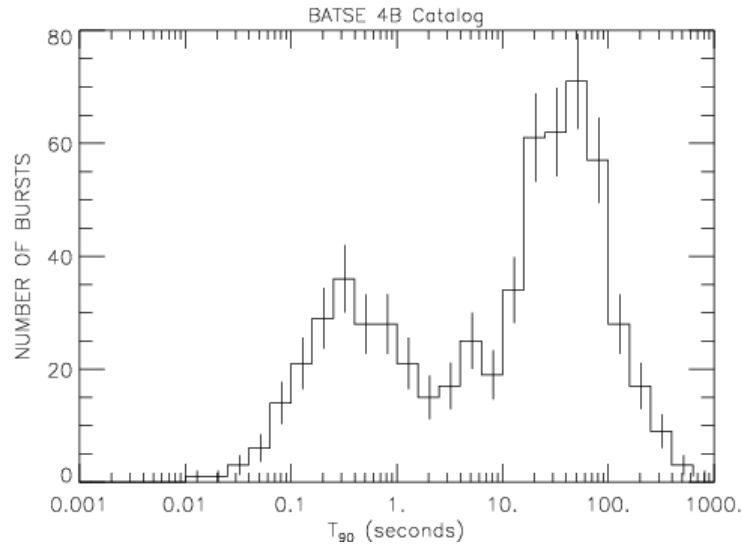


Figure 1.3: BATSE Histogram of GRB with the duration of  $T_{90}$ . The bimodal distribution is associated to two different progenitors for GRBs with a division at  $T_{90} = 2$  seconds. Credits: NASA Compton Gamma-Ray Observatory

break (Kouveliotou et al. 1993): *short gamma-ray bursts (SGRBs)* which have  $T_{90} < 2$  seconds and *long gamma-ray bursts (LGRBs)* which have  $T_{90} > 2$  seconds. Nowadays, it is known that these two groups have different progenitors. In next section we will the main models and characteristics of two groups.

### 1.1.3.1 LGRBs

In order to explain LGRBs, Woosley (1993) proposed the idea of a collapsar rotating around stars whose iron core eventually collapses directly to form a black hole. Seconds after this, the black hole accretes the residual matter of the core and emits a powerful relativistic jet that can be observed as a GRB if it is directed toward the Earth. The progenitors of collapsars are commonly Wolf Rayet stars which also are the progenitors of type Ib/Ic type supernovae.

According to Woosley (1993), there are three conditions needed for the collapsar model: a massive core, the removal of the hydrogen envelope, and the high angular momentum in the core to support the accretion disk around the black hole resulting of the collapse of the massive star.

Woosley (1993) considered stars with main sequence masses greater than  $35M_{\odot}$  which lost their hydrogen envelopes before their death. Using numerical codes, MacFadyen & Woosley (1998) mod-

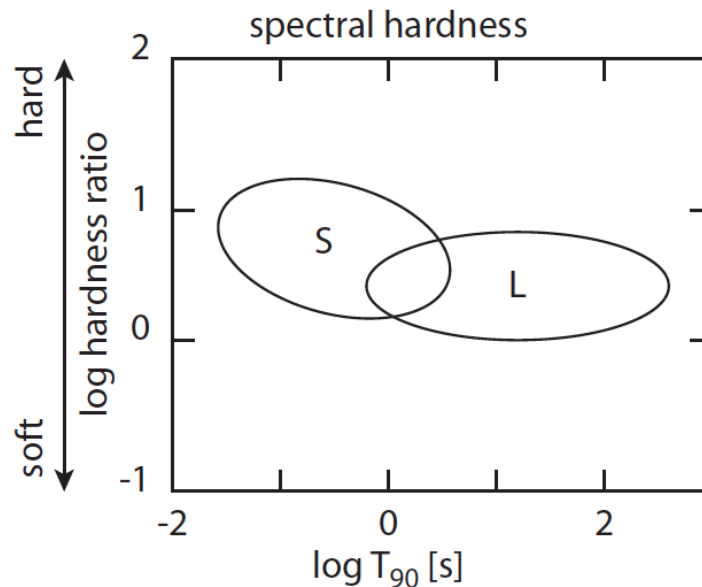


Figure 1.4: Spectral hardness versus observed duration  $T_{90}$ . Credits: [Gehrels et al. \(2009\)](#)

eled a iron core of a rapidly rotating helium star; first, in a neutron star and then in a black hole due to the outgoing shock when it is impossible for it to escape from the collapsing iron core. At the same time, the in-falling matter in the equatorial plane is piled into a disk. A hugely energetic stellar explosion (about  $10^{52}$  erg) is observed powering by hyper-accretion into the black hole. The geometry to produce a jet outflow is likely due to the in-fall into the black hole of the matter along the rotational axis.

Moreover, the jet can be energized by neutrino transport or by magnetohydrodynamical processes. [MacFadyen & Woosley \(1998\)](#) reported a neutrino energy emission up to  $10^{53}$  erg, the a total energy deposited by neutrino annihilation along the rotational axis would be about  $10^{51}$  erg. Thus, the jet is capable of breaking out of the star in about 10 seconds, maintaining the collimation and relativistic speeds. This is the most common accepted explanation for the central engine phase of the LGRBs.

Additionally, the  $\gamma$ -ray emission of LGRBs is *softer* than the emission launched by SGRBs as is shown in Figure 1.4. This means that the ratio between the photon numbers in the detectors' low-energy and high-energy bands is larger for LGRBs than for SGRBs ([Zhang 2014](#)).

**1.1.3.1.1 GRB-SN connection** [Woosley \(1993\)](#) proposed that certain LGRB are associated with SNe. Here, the optical emission from the SN appears a few days after the burst of the GRB,

when the ejecta are optically thin. The *BeppoSAX* mission, launched in 1997, obtained the first data of the SN 1998bw related to GRB980425, giving the observational basis for the connection between GRBs and supernovae.

There are two ways to identify the presence of a SN associated with a GRB. First, by the evolution in the broad spectral lines observed a few days after the burst, the spectrum of GRB turn to a typical SN spectrum. Second, through the rebrightening in the light curve of the GRB after a few days which is due to a supernova. The first confirmed case was in 1998, with the discovery of SN 1998bw within the error box of GRB 980425 (Galama et al. 1998). Subsequently, other LGRB have been identified with a SNe. Confirmed cases are listed in the Table 1.1. Most of these SN are type Ic. Usually, the host galaxies of GRB-SNe are blue, young, star-forming (Fynbo et al. 2000; Foley et al. 2006; Hammer et al. 2006) and likely with a low metallicity environment (Modjaz et al. 2008).

Nevertheless, not all the long GRBs produce a SN explosion. Woosley (1993) suggested two possibilities to explain that. On one hand, there is the *failed Ib* SN scenario, which occurs when a fall-back SNe exists that produces a black hole without an accretion disk in which  $^{56}\text{Ni}$  could be formed. On the other hand, could be due to the low energy deposition at the moment when the jet penetrates the star (Nomoto et al. 2006; Tominaga et al. 2007). Observationally, the low association can also be explained by the difficulty to observe SN II at  $z < 0.5$  due to their low luminosity (compared with the GRB's luminosity) and unfortunately, the sample of GRBs occurred at that distances are just a few (see Figure 1.1).

Table 1.2 summarizes the estimated rate of mergers for several compact objects and compares it with the rate of SNe events. Last ones, will be explained in §1.1.3.2.

### 1.1.3.2 SGRBs

The merger of compact binaries (black holes (BH), neutron stars (NS) and white dwarfs (WD)) scenario was introduced by Paczynski (1986); Goodman (1986); Goodman et al. (1987); Eichler et al. (1989) as candidates for GRBs progenitors. A few years before, in 1975, the first binary pulsar PSR 1913+16 was discovered by Hulse and Taylor. This event brought about the prediction of final stages for binary systems of two neutron stars with a small orbital separation. This separation decreases in time by the gravitational radiation, and therefore, produces the inevitable coalescence of the two neutron stars.

The coalescence between NS-NS depends on the mass. If both helium stars are less massive than  $3M_{\odot}$  and expand their envelopes during core carbon burning, they need a second spiral to produce

GRB	SN	$z$	Evidence	Reference
GRB 980425	SN 1998bw	0.0085	A	1
GRB 011121	SN 2001ke	0.362	B	2, 3, 4
GRB 021211	SN 2002lt	1.006	B	5
GRB 030329	SN 2003dh	0.1687	A	6, 7
GRB 031203	SN 2003lw	0.105	A	8, 9, 10
GRB 050525A	SN 2005nc	0.606	B	11
GRB 060218	SN 2006aj	0.0335	A	12, 13, 14, 15, 16
GRB 081007	SN 2008hw	0.530	B	17, 18, 19
GRB 091127	SN 2009nz	0.49	A	20, 21
GRB 100316D	SN 2010bh	0.059	A	22, 23, 24, 25, 26
GRB 120422A	SN 2012bz	0.283	A	27, 28
GRB 130427A	SN 2013cq	0.34	A	29, 30, 31
GRB 130702A	SN 2013dx	0.145	A	32, 33
GRB 140606B	iPTF14bfu	0.384	A	34

Table 1.1: GRB with SN associated. The evidence for the GRB-SN connection according to the authors is listed in column (4) according to the criteria: A: Strong spectroscopic evidence. B: A clear light curve bump as well as some spectroscopic evidence resembling a GRB-SN. (1) Galama et al. (1998); (2) Bloom et al. (2002); (3) Garnavich et al. (2003); (4) Greiner et al. (2003); (5) Della Valle et al. (2003); (6) Stanek et al. (2003); (7) Matheson et al. (2003); (8) Malesani et al. (2004); (9) Gal-Yam et al. (2004); (10) Thomsen et al. (2004); (11) Della Valle et al. (2006); (12) Campana et al. (2006); (13) Modjaz et al. (2008); (14) Mirabal et al. (2006); (15) Ferrero et al. (2006); (16) Pian et al. (2006); (17) Berger et al. (2008); (18) Della Valle et al. (2008); (19) Soderberg et al. (2008); (20) Cobb et al. (2010); (21) Berger et al. (2011); (22) Starling et al. (2011); (23) Bufano et al. (2012); (24) Olivares E. et al. (2012); (25) Cano et al. (2011); (26) Chornock et al. (2010); (27) Melandri et al. (2012); (28) Schulze et al. (2014); (29) de Ugarte Postigo et al. (2013); (30) Xu et al. (2013); (31) Becerra et al. (2017); (32) Toy et al. (2016); (33) D’Elia et al. (2015); (34) Cano et al. (2015)

<b>Progenitor</b>	<b>Rate (z=0)</b> [ $yr^{-1}Gpc^{-3}$ ]
NS-NS (LIGO)	0.3-4.7
BH-NS	0.1-1000
BH-WD	0.01-100
WD-WD	3000
BH-BH (LIGO)	12-213
SN Ib/c	60000
SN Ia	150000
SGRBs	$1540^{+300}_{-1220}$

Table 1.2: The rates of the likely progenitors of SGRBs. Credits: [Lee & Ramirez-Ruiz \(2007\)](#); [Belczynski et al. \(2018\)](#); [Mandhai et al. \(2018\)](#).

a merger within a Hubble time. On the other hand, for more massive cores producing a black hole remnant which does not expand too much, the second spiral is not needed ([Lee & Ramirez-Ruiz 2007](#)). The rate of BH-NS and NS-NS are similar, but the fraction of them that end in a merger depends on the mass transfer and spiral-in which determinates the final period distribution.

Table 1.3 summarizes the main features for both, LGRBs and SGRBs.

In observational tests, [Lee & Ramirez-Ruiz \(2007\)](#) reported environment densities for SGRBs lower than the ISM (assumed for usual models). This could be produced by the ejection of the binary system from the host galaxy into an external environment after the kinetic kick predicted in the SGRs model for the coalescence of compact objects [Lee & Ramirez-Ruiz \(2007\)](#).

Recently, the detection of the gravitational waves in 2015 resulting from a coalescence of two black holes by the LIGO collaboration ([Abbott et al. 2016](#)), the first observation of the collision of two neutron stars signal also by LIGO ([Abbott et al. 2017a](#)) and the different electromagnetic observations later, have reactivate the study of the gamma-ray bursts. These events have given us new clues and constrains about the progenitors of SGRBs as well as their rates. The kilonova associated to this event add information to a better understanding of the origin of heavy metals (see e.g. [Abbott et al. 2017c](#)). Moreover, GRB 170817A is the first GRB observed *off axis* ([Troja et al. 2018](#)). This implies the study of others components of the jet, the contribution to the the emission from the cocoon and the projection of the jet ([Mooley et al. 2018](#)).



Feature	SGRB	LGRB	Reference
Duration $T_{90}$	$< 2$ s	$> 2$ s	1, 10, Figure 1.3
Progenitors	Merger between CO	Massive star	1, 2
Mean redshift $z$	0.5	2	3, 4, 5, Figure 1.1
Spectral hardness (Fluence in 50–100 keV / 20–50 keV)	2	1	1, Figure 1.4
Host galaxy star formation	Low	High	5, 6, 7, 8, 9
Host galaxy type	Irregular, regular, spiral elliptical galaxies	Spiral	10, 11, 12, 13

Table 1.3: Main features of short and large GRBs. (1) Gehrels et al. (2009); (2) Lee & Ramirez-Ruiz (2007); (3) Berger et al. (2007); (4) Jakobsson et al. (2006); (5) Berger (2014); (6) Gehrels et al. (2005), (7) Bloom et al. (2006); (8) Fox et al. (2005), (9) Le Floc’h et al. (2005), (10) Leibler & Berger (2010), (11) Kouveliotou et al. (1993)

From the GW 170817A/GRB 170817A, we are able to understand better the radiation mechanisms involved and even more important: they have opened up the multi-messenger era for the transients astronomy (Abbott et al. 2017b).

## 1.2 Fireball model

The most accepted theory to explain the GRBs is the *fireball model*. The traditional fireball model (sketched in Figure 1.5) assumes a thermally-driven explosion, with gravitational energy released during a catastrophic event (such as a massive star core collapse or the merger of two compact stars, as was mentioned in § 1.1.3.2) which is deposited at the base of the central engine (Zhang 2014). The isotropic energy emitted is described by  $E_{iso} = (4\pi/\Omega_j)E_j$  where  $\Omega_j$  is the jet solid angle, and the suffix  $j$  refers to the *jet*. The luminosity of the outflowing material is  $L_{iso} \sim E_{iso}/t$ , where  $t$  is the duration of the GRB.

This fireball expands under its own thermal pressure and accelerates to relativistic speeds. Most of the thermal energy is converted into the kinetic energy of the outflow (Rees & Meszaros 1992). The kinetic energy of the outflow is further dissipated in the internal and external (forward and reverse) shocks as the ejecta is decelerated by the environment. The internal shocks power the prompt emission and the external shock powers the afterglow (Grupe et al. 2013). The following subsections describe in more detail the main stages in the fireball model.

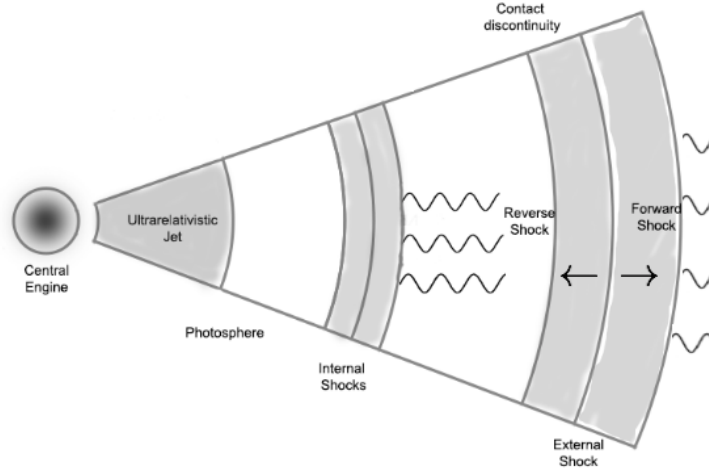


Figure 1.5: Fireball model

### 1.2.1 Central engine

Any successful GRB central engine model should be able to launch an extremely energetic and luminous jet whose luminosity greatly exceeds the Eddington luminosity; the jet must be clean, i.e. energy per baryon must be larger than  $m_p c^2$ , so that the outflow can reach ultra-relativistic speed with Lorentz factor greater than  $10^2$ ; the engine should be intermittent as observationally suggested by the erratic rapidly variable light curves, and the central engine should be able to re-activate at later times to power softer flares (Zhang 2014). Nowadays, there are two types of candidates for central engines that can satisfy these requirements: a hyper-accreting stellar-mass black hole (Woosley 1993), and a rapidly spinning, highly magnetized, neutron star or a fast magnetar (Usov 1992).

As was explained in § 1, SGRBs are the result of the coalescence of two compact objects. Janiuk et al. (2017) explain the central engine for this process using a hot and dense accretion disk with a hyper-Eddington accretion rate near a spinning BH. For this environment and due to the high densities and temperatures, it is impossible assuming an equation of state of an ideal gas. The pressure and chemical balance is required by the nuclear reactions that take part between the free protons, neutrons, and electron-positron pairs abundant in the plasma. There are many  $\beta$  reactions and therefore, neutrinos. The partially trapped neutrinos contribute to the pressure in the plasma, together with nucleons, electron-positron pairs, radiation, and helium particles and are very important for explaining the cooling processes. Moreover, the neutrinos are possible candidates to power the GRB jet in this kind of events.

On the other hand, for LGRBs Levan et al. (2016) discusses the millisecond-magnetar model.

Millisecond-magnetars are likely created from the collapse of some fraction of massive stars formed via the merger of either white dwarfs or neutron stars with a resulting mass below the maximum mass of a neutron star. These neutron stars with extreme magnetic fields can have rapid spin-down times, or may even be unstable and centrifugally supported. This model of millisecond-magnetars provide a route to explain not only energy input into the GRB afterglow on timescales of minutes to hours after the initial burst but also the most luminous SNe. In this case, the energy extracted from the millisecond-magnetar re-energises the outgoing supernova shock and creates the additional luminosity.

### 1.2.2 Prompt emission: Internal shocks

The prompt emission phase is defined as the temporal interval during which gamma-ray emission from a GRB is detected by an instrument above its background level. The prompt  $\gamma$ -rays from a GRB are emitted when a significant fraction of the fireball kinetic energy is converted back to radiation energy. The most accepted model for prompt  $\gamma$ -ray emission is called *internal shocks* which consists in collisions between shells of plasma or fireballs, with different Lorentz's factors, generating shocks, where a fraction of their bulk kinetic energy is converted into random motion. Finally, this energy will be radiated via synchrotron emission, and observed as non-thermal  $\gamma$ -rays emission. This model is shown in Figure 1.6.

#### 1.2.2.1 Derivation

Internal shocks occur when a faster shell catches a slower one. The radius in which this takes place is defined by:

$$R_{int} = c\delta t\Gamma^2 = 3 \times 10^{14}\Gamma_{100}^2\overline{\delta t} \quad cm, \quad (1.3)$$

where  $\Gamma_{100}$  is a typical value for the Lorentz factor in units of 100 and  $\overline{\delta t}$  is the time difference between the emission of the two shells. Considering the collisions between two shells with masses  $m_r$  and  $m_s$  ( $r$  and  $s$  are the subfixes related with *slow* and *rapid*) that have different velocities:  $\Gamma_r \gtrsim \Gamma_s \gg 1$ , the resulting Lorentz factor of the collision is:

$$\Gamma_m \simeq \sqrt{\frac{m_r\Gamma_r + m_s\Gamma_s}{m_r/\Gamma_r + m_s/\Gamma_s}}. \quad (1.4)$$

The internal energy  $E_{int}$  is defined as the difference of the kinetic energy before and after the

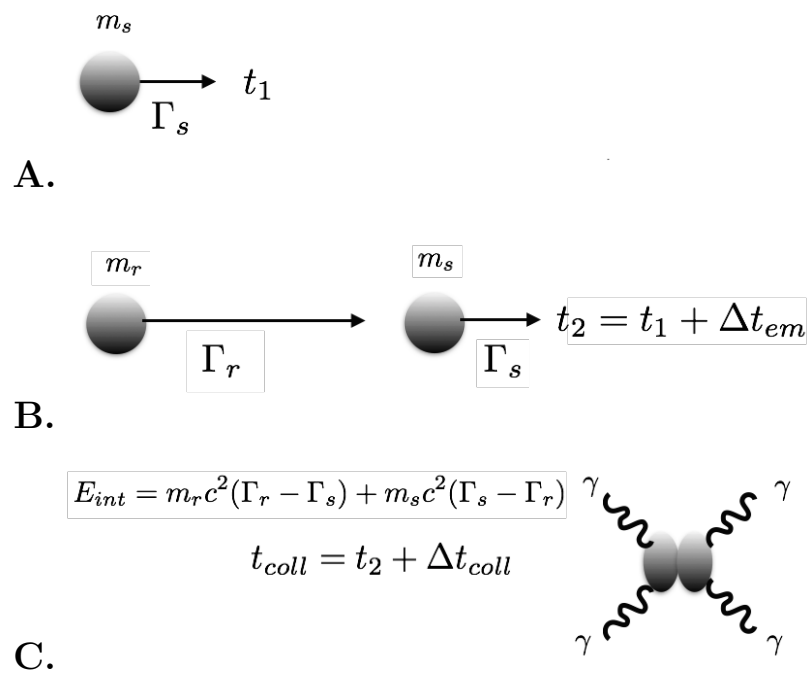


Figure 1.6: Gamma-rays production by internal shocks. A) A first shell with a Lorentz's factor  $\Gamma_s$  and mass  $m_s$  is produced at  $t_1$  and chased by another shell faster with a Lorentz's factor  $\Gamma_r$  with mass  $m_r$  emitted later in B) at  $t_2$ . The collision appears in C) when the second shell catches the first one at time  $t_{coll}$ .

collision and is given by:

$$E_{int} = m_r c^2 (\Gamma_r - \Gamma_m) + m_s c^2 (\Gamma_s - \Gamma_m). \quad (1.5)$$

The efficiency of conversion of kinetic energy into internal energy is:

$$\epsilon = 1 - \frac{(m_r + m_s)\Gamma_m}{m_r\Gamma_r + m_s\Gamma_s}. \quad (1.6)$$

For this mechanism of conversion to convert a significant fraction of the kinetic energy into internal energy, we require a large difference in velocities between the shells, i.e.,  $\Gamma_r \gg \Gamma_s$  and with that masses be comparable (Kobayashi et al. 1999; Guetta et al. 2001). Several computational simulations (e.g., see Kobayashi et al. 1999; Guetta et al. 2001) have shown that the value of efficiency is around  $\epsilon = 0.1$  and therefore, the necessary Lorentz factors are between 10 and 10000.

The internal shocks model reproduces the pulse width and pulse separations observed in the light curves. Considering two shells with a separation  $L$  with Lorentz factors of  $\Gamma_s$  and  $\Gamma_r$  for the slower and faster shell respectively. For an efficient collision we required that  $\Gamma_r = a\Gamma_s$  with  $a > 2$  (Beloborodov 2000). The ejecta time of the shells are  $t_1$  and  $t_2 \approx t_1 + L/c$  and therefore, the collision happens at a radius  $R_s \approx 2\Gamma^2 L$ . The emitted photons from the collision will be detected by the observer at time:

$$t_o \approx t_1 + R_s/(2c\Gamma^2) \approx t_1 + L/c \approx t_2. \quad (1.7)$$

### 1.2.2.2 Temporal features

The photons produced from this pulse are observed almost at the same time that the photons emitted from the central engine together with the second shell. Thus, the temporal activity observed by the source can be explained by internal shocks. Observationally, there are some characteristics that are common in most GRBs:

- The duration  $T_{90}$  ranges from milliseconds to thousands of seconds.
- The light curves are irregular and different.
- There is evidence that the GRBs light curves are the superposition of slow and fast components (Vetere et al. 2006).

- The shape of the pulses is not symmetric, usually it is modeled as a FRED (Fast-Rising Exponential-Decay) function (Kouveliotou et al. 2013).
- Light curves can depend on the band energy.

### 1.2.3 Afterglow: External shock

The afterglow theory was proposed because the internal shocks are not able to explain the total duration of the emission of GRBs observed at lower frequencies (optical, IR and radio). For that, it was necessary to take into account the interaction between the relativistic jet and the circumburst medium, i.e., the relativistic blast wave. This blast wave is usually described by a density profile  $n(r) = Ar^{-k}$  with  $k = 0$  for a constant ISM density and  $k = 2$  in a stellar wind environment. Both, temporal and spectral evolution are described using power-law segments. This model was proposed by Paczynski & Rhoads (1993); Mészáros & Rees (1997) before the first detection of an X-ray afterglow in 1997 by the *BeppoSAX* satellite. The complete relativistic shock model is developed by Blandford & McKee (1976).

When a cold relativistic shell moves into the ISM, two shock regions are formed: an outgoing shock that propagates into the surrounding medium and a reverse shock that propagates into the inner shell, with a contact discontinuity between the shocked material. These regions are also divided into four distinct regions according to Piran (2004). These regions are shown in Figure 1.7:

The dynamics of the reverse shock is more complicated than the solution for the forward shock component. Nevertheless, the effect can help to understand better the GRB jet composition. This component is discussed in Sari & Piran (1999), and its effect can be observed in several light curves. However, the reverse shock is less energetic than the forward shock, and therefore, it is not always observable.

It is easiest to understand the external shock in a comoving frame, where a shocked fluid is traveling with a Lorentz factor  $\Gamma$  with respect to the unshocked fluid. The density of the unshocked medium is  $n\Gamma$ . In the shock, there is a randomization of the particle velocity vectors (which does not affect their Lorentz factors) and therefore, when they cross the shock front, the thermal energy of protons is  $\Gamma m_p c^2$  whereas in the observer's frame it is  $\Gamma^2 m_p c^2$ .

The deceleration radius  $R_d$  (radius in which the Lorentz factor decreases by a factor of 2 from the initial value  $\Gamma_0$ ) is obtained for a constant density profile as:

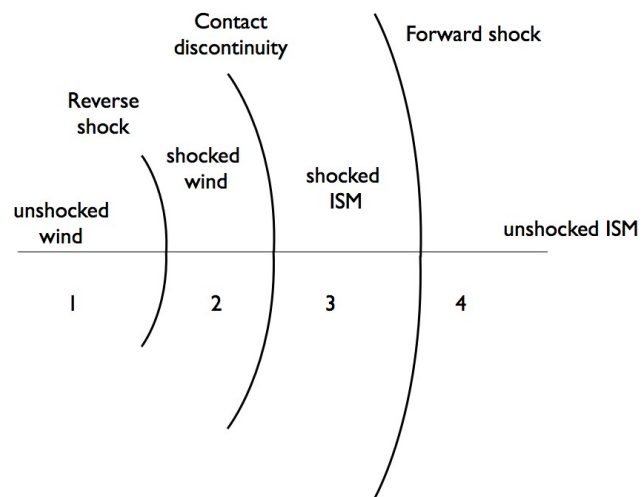


Figure 1.7: Regions observed in a model of a cold relativistic shell moves into the ISM, the shock responsible of the afterglow is represented by the contact discontinuity. Two components are formed, the reverse shock behind of it (region 2) and the forward shock component (region 3) along the jet's direction. Regions 1 and 4 represents the material unshocked by the reverse and forward component respectively. Credits: [Lyutikov \(2017\)](#).

$$R_d \sim (1.2 \times 10^{17} \text{ cm}) E_{53}^{1/3} n^{-1/3} \Gamma^{-2/3}. \quad (1.8)$$

where  $E_{53}$  is the energy in units of  $10^{53}$  erg,  $n$  is the density and  $\Gamma$  is the initial Lorentz factor.

The accelerated particles produce a power-law distribution function and generate magnetic fields. The equations which describes the conservation of baryon number, energy and momentum fluxes across the shock front are calculated in the work of [Blandford & McKee \(1976\)](#):

$$\frac{e_2}{n_2} = (\Gamma_{21} - 1) m_p c^2, \quad (1.9)$$

$$\frac{n_2}{n_1} = \frac{\hat{\Gamma} \Gamma_{21} + 1}{\hat{\Gamma} - 1}, \quad (1.10)$$

$$\Gamma_{1s}^2 = (\Gamma_{21} + 1) [\hat{\Gamma}(\Gamma_{21} - 1) + 1]^2 \hat{\Gamma} (2 - \hat{\Gamma}) (\Gamma_{21} - 1) + 2, \quad (1.11)$$

where  $m_p$  is the proton mass,  $c$  the speed of light, the subscripts 2 and 1 are the shocked and unshocked medium respectively,  $e$  and  $n$  are the internal density and proton number density,  $\hat{\Gamma}$  is the adiabatic index of the fluid,  $\Gamma_{21}$  and  $\Gamma_{1s}$  are the relative Lorentz factor between regions 2 & 1 and the relative Lorentz factor between region 1 and the shock front.

#### 1.2.4 Synchrotron emission

The process most important in a GRB is synchrotron emission. The complete description is in [Rybicki & Lightman \(1985\)](#). This is explained considering an electron with a Lorentz factor  $\Gamma_e$ , and speed  $v_e$ , moving perpendicular to a magnetic field of strength  $B$ . The electric field in the electron's rest frame is:

$$E = \Gamma_e v_e B / c. \quad (1.12)$$

Using the Larmor formula:

$$P = \frac{2q^4 E^2}{3c^3 m_e^2}, \quad (1.13)$$

the power radiated is therefore:

$$P_{syn} = \frac{2q^4 B^2 \Gamma_e^2 v_e^2}{3c^5 m_e^2} = \frac{\sigma_T B^2 \Gamma_e^2 v_e^2}{4\pi c}, \quad (1.14)$$



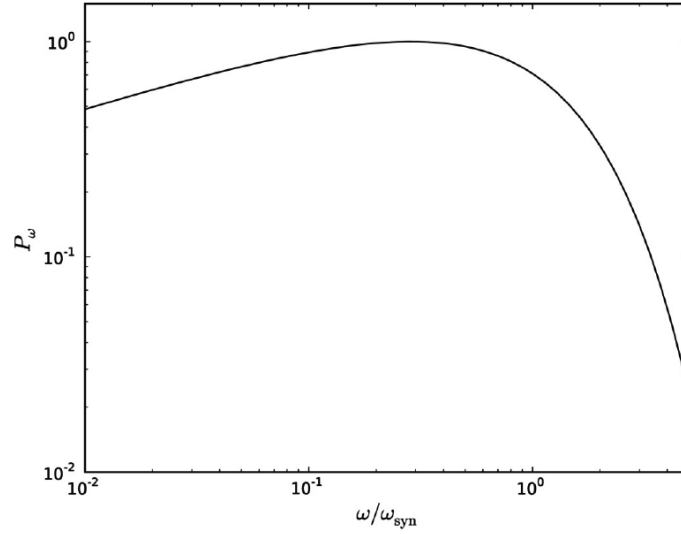


Figure 1.8: Synchrotron spectrum for a single electron; the flux is normalized to the flux in the peak and the frequency is in units  $\omega_{syn}$ . Credits: [Rybicki & Lightman \(1985\)](#)

and the Larmor frequency of the electron is:

$$\omega_L = \frac{qB}{\Gamma_e m_e c}. \quad (1.15)$$

Due to the relativistic beaming effects, the radiation received by an observer is confined to the time when the electron velocity vector lies within an angle  $1/\Gamma_e$  for the observer. The fraction of orbital time when this condition is satisfied is about  $1/\pi\Gamma_e$  and therefore the duration of the radiation pulse received by the observer in each orbit is:

$$\delta t_{obs} \sim \frac{2}{\Gamma_e \omega_L} \frac{1}{2\Gamma_e^2} \sim \frac{m_e c}{qB\Gamma_e^2}, \quad (1.16)$$

The inverse of this time is the characteristic frequency for synchrotron radiation which is given by:

$$\omega_{syn} = \frac{qB\Gamma_e^2}{m_e c}, \quad \nu_{syn} = \frac{\omega_{syn}}{2\pi} \sim \frac{qB\Gamma_e^2}{2\pi m_e c}, \quad (1.17)$$

where  $\nu_{syn}$  is the cyclic frequency. The synchrotron spectrum (Figure 1.8) peaks at  $\sim \nu_{syn}$ . The spectrum below the peak scales as  $P_{syn}(\nu) \propto \nu^{1/3}$  and it declines exponentially for  $\nu > \nu_{syn}$ .

For a power-law distribution of electrons,  $dn_e/d\Gamma_e \propto \gamma_e^{-p}$ , the total synchrotron emission can be calculated by adding the contributions to the specific flux at  $\nu$  from those electrons with Lorentz factors larger than:

$$\Gamma_\nu \left( \frac{2\pi\nu m_e c}{qB} \right)^{1/2}, \quad (1.18)$$

therefore, the total emission is:

$$F_\nu = \int_{\Gamma_\nu}^{\infty} d\Gamma_e \frac{dn_e}{d\Gamma_e} P_{syn}(\nu) \propto \nu^{-(p-1)/2} \quad (1.19)$$

with  $P_{syn}(\nu) \propto (\nu/\nu_{syn})^{1/3}$  for  $\nu < \nu_{syn}$  and the equation 1.17 for  $\nu_{syn}$ . Typically, the  $p$  parameter is  $2 < p < 3$ .

#### 1.2.4.1 Synchrotron cooling

Considering that the electrons are accelerated by the shock, and then cool via synchrotron radiation for time duration  $t_0$ , the electrons with Lorentz factor larger than  $\Gamma_c$  defined by:

$$\frac{dm_e c^2 \Gamma_e}{dt} = \frac{-\sigma_T}{6\pi} B^2 \Gamma_e^2, \quad \Gamma_c \sim \frac{6\pi m_e c}{\sigma_T B^2 t_0} \quad (1.20)$$

lose their energy during this time and therefore their Lorentz factor decreases below  $\Gamma_c$ . The synchrotron cooling frequency is:

$$\nu_c = \frac{3qB\Gamma_c^2}{4\pi m_e c} \sim \frac{27\pi q m_e c}{\sigma_T^2 B^3 t_0^2}. \quad (1.21)$$

The characteristic frequency  $\nu_c$  depends on the regime of GRB, this will discuss in §1.2.4.3. For a slow-cooling regime, the typical  $\nu_c$  is about  $10^{16}$  Hz whereas for a fast-cooling, the typical  $\nu_c$  is about  $10^{14}$  Hz (Granot & Sari 2002).

#### 1.2.4.2 Synchrotron self-absorption

There is another characteristic frequency,  $\nu_a$ , corresponding to the case of absorption by photons due to the inverse-synchrotron process. Using the Kirchhoff's law, the emergent specific flux cannot exceed the black-body flux corresponding to the appropriate electron temperature which is:

$$k_B T \sim \frac{\max(\Gamma_a, \min[\Gamma_m, \Gamma_c]) m_e c^2}{2.7}, \quad (1.22)$$

where  $k_B$  is the Boltzmann constant. The synchrotron self-absorption frequency ( $\nu_a$ ) is the frequency at which the emergent synchrotron flux is equal to the black-body flux:

$$2m_e c^2 \nu_a^2 \frac{\max(\Gamma_a, \min[\Gamma_m, \Gamma_c])}{2.7 c^2} \sim \frac{\sigma_T B m_e c^2 N_{>}}{4\pi q}, \quad (1.23)$$

where the left side is Planck's law in the Rayleigh-Jeans limit, and  $N_{>}$  is the column density of the electrons with Lorentz factor larger than  $\max(\Gamma_a, \min[\Gamma_m, \Gamma_c])$ .

The characteristic frequency  $\nu_a$  depends on the regime of GRB, this will discuss in §1.2.4.3. For a slow-cooling regime, the typical  $\nu_a$  is about  $10^{13} - 10^{15}$  Hz whereas for a fast-cooling, the typical  $\nu_c$  is about  $10^{12} - 10^{13}$  Hz (Granot & Sari 2002).

### 1.2.4.3 Afterglow synchrotron spectrum

Using the frequencies described in previous sections ( $\nu_{syn}$ ,  $\nu_a$  and  $\nu_c$ ),  $\Gamma_m$ ,  $\Gamma_a$  and  $\Gamma_c$ , it is possible to describe the spectrum of the afterglow. In this subsection, we summarize the main results.

The afterglow spectrum is characterized by a multi-segment power-law (Sari et al. 1998) in which the break frequencies are described in previous sections: the typical synchrotron frequency of accelerated electrons with the minimum Lorentz factor  $\nu_m$ , the cooling frequency  $\nu_c$  and the synchrotron self-absorption frequency  $\nu_a$ . At early phases of the afterglow (days), the self-absorption is smaller than the other two. Thus, the spectrum can be classified according to the order of  $\nu_m$  and  $\nu_c$ ; if  $\nu_m < \nu_c$  the spectrum is called *slow cooling* and is described by:

$$F_\nu = \begin{cases} F_{\nu, \max} \left( \frac{\nu_a}{\nu_m} \right)^{1/3} \left( \frac{\nu}{\nu_a} \right)^2 & \nu < \nu_a, \\ F_{\nu, \max} \left( \frac{\nu}{\nu_m} \right)^{1/3} & \nu_a < \nu < \nu_m, \\ F_{\nu, \max} \left( \frac{\nu}{\nu_m} \right)^{-(p-1)/2} & \nu_m < \nu < \nu_c, \\ F_{\nu, \max} \left( \frac{\nu_c}{\nu_m} \right)^{-(p-1)/2} \left( \frac{\nu}{\nu_c} \right)^{-p/2} & \nu > \nu_c, \end{cases} \quad (1.24)$$

whereas, if  $\nu_c < \nu_m$ , the spectrum is *fast cooling* and is described by:

$$F_\nu = \begin{cases} F_{\nu,\max} \left(\frac{\nu_a}{\nu_c}\right)^{1/3} \left(\frac{\nu}{\nu_a}\right)^2 & \nu < \nu_a, \\ F_{\nu,\max} \left(\frac{\nu}{\nu_c}\right)^{1/3} & \nu_a < \nu < \nu_c, \\ F_{\nu,\max} \left(\frac{\nu}{\nu_c}\right)^{-1/2} & \nu_c < \nu < \nu_m, \\ F_{\nu,\max} \left(\frac{\nu_m}{\nu_c}\right)^{-1/2} \left(\frac{\nu}{\nu_c}\right)^{-p/2} & \nu > \nu_m, \end{cases} \quad (1.25)$$

where  $F_{\nu,\max}$  is the maximum flux density  $F_\nu(\nu_m)$  for slow cooling, and is  $F_\nu(\nu_c)$  for fast cooling. The Figure 1.9 shows a general picture of both regimes.

There are many works where are the complete description of more complex scenarios than power-law segments described previously and the evolution of them. [Kobayashi & Zhang \(2007\)](#) discusses the reference time  $t_0$  of afterglow light curves in the context of the standard internal-external shock model. The importance of this study is to show that this reference time modifies the decay index of early afterglow, and in order to understand the nature of early afterglow, it is essential to take it correctly. Other work, [Fraija et al. \(2016\)](#) explains in the synchrotron emission from the adiabatic forward shock of SGRB 090510 using synchrotron self-Compton emission from the reverse shock in a environment with strong magnetic fields and study the evidence of magnetic field amplification in the neutron star merger. Another example is a leptonic model based on an early afterglow that evolves in a stellar wind of its progenitor developed by [Fraija \(2015\)](#).

#### 1.2.4.4 Afterglow light curve

The canonical X-ray light curve for the afterglow is shown in the Figure 1.10. In there are mentioned the characteristic values for temporal indexes and durations for each phase. The main phases described in ([McBreen et al. 2010](#)) which are observed in X-ray light curves can be listed:

1. **Steep decay.** It is the tail of the prompt emission. It has a temporal decay index steeper than -2. This phase is interpreted as the high altitude emission associated with the prompt gamma-rays when the central engine turns off faster than the decline of X-ray light curve. If the emission region has a radius much smaller than  $R=10^{15}\text{cm}$ , this phase reflects the time dependence of the central engine activity.
2. **Shallow decay phase or plateau phase:** The temporal decay is shallow with a slope of  $-0.5$  or flatter. To incorporate this phase in the external shock model, one must consider continuous energy injection into the blast wave.

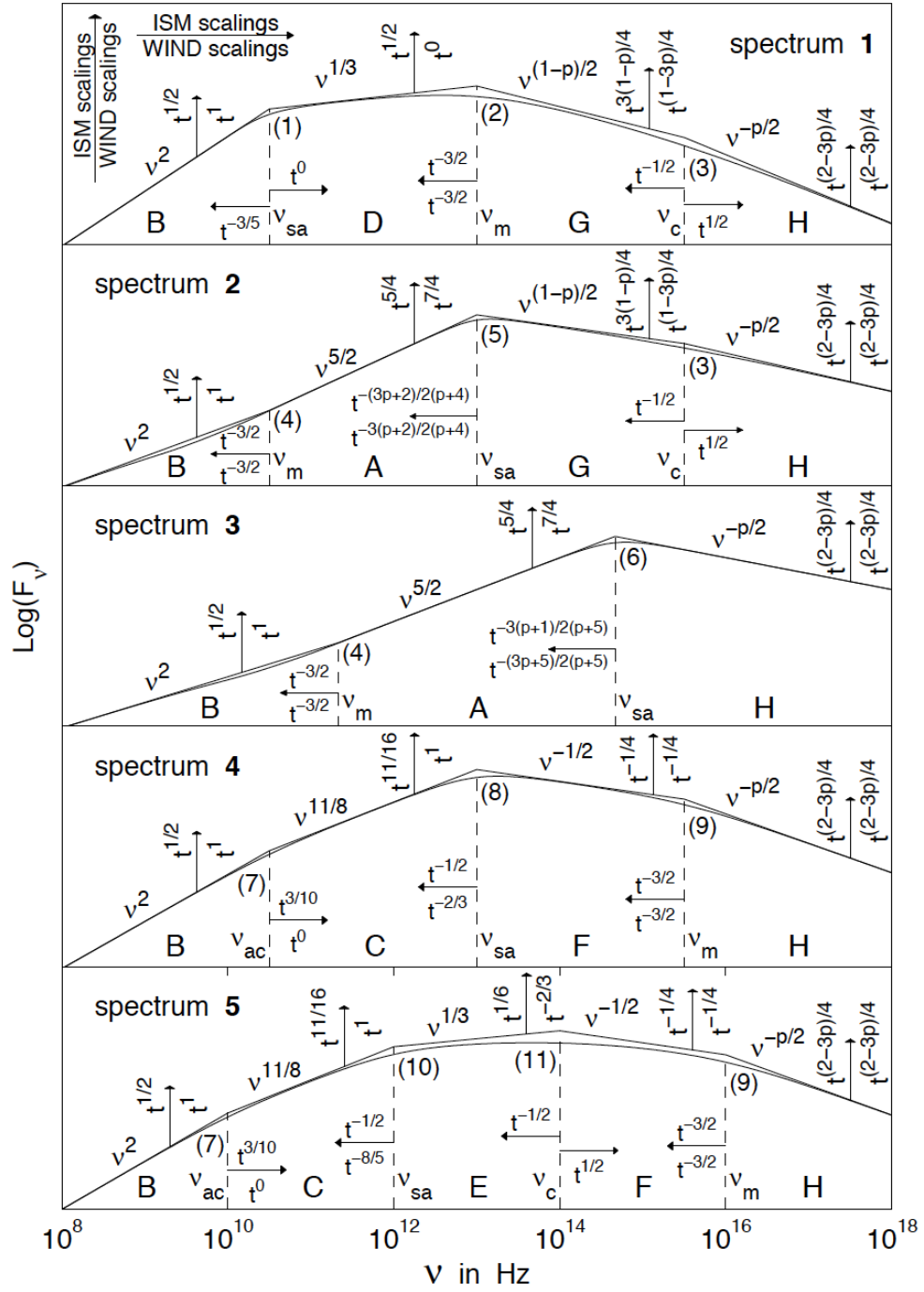


Figure 1.9: Different synchrotron spectra from a relativistic blast wave that accelerates the electrons to a power-law distribution of energies. The top two panels (spectra 1 and 2) correspond to slow cooling ( $\nu_m < \nu_c$ ). Spectrum 1 applies when  $\nu_{sa} < \nu_m$ , while spectrum 2 applies when  $\nu_m < \nu_{sa} < \nu_c$ . The two bottom panels (spectra 4 and 5) correspond to fast cooling ( $\nu_c < \nu_m$ ). Spectrum 5 applies when  $\nu_{sa} < \nu_c$ , and spectrum 4 applies when  $\nu_c < \nu_{sa} < \nu_m$ . Spectrum 3 (middle panel) applies when  $\nu_{sa} > \nu_m$ . Credits: [Granot & Sari \(2002\)](#).

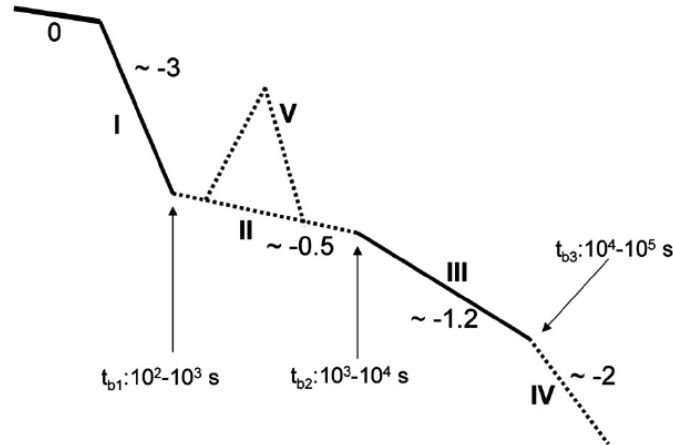


Figure 1.10: Canonical X-ray light curve afterglow. Each phase shows the typical values for temporal indexes and durations. 0: Counterpart of prompt emission. I: Steep decay. II: Plateau. III: Normal decay. IV: Late steep decay. V: X-rays flares. Credits: [McBreen et al. \(2010\)](#).

3. **Normal decay phase:** This phase has a typical temporal index about -1, which is expected by the standard forward shock model.
4. **Late steep decay phase:** In the standard forward shock model it is expected as a jet break (it is a chromatic break in the afterglow light curve due to the sideways beaming of the relativistic emission) proposed by [Piran \(2004\)](#). It has a temporal index about -2 or steeper.
5. **X-ray flares:** They are powered typically by late central engine activity and share many properties with prompt emission.

The jet break is seen in the light curve in the steepening phase and is produced by the *edge* effect. For a jets moving with a Lorentz factor  $\Gamma$ , the photons emitted at any point are beamed within a  $\theta_j = 1/\Gamma$  cone in the lab frame ([Rybicki & Lightman 1985](#)). At early times, the observer only sees the radiation from a small fraction of the jet, but, when the jet decelerates, the  $1/\Gamma$  increases and the photon beaming are comparable to the opening angle of jet-cone. The jet break happens when these condition is satisfied.

In this section, we described the X-ray canonical light curve due to the larger sample of afterglows detected in X-rays. For optical, IR and radio bands, the analysis and interpretations of the different regions are basically the same and the temporal behavior can be considerer achromatic.

## Chapter 2

# Previous observations and current optical ground telescopes

### 2.1 Space observatories

After more than 50 years of the first detection of a GRB in 1967 by the Vela satellites, the most important current space missions for the study of GRBs are the *Swift* and *Fermi* satellites (Gehrels & Razzaque 2013).

Before them, the study of GRBs was carried on mainly by the Burst and Transient Source Experiment (*BATSE*), *BeppoSAX* and the High Energy Transient Explorer (*HETE-2*). *BATSE* data allowed the classification by duration into two categories, long and short, and determined that the distribution of the burst around the entire sky is isotropic. Moreover, *BeppoSAX* obtained the first detection of an X-rays afterglow and proved the cosmological origin of the GRBs. *HETE-2* obtained spectroscopic data of the GRB030329 as another confirmation of the GRB-SN connection.

Nowadays, the *Swift* and the *Fermi* satellites are complementary between them. A brief description of both is presented below.

#### 2.1.1 SWIFT

The Neil Gehrels Swift Observatory ([http://swift.gsfc.nasa.gov/about\\_swift/](http://swift.gsfc.nasa.gov/about_swift/)), launched in 2004 and shown in Figure 2.1, is an observatory whose purpose is the study of GRBs. Within its objectives are determining their origin, classifying them, giving information about their environment and studying the early universe. *Swift* has three instruments:

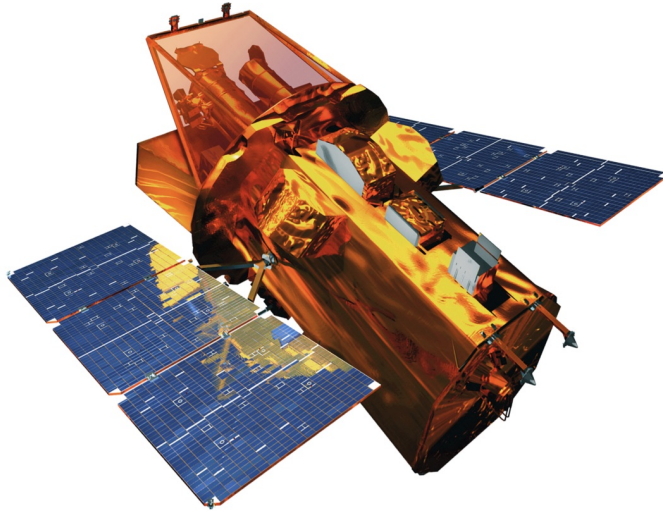


Figure 2.1: *Swift* satellite. Credits: NASA

- Burst Alert Telescope (*BAT*): It detects emissions in  $\gamma$ -rays. When *BAT* detects a burst, the satellite slew to that, *XRT* and *UVOT* (see below) point at the event. Approximately 80% of the *BAT*-detected GRBs have rapid repointing (typically within 100 seconds) whereas the other 20% have spacecraft constraints that prevent rapid slewing. This detector covers the range from 15-150 keV in a field-of-view of 2 steradians.
- X-Ray Telescope (*XRT*): It is used mainly to observe GRB afterglows in X-ray by filling the gap between the prompt emission and the afterglow. Its detector covers the range from 0.3-10 keV.
- UV Optical Telescope (*UVOT*): The fraction of rapid-pointing GRBs detected by *UVOT* is about 35% (Gehrels & Mészáros 2012). The images taken with *UVOT* can be used to determinate the redshift of the GRB via the observed wavelength of the Lyman-alpha cut-off. Its detector covers the range from 170-600 nm and therefore, cannot be used to constrain events of high redshifts.

*Swift* discovers approximately 100 bursts per year. The *BAT* instrument detects GRBs and accurately determines their positions on the sky. *Swift* relays a 3 arcminute position estimated with *BAT*, and then about 90 seconds later, the arcsecond-precision coordinates are determined by *XRT* and/or *UVOT*.





Figure 2.2: *Fermi* satellite. Credits: NASA

### 2.1.2 FERMI

The Fermi Gamma-ray Space Telescope (<http://fermi.gsfc.nasa.gov/>) launched in 2008 and shown in Figure 2.2, has a wider energy range of detection (8 keV-300 GeV) than *Swift*. The instruments on board of *Fermi* are:

- Large Area Telescope (*LAT*): It has a large field of view, over 2 steradians. It is able to determinate the position of a GRB to about 1 arcmin. The detector covers the energy range from 20 MeV to 300 GeV and is able to recognize the signal generated by cosmic rays in order to discard it. *LAT* cover the entire sky every three hours. It measures spectra of sources and positions them to an accuracy less than  $1^\circ$ .
- Gamma-ray Burst Monitor (*GBM*): The *GBM* instrument has scintillation detectors and covers the energy range from 8 keV to 40 MeV. It measures spectra of GRBs and determines their position. It has 12 detectors located on opposite sides to see different directions in the sky allowing a better position determination (about  $5^\circ$ ) using the arrival direction of the photons.

The *GBM* detects GRBs at a rate of about 300 per year, of which on average 20% are short bursts. The *LAT* detects bursts at a rate of about 10 per year.

## 2.2 Ground telescopes

GRBs are detected mainly by *Swift* and *Fermi*. These satellites send the alerts to the GRB Coordinates Network *GCN/TAN* (<https://gcn.gsfc.nasa.gov/>). The *GCN/TAN* works in real-time,

i.e, while the GRB's stills bursting, the GCN network sends to the ground telescopes the corresponding position and information of the GRB. Therefore, the arrival delay time of these alerts are just constrained by telemetry down-link delays.

Around the world, the main networks of telescopes focused on the observation of the prompt optical counterpart emission from GRBs are *RAPTOR*, *BOOTES*, *MASTER* and *TAROT*. Their most important features are described in Table 2.1 and they are described below.

### 2.2.1 *MASTER*

The *MASTER* Net of Mobile AStronomical TElescopes-Robots (<http://observ.pereplet.ru/>) started operations in 2012. Nowadays, the *MASTER* network consists in five identical binocular telescopes with a total of ten 0.4 meters tubes. They are situated in five locations spread over six time zones. The continuous monitoring using identical instruments allows the coverage of about 5000  $deg^2$  per night with a limiting AB magnitude about  $r = 20$  (Denisenko 2013). The main achievements of the project includes discovering optical transients (supernovae, cataclysmic variables and other fast transients of unknown nature). One of the advantages of this network is that it obtains polarization measurements for some transients.

### 2.2.2 *BOOTES*

The (B)urst (O)bserver and (O)ptical (T)ransient (E)xploring (S)ystem (*BOOTES*) (<http://bootes.iaa.es/>), is a set of instruments that include five astronomical stations in Spain (two), New Zealand, China and México. The scientific goals of the project are the observation of the GRB error box simultaneously to the GRB occurrence and the detection of optical flashes.

### 2.2.3 *TAROT*

The *TAROT* telescopes are two robotic autonomous observatories with identical suites of instrumentation, each one located in different hemisphere. It started operations in 2006. The main goal of the *TAROT* network is to catch the optical counterparts of GRBs (Gendre et al. 2008).

### 2.2.4 *RAPTOR*

The RAPid Telescopes for Optical Response (*RAPTOR*) experiment ([https://www.lanl.gov/quarterly/q\\_fall103/telescope.shtml](https://www.lanl.gov/quarterly/q_fall103/telescope.shtml)) is an autonomous closed-loop monitoring system that

Telescope	Location	Diameter $\phi$ [cm]	FoV	Pixel scale ["]	Detection limit	Exposure time [s]	Slewing speed [°/sec]
<b>UVOT</b>	<i>Swift</i>	30	$17' \times 17'$	0.50"	B=22.3	1000	—
<b>RAPTOR</b>	United States	40	60 deg <sup>2</sup>	0.76"	R=16	30	>30
	United States	40	60 deg <sup>2</sup>	0.76"	R=16	30	>30
<b>BOOTES</b>	El Arenosillo	20	180°	2.2'	R=8-10	30	100
	Spain	60	$10' \times 10'$	0.59"	r'=18	30	20
	New Zealand	60	$10' \times 10'$	0.59"	r'=18	30	20
	China	60	$10' \times 10'$	0.59"	r'=18	30	20
	México	60	$10' \times 10'$	0.59"	r'=18	30	20
<b>MASTER</b>	Kislovodsk	40	8 deg <sup>2</sup>	1.85	20-21 (unfilter)	500-1000	30
	Ural	40	8 deg <sup>2</sup>	1.85	20-21 (unfilter)	500-1000	30
	Tunka	40	8 deg <sup>2</sup>	1.85	20-21 (unfilter)	500-1000	30
	Amur	40	8 deg <sup>2</sup>	1.85	20-21 (unfilter)	500-1000	30
	Argentina	40	8 deg <sup>2</sup>	1.85	20-21 (unfilter)	500-1000	30
	Domodedovo	40	8 deg <sup>2</sup>	1.85	20-21 (unfilter)	500-1000	30
<b>TAROT</b>	Calern Observatory	25	$2^\circ \times 2^\circ$	3.3	V=17	60	> 60°/s
	Spain	25	$2^\circ \times 2^\circ$	3.3	V=17	60	> 60°/s

Table 2.1: Main features of ground optical telescope networks.

identifies and makes follow-up observations of rapid optical transients in real time. The system is composed by two identical telescope arrays, separated by 38 kilometers, that stereoscopically monitor a field of about 1300 deg<sup>2</sup> for celestial transients down to about AB magnitude R about 16 in 30 seconds. Each array contains a sensitive, high resolution telescope, and they are mounted on rapidly slewing mounts (can point an event in the sky in less than 3 seconds) so that the telescope can be rapidly directed for follow-up observations of any interesting transient identified by the wide-field system (Vestrand et al. 2003).

The main advantage of *RAPTOR* in comparison with other ground telescopes is its system to determine the transient nature of up to 250,000 objects in a wide-field image. This is possible making previous scans to compare position and brightness of each object. The event is considered transient only if the object is detected by both telescopes.

## 2.3 GCN published

Using the information in the *GCN* circulars (<http://gcn.gsfc.nasa.gov/>), it is possible to compare the number of GRBs detected in the early prompt emission or early afterglow (up to a couple of minutes from the trigger) by each one of these optical telescopes in the last years (Table 2.2). Table 2.2 shows that in six years the total follow-up observations of GRBs made for these collaborations are a few dozens of events. Moreover, this number is much smaller than the total GCN alerts sent by BAT annually.

	2012	2013	2014	2015	2016	2017
Total alerts ( <i>BAT</i> )	98	95	98	83	89	87
<i>UVOT</i>	40	48	29	27	29	20
<i>RAPTOR</i>	3	2	3	3	2	0
<i>BOOTES</i>	1	0	1	0	1	2
<i>MASTER</i>	3	2	7	5	5	18
<i>TAROT</i>	3	2	0	0	3	0

Table 2.2: Number of GRBs with early detections or observations with each one of the main GRB ground optical telescope networks by year in prompt emissions and early afterglows (up to a couple of minutes from the trigger).

This fact was the main motivation to design the *COATLI* telescope (described in next section). This telescope was planned in order to help to expand this sample.

## Chapter 3

# COATLI telescope

COATLI (<http://coatli.astroscu.unam.mx/>), the acronym derived from *Corrector Óptica Activa Tilt al Límite de difracción*, is a  $\phi = 50$  cm robotic telescope located at the Observatorio Astronómico Nacional, San Pedro Mártir, México (OAN-SPM) (Watson et al. 2016). COATLI is shown in Figure 3.1. COATLI also means *twins* in the indigenous Mexican Nahuatl language referring to the two channels and two detectors in its infrared definitive instrument.

The project has the main purpose to obtain the best quality for optical images at the OAN-SPM (better images than a seeing-limited images). It was designed for avoid the typical problems found in other optical ground telescope as dome seeing, static aberrations, guiding problems, and/or induced vibration in order to improve the current quality of the images from FWHM=1.0-1.5 arcsec to FWHM=0.25-0.30 using a combination of fast tilt correction (fast guiding or fast image stabilization) and active optics.

COATLI was developed in two stages. First, an interim system which was installed in fall of 2016 and the definitive system will be ready in 2020.

### 3.1 Description

The COATLI telescope is an ASTELCO Systems 50-cm f/8 Ritchey-Chrétien reflector with protected aluminum coatings. It has a fast Astelco NTM-500 equatorial mount (<http://www.astelco.com/html/projects.htm#coatli>), which is able to point in any position with a distance larger than  $60^\circ$  from zenithal angle with an accuracy of  $60''$  in less than 10 seconds.

One of the main scientific goals of COATLI is related to this fast response: the study of transients

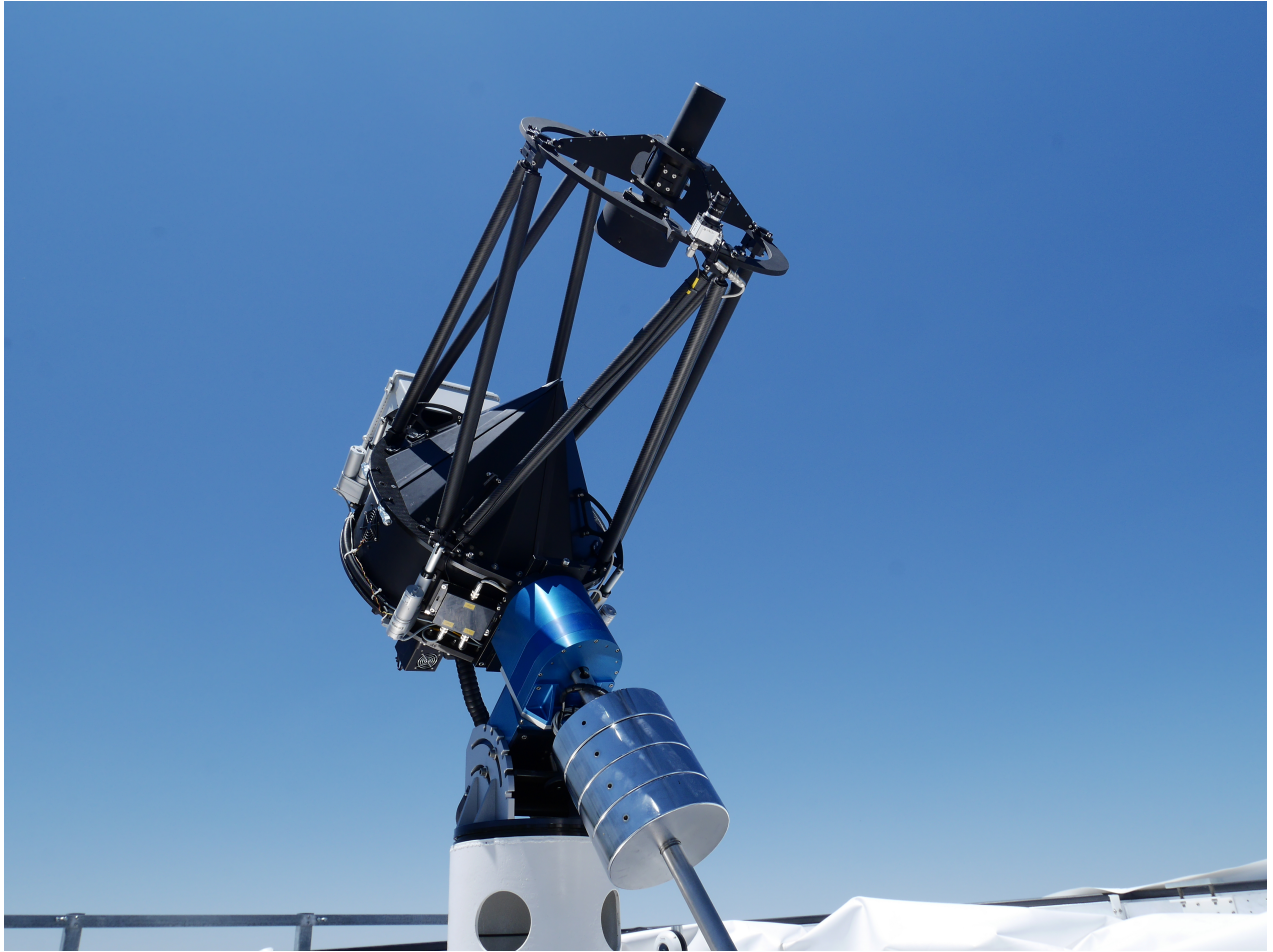


Figure 3.1: Robotic telescope COATLI.

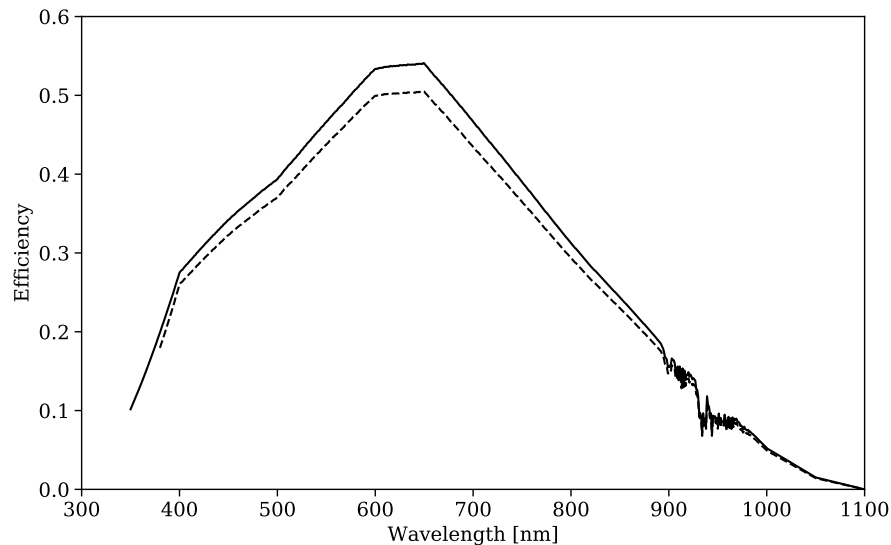


Figure 3.2: The estimated system efficiency of the COATLI telescope and interim imager at an airmass of 1.5. The continuous line shows the system efficiency without filters whereas the dashed line shows the system efficiency with the  $w$ -filter (clear filter). Figure from [Becerra et al. \(2019\)](#).

as GRBs. COATLI is able to observe the optical emission starting 10 seconds after receiving the GCN alert by BAT, and therefore, it is possible the study of these phenomena from the prompt emission or early afterglow (depending on the duration of the burst).

According to ASTELCO, the dome can open and close in a 90 km/h wind and survive a 180 km/h wind. Fortunately, the OAN team have registered the strongest gust of 125 km/h in the 10 last years.

The telescope is equipped with an interim instrument consisting of a Finger Lakes Instruments ML3200 detector with a Kodak KAF-3200ME monochrome CCD and a Finger Lakes Instruments CFW-1-5 filter wheel. Our medium-term plans are to replace this with an imager with fast guiding and active optics ([Watson et al. 2016](#)). The CCD has  $2184 \times 1472$  photoactive pixels each 6.8 microns or 0.35 arcsec to a side. We typically bin the CCD  $2 \times 2$  to give 0.70 arcsec pixels. The field is  $12.8 \times 8.7$  arcmin with the long axis roughly north-south. The CCD has good peak quantum efficiency from 550 to 700 nm, but is poor to the blue of 400 nm and to the red of 800 nm. The read noise is about 11 electrons. The filter wheel has  $BVRIw$  filters. The  $BVRI$  filters are Bessell filters supplied by Custom Scientific. The  $w$  filter is an Edmund Optics fused silica window with VIS-NIR anti-reflection coatings (part number 84-458). All filters are 5 mm thick and 50 mm in diameter.



Figure 3.2 shows the estimated system efficiency of the COATLI telescope and interim imager at an airmass of 1.5 with and without the  $w$  filter. The transmission of the  $w$  filter below 380 nm is uncertain; the anti-reflection is optimized for 400-1000 nm, and we have no information on its performance below 380 nm. However, the Figure 3.2 shows that even without the filter the efficiency is falling rapidly into the UV. The pivot wavelength of the system efficiency with the  $w$  filter, defined by equation (A16) of [Bessell & Murphy \(2012\)](#), is 630 nm.

The response of the COATLI  $w$  filter is quite different to that of the Pan-STARRS1  $w$  filter ([Tonry et al. 2012](#)). The rising response from 400 to 650 nm is similar, but the Pan-STARRS1 response is then flat to the sharp filter cutoff at 800 nm, whereas the COATLI response falls from 700 nm out to the limit of the CCD response at 1100 nm.

## 3.2 Extinction correction

The COATLI  $w$ -filter is wide, and so the relation between the extinction in the filter  $A_w$  and the reddening  $E_{B-V}$  is not trivial. Even for a fixed extinction law  $A_\lambda/E_{B-V}$ , the relation depends on the spectrum of the source (since blue spectra are more strongly extinguished than red spectra) and is non-linear (since extinction gradually reddens the spectrum).

Using the [Cardelli et al. \(1989\)](#) mean extinction curve for  $R_V = 3.1$ , we modeled the extinction  $A_w$  as a function of the reddening  $E_{B-V}$  for sources with unreddened spectra  $F_\nu \propto \nu^{-\beta}$  with  $-2 \leq \beta \leq +4$  and reddening  $0 \leq E_{B-V} \leq 1$ . We then fitted the results, and found

$$A_w/E_{B-V} \approx (a_0 + a_1\beta) + (b_0 + b_1\beta)E_{B-V}, \quad (3.1)$$

in which  $a_0 = +2.898$ ,  $a_1 = -0.187$ ,  $b_0 = -0.300$ , and  $b_1 = +0.026$ . The deviations between the model results and the fit are at worst 2%, and so are dwarfed by typical uncertainties in the reddening  $E_{B-V}$ .

## 3.3 Interim system

The interim system is an optic system formed by the 50 cm telescope, filters and detector. The best performance for the interim system is obtained at a AB magnitude of  $m=18.5$  with 5 seconds of exposure with  $w$ -filter. This is described in next section. The interim instrument consists in the CCD described in § 3, it is well-suited to seeing-limited observations, and has a filter wheel with BVRI and clear ( $w$ ) filters.



Mode	Binning	$g$	Readout noise	Dark current
1 MHz	1x1	$5.4 e^-/\text{DN}$	$08 e^-$	0.35 ADU
1 MHz	2x2	$5.7 e^-/\text{DN}$	$10 e^-$	0.35 ADU
6 MHz	1x1	$4.8 e^-/\text{DN}$	$15 e^-$	0.57 ADU
6 MHz	2x2	$5.2 e^-/\text{DN}$	$25 e^-$	0.57 ADU

Table 3.1: Gain, readout noise and dark current for the COATLI telescope.

### 3.4 Measurements Signal-to-Noise

In the very beginning of operations of the COATLI telescope, we compared the different read modes and binning in order to decide the best option according to the object to be observed. It was done the correlation between the flux measured in the *IRAF* software of standard candles and their magnitudes reported by *SIMBAD*. Using the values of readout noise, gain and dark current measured for COATLI (Table 3.4), the Figure 3.3 shows the behavior of the SN-value expected as function of the magnitude of the observed object.

From these data we decided that a read mode of 1 MHz and a binning of  $2 \times 2$  for individual frames of 5 second exposure to observe the early emission of GRBs as this gives a good balance between spatial sampling, temporal sampling, and sensibility.

### 3.5 Response time

As previously mentioned, COATLI has a fast mount in order to point quickly to any alert sent by GCN in the shortest possible time. However, in §4 we mentioned the other factor in the total time for response to an event is the time spent by GCN sending the alerts. This is not always constant. In Table 3.5 is listed the response time to all the events observed by COATLI until December 2018. It is important to remark that the first follow-up detection done with COATLI at 2017-04-28 which has a response time much larger (342 seconds) than the subsequents (about 15-40 seconds) was the first real test for the *pointing protocol*, and using the information and the learning from this, it was possible to improve it for the future.

### 3.6 Transformation of w to PANSTARRS filters

During the summer of 2017, we observed fields SA92-500, SA92-SF2, F-24, PG0231+051, SA95-112, SA95-SF3, GD-71, SA98-SF1, SA98-SF2, Ru149, Ru152, PG0942-029, SA101-341, GD-108,

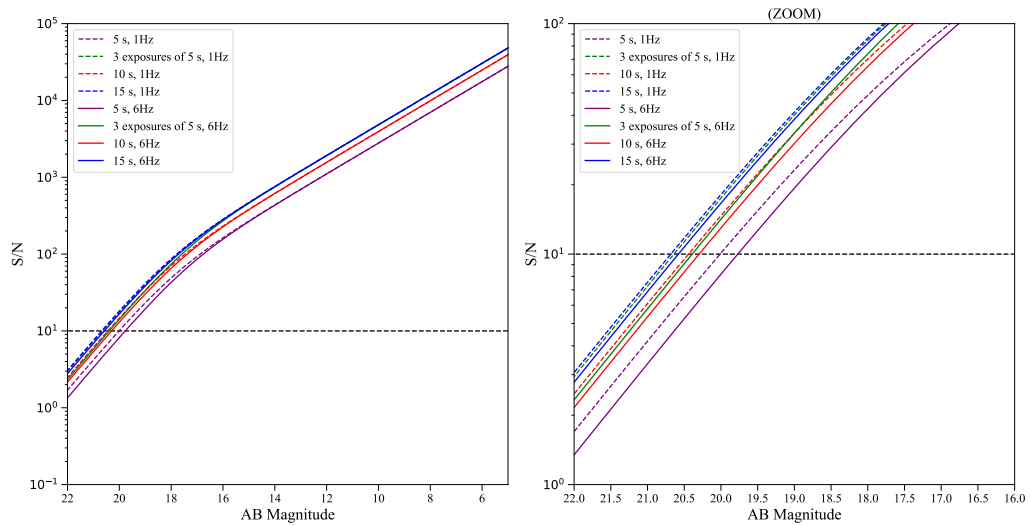


Figure 3.3: *Left:* Comparison of the S/N in the possible combinations of the read mode of the detector (1 MHz or 6 MHz) and the exposure time (5, 10 and 15 seconds and the combination of three frames of 5 seconds exposure) and a binning of  $2 \times 2$  used to determinate the best configuration to observe GRBs with the COATLI telescope. For this estimation we assumed a sky brightness of  $19 \text{ mag/arcsec}^2$ . *Right:* Zoom of the left panel. The data are extrapolation for standard candels measured with COATLI in all the combinations (read mode, exposure time and coadded/individual frames) presented.

Date	Trigger	Time (s)
2017-04-28	750298	342.269
2017-06-22	758168	28.23
2017-07-05	760064	8585.493*
2017-07-08	760835	2638.404*
2017-07-10	761119	12946.681*
2017-07-20	763539	66.931
2017-08-27	769567	1099.732*
2017-09-06	770957	8191.263*
2017-09-08	771371	167.378
2017-09-12	772006	30455.076*
2018-02-04	808483	12.843
2018-02-05	808625	6.476
2018-02-10	809374	7014.402*
2018-02-21	811074	362.425
2018-04-07	823001	7808.774*
2018-06-20	843122	21.1
2018-07-06	846395	46.4
2018-07-15	848048	34380*
2018-08-12	852903	43.1

Table 3.2: Response time of COATLI to *Swift* alerts. The marker \* means that these GRBs happened in the day of OAN-SPM and therefore the follow-up began up to the corresponding nights.

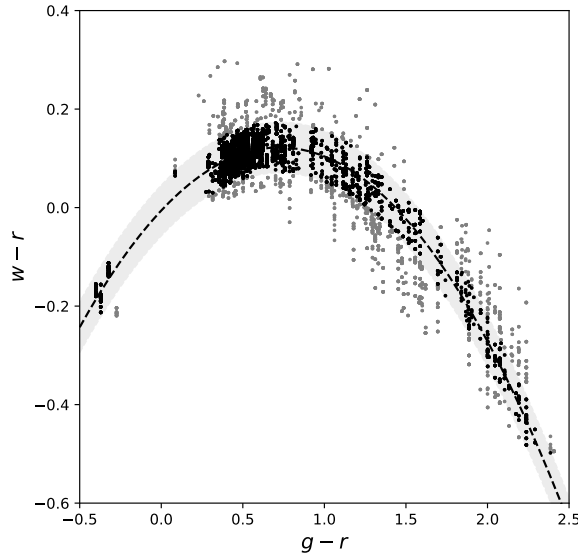


Figure 3.4: The transformation between  $w'$  and *Pan-STARRS1*  $gr$ . The black solid line is the quadratic model and the grey dashed lines are  $\pm 3$  times the RMS deviation from the model. The black data are fitted observations. The grey data are rejected observations. The error bars are  $1\sigma$ . Figure from [Becerra et al. \(2019\)](#).

G163-50C, SA104-SF1, PG1323-086, PG1407-013, PG1525-071, PG1528+062, SA107-SF1, SA107-SF2, PG1633+099, PG1657+078, SA110-315, SA110-SF2, SA110-SF3, Mark-A, G93-48, SA113-SF1, SA113-SF3, SA113-SF4, PG2213-006, GD-246 from [Landolt \(1992\)](#). We obtained raw aperture photometry using SExtractor ([Bertin & Arnouts 1996](#)) with a 3.5 arcsec diameter aperture (5 pixels). We chose the aperture equal to 5 pixels after varying the aperture value between 3 and 7 pixels and observing lower noise in the light curves of the field stars.

Observations of about 3000 *Pan-STARRS1* stars (Figure 3.4) show that for normal stars the transformation from *Pan-STARRS1*  $g$  and  $r$  AB magnitudes ([Magnier et al. 2016](#)) to the natural  $w$  AB magnitudes of COATLI is well fitted for  $-0.5 \leq (g' - r') \leq 2.5$  by

$$(w - r') = 0.353(g' - r') - 0.243(g' - r')^2, \quad (3.2)$$

with a standard deviation of  $\sigma = 0.017$ .

For all the photometry reported by COATLI collaboration in scientific papers, we applied this equation to *Pan-STARRS1* photometry of stars in the field to obtain local  $w$  standards. We used these local standards to calibrate our raw photometry and produce natural  $w$  AB magnitudes of the

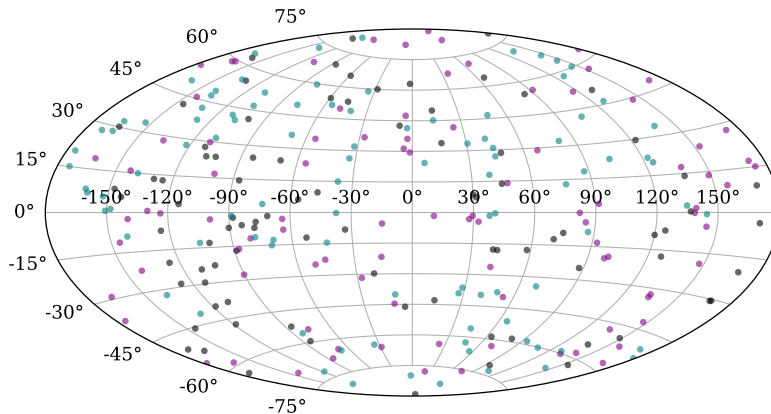


Figure 3.5: GRBs detected by *Swift*/BAT instrument of 2012 (black points), 2013 (purple points) and 2014 (blue points).

events and, particularly, of the afterglows.

### 3.7 First Results

Taking into account all the number GRBs detected between 2012 and 2014 by *Swift*/BAT, reported by GCN/TAN (about 94 events per year) and showed in Figure 3.5, using a limited AB magnitude  $m=18$  for an exposure time of five seconds, the coordinates of COATLI (Latitude= $30.75$ , Longitude= $-115.22$ ), the observing time about 10 hours per night and, the restriction given by the altitude to which the telescope can reach (zenital angle= $60^\circ$ ), the time of operation of the OAN-SPM (holiday periods, maintenance) i.e. 70%, we expected that COATLI would be able to observe prompt and early afterglow emission of eight GRBs per year.

In Table 3.7 are listed the number of GCNs published by the COATLI collaboration. It is important to mention that in 2018, COATLI telescope was out of operations for three months by technical problems. Then, the number of GCNs published by COATLI collaboration in the last year join the photometry of GRB 180205A (not included in GCN) and described in § 4.1, matches perfectly with the previous expectations and shows the excellent performance compared with the results from the main ground follow-up optical network mentioned in § 4.

---

Telescope	GCNs
COATLI	5
BOOTES	1
TAROT	1
RAPTOR	0
MASTER	12

---

Table 3.3: Comparison of GCNs published by COATLI and other follow-up collaborations in 2018 related with prompt and early afterglow optical emission from GRBs

## Chapter 4

# Observations and publications

In this chapter I present the three articles written as part of this dissertation. First, the early optical photometry and analysis of GRB 180205A in § 4.1. These work was done with the COATLI instrument data. The analysis of GRB 180418A is presented in § 4.2, these study was done with the early data from TAROT and late data from the RATIR instrument. Finally, § 4.3 describes the photometric confirmation of SN 2013cq, the supernova associated to GRB 130427A, the most energetic gamma-ray burst observed to date.

### 4.1 Late Central Engine Activity in GRB 180205A

GRB 180205A is one of the brightest gamma-ray burst in the last few years and presents a bright optical counterpart. In total, there have been 22 GCN Circulars related to GRB 180205A. Its redshift was measured to be  $z = 1.409$  with absorption features including C II, Si II, Si II\*, Al II, Fe II, Mg II, Mg I (Tanvir et al. 2018).

The photometric data set associated with this event was the first scientific result obtained by the robotic telescope COATLI placed at the Observatorio Astronómico Nacional in Sierra de San Pedro Mártir. This work involves the photometry and multiwavelength analysis of GRB 180205A since 200 s up to  $\sim 5$  days from the BAT trigger.

COATLI, as is mentioned in § 3 is connected to the GCN/TAN alert system and received an XRT alert packet for GRB 180205A at 04:28:55.6 UTC ( $T + 206.3$  seconds). It immediately slewed to the burst and began observing, with the first exposure starting at 04:29:02.1 UTC ( $T + 212.8$  seconds), only 6.5 seconds after the alert. This quick response allowed us to have the earliest optical data for a ground-based telescope and a better temporal sampling than the *SWIFT/UVOT* instrument which

---

began to observe 20 seconds before than COATLI.

The early-time optical light curve exhibits a flat plateau in temporal coincidence with an X-ray flare. The late-time light curves and spectra are consistent with the standard forward-shock scenario.





Several scenarios based on internal and external shocks were explored in this work in order to describe the multiwavelength light curves of GRB 180205A, including neutron decoupling, reverse shock component, two jets or late central activity. Finally, we conclude that the synchrotron forward-shock model evolving in the interstellar medium together with the late activity of the central engine are the most favored scenarios to interpret GRB 180205A due to the temporal and spectral analysis found for this event.

This paper is published in ApJ and is attached below.





## Late Central-engine Activity in GRB 180205A

R. L. Becerra<sup>1</sup>, A. M. Watson<sup>1</sup>, N. Fraija<sup>1</sup> , N. R. Butler<sup>2</sup> , W. H. Lee<sup>1</sup>, E. Troja<sup>3,4</sup> , C. G. Román-Zúñiga<sup>5</sup> , A. S. Kuttyrev<sup>3,4</sup>,  
L. C. Álvarez Nuñez<sup>1</sup>, F. Ángeles<sup>1</sup>, O. Chapa<sup>1</sup>, S. Cuevas<sup>1</sup>, A. S. Farah<sup>1</sup>, J. Fuentes-Fernández<sup>1</sup>, L. Figueroa<sup>5</sup>, R. Langarica<sup>1</sup>,  
F. Quirós<sup>5</sup>, J. Ruíz-Díaz-Soto<sup>1</sup>, C. G. Tejada<sup>5</sup>, and S. J. Tinoco<sup>1</sup>

<sup>1</sup> Instituto de Astronomía, Universidad Nacional Autónoma de México, Apartado Postal 70-264, 04510 México, CDMX, México

<sup>2</sup> School of Earth and Space Exploration, Arizona State University, Tempe, AZ 85287, USA

<sup>3</sup> Department of Astronomy, University of Maryland, College Park, MD 20742-4111, USA

<sup>4</sup> Astrophysics Science Division, NASA Goddard Space Flight Center, 8800 Greenbelt Road, Greenbelt, MD 20771, USA

<sup>5</sup> Instituto de Astronomía, Universidad Nacional Autónoma de México, Unidad Académica en Ensenada, 22860 Ensenada, BC, Mexico

Received 2018 October 17; revised 2019 January 14; accepted 2019 January 17; published 2019 February 19

### Abstract

We present optical photometry of the afterglow of the long GRB 180205A with the COATLI telescope from 217 s to about 5 days after the *Swift*/BAT trigger. We analyze this photometry in conjunction with the X-ray light curve from *Swift*/XRT. The late-time light curves and spectra are consistent with the standard forward-shock scenario. However, the early-time optical and X-ray light curves show atypical behavior: the optical light curve exhibits a flat plateau while the X-ray light curve shows a flare. We explore several scenarios and conclude that the most likely explanation for the early behavior is late activity of the central engine.

**Key words:** gamma-ray burst: individual (GRB 180205A)

**Supporting material:** machine-readable table

### 1. Introduction

Gamma-ray bursts (GRBs) are, during their brief lives, the most luminous events in the universe. Observationally, they are typically classified according to their duration  $T_{90}$  (Kouveliotou et al. 1993) as short GRBs and long GRBs. Short GRBs are thought to arise from the fusion of compact objects (Lattimer & Schramm 1976; Paczynski 1989, 1991; Lee & Ramirez-Ruiz 2007), whereas long GRBs are thought to arise from core-collapse supernovae in massive stars (Woosley 1993; MacFadyen & Woosley 1999).

The most successful theory for interpreting the electromagnetic radiation from both types of GRBs is the fireball model (recently reviewed by Kumar & Zhang 2015). This model distinguishes two stages: the prompt or early phase and the afterglow or late phase. The prompt phase is simultaneous with bright emission in gamma-rays produced by internal shocks in the jet driven by the central engine. The afterglow phase is produced by the external shocks between the outflow and the circumstellar environment (e.g., Kumar & Piran 2000; Fraija 2015). While the general ideas behind the fireball model seem to be clear, it is important to compare the detailed predictions of the model with observational data of GRBs in order to determine which facets of the model are important in the individual case, to determine the ranges of macrophysical and microphysical parameters, and to understand the diversity of GRBs. This process leads to a better understanding both of GRBs and of the environments in which they develop.

These ideas are the main motivation of this paper. Here, we present photometric observations of the long GRB 180205A in the optical and in X-rays during the afterglow phase and compare them to the detailed predictions of the fireball model.

GRB 180205A was one of the brightest GRBs in the last few years and presented a bright optical counterpart. It was well observed by many collaborations; in total, there were 22 GCN Circulars related to GRB 180205A.

In this paper we present new optical photometry of the bright GRB 180205A with the COATLI telescope in the  $w$  filter. This paper is organized as follows: in Section 2, we present our observations with COATLI and observations from other telescopes. In Section 3, we explain the afterglow model that we use, and we fit the data using segments of power law. In Section 4, we interpret the observations in the context of the fireball model. Finally, in Section 5, we discuss the results and summarize our conclusions. In the Appendix, we describe briefly the state and main features of COATLI as well as its characterization and response.

### 2. Observations

#### 2.1. Fermi Observations

The *Fermi*/GBM instrument triggered on GRB 180205A at 2018 February 5 04:25:25.393 UTC (trigger 539497530/180205184) and observed several pulses with a  $T_{90}$  duration of  $15.4 \pm 1.4$  s, making GRB 180205A a long GRB, and a 10–1000 keV fluence of  $(2.1 \pm 0.1) \times 10^{-6}$  erg cm<sup>-2</sup> (Narayana Bhat et al. 2016; von Kienlin 2018). The burst was apparently not detected by the *Fermi*/LAT instrument.

Taking into account the values of the fluence and peak energy reported by the *Fermi*/GBM collaboration (von Kienlin 2018), the corresponding total isotropic energy is approximately  $1.1 \times 10^{52}$  erg for  $z = 1.401$  (Amati et al. 2002).

#### 2.2. Neil Gehrels Swift Observatory

The *Swift*/BAT instrument triggered on GRB 180205A at  $T = 2018$  February 5 04:25:29.33 UTC (trigger 808625) and observed a multi-peaked structure from about  $T - 7$  s to about  $T + 11$  s, with major peaks at about  $T - 5$  s and  $T + 0$  s (Krimm et al. 2018).

The *Swift*/XRT instrument started observing the field at  $T + 162$  s in WTSLEW mode and at  $T + 181$  s in WT mode. It detected a bright, fading source at 08:27:16.72 +11:32:31.6

J2000 with a 90% uncertainty radius of 1.5 arcsec (Evans et al. 2018; Page et al. 2018). The 0.2–10 keV flux in the initial 2.5 s image was  $9.50 \times 10^{-10}$  erg cm $^{-2}$  s $^{-1}$  (Evans et al. 2018). We reduced the WT and PC mode data using the pipeline described by Butler (2007) and Butler et al. (2007). We then extended the light curve to earlier times using the WTSLEW data reduced by the UK *Swift* Science Data Centre (Evans et al. 2009) using the same counts-to-flux-density calibration as in our analysis of the WT and PC data.

The *Swift*/UVOT instrument started observing the field at  $T + 181$  s and detected a bright, fading source at 08:27:16.74 + 11:32:30.9 J2000 with a 90% uncertainty radius of 0.42 arcsec (Emery & Evans 2018; Page et al. 2018). The source faded in the white filter from magnitude  $15.75 \pm 0.02$  at  $T + 182$  to  $T + 331$  s to magnitude  $16.33 \pm 0.02$  at  $T + 540$  to  $T + 732$  s (Emery & Evans 2018).

### 2.3. COATLI

COATLI<sup>6</sup> is a robotic 50 cm telescope at the Observatorio Astronómico Nacional on the Sierra de San Pedro Mártir in Baja California, Mexico (Watson et al. 2016). COATLI is currently operating with an interim instrument, a CCD with a field of view of  $12.8 \times 8.7$  arcmin and *BVR<sub>I</sub>w* filters. Our observations of GRB 180205A with COATLI are discussed in detail in the Appendix, and are summarized briefly here.

COATLI started to observe GRB 180205A at 04:29:06.3 UTC, which was only 10.7 s after receiving the GCN/TAN alert packet. However, despite this fast response, our first observation started at  $T + 217.0$  s. The relatively long delay was due to a satellite telemetry problem (Evans et al. 2018), which meant that COATLI did not receive the usual GCN/TAN BAT alert packets but only the later GCN/TAN XRT alert packet.

All of our COATLI observations are 5 s exposures in the clear *w* filter. The read time for the CCD is about 4 s, so the cadence was typically about 9 s. The telescope dithered, taking 10 images in one dither position before moving to the next dither position. Up to  $T + 1500$  s, we consider the exposures individually. From  $T + 1500$  s to  $T + 9000$  s, we combine sets of 10 exposures taken over about 86 s. From  $T + 9000$  s to the end of the first night we combine sets of 50 exposures taken over about 500 s to improve the signal-to-noise ratio. On subsequent nights, we combine all the frames with an FWHM of 2.8 arcsec or less.

We performed aperture photometry using SExtractor (Bertin & Arnouts 1996) with an aperture of 3.5 arcsec diameter. Table 3 gives our aperture photometry. For each image it gives the start and end times of the observation,  $t_i$  and  $t_f$ , relative to the trigger time  $T$  the total exposure time,  $t_{\text{exp}}$ , the AB magnitude  $w$  (not corrected for Galactic extinction), and the  $1\sigma$  total uncertainty in the magnitude (including both statistical and systematic contributions).

For a wide filter like the COATLI *w* filter, the extinction in general depends on the spectral shape (see the Appendix). Table 2 shows the estimated spectral indices  $\beta$  using colors reported by the GROND team (Bolmer & Kann 2018a, 2018b) at two epochs and the corresponding values of  $A_w$  for an extinction of  $E(B - V) = 0.03$  (Bolmer & Kann 2018b). For such a low extinction the dependence on the spectral shape is weak, and so we adopt  $A_w = 0.08$ .

Figure 1 shows the COATLI light curve and photometry from *Swift*/UVOT (Emery & Evans 2018; Evans et al. 2018), GROND (Bolmer & Kann 2018a, 2018b), Hankasalmi (Oksanen & Malesani 2018), Mondy (Mazaeva et al. 2018), Nanshan (Zhu et al. 2018), DOAO (Im et al. 2018b), and Nickel/KAIT (Falcon et al. 2018; Zheng & Filippenko 2018).

### 2.4. Other Terrestrial Observations

Zheng & Filippenko (2018) confirmed the bright, fading optical counterpart in observations with KAIT, which started observing the field at  $T + 371$  s. They detected the source in their clear filter at about 15.6 mag, and observed that it faded by about 1.2 mag over the next 22.5 minutes. Bolmer & Kann (2018b) reported early *grizJHK* magnitudes obtained by GROND at about  $T + 13$  minutes. Further photometry was published by Bolmer & Kann (2018a), Xin et al. (2018), Im et al. (2018a, 2018b), Oksanen & Malesani (2018), and Cunningham et al. (2018).

Tanvir et al. (2018) obtained a spectrum at  $T + 1.5$  hr that showed many absorption features, including C II, Si II, Si II<sup>\*</sup>, Al II, Fe II, Mg II, and Mg I, at a common redshift of  $z = 1.409$  and concluded that this was the redshift of the GRB.

Wiersema & Covino (2018) measured a low polarization of  $P \sim 0.9\%$  in *R* at  $T + 2.5$  hr.

## 3. X-Ray and Optical, Temporal and Spectral Analysis

### 3.1. Temporal Analysis

The prompt emission from the GRB detected by *Fermi*/GBM and *Swift*/BAT lasted until about  $T + 11$  s. The earliest complementary data are from *Swift*/XRT starting at  $T + 162$  s, *Swift*/UVOT at  $T + 181$  s, and COATLI at  $T + 217$  s. Therefore, we focus our analysis on the afterglow. In our analysis of the early afterglow, we mainly use the XRT and COATLI data, because the UVOT data are in different filters and have relatively long exposures (39–147 s).

Figure 2 shows the optical and X-ray light curves for GRB 180205A corrected by galactic extinction. We will fit the light curves with segments of temporal power laws  $F_\nu \propto t^{-\alpha}$ , in which  $F_\nu$  is the flux density,  $t$  is the time since the BAT trigger, and  $\alpha$  is the temporal index. The power-law fits are summarized in Table 1. The relevant stages are as follows:

1. The X-ray light curve for  $t < 260$  s. In  $163 < t < 260$  s, we see a bright flare in X-rays with a peak at about  $t = 188$  s. Currently, there is no widely accepted standard model for fitting an X-ray flare. Empirically, we fit two broken power-law segments in order to obtain parameters to describe it. The rise has  $\alpha_{\text{X,rise}} = -4.82 \pm 1.88$  for  $163 < t < 188$  s and the decay has  $\alpha_{\text{X,decay}} = 6.08 \pm 1.15$  for  $188 < t < 260$  s. We note that the uncertainty on the rising index is large due to the short time over which it is observed ( $163 < t < 188$  s and only 7 XRT data points). Nevertheless, it is clear that the behavior prior to peak is not consistent with an extrapolation to earlier times of the subsequent decay.
2. The X-ray light curve for  $t > 260$  s. This region can be fitted as a power law with a temporal index of  $\alpha_{\text{X,normal}} = 0.98 \pm 0.03$ . This is a typical normal decay phase seen in many afterglows (Zhang et al. 2006).
3. The optical light curve for  $t < 454$  s. This region can be fitted with a temporal index of  $\alpha_{\text{O,plateau}} = 0.53 \pm 0.02$ . This is a plateau phase.

<sup>6</sup> <http://coatli.astroscu.unam.mx/>

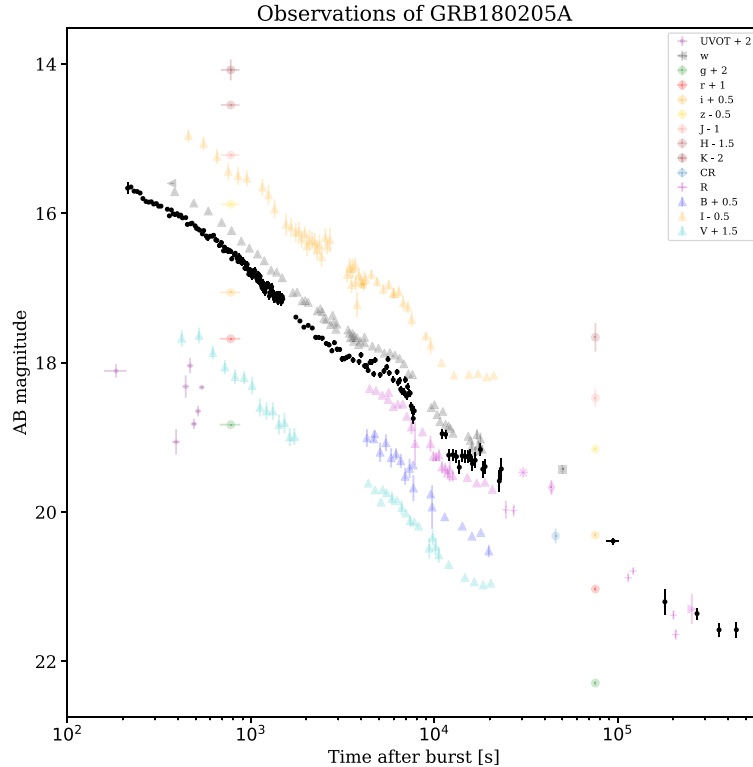


**Figure 1.** Light curve of GRB 180205A in different filters: *Swift*/UVOT (points; Emery & Evans 2018; Evans et al. 2018), GROND (circles; Bolmer & Kann 2018a, 2018b), Mondy (crosses; Mazaeva et al. 2018), Hankasalmi (squares; Oksanen & Malesani 2018), Nanshan (diamonds; Zhu et al. 2018), DOAO (pluses; Im et al. 2018b), Nickel/KAIT (triangles; Falcon et al. 2018; Zheng & Filippenko 2018), and COATLI (stars; this work). The photometry has not been corrected for Galactic extinction.

Our optical observations begin at  $t = 217$ , significantly after the peak of the X-ray flare at  $t = 188$  s but nevertheless before the end of the flare at  $t = 260$  s. We see no strong evidence for a counterpart optical flare; between  $t = 188$  and  $t = 260$  s the X-ray flux falls as  $F \propto t^{-6.08}$ , but the optical flux only falls as  $F \propto t^{-0.53}$  in accordance with the gentle power-law decline that continues to later times.

4. The optical light curve for  $t > 454$ . This region can be fitted as a power law with a temporal index of  $\alpha_{\text{O,normal}} = 0.78 \pm 0.01$ . This is a typical normal decay phase seen in many afterglows (Zhang et al. 2006).

### 3.2. Spectral Analysis

We fit the photometry with a spectral power law  $F_\nu \propto \nu^{-\beta}$ , in which  $F_\nu$  is the flux density,  $\nu$  is the frequency, and  $\beta$  is the spectral index.

Figure 3 shows the evolution of the SED. The dashed line shows the spectral index obtained from our fits to the COATLI and XRT light curves. The points are directly calculated from the COATLI and XRT flux densities. The spectrum evolves rapidly from  $\beta \approx 0.5$  during the flare to a steeper spectrum

with  $\beta \approx 0.75$  to  $0.8$  during the optical plateau, and then evolves more slowly to about  $\beta \approx 1.0$  at late times.

Figure 4 shows the spectrum at late time in more detail. We produced the *Swift*/XRT X-ray spectrum for  $10,000 < t < 918,651$  s using the pipeline described by Butler (2007) and Butler et al. (2007) and added the optical point from our COATLI data interpolated over the same interval. Fitting the XRT spectrum directly, we obtain an X-ray index of  $\beta_{\text{X,normal}} = 1.13 \pm 0.10$ , whereas at the same time the global index from the optical to X-rays is  $\beta = 0.7\text{--}0.8$ . This suggests that there is a spectral break between the optical and the X-rays, with a predicted spectral index of  $\beta_{\text{O,normal}} = 0.52 \pm 0.02$  in the optical; this is explained in more detail in the next section.

## 4. Theoretical Interpretation

The long-lived emission of the afterglow is most commonly explained by the synchrotron forward-shock model. The distribution of electron energies is assumed to be given by a power law  $N(\gamma) \propto \gamma^{-p}$  in which  $\gamma$  is the Lorentz factor of the electron and  $p$  is the index. The observed synchrotron flux is formed by a series of power-law segments  $F_\nu \propto t^{-\alpha} \nu^{-\beta}$  in time  $t$  and frequency  $\nu$ . Sari et al. (1998) and Chevalier & Li (2018) derived the synchrotron light curves when the outflow is decelerated by a constant-density interstellar medium (ISM)

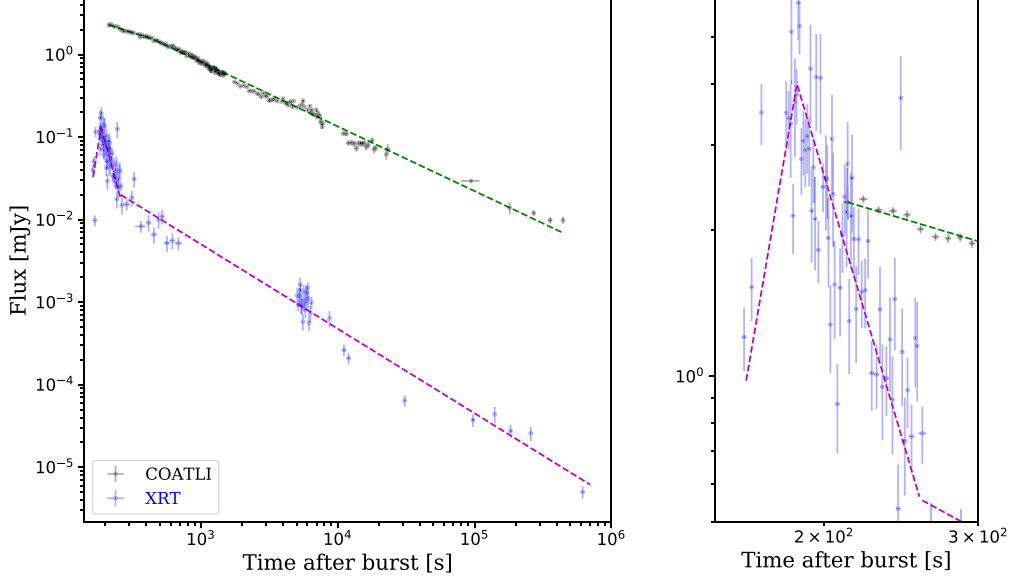


**Figure 2.** Left: light curves and broken power-law fits of GRB 180205A in  $w$  from COATLI (black data and green fits) and X-rays from *Swift*/XRT (blue data and pink fits) at 1 keV. Right: X-ray flare multiplied by a factor of 30 and the beginning of the optical plateau.

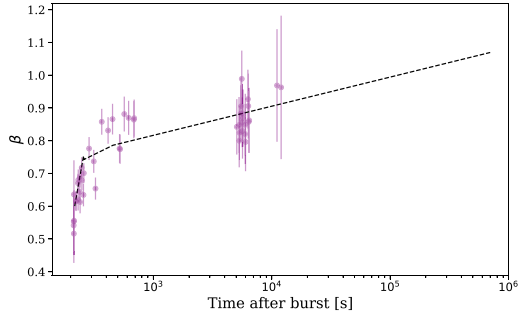


**Figure 3.** Temporal evolution of the spectral index  $\beta$ . The dashed line shows the spectral index obtained from our fits to the COATLI and XRT light curves. The points are directly calculated from the COATLI and XRT flux densities.

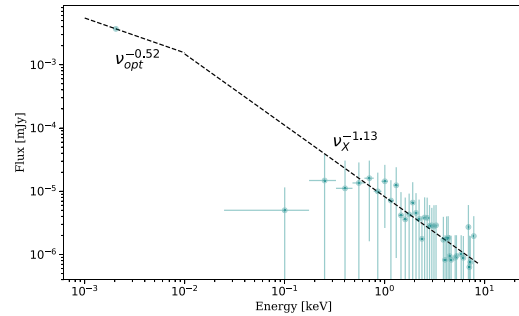


**Figure 4.** SED of GRB 180205A from X-rays to the optical. The data are from COATLI and XRT in the interval  $10,000 < t < 918,651$  s. The dashed line is a combination of the fitted spectrum at high frequency and the predicted spectrum below the cooling break at lower frequency.

**Table 1**  
Temporal and Spectral Power-law Indices

Stage	Time Interval	Parameter	Index
X-ray flare rise	$163 < t < 188$	$\alpha_{X,\text{rise}}$	$-4.82 \pm 1.88$
X-ray flare decay	$188 < t < 260$	$\alpha_{X,\text{decay}}$	$6.08 \pm 1.15$
X-ray normal decay	$260 < t$	$\alpha_{X,\text{normal}}$	$1.02 \pm 0.03$
	$10000 < t < 918651$	$\beta_{X,\text{normal}}$	$1.13 \pm 0.10$
Optical plateau	$217 < t < 454$	$\alpha_{O,\text{plateau}}$	$0.53 \pm 0.02$
Optical normal decay	$454 < t < 500000$	$\alpha_{O,\text{normal}}$	$0.78 \pm 0.01$

and the stellar wind of the progenitor. The proportionality constants of synchrotron fluxes in both regimes are explicitly computed by Fraija et al. (2016b) and Fraija (2015) for an ISM and stellar-wind densities, respectively.

Assuming an efficiency of  $\eta \approx 20\%$  and a typical value for ISM density  $n = 1 \text{ cm}^{-3}$  (e.g., see Sari et al. 1996; Nysewander et al. 2009; Santana et al. 2014), we derive, using the theoretical model described by Fraija et al. (2017c) and the chi-square minimization method (Brun & Rademakers 1997), the microphysical parameters that describe the X-ray and optical afterglow of GRB 180205A. We obtain values of  $\epsilon_B = 8 \times 10^{-4}$  and  $\epsilon_e = 0.1$ , which agree with previous estimations of these parameters (see, e.g., Kumar & Barniol Duran 2010; Fraija et al. 2017c).

The light curves of GRB 180205A in X-rays and in the optical are not untypical. At early times, we see an X-ray flash and a plateau in the optical. At later times, both light curves decrease more steeply in a normal decay phase. We begin by

**Table 2**  
Spectral Index  $\beta$  and Extinction  $A_w$  Estimation

Color	$\beta$	Time [s]	Extinction $A_w$
$g - r$	0.51	780	0.084
$g - i$	0.52	780	0.084
$r - i$	0.55	780	0.084
$g - r$	0.88	75600	0.082
$g - i$	0.93	75600	0.081
$r - i$	0.99	75600	0.081

analyzing the normal decay phase in order to provide a constraint on the population of relativistic electrons. We then assume continuity in this population and consider the earlier phase and possible explanations for the X-ray flare and the absence of a counterpart optical flare.

#### 4.1. Normal Decay Phase

For  $t > 454$  s, the X-ray light curve (Figure 2) can be fitted with a simple power law with a temporal index of  $\alpha_{X,\text{normal}} = 1.02 \pm 0.03$ . Furthermore, for  $T + 10,000$  to  $T + 918,651$  s the X-ray spectrum can be fitted with a simple power law with a spectral index of  $\beta_{X,\text{normal}} = 1.13 \pm 0.1$ . We suggest that this X-ray emission rises above the cooling break ( $\nu_c < \nu$ ) in a slow-cooling scenario (Sari et al. 1998), and so expect  $F_\nu \propto \nu^{-p/2} t^{(2-3p)/4}$ . Our observed value of  $\alpha_{X,\text{normal}}$  implies  $p = 2.03 \pm 0.04$  and subsequently  $\beta_{X,\text{normal}} = 1.02 \pm 0.02$ . The value of  $p$  is consistent with the range of values typically for GRB afterglows and the predicted value of  $\beta_{X,\text{normal}}$  is consistent with our observation of  $\beta_{X,\text{normal}} = 1.13 \pm 0.1$ .

For the optical, we suggest emission below the cooling break ( $\nu_m < \nu < \nu_c$ ) in a slow-cooling scenario, and expect  $F_\nu \propto \nu^{-(p-1)/2} t^{3(1-p)/4}$  for the jet being driven into a constant-density environment (Sari et al. 1998). Our predicted value of  $p$  gives a predicted value of  $\alpha_{O,\text{normal}} = 0.77 \pm 0.03$ , in good agreement with the observed value of  $0.78 \pm 0.01$ . A jet being driven into a decreasing-density stellar-wind environment would give a much steeper decay ( $1.27 \pm 0.03$ ), which is not consistent with the observed behavior. Our predicted value of  $p$  also predicts a spectral index  $\beta_{O,\text{normal}} = 0.52 \pm 0.02$ , which is in good agreement with the values of 0.51–0.55 observed by GROND at 780 s (Table 2) but not such a good agreement with the redder values observed at later times by the same group (Table 2). This may indicate that the cooling break is approaching the optical at later times. In Figure 4, we show the combined spectrum from the optical to the X-rays, which supports the presence of a cooling break between these regimes.

It is clear that the light curves in the normal phase are not perfect power laws. For example, there appear to be excesses in the optical from 5000 to 8000 s and perhaps on the second night at around 80,000 s. These departures in the light curve might be produced by density variations (Lazzati et al. 2002).

#### 4.2. Plateau Phase

For  $t < 454$  s, the optical light curve exhibits a flat plateau with a temporal index of  $\alpha_{O,\text{plateau}} = 0.53 \pm 0.02$ . A priori, one might think that this phase corresponded to emission above the cooling break ( $\nu_c < \nu < \nu_m$ ) in the fast-cooling scenario (Sari et al. 1998), which would give  $\alpha = 0.25$ . However, we are unable to find values of microphysical parameters and circumburst density that give a transition time (at which  $\nu_c = \nu_m$ ) to the normal decay

**Table 3**  
COATLI Observations of GRB 180205A

$t_i$ (s)	$t_f$ (s)	$t_{\text{exp}}$ (s)	$w$ (AB)
217.0	217.8	0.8	15.639 $\pm$ 0.078
221.8	226.8	5.0	15.568 $\pm$ 0.017
230.8	235.8	5.0	15.624 $\pm$ 0.018
239.8	244.8	5.0	15.629 $\pm$ 0.018
248.8	253.8	5.0	15.648 $\pm$ 0.018
257.8	262.8	5.0	15.723 $\pm$ 0.019
268.1	273.1	5.0	15.762 $\pm$ 0.020
277.2	282.2	5.0	15.771 $\pm$ 0.020
286.2	291.2	5.0	15.766 $\pm$ 0.021
295.2	300.2	5.0	15.796 $\pm$ 0.021
305.3	310.3	5.0	15.791 $\pm$ 0.021
314.3	319.3	5.0	15.825 $\pm$ 0.021
323.3	328.3	5.0	15.824 $\pm$ 0.021
350.4	355.4	5.0	15.866 $\pm$ 0.021
359.3	364.3	5.0	15.954 $\pm$ 0.022
368.3	373.3	5.0	15.876 $\pm$ 0.021
377.4	382.4	5.0	15.928 $\pm$ 0.022
386.4	391.4	5.0	15.936 $\pm$ 0.022
396.4	401.4	5.0	15.925 $\pm$ 0.023
405.4	410.4	5.0	15.956 $\pm$ 0.022
414.4	419.4	5.0	15.945 $\pm$ 0.022
423.4	428.4	5.0	15.981 $\pm$ 0.023
441.4	446.4	5.0	15.978 $\pm$ 0.023
450.4	455.4	5.0	16.069 $\pm$ 0.024
468.4	473.4	5.0	16.061 $\pm$ 0.024
477.4	482.4	5.0	16.053 $\pm$ 0.024
496.6	501.6	5.0	16.088 $\pm$ 0.024
505.6	510.6	5.0	16.122 $\pm$ 0.025
515.1	520.1	5.0	16.131 $\pm$ 0.025
525.5	530.5	5.0	16.146 $\pm$ 0.026
543.6	548.6	5.0	16.195 $\pm$ 0.026
552.6	557.6	5.0	16.151 $\pm$ 0.026
570.6	575.6	5.0	16.225 $\pm$ 0.027
580.8	585.8	5.0	16.253 $\pm$ 0.029
598.8	603.8	5.0	16.228 $\pm$ 0.026
616.8	621.8	5.0	16.226 $\pm$ 0.026
625.8	630.8	5.0	16.215 $\pm$ 0.026
643.8	648.8	5.0	16.277 $\pm$ 0.028
652.8	657.8	5.0	16.284 $\pm$ 0.028
673.2	678.2	5.0	16.352 $\pm$ 0.029
682.2	687.2	5.0	16.344 $\pm$ 0.029
691.2	696.2	5.0	16.313 $\pm$ 0.029
709.2	714.2	5.0	16.422 $\pm$ 0.031
718.2	723.2	5.0	16.373 $\pm$ 0.030
727.2	732.2	5.0	16.400 $\pm$ 0.031
736.2	741.2	5.0	16.418 $\pm$ 0.031
745.2	750.2	5.0	16.404 $\pm$ 0.031
754.2	759.2	5.0	16.432 $\pm$ 0.031
764.1	769.1	5.0	16.417 $\pm$ 0.033
777.0	782.0	5.0	16.430 $\pm$ 0.031
786.0	791.0	5.0	16.530 $\pm$ 0.033
813.1	818.1	5.0	16.472 $\pm$ 0.032
822.2	827.2	5.0	16.455 $\pm$ 0.032
840.2	845.2	5.0	16.519 $\pm$ 0.033
850.5	855.5	5.0	16.564 $\pm$ 0.034
860.7	865.7	5.0	16.497 $\pm$ 0.034
869.7	874.7	5.0	16.512 $\pm$ 0.033
878.7	883.7	5.0	16.567 $\pm$ 0.034
891.1	896.1	5.0	16.583 $\pm$ 0.035
900.1	905.1	5.0	16.548 $\pm$ 0.034
909.1	914.1	5.0	16.566 $\pm$ 0.035
918.1	923.1	5.0	16.576 $\pm$ 0.034
927.1	932.1	5.0	16.654 $\pm$ 0.037
936.1	941.1	5.0	16.652 $\pm$ 0.036

**Table 3**  
(Continued)

$t_i$ (s)	$t_f$ (s)	$t_{\text{exp}}$ (s)	$w$ (AB)
945.1	950.1	5.0	16.605 ± 0.035
955.2	960.2	5.0	16.604 ± 0.039
964.2	969.2	5.0	16.670 ± 0.037
973.2	978.2	5.0	16.735 ± 0.038
982.2	987.2	5.0	16.687 ± 0.037
991.2	996.2	5.0	16.677 ± 0.037
1000.2	1005.2	5.0	16.715 ± 0.038
1018.2	1023.2	5.0	16.769 ± 0.040
1027.2	1032.2	5.0	16.728 ± 0.038
1036.2	1041.2	5.0	16.688 ± 0.037
1048.4	1053.4	5.0	16.685 ± 0.037
1066.4	1071.4	5.0	16.761 ± 0.040
1077.6	1082.6	5.0	16.794 ± 0.040
1086.7	1091.7	5.0	16.824 ± 0.041
1095.7	1100.7	5.0	16.732 ± 0.038
1104.7	1109.7	5.0	16.783 ± 0.040
1113.8	1118.8	5.0	16.828 ± 0.041
1122.8	1127.8	5.0	16.763 ± 0.040
1131.8	1136.8	5.0	16.821 ± 0.041
1141.9	1146.9	5.0	16.885 ± 0.045
1150.9	1155.9	5.0	16.917 ± 0.045
1159.9	1164.9	5.0	16.847 ± 0.042
1168.9	1173.9	5.0	16.934 ± 0.044
1178.0	1183.0	5.0	16.912 ± 0.044
1187.0	1192.0	5.0	16.962 ± 0.046
1196.0	1201.0	5.0	16.976 ± 0.046
1205.0	1210.0	5.0	16.919 ± 0.044
1214.0	1219.0	5.0	16.892 ± 0.043
1223.0	1228.0	5.0	16.873 ± 0.043
1233.0	1238.0	5.0	16.873 ± 0.047
1242.0	1247.0	5.0	16.878 ± 0.043
1251.0	1256.0	5.0	16.885 ± 0.043
1261.7	1266.7	5.0	17.029 ± 0.048
1270.7	1275.7	5.0	16.981 ± 0.047
1279.7	1284.7	5.0	16.917 ± 0.045
1288.7	1293.7	5.0	16.926 ± 0.045
1297.7	1302.7	5.0	16.905 ± 0.045
1306.7	1311.7	5.0	16.994 ± 0.046
1315.8	1320.8	5.0	17.009 ± 0.048
1325.9	1330.9	5.0	16.983 ± 0.050
1334.9	1339.9	5.0	17.007 ± 0.047
1343.9	1348.9	5.0	17.069 ± 0.050
1352.9	1357.9	5.0	17.028 ± 0.049
1361.9	1366.9	5.0	17.060 ± 0.050
1381.2	1386.2	5.0	17.016 ± 0.049
1399.2	1404.2	5.0	17.100 ± 0.052
1418.3	1423.3	5.0	17.011 ± 0.049
1427.3	1432.3	5.0	17.072 ± 0.050
1436.3	1441.3	5.0	17.028 ± 0.048
1447.1	1452.1	5.0	17.019 ± 0.048
1465.1	1470.1	5.0	17.110 ± 0.052
1474.2	1479.2	5.0	17.054 ± 0.050
1483.1	1488.1	5.0	17.034 ± 0.049
1492.1	1497.1	5.0	17.068 ± 0.050
1806.7	1889.7	50.0	17.362 ± 0.024
1898.7	1986.7	50.0	17.445 ± 0.025
1995.7	2106.7	50.0	17.421 ± 0.025
2115.7	2199.7	50.0	17.456 ± 0.026
2208.7	2291.7	50.0	17.581 ± 0.028
2300.7	2382.7	50.0	17.583 ± 0.029
2391.7	2513.7	50.0	17.591 ± 0.028
2522.7	2614.7	50.0	17.663 ± 0.030
2624.7	2707.7	50.0	17.683 ± 0.029

**Table 3**  
(Continued)

$t_i$ (s)	$t_f$ (s)	$t_{\text{exp}}$ (s)	$w$ (AB)
2719.7	2800.7	50.0	17.762 ± 0.030
2810.7	2891.7	50.0	17.653 ± 0.029
2901.7	2995.7	50.0	17.738 ± 0.032
3004.7	3087.7	50.0	17.744 ± 0.032
3096.7	3178.7	50.0	17.870 ± 0.034
3187.7	3271.7	50.0	17.870 ± 0.033
3290.7	3381.7	50.0	17.846 ± 0.033
3390.7	3472.7	50.0	17.832 ± 0.033
3481.7	3833.7	50.0	17.885 ± 0.036
3842.7	3925.7	50.0	17.905 ± 0.034
3934.7	4017.7	50.0	17.815 ± 0.034
4118.7	4212.7	50.0	17.961 ± 0.036
4221.7	4303.7	50.0	17.959 ± 0.036
4313.7	4398.7	50.0	18.025 ± 0.039
4407.7	4511.7	50.0	17.917 ± 0.035
4520.7	4605.7	50.0	17.906 ± 0.034
4623.7	4705.7	50.0	18.071 ± 0.039
4714.7	4807.7	50.0	17.886 ± 0.034
5024.7	5118.7	50.0	18.081 ± 0.038
5270.7	5353.7	50.0	18.032 ± 0.038
5455.7	5538.7	50.0	17.976 ± 0.037
5547.7	5629.7	50.0	17.876 ± 0.034
5638.7	5720.7	50.0	18.057 ± 0.038
5913.7	6023.7	50.0	18.150 ± 0.041
6224.7	6305.7	50.0	18.043 ± 0.037
6315.7	6400.7	50.0	18.185 ± 0.041
6414.7	6506.7	50.0	18.157 ± 0.043
6515.7	6597.7	50.0	18.276 ± 0.046
6606.7	6701.7	50.0	18.302 ± 0.045
6802.7	6902.7	50.0	18.317 ± 0.048
6911.7	6997.7	50.0	18.150 ± 0.042
7006.7	7093.7	50.0	18.369 ± 0.046
7102.7	7197.7	50.0	18.242 ± 0.043
7206.7	7335.7	50.0	18.329 ± 0.047
7345.7	7426.7	50.0	18.328 ± 0.046
7436.7	7525.7	50.0	18.499 ± 0.052
7536.7	7628.7	50.0	18.544 ± 0.056
7637.7	7719.7	50.0	18.668 ± 0.063
7728.7	7811.7	50.0	18.565 ± 0.058
10806.7	11270.7	250.0	18.871 ± 0.064
11279.7	11758.7	250.0	18.881 ± 0.062
11767.7	12221.7	250.0	19.158 ± 0.080
12230.7	12946.7	250.0	19.152 ± 0.080
12957.7	13447.7	250.0	19.177 ± 0.083
13456.7	13934.7	250.0	19.321 ± 0.091
13943.7	14438.7	250.0	19.167 ± 0.083
14447.7	14939.7	250.0	19.176 ± 0.087
14949.7	15401.7	250.0	19.177 ± 0.087
15412.7	15893.7	250.0	19.169 ± 0.086
15902.7	16386.7	250.0	19.272 ± 0.096
16395.7	17053.7	250.0	19.227 ± 0.099
17577.7	18071.7	250.0	19.083 ± 0.087
18080.7	18648.7	250.0	19.346 ± 0.108
18657.7	19226.7	250.0	19.311 ± 0.099
22264.7	22916.7	250.0	19.505 ± 0.146
22925.7	23495.7	250.0	19.343 ± 0.143
78412.8	110409.6	29230.0	20.309 ± 0.042
164722.3	197031.0	3400.0	21.122 ± 0.171
251164.0	290421.4	19175.0	21.280 ± 0.076
337589.2	376417.5	20035.0	21.498 ± 0.091
424008.9	463199.5	18930.0	21.497 ± 0.101

(This table is available in machine-readable form.)



phase of around 454 s (Fraija et al. 2017b). Even with extreme microphysical conditions, this break occurs no later than  $T + 10$  s. Therefore, we reject this idea and postulate that the plateau phase is powered by late central-engine activity.

#### 4.3. X-Ray Flare

While the optical light curve shows a plateau, the X-ray light curve shows a bright X-ray flare with a peak at  $t = 188$  s and a variability timescale of  $\delta t/t \sim 0.3$ . The X-flare can be fitted with two power laws with rising and decaying indices of  $\alpha_{X,\text{rise}} = -4.82 \pm 1.88$  and  $\alpha_{X,\text{decay}} = 6.08 \pm 1.15$ , respectively. The X-ray flux at the peak of the flare is about seven times larger than the X-ray flux in the normal decay phase immediately after the flare. The X-ray flare released about 5% of the total energy observed in gamma-rays during the prompt phase. Notably, the X-ray flare does not have a counterpart in the optical. In the following subsections, we discuss the possible explanations of the origin of this flare. For the analysis, we assume the same electron index  $p = 2.03 \pm 0.04$  derived in Section 4.1.

##### 4.3.1. Reverse Shock Emission

A reverse shock is expected when the expanding relativistic ejecta encounters the ISM; a forward shock is driven into the ISM and a reverse shock is driven upstream. In the reverse shock, electrons are heated and cooled primarily by synchrotron and Compton scattering emission. A reverse shock is predicted to produce a single flare (see, e.g., Kobayashi et al. 2007; Fraija et al. 2012, 2017a; Fraija & Veres 2018). After the peak of the reverse shock, no new electrons are injected and the shell material cools adiabatically (Fraija et al. 2016a). The evolution of reverse shock can be considered in the regime where the flare is overlapped (thick) or separated (thin) from the prompt emission. Since the X-ray flare in GRB 180205A occurs much later than the prompt emission, any corresponding reverse shock must have evolved in the thin-shell case.

Kobayashi et al. (2007) discussed the generation of an X-ray flare by Compton scattering emission in the early afterglow phase when the reverse shock evolves in the thin-shell case. They found that the X-ray emission created in the reverse region displays a time variability scale of  $\delta t/t \sim 1$  and varies as  $F_\nu \propto t^{5(p-1)/4}$  before the peak and  $\propto t^{-(3p+1)/3}$  after the peak. However, when the high-latitude emission due to the curvature effect is present, the flux decays as  $F_\nu \propto t^{-(3+p)/2}$ . For an electron spectral index of  $p = 2.03 \pm 0.04$ , we expect the temporal index of the rise to be 1.6 and for the decay to be 2.5 in the absence of curvature effects and 2.6 in their presence. Thus, these values cannot account for the observed values of  $\alpha_{X,\text{rise}} = -4.82 \pm 1.88$  and  $\alpha_{X,\text{decay}} = 6.08 \pm 1.15$ . Furthermore, as indicated by Kobayashi et al. (2007), this mechanism cannot produce the short variability timescale of  $\delta t/t \approx 0.3$  observed in GRB 180205A. Finally, a reverse shock would be expected to produce an optical counterpart to the X-ray flare, and this is not seen. Therefore, we conclude that a reverse shock is not a plausible mechanism for the X-ray flare of GRB 180205A.

##### 4.3.2. Neutron Signature

Another important mechanism that might explain the X-ray flare is the presence of neutrons in the fireball (Derishev et al. 1999; Fraija 2014a, 2014b). At a large distance from the

progenitor, when neutrons and ions have been fully decoupled, ions begin to slow down and neutrons form a leading front. Later, a rebrightening in the early afterglow is expected when neutrons decay and their daughter products in turn interact with the slowing ions (Beloborodov 2003).

Fan & Wei (2005) developed this mechanism analytically and predicted the light curve. They reported that when the ejecta evolve in ISM, the variability timescale should satisfy  $\delta t/t \sim 1$ , the flare should be present in all electromagnetic bands, and the light curve should be characterized by a slowly rising flux followed by a sharp rebrightening bump. This does not describe the flare in GRB 180205A which exhibited a variability timescale of  $\delta t/t \approx 0.3$ , a fast rising index of  $-4.82 \pm 1.88$ , and no counterpart flare in the optical. Therefore, we conclude that neutron-proton decoupling is not a plausible mechanism for the X-ray flare of GRB 180205A.

##### 4.3.3. Two-component Jet

Ejecta with two components (one ultra relativistic and another mildly relativistic) have been proposed to explain the X-ray/optical flares and/or rebrightening emission in afterglow light curves (Granot 2005; Racusin et al. 2008; Fraija et al. 2018). Granot (2005) derived the two-component jet light curves and found that this model cannot produce very sharp features in the light curve. In addition, the flux decay after the peak of the second component should be described by the standard afterglow model, and the variability timescale should satisfy  $\delta t/t \sim 1$ . Again, this model cannot reproduce the variability timescale  $\delta t/t \approx 0.3$  and the fast rise and decay of the X-ray flare.

##### 4.3.4. Late Central-engine Activity

In the context of late central-engine activity, the relativistic jet contains multiple shells and the X-ray and optical flares are the result of repeated internal shocks between these shells. The light curves are the superposition of the normal prompt emission and afterglow from the initial activity and flares from late activity.

Diverse origins have been suggested for late activity, including fragmentation of the core associated with the progenitor during the collapse (King et al. 2005), rupture of the accretion disk due to gravitational instability at large radii in different time intervals (Perna et al. 2006; Proga & Zhang 2006), and a neutron star with differential rotation (Dai et al. 2006).

The fast rise comes naturally from the short time variability of the central engine and of the internal shocks. The observed variability timescale of the X-ray flare is much shorter than the duration of the late activity  $\delta t/t < 1$ . For a randomly comoving magnetic field due to internal shell collisions, the flux, in the emitting region, decays as  $F_\nu \propto t^{-2p}$  in the slow-cooling regime (see, e.g., Zhang et al. 2006).

Internal shocks induced by the late activity can account for an X-ray flare without a strong counterpart flare in the optical bands (e.g., Burrows et al. 2005). For instance, the typical synchrotron energy is  $E_p^{\text{syn}} = 3 \text{ keV } \epsilon_{e,-0.3}^2 \gamma_{\text{sh}} \times \left( \frac{4.512}{1+z} \right) \sqrt{\gamma_{\text{sh}}} \epsilon_{B,-1}^{1/2} t_{\nu,-1}^{-1} \Gamma_{\text{is},3}^{-2} L_{j,52}^{1/2}$  (Fraija et al. 2017b) which, for typical values of the luminosity  $L$ , Lorentz factor  $\Gamma$ ,  $\epsilon_B$ , and  $t_\nu$  is only observable in X-rays.

For GRB 180205A, assuming continuity in the value of electron spectral index  $p = 2.03 \pm 0.04$ , the X-ray flux is expected to decline rapidly with an index of  $4.06 \pm 0.08$ .

Therefore, the value of the decaying index is in agreement with the best-fit value  $\alpha_{X,\text{decay}} = 6.08 \pm 1.15$ . (We note that late activity might produce electrons with a different value of  $p$  to the normal phase, but even so we do not expect a value that is much different from  $p = 2.0\text{--}2.3$ , and so this conclusion would remain the same.) The variability timescale of  $\delta t/t \sim 0.3$  is consistent with an expected value around  $\delta t/t \simeq 0.1$  for late activity.

Finally, the absence of a strong optical counterpart flare is also consistent with late activity. The total energetics of the flare suggest that late activity released about 5% of the energy that was released during the prompt emission.

GRB 180205A is not the first event to show signatures of late central activity from early observations; there are several cases explained using this scenario, for example GRB 011121 (Fan & Wei 2005), GRB 050406 (Burrows et al. 2005), GRB 050502B (Burrows et al. 2005), GRB 100814A (Nardini et al. 2014), and GRB 161017A (Tachibana et al. 2018). Dall’Osso et al. (2017) studied the flares cataloged by Margutti et al. (2010) and concluded that many could be explained by late activity. The flare observed in GRB 180205A is similar to many of these other flares in terms of  $t_{\text{peak}}$ , duration, and  $t_{\text{decay}}$ , which further motivates our interpretation of its origin as being due to late central-engine activity.

## 5. Summary

We have presented optical photometry of the afterglow of GRB 180205A with the COATLI telescope and interim instrument (Watson et al. 2016). COATLI received an automated alert at  $T + 206.3$  s, and its quick response allowed us to obtain photometry of the early afterglow from  $T + 217.0$  s, only 10.7 s after the alert.

We compare the optical light curve from COATLI with the X-rays light curve from XRT. We see an early X-ray flare from the start of the observations at  $T + 163$  s, with a peak at about  $T + 188$  s, and lasting until about  $T + 260$  s. The X-ray flare does not have a detectable optical counterpart flare; the early optical light curve shows a plateau to about  $T + 454$  s. The flare and plateau are followed by a normal decay in both X-rays and the optical.

We compare the data to the predictions of models. We find that the normal decay of the afterglow is most convincingly explained as a forward shock against a surrounding homogeneous ISM rather than against a remnant stellar wind. The properties of the flare cannot be easily explained by reverse shock emission, neutron–proton decoupling, or a two-component jet. The flare is most consistently explained by late activity of the central engine; this can explain the fast rise and fall and the absence of an optical counterpart flare.

Our observations of GRB 180205A add to our understanding of the early stages of GRB evolution and the transition from the prompt phase to the early afterglow. While earlier observations give hints of the range of behavior in this transition, we think it is fair to say that observations have not yet really been able to provide strong guidance for theory. Over the next few years, we plan to use the COATLI telescope to conduct early follow-up observations of GRBs discovered by the *Neil Gehrels Swift Observatory*, and anticipate that these efforts will expand our empirical understanding of this important area.

We thank the staff of the Observatorio Astronómico Nacional on the Sierra de San Pedro Mártir. We thank the anonymous referee for a very helpful report.

Some of the data used in this paper were acquired with the COATLI telescope and interim instrument at the Observatorio Astronómico Nacional on the Sierra de San Pedro Mártir. COATLI is funded by CONACyT (LN 232649, 260369, and 271117) and the Universidad Nacional Autónoma de México (CIC and DGAPA/PAPIIT IT102715, IG100414, and IN109408) and is operated and maintained by the Observatorio Astronómico Nacional and the Instituto de Astronomía of the Universidad Nacional Autónoma de México.

This work made use of data supplied by the UK *Swift* Science Data Centre at the University of Leicester.

This work made use of data from the Pan-STARRS1 DR1. The Pan-STARRS1 Surveys (PS1) and the PS1 public science archive have been made possible through contributions by the Institute for Astronomy, the University of Hawaii, the Pan-STARRS Project Office, the Max-Planck Society and its participating institutes, the Max Planck Institute for Astronomy, Heidelberg and the Max Planck Institute for Extraterrestrial Physics, Garching, The Johns Hopkins University, Durham University, the University of Edinburgh, the Queen’s University Belfast, the Harvard-Smithsonian Center for Astrophysics, the Las Cumbres Observatory Global Telescope Network Incorporated, the National Central University of Taiwan, the Space Telescope Science Institute, the National Aeronautics and Space Administration under grant No. NNX08AR22G issued through the Planetary Science Division of the NASA Science Mission Directorate, the National Science Foundation grant No. AST-1238877, the University of Maryland, Eotvos Lorand University (ELTE), the Los Alamos National Laboratory, and the Gordon and Betty Moore Foundation.

## Appendix COATLI Observations

### A.1. Hardware

The COATLI telescope is an ASTELCO Systems 50 cm f/8 Ritchey–Chrétien reflector with protected aluminum coatings. The telescope does not currently give images better than 1.4 arcsec FWHM because of incorrectly figured mirrors; the vendor plans to replace the mirrors in fall 2018.

COATLI is equipped with an interim instrument consisting of a Finger Lakes Instruments ML3200 detector with a Kodak KAF-3200ME monochrome CCD and a Finger Lakes Instruments CFW-1-5 filter wheel. Our medium-term plans are to replace this with an imager with fast guiding and active optics (Watson et al. 2016).

The CCD has  $2184 \times 1472$  photoactive pixels each 6.8 microns or 0.35 arcsec to a side. We typically bin the CCD  $2 \times 2$  to give 0.70 arcsec pixels. The field is  $12.8 \times 8.7$  arcmin with the long axis roughly north–south. The CCD has good peak quantum efficiency from 550 to 700 nm, but is poor to the blue of 400 nm and to the red of 800 nm. The read noise is about 11 electrons.

The filter wheel has *BVRlw* filters. The *BVRI* filters are Bessell filters supplied by Custom Scientific. The *w* filter is an antireflection coated BK-7 filter supplied by Custom Scientific. All filters are 5 mm thick and 50 mm in diameter.



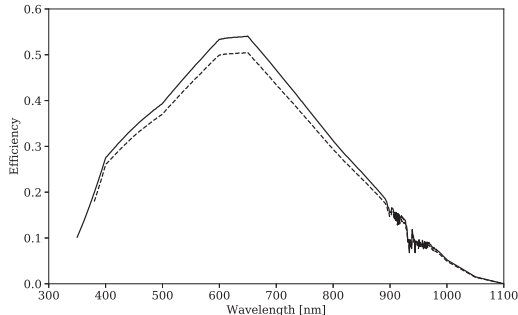


**Figure 5.** Estimated system efficiency of the COATLI telescope and interim imager at an airmass of 1.5. The continuous line shows the system efficiency without filters and the dashed line shows the system efficiency with the  $w$  filter.

Figure 5 shows the estimated system efficiency of the COATLI telescope and interim imager at an airmass of 1.5 with and without the  $w$  filter. The transmission of the  $w$  filter below 380 nm is uncertain; the antireflection is optimized for 400–1000 nm, and we have no information on its performance below 380 nm. However, the figure shows that even without the filter the efficiency is falling rapidly into the UV. The pivot wavelength of the system efficiency with the  $w$  filter, defined by Equation (A16) of Bessell & Murphy (2012), is 630 nm.

The response of the COATLI  $w$  filter is quite different from that of the Pan-STARRS1  $w$  filter (Tonry et al. 2012). The rising response from 400 to 650 nm is similar, but the Pan-STARRS1 response is then flat to the sharp filter cutoff at 800 nm, whereas the COATLI response falls from 700 nm out to the limit of the CCD response at 1100 nm.

#### A.2. Response to GRB 180205A

COATLI is connected to the GCN/TAN alert system and received an XRT alert packet for GRB 180205A at 04:28:55.6 UTC ( $T + 206.3$  s). It immediately slewed to the burst and began observing, with the first exposure starting at 04:29:02.1 UTC ( $T + 212.8$  s), only 6.5 s after the alert.

This quick response is due to several factors: the telescope is mounted on an ASTELCO Systems NTM-500 mount that accelerates at up to  $10 \text{ deg s}^{-2}$  to a maximum velocity of  $30 \text{ deg s}^{-1}$ ; the control system, derived from the one used at the nearby 1.5 m Johnson telescope with the RATIR instrument (Watson et al. 2012), has been tuned to avoid latency; and the scheduler favors observational programs on the same side of the meridian as the center of the *Swift* field, which helps avoid the maneuver necessary to move from one side of the meridian to the other (because the mount is used in a German equatorial configuration).

Unfortunately, in this particular case, the rapid response was somewhat in vain. The usual GCN/TAN BAT alert packets were not sent apparently because of a satellite telemetry problem (Evans et al. 2018). Therefore, while the first exposure started 6.5 s after the alert, this corresponded to  $T + 212.8$  s after the Swift/BAT trigger.

Furthermore, there is evidence that the telescope had not settled before the first exposure started; there are streaks in the image and the raw count levels of field stars is lower than in subsequent images by a factor of 6. Therefore, we believe that

the exposure effectively started at 04:29:06.3 UTC ( $T + 217.0$  s) or 10.7 s after the alert and had an effective exposure time of 0.8 s.

On the first night of 2018 February 5 UTC, the telescope observed the burst almost continuously from 04:29 UTC to the end of astronomical twilight at 13:21 UTC, interrupting only to refocus about once per hour. The telescope also observed the burst on subsequent nights, finishing on 2018 February 10.

Normally, the control system takes 5 s exposures for the first half hour after the trigger and then switches to 30 s exposures, gaining sensitivity for a given total observing time. However, because the GCN/TAN XRT alert packet does not give the trigger time and because the GCN/TAN BAT alert packets were not sent, no trigger time was available and the control system persisted in using relatively inefficient short exposures. Furthermore, we did not notice this and so failed to manually switch to longer exposures on subsequent nights. (To avoid this in the future, we have now changed the control system to switch to 30 s exposures either half an hour after the trigger or half an hour after the first alert.)

#### A.3. Reduction

The raw images from the COATLI interim imager have a read noise of about 11 electrons and are sampled at 6.2 electrons per DN. This sampling is normally adequate. However, problems can arise if, for example, the sample median of a set of pixels is used as an estimator of the population median, because the sample median can differ from the population median by up to half a DN. This problem appears in SExtractor (Bertin & Arnouts 1996), which by default estimates the background as 2.5 times the sample median minus 1.5 times the sample mean. To avoid this problem, we add uniform noise between 0 and 1 DN to every pixel prior to reduction. The additional noise of  $1/\sqrt{12}$  DN or 1.8 electrons is negligible compared to the read noise.

Our reduction pipeline performs bias subtraction, dark subtraction, flat-field correction, and cosmic-ray cleaning with the *cosmicrays* task in IRAF (Tody 1986). We performed astrometric calibration of our images using the *astrometry.net* software (Lang et al. 2010).

For coadding images, we measured the offsets between the brightest star of the field and then used the *imcombine* routine of IRAF (Tody 1986).

#### A.4. Photometry

We obtained raw aperture photometry using SExtractor (Bertin & Arnouts 1996) with a 3.5 arcsec diameter aperture (5 pixels). We chose the aperture equal to 5 pixels after varying the aperture value between 3 and 7 pixels and observing lower noise in the light curves of the field stars.

Observations of about 3000 Pan-STARRS1 stars in other fields (Figure 6) show that for normal stars the transformation from Pan-STARRS1  $g$  and  $r$  AB magnitudes (Magnier et al. 2016) to the natural  $w$  AB magnitudes of COATLI is well fitted for  $-0.5 \leq (g' - r') \leq 2.5$  by

$$(w - r') = 0.353(g' - r') - 0.243(g' - r')^2, \quad (1)$$

with a standard deviation of  $\sigma = 0.017$ .

We applied this equation to Pan-STARRS1 photometry of stars in the field of GRB 180205A to obtain local  $w$  standards.

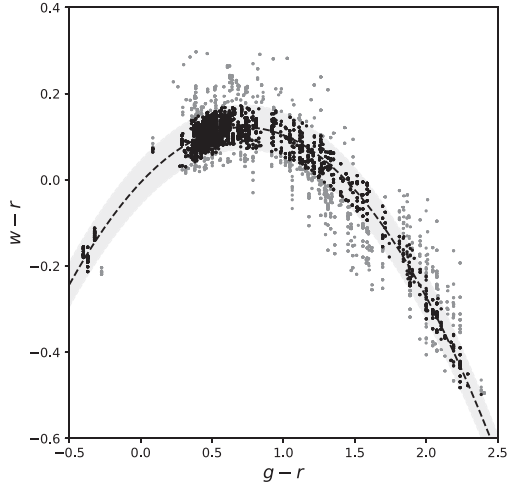


**Figure 6.** Transformation between  $w'$  and Pan-STARRS1  $gr$ . The black solid line is the quadratic model and the gray dashed lines are  $\pm 3$  times the rms deviation from the model. The black data are fitted observations. The gray data are rejected observations. The error bars are  $1\sigma$ .

We used these local standards to calibrate our raw photometry and produce natural  $w$  AB magnitudes of the afterglow.

#### A.5. Extinction Correction

The COATLI  $w$  filter is wide, and so the relation between the extinction in the filter  $A_w$  and the reddening  $E_{B-V}$  is not trivial. Even for a fixed extinction law  $A_\lambda/E_{B-V}$ , the relation depends on the spectrum of the source (because blue spectra are more strongly extinguished than red spectra) and is nonlinear (because extinction gradually reddens the spectrum).

Using the Cardelli et al. (1989) mean extinction curve for  $R_V = 3.1$ , we modeled the extinction  $A_w$  as a function of the reddening  $E_{B-V}$  for sources with unreddened spectra  $F_\nu \propto \nu^{-\beta}$  with  $-2 \leq \beta \leq +4$  and reddening  $0 \leq E_{B-V} \leq 1$ . We then fitted the results, and found

$$A_w/E_{B-V} \approx (a_0 + a_1\beta) + (b_0 + b_1\beta)E_{B-V}, \quad (2)$$

in which  $a_0 = +2.898$ ,  $a_1 = -0.187$ ,  $b_0 = -0.300$ , and  $b_1 = +0.026$ . The deviations between the model results and the fit are at worst 2%, and thus are dwarfed by typical uncertainties in the reddening  $E_{B-V}$ .

Schlegel et al. (1998) estimate  $E(B-V) = 0.03$  in the direction of the GRB.

#### ORCID iDs

N. Fraija <https://orcid.org/0000-0002-0173-6453>  
 N. R. Butler <https://orcid.org/0000-0002-9110-6673>  
 E. Troja <https://orcid.org/0000-0002-1869-7817>  
 C. G. Román-Zúñiga <https://orcid.org/0000-0001-8600-4798>

#### References

Amati, L., Frontera, F., Tavani, M., et al. 2002, *A&A*, 390, 81  
 Beloborodov, A. M. 2003, *ApJL*, 583, L19  
 Bertin, E., & Arnouts, S. 1996, *A&AS*, 117, 393

- Bessell, M., & Murphy, S. 2012, *PASP*, 124, 140  
 Bolmer, J., & Kann, D. A. 2018a, *GCN*, 22391, 1  
 Bolmer, J., & Kann, D. A. 2018b, *GCN*, 22383, 1  
 Brun, R., & Rademakers, F. 1997, *NIMPA*, 389, 81  
 Burrows, D. N., Romano, P., Falcone, A., et al. 2005, *Sci*, 309, 1833  
 Butler, N. R. 2007, *AJ*, 133, 1027  
 Butler, N. R., Kocevski, D., Bloom, J. S., & Curtis, J. L. 2007, *ApJ*, 671, 656  
 Cardelli, J. A., Clayton, G. C., & Mathis, J. S. 1989, *ApJ*, 345, 245  
 Chevalier, R. A., & Li, Z.-Y. 2018, *ApJ*, 536, 195  
 Cunningham, V., Neill, J. D., Cenko, S. B., & Walters, R. 2018, *GCN*, 22414, 1  
 Dai, Z. G., Wang, X. Y., Wu, X. F., & Zhang, B. 2006, *Sci*, 311, 1127  
 Dall'Osso, S., Perna, R., Tanaka, T. L., et al. 2017, *MNRAS*, 464, 4399  
 Derishev, E. V., Kocharovsky, V. V., & Kocharovsky, V. V. 1999, *ApJ*, 521, 640  
 Emery, S. W. K., & Evans, P. A. 2018, *GCN*, 22396, 1  
 Evans, P. A., Beardmore, A. P., Page, K. L., et al. 2009, *MNRAS*, 397, 1177  
 Evans, P. A., Kennea, J. A., Page, K. L., & Palmer, D. M. 2018, *GCN*, 22381, 1  
 Falcon, E., Yunus, S., Zheng, W., & Filippenko, A. 2018, *GCN*, 22390, 1  
 Fan, Y. Z., & Wei, D. M. 2005, *MNRAS*, 364, L42  
 Filgas, R., Greiner, J., Schady, P., et al. 2012, *A&A*, 546, A101  
 Fraija, N. 2014a, *ApJ*, 787, 140  
 Fraija, N. 2014b, *MNRAS*, 437, 2187  
 Fraija, N. 2015, *ApJ*, 804, 105  
 Fraija, N., De Colle, F., Veres, P., et al. 2017a, arXiv:1710.08514  
 Fraija, N., Gonzalez, M. M., & Lee, W. H. 2012, *ApJ*, 751, 33  
 Fraija, N., Lee, W. H., Araya, M., et al. 2017b, *ApJ*, 848, 94  
 Fraija, N., Lee, W. H., & Veres, P. 2016a, *ApJ*, 818, 190  
 Fraija, N., Lee, W. H., Veres, P., & Barniol Duran, R. 2016b, *ApJ*, 831, 22  
 Fraija, N., Pedreira, A. C., Caligula do, E. S., & Veres, P. 2018, arXiv:1803.02978  
 Fraija, N., & Veres, P. 2018, *ApJ*, 859, 70  
 Fraija, N., Veres, P., Zhang, B. B., et al. 2017c, *ApJ*, 848, 15  
 Granot, J. 2005, *ApJ*, 631, 1022  
 Granot, J., & Sari, R. 2002, *ApJ*, 568, 820  
 Hou, S. J., Geng, J. J., Wang, K., et al. 2014, *ApJ*, 785, 113  
 Im, M., Choi, C., Paek, G. S., et al. 2018a, *GCN*, 22397, 1  
 Im, M., Choi, C., Paek, G. S., et al. 2018b, *GCN*, 22404, 1  
 Jóhannesson, G., Björnsson, G., & Gudmundsson, E. H. 2006, *ApJ*, 647, 1238  
 King, A., O'Brien, P. T., Goad, M. R., et al. 2005, *ApJL*, 630, L113  
 Kobayashi, S., Zhang, B., Mészáros, P., & Burrows, D. 2007, *ApJ*, 655, 391  
 Kouveliotou, C., Meegan, C. A., Fishman, G. J., et al. 1993, *ApJL*, 413, L101  
 Krimm, H. A., Barthelmy, S. D., Cummings, J. R., et al. 2018, *GCN*, 22393, 1  
 Kumar, P., & Barniol Duran, R. 2010, *MNRAS*, 409, 226  
 Kumar, P., & Piran, T. 2000, *ApJ*, 532, 286  
 Kumar, P., & Zhang, B. 2015, *PhR*, 561, 1  
 Lang, D., Hogg, D. W., Mierle, K., Blanton, M., & Roweis, S. 2010, *AJ*, 139, 1782  
 Lattimer, J. M., & Schramm, D. N. 1976, *ApJ*, 210, 549  
 Lazzati, D., Rossi, E., Covino, S., Ghisellini, G., & Malesani, D. 2002, *A&A*, 396, L5  
 Lee, W. H., & Ramirez-Ruiz, E. 2007, *NJPh*, 9, 17  
 Li, L., Wu, X.-F., Huang, Y.-F., et al. 2015, *ApJ*, 805, 13  
 Liang, E.-W., Li, L., Gao, H., et al. 2013, *ApJ*, 774, 13  
 MacFadyen, A. I., & Woosley, S. E. 1999, *ApJ*, 524, 262  
 Magnier, E. A., Sweeney, W. E., Chambers, K. C., et al. 2016, arXiv:1612.05244  
 Margutti, R., Guidorzi, C., Chincarini, G., et al. 2010, *MNRAS*, 406, 2149  
 Mazaeva, Volnova, A., Pozanenko, A., & Klunko, E. 2018, *GCN*, 22430, 1  
 Narayana Bhat, P., Meegan, C. A., von Kienlin, A., et al. 2016, *ApJS*, 223, 28  
 Nardini, M., Elliott, J., Filgas, R., et al. 2014, *A&A*, 562, A29  
 Nysewander, M., Fruchter, A. S., & Pe'er, A. 2009, *ApJ*, 701, 824  
 Oksanen, A., & Malesani, D. 2018, *GCN*, 22401, 1  
 Paczynski, B. 1989, *ApJL*, 308, L43  
 Paczynski, B. 1991, *AcA*, 41, 257  
 Page, K. L., Beardmore, A. P., D'Avanzo, P., et al. 2018, *GCN*, 22394, 1  
 Panaitescu, A. 2008, *MNRAS*, 383, 1143  
 Perna, R., Armitage, P. J., & Zhang, B. 2006, *ApJL*, 636, L29  
 Proga, D., & Zhang, B. 2006, *MNRAS*, 370, L61  
 Racusin, J. L., Karpov, S. V., Sokolowski, M., et al. 2008, *Natur*, 455, 183  
 Santana, R., Barniol Duran, R., & Kumar, P. 2014, *ApJ*, 785, 29  
 Sari, R., Narayan, R., & Piran, T. 1996, *ApJ*, 473, 204  
 Sari, R., & Piran, T. 1999, *ApJ*, 520, 641  
 Sari, R., Piran, T., & Halpern, J. P. 1999, *ApJ*, 519, 17  
 Sari, R., Piran, T., & Narayan, R. 1998, *ApJ*, 497, 17

- Schlegel, D. J., Finkbeiner, D. P., & Davis, M. 1998, *ApJ*, 500, 525
- Swenson, C. A., Maxham, A., Roming, P. W. A., et al. 2010, *ApJL*, 718, L14
- Tachibana, Y., Arimoto, M., Asano, K., et al. 2018, *PASJ*, 70, 92
- Tanvir, N., Heintz, K. E., Selsing, J., et al. 2018, GCN, 22384, 1
- Tody, D. 1986, *Proc. SPIE*, 627, 733
- Tonry, J. L., Stubbs, C. W., Lykke, K. R., et al. 2012, *ApJ*, 750, 99
- Uehara, T., Uemura, M., Kawabata, K. S., et al. 2010, *A&A*, 519, A56
- von Kienlin, A. 2018, GCN, 22386, 1
- Wang, X.-G., Zhang, B., Liang, E.-W., et al. 2015, *ApJS*, 219, 9
- Wang, Y., Aimuratov, Y., Moradi, R., et al. 2018, *MmSAI*, 89, 293
- Watson, A. M., Cuevas Cardona, S., Alvarez Nuñez, L. C., et al. 2016, *Proc. SPIE*, 9908, 99085O
- Watson, A. M., Richer, M. G., Bloom, J. S., et al. 2012, *Proc. SPIE*, 8444, 84445L
- Wiersema, K., & Covino, S. 2018, GCN, 22388, 1
- Woosley, S. E. 1993, *ApJ*, 405, 273
- Xin, L. P., Pi, F. Q., Wei, J. Y., et al. 2018, GCN, 22392, 1
- Zhang, B., Fan, Y. Z., Dyks, J., et al. 2006, *ApJ*, 642, 354
- Zheng, W., & Filippenko, A. 2018, GCN, 22382, 1
- Zhu, Z. P., Feng, H. X., Xu, D., et al. 2018, GCN, 22395, 1

## 4.2 Reverse shock emission revealed in early photometry in the possible short GRB 180418A

In this work, we present the photometry of the early and late afterglow of GRB 180418A with data set from the TAROT and the RATIR instruments. Early data from TAROT shows a bright rise in the flux between  $T + 28$  and  $T + 90$  seconds that we interpret as the reversal shock signature. About  $T + 2$  minutes, RATIR began to observe the field of GRB 180418A and complements the photometry for this event.

In first instance, this transient was reported by GCN/Alerts as a short GRB but, this identification was not confirmed by subsequent analysis. We reanalyze the data from *Fermi*/GBM and *Swift*/BAT in order to confirm the duration and the hardness of the event. The results, although are not conclusive, show that GRB 180418A is likely to be a short GRB. Then, we suggest that GRB 180418A is the first short GRB which present a reverse shock signature. We fit the data using the fireball model and specifically the afterglow standard theory. We do not observe any jet break in the optical nor X-rays and, therefore, we can estimate a lower limit for the angle of the jet  $\theta_j > 7^\circ$ .

Using deep late time optical observations we place an upper limit of  $r > 24$  AB mag on any underlying host galaxy. The afterglow detection in the *Swift* UV filters constrains the GRB redshift to  $z < 1.3$ , thus placing an upper bound to the  $\gamma$ -ray isotropic equivalent energy  $E_{\gamma,\text{iso}} < 3 \times 10^{51}$  erg. The properties of this GRB (e.g. duration, hardness ratio, energetics and environment) lie at the intersection between merger and collapsar burst, and we can not conclusively identify its progenitor.

This paper will be sent to ApJ in about one month and is attached below.

## REVERSE SHOCK EMISSION REVEALED IN EARLY PHOTOMETRY IN THE SHORT GRB 180418A

BECERRA, R. L.<sup>1</sup>; DICHIARA, S.<sup>2,3</sup>; WATSON, A. M.<sup>1</sup>; TROJA, E.<sup>2,3</sup>; FRAIJA, N.<sup>1</sup>; KLOTZ, A.<sup>4</sup>; BUTLER, N. R.<sup>5</sup>.  
LEE, W. H.<sup>1</sup>; VERES, P.<sup>6</sup>; BLOOM, J. S.<sup>2</sup>; BOER, M.<sup>7</sup>; GONZÁLEZ, J. J.<sup>1</sup>; KUTYREV, A. S.<sup>3</sup>; PROCHASKA, J. X.<sup>3</sup>;  
RAMÍREZ-RUIZ, E.<sup>8</sup>; RICHER, M. G.<sup>9</sup>; ROMÁN-ZÚÑIGA, C. G.<sup>9</sup>; TURPIN, D.<sup>4</sup>

- <sup>1</sup> Instituto de Astronomía, Universidad Nacional Autónoma de México, Apartado Postal 70-264, 04510 México, CDMX, México;  
<sup>2</sup> Department of Astronomy, University of Maryland, College Park, MD 20742-4111, USA;  
<sup>3</sup> Astrophysics Science Division, NASA Goddard Space Flight Center, 8800 Greenbelt Road, Greenbelt, MD 20771, USA;  
<sup>4</sup> Institut de Recherche en Astrophysique et lanéologie, 14 Avenue Edouard Belin, 31400 Toulouse, France;  
<sup>5</sup> School of Earth and Space Exploration, Arizona State University, Tempe, AZ 85287, USA;  
<sup>6</sup> Center for Space Plasma and Aeronomic Research (CSPAR), University of Alabama in Huntsville, Huntsville, AL 35899, USA;  
<sup>7</sup> ARTEMIS, UMR 7250 (CNRS/OCA/UNS), boulevard de l'Observatoire, BP 4229, F 06304 Nice Cedex, France;  
<sup>8</sup> Department of Astronomy and Astrophysics, UCO/Lick Observatory, University of California, 1156 High Street, Santa Cruz, CA 95064, USA;  
<sup>9</sup> Instituto de Astronomía, Universidad Nacional Autónoma de México, Unidad Académica en Ensenada, 22860 Ensenada, BC, Mexico;

*Draft version March 19, 2019*

### ABSTRACT

We present observations of the short duration GRB 180418A in  $\gamma$ -rays, X-rays, and in the optical band. Early optical photometry with the TAROT and RATIR instruments show a bright peak ( $\approx 14.2$  AB mag) between  $T + 28$  and  $T + 90$  seconds that we interpret as the reversal shock signature. This is the first time that such signature is identified in the optical afterglow of a short GRB, suggesting a weakly magnetized jet ( $R_B \approx 14$ ). Later observations can be modeled by a standard forward shock model and show no evidence of jet break, allowing us to constrain the jet collimation to  $\theta_j > 7^\circ$ .

Using deep late time optical observations we place an upper limit of  $r > 24$  AB mag on any underlying host galaxy. The afterglow detection in the *Swift* UV filters constrains the GRB redshift to  $z < 1.3$ , thus placing an upper bound to the  $\gamma$ -ray isotropic equivalent energy  $E_{\gamma, \text{iso}} < 3 \times 10^{51}$  erg. The properties of this GRB (e.g. duration, hardness ratio, energetics and environment) lie at the intersection between merger and collapsar burst, and we can not conclusively identify its progenitor.

*Subject headings:* (stars) gamma-ray burst: individual (GRB 180418A).

### 1. INTRODUCTION

Gamma-ray burst (GRBs) are the brightest events in the universe. There are two main populations of GRBs: short GRBs (SGRBs) and long GRBs (LGRBs). The populations are distinguished by their duration  $T_{90}$ , the interval in the observer's frame over which 90% of the total background-subtracted counts are observed (Kouveliotou et al. 1993), and other secondary parameters such as hardness and spectral lag. The population of SGRBs typically has  $T_{90} < 2$  seconds and harder spectra whereas the population of LGRBs typically has  $T_{90} > 2$  seconds and softer spectra (Gehrels, & Razzaque 2013). Nevertheless, there is some overlap between the distributions of  $T_{90}$  and hardness, and in some cases it is not clear whether a burst with intermediate properties belongs to the population of SGRBs or LGRBs.

SGRBs are thought to be the consequence of mergers between binary neutron stars driven by angular momentum and energy losses to gravitational radiation (e.g. Eichler et al. 1989; Narayan et al. 1992; Ruffert & Janka 1998; Rosswog & Ramirez-Ruiz 2002; Giacomazzo et al. 2011; Lee & Ramirez-Ruiz 2007). The resulting system cannot survive as a single neutron star and collapses to a black hole. The gravitational waves emitted during the merger provide information on the masses of the objects (Abbott et al. 2017a). The first discovery of a binary neutron star merger (GW170817) in gravitational waves revealed the importance of the multi-messenger

approach. Combined detection of electromagnetic counterparts (kilonova, GRB prompt and afterglow) is crucial for the understanding of these peculiar phenomena (Abbott et al. 2017b).

On the other hand, most of LGRBs arise from the core collapse of massive stars (Hjorth et al. 2003) and are associated with hydrogen poor, high-velocity type Ic supernovae (Cano 2013).

Both SGRBs and LGRBs produce relativistic jets. The standard model for their electromagnetic emission is the fireball model (Paczynski & Rhoads 1993; Piran 1999; Zhang & Mészáros 2004; Kumar & Zhang 2015). This model distinguishes between the prompt and afterglow stages. The prompt phase is dominated by internal shocks within the relativistic jet, whereas the afterglow phase is dominated by external shocks between the jet and the circumstellar medium (Piran 1999). Two kinds of external shocks are important: long-duration forward shocks which propagate outward sweeping up the circumstellar medium and a short-lived and a short-duration reverses shock which propagate back into the jet (Meszaros & Rees 1993).

Emission from forward shocks explains the afterglow phase of most GRBs. The dynamics of the forward shocks have been amply explored (Meszaros and Rees 1997; Sari & Piran 1999; Granot & Sari 2002). Detailed studies of the afterglow emission and especially the forward shock component, provide valuable informa-

tion about the total energy, geometry, and the structure of the circumburst medium (e.g. Stratta et al. 2007; De Pasquale et al. 2010; Burrows et al. 2006; Troja et al. 2016; Fraija et al. 2019). On the other hand, the reverse shock emission is useful for understanding the initial bulk Lorentz factor, the ejecta composition and magnetization (e.g. Steele et al. 2009; Mundell et al. 2013; Fraija et al. 2016).

Reverse shocks are discussed by Meszaros and Rees (1997); Sari & Piran (1999); Kobayashi (2000); Gao & Mészáros (2015) and are predicted to generate a strong optical flash observable in the very early stages of the afterglow. After the flare no new electrons are injected and the shell material cools adiabatically.

Rapid (within minutes) and sensitive optical observations are crucial to study the reverse shock emission. Bright optical flashes have been observed in many LGRBs (e.g. Akerlof et al. 1999; Bloom et al. 2009; Vestrand et al. 2014; Troja et al. 2017; Fraija & Veres 2018) and are inconsistent with a simple forward shock scenario. They are normally explained as a emission from a reverse shock (Japelj et al. 2014; Fraija et al. 2017). Reverse shock component in the afterglow of SGRBs have been previously suggested on the basis of gamma and radio observations (e.g. Burrows et al. 2006; Lloyd-Ronning 2018; Fraija et al. 2019, 2016), but they have not previously been identified in the optical.

In this work, we present the photometric data and analysis of GRB 180418A, detected with TAROT 28 seconds after the gamma-ray trigger. We show that it is likely to be the first SGRB showing reverse shock emission in the optical.

The paper is organized as follows. In §2, we present the observations with *Swift*, *Fermi*, TAROT, RATIR and other telescopes. In §3 we present a temporal and spectral analysis and discuss the nature of this GRB. In §4 we explain their implications and discuss the results. Finally, in §5 we summarize our conclusions. In Appendix A, we present our search for the GRB host galaxy.

## 2. OBSERVATIONS

### 2.1. Neil Gehrels Swift Observatory

The *Swift*/BAT instrument triggered on GRB 180418A at  $T = 2018$  March 25 06:44:06.012 UTC (trigger 826428) (D’Elia et al. 2018). The BAT light curve showed a single FRED-like pulse that started at  $T + 0$  seconds, peaked at about  $T + 0.4$  seconds, and ended at about  $T + 3.5$  seconds. The BAT light curve is shown in Figure 1.

The *Swift*/BAT data of GRB 180418A were processed using HEASOFT package (v6.25). Energy calibration was applied with BATECONVERT and the mask weighting was included with BATMASKWTEVT. We used BATTBLOCKS to run the Bayesian Block algorithm over the 16 ms, background-subtracted, 15–350 keV light curve and determined  $T_{90} = 1.504 \pm 0.380$ . BATTBLOCKS was run with the default configuration options except the background-subtraction parameter *bkgsb* was set to ‘YES’.

The 15–150 keV spectrum integrated over the  $T_{90}$  interval (from 0.272 s to 1.776 s) is well fitted by a simple power law with photon index of  $1.43 \pm 0.11$  ( $\chi^2/\text{d.o.f.} = 1.02$ ) and a fluence of  $(2.72 \pm 0.11) \times 10^{-7}$  erg cm<sup>2</sup>. From this spectrum we derive a hardness ratio of  $S(100 -$

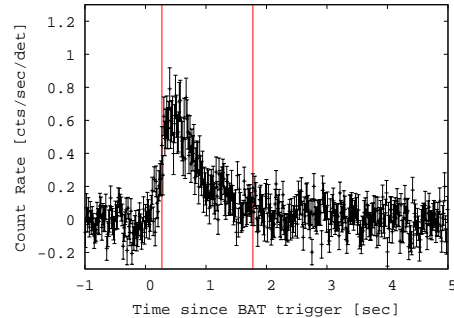


FIG. 1.— *Swift*/BAT light curve using a binning of 16 ms and observed in the range 15–350 keV. The red lines mark the start and end of the  $T_{90}$  interval.  $50)/S(25 - 50) = 1.48$ .

The 15–150 keV peak flux was derived from the spectrum integrated in the interval from 0.144 s to 1.144 s. The peak spectrum is well fitted by a power law with a photon index of  $1.41 \pm 0.11$ , a peak flux of  $(2.36 \pm 0.17) \times 10^{-7}$  erg cm<sup>-2</sup> s<sup>-1</sup>, and a peak photon flux of  $(2.98 \pm 0.17)$  cm<sup>-2</sup> s<sup>-1</sup>.

Due to an observing constraint, *Swift* did not slew to the source until  $T + 49.6$  minutes (D’Elia et al. 2018), and so the *Swift*/XRT instrument only started observing the field at  $T + 3081.4$  seconds. It detected a fading source at 11:20:29.17 +24:55:59.1 J2000 with a 90% uncertainty radius of 1.8 arcsec (Osborne et al. 2018; Goad et al. 2018; Liu et al. 2018). The X-ray spectrum could be fitted with an absorbed power-law with a photon spectral index of  $2.02^{+0.28}_{-0.26}$  and an absorption column of  $8.0^{+7.1}_{-5.8} \times 10^{20}$  cm<sup>-2</sup>, in excess of the Galactic value of  $1.1 \times 10^{20}$  cm<sup>-2</sup> (Liu et al. 2018). For our analysis in this paper, we used the X-ray light curve and the spectrum obtained from the pipeline of Butler (2007) and Butler et al. (2007).

The *Swift*/UVOT instrument started observing the field at  $T + 3086$  seconds and detected a fading source at 11:20:29.21 +24:55:59.2 J2000 with a 90% uncertainty radius of 0.49 arcsec (Siegel & D’Elia 2018). We download UVOT data from the online archive<sup>1</sup> and derived magnitudes and signal-to-noise ratios. Table 1 shows the filter, initial time  $t_i$  and the final time  $t_f$  (relative to  $T$ ), the AB magnitude, and the signal-to-noise ratio. For UVOT, the exposure time is simply  $t_f - t_i$ .

### 2.2. Fermi Gamma-Ray Observatory

The *Fermi*/GBM instrument triggered on GRB 180418A at 2018 April 18 06:44:06.28 UTC (trigger 545726651/180418281) and observed a single FRED-like peak (Figure 2), in agreement with the *Swift*/BAT light curve, with a  $T_{90}$  duration of  $2.56 \pm 0.20$  seconds and a 10–1000 keV fluence of  $(5.9 \pm 0.1) \times 10^{-7}$  erg cm<sup>-2</sup> (Bissaldi & Veres 2018; Narayana Bhat et al. 2016). The GBM light curve is shown in Figure 2. The burst was not detected by the *Fermi*/LAT instrument.

### 2.3. TAROT Observations

<sup>1</sup> <https://swift.gsfc.nasa.gov/archive/>



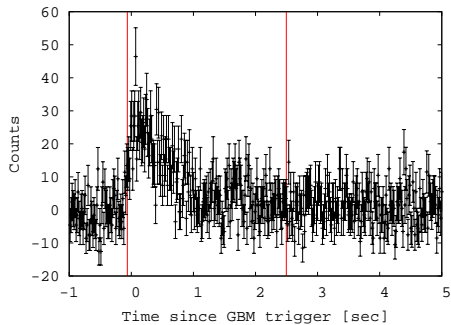


FIG. 2.— GBM light curve since the GBM trigger. The energy range is 8–1000 keV and the binning of 16 ms. The red lines mark the start and end of the  $T_{90}$  interval.

TAROT<sup>2</sup> La Silla is a 25-cm robotic telescope located at the European Southern Observatory, La Silla Observatory, in Chile. TAROT is equipped with a CCD and a filter wheel with *BVRIC* filters (Klotz et al. 2008).

TAROT is connected to the GCN/TAN alert system and received a BAT quick look alert packet for GRB 180418A at 06:44:21 UTC ( $T + 15$  seconds). It immediately slewed to the burst and began observing in the clear *C* filter, with the first exposure starting at 06:44:34 UTC ( $T + 28$  seconds). The first exposure is trailed with a duration of 60 seconds to allow continuous monitoring of the light curve (Klotz et al. 2006). Subsequent exposure were taken in sidereal tracking mode with exposure times of 30 to 90 seconds and read times of about 10 seconds. We use TAROT data from  $T + 28$  seconds to  $T + 392$  seconds (Klotz et al. 2018).

Table 2 gives our photometry from TAROT. For each exposure it gives the initial time  $t_i$  and the final time  $t_f$  (relative to  $T$ ) and the AB  $r$  magnitude (obtained from the *C* magnitude and not corrected for Galactic extinction) with the the  $1\sigma$  total uncertainties (including both statistical and systematic contributions). For TAROT, the exposure time is simply  $t_f - t_i$ . Figure 3 shows the photometry from TAROT and other sources.

#### 2.4. RATIR Observations

RATIR<sup>3</sup> is a four-channel simultaneous optical and near-infrared imager mounted on the 1.5-meter Harold L. Johnson Telescope at the Observatorio Astronómico Nacional in Sierra San Pedro Mártir in Baja California, Mexico (Butler et al. 2012; Watson et al. 2012; Littlejohns et al. 2015). RATIR usually obtains simultaneous photometry in *riZJ* or *riYH*, but at the time of these observations the *ZY* and *JH* channels were not operational. Therefore, RATIR only obtained photometry in *ri*.

RATIR is connected to the GCN/TAN alert system and received a BAT quick look alert packet for GRB 180418A at 06:44:20.3 UTC ( $T + 14.3$  seconds). It immediately slewed to the burst and began observing, with the first exposure starting at 06:46:06.3 UTC ( $T + 120.6$  seconds). It took simultaneous exposures in  $r$  and  $i$  with

an exposure time of 80 seconds and a cadence of about 100 seconds. On the nights of 2018 April 18, 19, 20, and 21 UTC, RATIR observed from  $T + 120.6$  seconds to  $T + 3.64$  hours (Troja et al. 2018), from  $T + 20.47$  to  $T + 27.09$  hours (Troja et al. 2018), from  $T + 44.62$  to  $T + 51.37$  hours, and from  $T + 68.55$  to  $T + 75.27$  hours.

The RATIR reduction pipeline performs bias subtraction and flat-field correction, followed by astrometric calibration using the *astrometry.net* software (Lang et al. 2010), iterative sky-subtraction, coaddition using SWARP, and source detection using SEXTRACTOR (Littlejohns et al. 2015). The images were calibrate against SDSS (Littlejohns et al. 2015).

Table 3 gives our RATIR photometry. For each exposure or coadded exposure it gives the initial time  $t_i$  and final time  $t_f$  (relative to  $T$ ), the total exposure time  $t_{\text{exp}}$ , and the  $r$  and  $i$  magnitudes (not corrected for Galactic extinction) with their  $1\sigma$  total uncertainties (including both statistical and systematic contributions). Figure 3 shows the photometry from RATIR and other sources.

#### 2.5. Other Terrestrial Observations

Zheng & Filippenko (2018) began to observe the field of GRB 180418A with KAIT at 06:46:41 UTC ( $T + 125$  seconds). They reported an optical transient that faded from about magnitude 15.8 at  $T + 135$  seconds. Due to the delay in the *Swift*/XRT observations, this was the first precise localization of the counterpart of GRB 180418A. Additional photometry was reported by Guidorzi et al. (2018); Sota et al. (2018); Fong et al. (2018); Malesani et al. (2018); Schady (2018); Misra et al. (2018); Schady & Chen (2018); Choi et al. (2018); Horiuchi et al. (2018).

Schady (2018) mentioned that the source was not clearly point-like in their images and suggested this might be due to the presence of a host galaxy close to the afterglow. However, our RATIR observations from 2018 April 19 ( $T + 68.5$  to  $T + 75.3$  hours) revealed no detection to a  $3\sigma$  limiting magnitudes of  $r > 24.0$  and  $i > 23.9$ , which places a limit on the magnitude of any close host galaxy.

### 3. ANALYSIS

#### 3.1. Temporal Analysis

The prompt emission from the GRB detected by *Fermi*/GBM and *Swift*/BAT lasted until about  $T + 2.5$  seconds. The earliest data from *Swift*/XRT start at  $T + 52$  minutes. Our optical observations from TAROT and RATIR begin at  $T + 28$  and  $T + 121$  seconds, respectively, significantly after the end of prompt emission. Therefore, we focus our analysis on the afterglow.

##### 3.1.1. Optical Temporal Analysis

We use TAROT/RATIR  $r$ -filter data for the analysis, as we have more data in this band and the  $i$ -filter of RATIR shows the same qualitative behavior. We complement our data set with information published in GCNs Zheng & Filippenko (2018); Guidorzi et al. (2018); Fong et al. (2018); Schady (2018). Figure 4 shows the optical and X-ray light curves for GRB 180418A.

The optical light curve appears to be a smooth power-law decline but with an excess of emission at early times up to about 500 seconds. The later normal decay is present in most afterglows (Zhang et al. 2006).

<sup>2</sup> <http://tarot.obs-hp.fr/>

<sup>3</sup> <http://ratir.astroscu.unam.mx/>

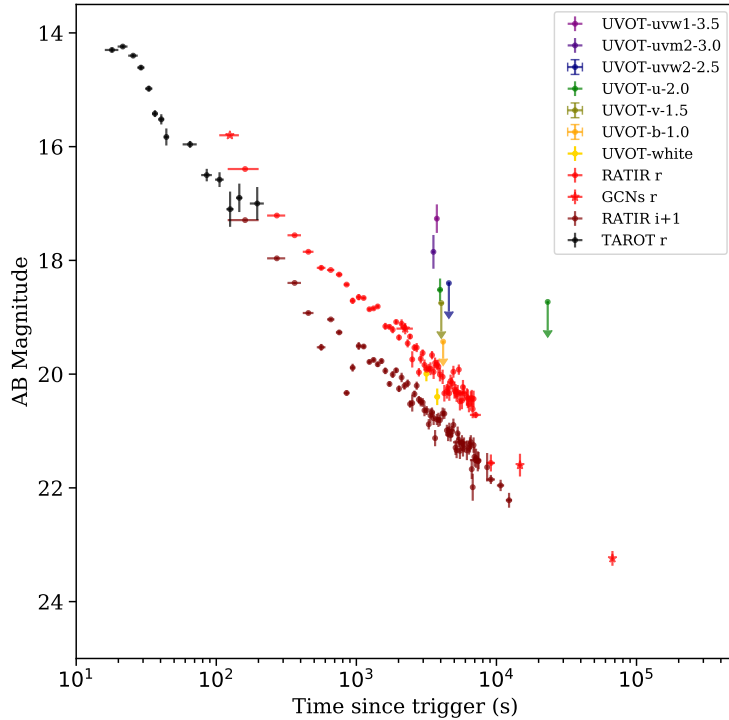


FIG. 3.— GRB 180418A photometry from this work (TAROT, RATIR, and UVOT) and GCNs (Zheng & Filippenko 2018; Guidorzi et al. 2018; Fong et al. 2018; Schady 2018)

We fit the optical light curve for  $t > 1000$  seconds using a simple forward external shock component into a constant-density ISM under the supposition of a thin-shell evolving in the slow-cooling regime below the cooling break (Kobayashi 2000), which has a temporal index  $\alpha_{\text{forward}} = 1.01 \pm 0.01$ . The temporal index  $\alpha_{\text{forward}}$  is expected to be related to the electron energy index  $p$  by  $\alpha_{\text{forward}} = 3(p-1)/4$ , so we predict  $p = 2.35 \pm 0.01$ .

The light curve for the forward-shock component is shown in the left panel of Figure 4. However, extrapolating this fit to earlier times, it is clear that there is a significant excess of emission, and this is shown in the right panel of Figure 4. This excess is present from our earliest observation at  $t = 28$  seconds until  $t \approx 100$ –300 seconds and has a peak at  $t \approx 40$  seconds. A priori, there are several different scenarios which might explain this excess.

First, we consider the possibility of late central activity. The timing of the excess corresponds to a range of the relative duration  $\delta t/t$  (duration over the peak time) of about 2, whereas late central engine activity typically yields  $\delta t/t \ll 1$  Zhang et al. (2006) and is therefore un-

likely to power the observed rebrightening.

Second, we consider a two-component jet scenario Peng et al. (2005). However, in that case, the excess would appear a couple of hours after the trigger, and so this cannot explain a very early excess like the one seen here in GRB 180418A.

Finally, we consider emission from a reverse external shock (Kobayashi 2000) in addition to a standard forward shock. For this model, the temporal indexes of the rise and the decay are related to the peak time of the emission of the reverse shock  $t_\gamma$  and the electron index  $p$  (assumed to be the same for both the forward and reverse shocks) by  $\alpha_{\text{reverse,R}} = 3/2 - 3p$  and  $\alpha_{\text{reverse,D}} = (27p + 7)/35$ , respectively. Thus, the free parameters of the model for the total emission from both shocks are  $p$ ,  $t_\gamma$ , and the normalization of the two components. The final fit for both components is shown in the right panel of Figure 4 and has a  $\chi^2/d.o.f. = 0.98$  with an electron index  $p = 2.35 \pm 0.03$ . The parameters for this model are shown in Table 4. (The temporal indexes  $\alpha$  are labeled with suffixes for reverse and forward and with  $R$  or  $D$  to refer to the rise and decay phase of the reverse component.)



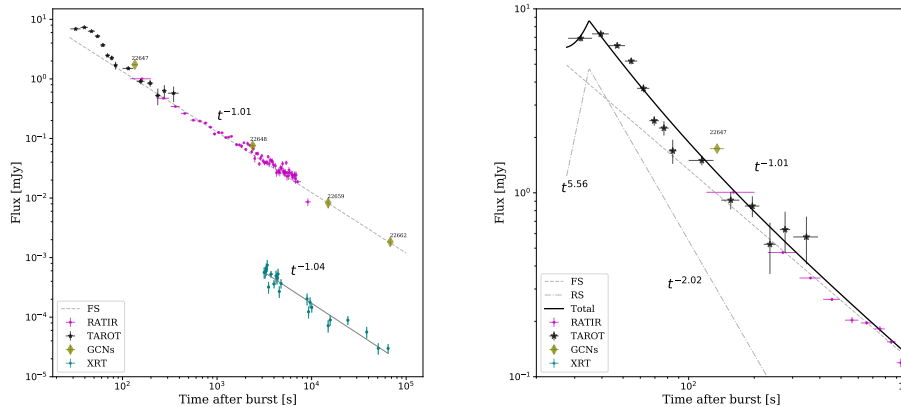


FIG. 4.— Left: Fitting of the GRB 180418A light curve with a single power-law. Points red and blue are observations in  $r$ -band and X-rays respectively. The X-ray and  $r$ -band show a non break up to  $10^5$ s. Right: Zoom of GRB 180418A light curve at early times with a fit using a reverse (RS) and a forward shock (FS) components. The final fit for optical is the black line (which includes the sum of forward and reverse shock)

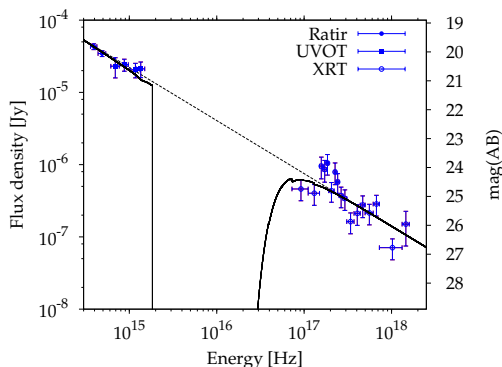


FIG. 5.— The SED of GRB 180418A from X-rays to the optical at  $t = 4000$  seconds. The data are from *Swift*/XRT, *Swift*/UVOT, and RATIR. The dotted line is a simple power law with index  $\beta = 0.73$ . The solid line is the best fit from XSPEC.

### 3.1.2. X-Rays Temporal Analysis

We have *Swift*/XRT data for  $t > 51$  minutes. This region can be fitted as a power-law with a temporal index of  $\alpha_{X, \text{forward}} = 1.04 \pm 0.05$ . The similarity of this to the temporal index in the optical suggests that the emission in both wavelength regions arises from the same regime, which we assume to be a thin-shell evolving in the slow-cooling regime below the cooling break into a constant density ISM (Kobayashi 2000).

### 3.2. Spectral Analysis

We retrieved the *Swift*/XRT X-ray spectrum in the time interval 3091–4831 s from the online repository<sup>4</sup>. We interpolated our UVOT and RATIR photometry to

<sup>4</sup> [http://www.swift.ac.uk/xrt\\_spectra/](http://www.swift.ac.uk/xrt_spectra/)

$t = 4000$  s assuming a power-law decay with an index of  $\alpha_{\text{forward}} = 1.01$  (see §3.1.1). Figure 5 shows the resulting combined spectral energy distribution (SED).

From the X-ray to the optical, the SED can be fitted with a simple power law with index  $\beta = 0.73 \pm 0.03$ . Under our assumption of a thin-shell evolving in the slow-cooling regime with the cooling break above the X-rays (Kobayashi 2000), we would expect the spectral index to be  $(p - 1)/2$  or  $0.68 \pm 0.01$  for  $p = 2.35$ . Thus, our observed value is in good agreement with this prediction.

### 3.3. Photometric Redshift

No spectroscopic redshift for the burst has been reported, therefore we are forced to place limits on the redshift from the combined X-ray, UV, and optical broad-band SED. The SED fitting was carried out using XSPECv12.10.1 (Arnaud 1996) taking into account galactic extinction for IR, optical and UV energy bands due to dust (Cardelli et al. 1989), the IR/optical/UV extinction of the host galaxy, and the photoelectric absorption of soft X-rays (in the Galaxy and in the host galaxy). We set the redshift as a free parameter during the fit, and found an upper limit of  $z < 1.31$  at a 90% confidence level. This limit basically comes from the fit requiring that the Lyman continuum absorption fall below our detection in the UVOT *uvm2* filter.

### 3.4. Classification of the Burst

The values of  $T_{90}$  do not unambiguously identify GRB 180418A as a SGRB or LGRB. The value of  $T_{90} = 1.50 \pm 0.38$  from the *Swift*/BAT light curve would suggest a SGRB, although it is only below 2 seconds by  $1.3\sigma$ . However, the value of  $T_{90} = 2.56 \pm 0.20$  s from the *Fermi*/GBM light curve (Bissaldi & Veres 2018) would suggest a LGRB.

Additional information on the nature of a GRB can sometimes be obtained from the spectral hardness and

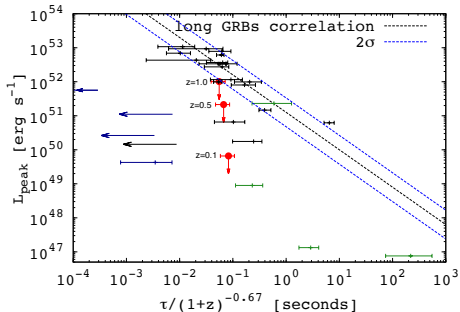


FIG. 6.— Relation between  $\tau$  and  $L_{peak}$ . The red data show the values for GRB 180418A assuming redshifts of  $z=0.1$ ,  $z=0.5$ ,  $z=1.0$ . The black dotted line is the relation from Norris et al. (2000) and the blue dotted lines show the  $2\sigma$  scatter. The figure also shows objects from Gehrels et al. (2006) including the energy band correction.

lag. The spectral hardness found from *Swift*/BAT instrument is  $S(100 - 50)/S(25 - 50) = 1.48$ , which corresponds to intermediate hardness in the classification of Bromberg et al. (2013) and does not help to resolve the ambiguity.

We also investigate lag between the arrival times between high- and low-energy photons  $t_{lag}$  and peak luminosity  $L_{peak}$  correlation for LGRBs reported by Norris et al. (2000). We used RMfit<sup>5</sup>, version 432, to analyze the spectrum around the peak of the GBM light curve in the time interval from  $-0.128$  to  $0.896$  s. The spectrum fits with a single power-law with index  $-1.46 \pm 0.07$  and flux  $= (6.01.2) \times 10^{-7}$  between 10 and 1000 keV. Using these parameters we derived an upper limits for the peak luminosity  $L_{peak}$  as a function of redshift, obtaining  $L_{peak} = 6.57 \times 10^{49}$  erg,  $L_{peak} = 2.14 \times 10^{51}$  erg and  $L_{peak} = 1.01 \times 10^{52}$  erg for  $z=0.1$ ,  $z=0.5$  and  $z=1.0$ , respectively. The time-lag between the energy bands 50-100 keV and 15-25 keV ( $\tau = 0.088 \pm 0.026$ ) was retrieved from the GCN notice 22658 Palmer et al. (2018). We applied the time dilation correction and energy correction due to the redshift considering the relation between the pulse width and energy (Norris 2002) and approximating the correction factor with  $(1+z)^{0.67}$  as proposed by Gehrels et al. (2006). The results of this analysis are shown in Figure 6 and compared with data presented by Gehrels et al. (2006) and the LGRB correlation of Norris et al. (2000). We see that GRB 180418A is only consistent with an LGRB provided the redshift is larger than about 1. Unfortunately, our photometric analysis in §3.3 only requires  $z < 1.3$ , and so we are unable to rule out the possibility and again cannot conclusively decide on the nature of the burst.

#### 4. DISCUSSION

We have presented a multi-wavelength study of the GRB 180418A. From the analysis of the  $\gamma$ -ray data, the probability to belong to the non-Collapsar (or merger) class lies between 10-30% (Bromberg et al. 2013). Using the well-known correlation of spectral lag and peak luminosity (Figure 6), we can consider GRB 180418A as a

<sup>5</sup> <https://fermi.gsfc.nasa.gov/ssc/data/analysis/rmfit/>

possible candidate to be a NS merger event, although its definitive classification depends on the distance scale.

No spectroscopic redshift was measured for this GRB. We studied the afterglow SED at  $t \sim 4,000$  s, combining data provided by RATIR, *Swift*/UVOT and *Swift*/XRT, and constrained the redshift to  $z < 1.31$ . Thanks to the rapid response of TAROT, we were able to detect the optical counterpart as early as 28 sec. This early afterglow shows evidence for emission from a reverse shock. GRB 180418A is not the first GRB to present a reverse shock signature in the optical range (see Table 6), although we suggest that it is the first short duration GRB to show this.

The presence of an optical peak at 39 seconds with an observed magnitude  $r = 14.2$  AB suggests a *Peak + Fast Decay* behavior, which was explored by Kann et al. (2010) and interpreted as evidence of an additional component superposed on the forward shock afterglow. This component is indeed attributed to a reverse shock flash (Japelj et al. 2014). Within the framework discussed by Fraija et al. (2017), the afterglow parameters were calculated using the  $\chi^2$  minimization within the ROOT software package (Brun & Rademakers 1997) and following the model from Kobayashi & Zhang (2003); Kobayashi et al. (2007). We derived the Lorentz factor  $\Gamma = 160$ , the Lorentz critical factor of  $\Gamma_c = 430$ , the microphysical parameters  $\epsilon_B = 10^{-3}$  and  $\epsilon_e = 0.1$ , and a jet magnetization  $R_B \approx 14$ . All these values are reported in Table 5.

We can estimate some parameters assuming a  $\Lambda$ CDM cosmology with a  $H_0 = 67.8$  km/Mpc/s (Planck Collaboration et al. 2014). For a typical value of  $z < 1.3$  we obtained a luminosity distance of  $\lesssim 9$  Gpc and  $E_{\gamma,iso} \lesssim 3 \times 10^{51}$  erg which is in the typical range for short GRBs (Berger 2014). The relation of optical luminosity at a rest-frame time of 7h ( $L_{opt,7}$ ) as function of  $E_{\gamma,iso}$  according to Berger (2014) is given by:

$$L_{opt,7} \approx 6.9 \times 10^{42} E_{\gamma,iso,51}^{0.74} \text{ erg s}^{-1}, \quad (1)$$

then  $L_{opt,7} \lesssim 10^{43}$  erg s<sup>-1</sup>, in agreement with the value reported in Table 4.

The multi-wavelength afterglow is described by a simple power-law decay for  $t > 100$  sec, and shows no evidence of a jet break. The relation between the jet break time and half opening angle  $\theta_j$  is related with density, energy, time of break and redshift as described in Sari et al. (1999):

$$\theta_j = 0.13 \left( \frac{t_j}{1+z} \right)^{3/8} \left( \frac{n}{E_{52}} \right)^{1/8}, \quad (2)$$

which, in the case of GRB 180418A, leads to  $\theta_j > 7^\circ$ .

#### 5. SUMMARY

We presented photometric data and analysis of the short GRB 180418A. Our results are based mainly on observations made by *Swift*, TAROT and RATIR instruments. We presented several arguments linking GRB 180418A to the class of SGRBs. We explained the early and late light curves within the standard fireball scenario using a forward+reverse model. The reverse shock component is present in GRB 180418A, with a peak emission at  $T + 35$  seconds. This is the earliest optical detection

of a SGRB. From the total fit, we calculated the afterglow parameters, which would be consistent with other SGRBs, and constrained the jet collimation to  $\theta_j > 7$  deg. There is not clear association with any host galaxy, although we derive an upper limit of  $z < 1.3$  from the afterglow broadband spectrum.

Photometry presented in this work adds to our understanding of the early stages of GRBs, and would represent the first evidence of a reverse shock component for a SGRB.

#### ACKNOWLEDGMENTS

We thank the staff of the Observatorio Astronómico Nacional on Sierra San Pedro Mártir. RATIR is a collaboration between the University of California, the Universidad Nacional Autónoma de México, NASA Goddard Space Flight Center, and Arizona State University, benefiting from the loan of an H2RG detector and hardware and software support from Teledyne Scientific and Imaging. RATIR, the automation of the Harold L. Johnson Telescope of the Observatorio Astronómico Nacional on Sierra San Pedro Mártir, and the operation of both are funded through NASA grants NNX09AH71G, NNX09AT02G, NNX10AI27G, and NNX12AE66G, CONACyT grants INFR-2009-01-122785 and CB-2008-101958, UNAM PAPIIT grants IG100414, IA102917 and IA102019, UC MEXUS-CONACyT grant CN 09-283, and the Instituto de Astronomía of the Universidad Nacional Autónoma de México. We acknowledge the vital contributions of Neil Gehrels and Leonid Georgiev to the early development of RATIR. TAROT has been built with the support of the Institut National des Sciences de l'Univers, CNRS, France. TAROT is funded by the CNES and thanks the help of the technical staff of the Observatoire de Haute Provence, OSU-Pythéas.

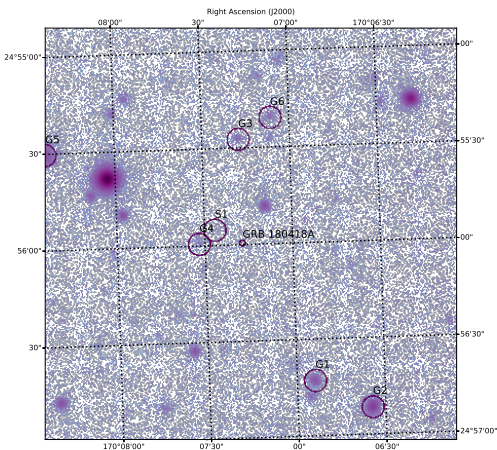


FIG. 7.— A deep RATIR  $r$  image of the neighborhood of GRB 180418A. Information on the detected galaxies is given in Table 7.

#### A. SEARCH FOR THE GRB HOST GALAXY

We obtained deep photometry of the field with RATIR on the fourth night, at about  $T + 72$  hours. Our  $r$ -band image is shown in Figure 7 and photometry of sources is given in Table 7. The first column is the object label as shown in Figure 7, the second is the SDSS DR12 ID, the

third and fourth columns are the J2000 coordinates, the fifth and sixth columns are  $r$  and  $i$  AB magnitude, respectively, the seventh column is the angular separation  $\delta R$  in arcseconds, and the last column is the probability of a chance alignment  $P(<\delta R)$  (Bloom et al. 2002).

We detect no source at the position of the GRB afterglow, thus any coincident host galaxy must be fainter than our  $3\sigma$  limits of  $r > 24.0$  and  $i > 23.9$ . Such a faint galaxy would be consistent with our limit  $z < 1.3$  on the GRB redshift and, if compared to field galaxies (Berger et al. 2007), might suggest  $z > 0.3$ .

Fong et al. (2018) noted that there were no extended sources within 30 arcsec of the afterglow position down to a limit of  $g > 23.4$  and  $r > 22.5$ . Thanks to our deeper photometry, we detect fainter sources, such as one at  $r = 24.0$  and  $i = 23.7$  at a separation of 9 arcsec from the afterglow. Our images have a FWHM of about 2 arcsec, so we can say little about whether these faint sources are extended or not, although at these magnitudes we expect the majority to be galaxies (Yasuda et al. 2001).

The two galaxies with the smallest chance probabilities are G4 with  $P(<\delta R) = 0.67$  and S1 with  $P(<\delta R) = 0.69$ . G4 appears in the SDSS DR12 catalog with a photometric redshift of  $z = 0.80 \pm 0.12$  and an absolute magnitude of  $M_r = -21.23$ . If it were the host galaxy, the projected distance to the GRB would be 325 kpc. S1 is not in the SDSS DR12 catalog, but if it were at a typical SGRB redshift of 0.5 (Berger 2014), the projected offset to the GRB would be 137 kpc. Both of these projected distances are large compared to the sample of Troja et al. (2008) and Berger (2014), whose offsets range up to 75 kpc. Thus, based both on the large chance probabilities  $P(<\delta R)$  and the large offset distances, neither of these galaxies are likely to be the host of the GRB.

#### REFERENCES

- Abbott, B. P., Abbott, R., Abbott, T. D., et al. 2017, *Physical Review Letters*, 119, 161101
- Abbott, B. P., Abbott, R., Abbott, T. D., et al. 2017, *ApJ*, 848, L12
- Akerlof, C., Balsano, R., Barthelmy, S., et al. 1999, *Nature*, 398, 400
- Amati, L., Guidorzi, C., Frontera, F., et al. 2008, *MNRAS*, 391, 577
- Arnaud, K. A. 1996, *Astronomical Data Analysis Software and Systems V*, 101, 17
- Barthelmy, S. D., Baumgartner, W. H., Cummings, J. R., et al. 2013, *GRB Coordinates Network, Circular Service, No. 14470, #1* (2013), 14470, 1
- Berger, E., Fox, D. B., Price, P. A., et al. 2007, *ApJ*, 664, 1000
- Berger, E. 2010, *ApJ*, 722, 1946
- Berger, E. 2014, *ARA&A*, 52, 43
- Bissaldi, E., & Veres, P. 2018, *GRB Coordinates Network, Circular Service, No. 22656, #1* (2018/April-0), 22656, 1
- Blandford, R. D., & McKee, C. F. 1976, *Physics of Fluids*, 19, 1130
- Bloom, J. S., Odewahn, S. C., Djorgovski, S. G., et al. 1999, *ApJ*, 518, L1
- Bloom, J. S., Kulkarni, S. R., & Djorgovski, S. G. 2002, *AJ*, 123, 1111
- Bloom, J. S., Perley, D. A., Li, W., et al. 2009, *ApJ*, 691, 723
- Breeveld, A. A., Landsman, W., Holland, S. T., et al. 2011, *American Institute of Physics Conference Series*, 1358, 373
- Bromberg, O., Nakar, E., Piran, T., et al. 2013, *ApJ*, 764, 179.
- Brun, R., & Rademakers, F. 1997, *Nuclear Instruments and Methods in Physics Research A*, 389, 81
- Burrows, D. N., Grupe, D., Capalbi, M., et al. 2006, *ApJ*, 653, 468
- Butler, N. R. 2007, *AJ*, 133, 1027
- Butler, N. R., Kocevski, D., Bloom, J. S., & Curtis, J. L. 2007, *ApJ*, 671, 656
- Butler, N., Klein, C., Fox, O., et al. 2012, *Proc. SPIE*, 8446, 844610
- Cano, Z. 2013, *MNRAS*, 434, 1098.
- Cardelli, J. A., Clayton, G. C., & Mathis, J. S. 1989, *ApJ*, 345, 245
- Castro-Tirado, A. J., Møller, P., García-Segura, G., et al. 2010, *A&A*, 517, A61
- Choi, C., Kim, Y., Park, W., Shin, S., & Im, M. 2018, *GRB Coordinates Network, Circular Service, No. 22668, #1* (2018/April-0), 22668, 1
- Cucchiara, A., Fox, D. B., Tanvir, N., & Berger, E. 2009, *GRB Coordinates Network*, 9873, 1
- Cucchiara, A., Cenko, S. B., Bloom, J. S., et al. 2011, *ApJ*, 743, 154
- Cummings, J., Barbier, L., Barthelmy, S., et al. 2005, *GRB Coordinates Network*, 3479, 1
- Cummings, J., Barbier, L., Barthelmy, S., et al. 2006, *GRB Coordinates Network*, 4538, 1
- da Silva, R., Fumagalli, M., Worsack, G., & Prochaska, X. 2011, *GRB Coordinates Network, Circular Service, No. 11635, #1* (2011), 11635, 1
- D’Elia, V., D’Ai, A., Evans, P. A., et al. 2018, *GRB Coordinates Network, Circular Service, No. 22646, #1* (2018/April-0), 22646, 1
- De Pasquale, M., Schady, P., Kuin, N. P. M., et al. 2010, *ApJ*, 709, L146
- de Ugarte Postigo, A., Jakobsson, P., Malesani, D., et al. 2009, *GRB Coordinates Network*, 8766, 1
- de Ugarte Postigo, A., Horváth, I., Veres, P., et al. 2011, *A&A*, 525, A109
- Eichler, D., Livio, M., Piran, T., et al. 1989, *Nature*, 340, 126

- Evans, P. A., Beardmore, A. P., Page, K. L., et al. 2009, *MNRAS*, 397, 1177
- Fan, Y. Z., & Wei, D. M. 2005, *MNRAS*, 364, L42
- Fan, Y. Z., Zhang, B., & Wei, D. M. 2005, *ApJ*, 628, L25
- Foley, R. J., Chen, H.-W., Bloom, J., & Prochaska, J. X. 2005, *GRB Coordinates Network*, 3483, 1
- Fong, W., Berger, E., Margutti, R., et al. 2012, *ApJ*, 756, 189
- Fong, W., Berger, E., Metzger, B. D., et al. 2014, *ApJ*, 780, 118
- Fong, W., Tanvir, N. R., Levan, A. J., & Chornock, R. 2018, *GRB Coordinates Network, Circular Service*, No. 22659, #1 (2018/April-0), 22659, 1
- Fraija, N., Lee, W. H. & Veres, P., 2016, *ApJ*, 818, 190
- Fraija, N., Lee, W. H., Veres, P., & Barniol Duran, R. 2016, *ApJ*, 831, 22
- Fraija, N., Lee, W. H., Araya, M., et al. 2017, *ApJ*, 848, 94
- Fraija, N., Veres, P., Zhang, B. B., et al. 2017, *ApJ*, 848, 15
- Fraija, N. & Veres, P. 2018, *ApJ*, 859, 70
- Fraija, N., De Colle, F., Veres, P. et al. 2019, *ApJ*, 871, 123
- Fraija, N., Pedreira, A. C. C. d. E. S. and Veres, P. 2019, *ApJ*, 871, 200
- Gao, H., Lei, W.-H., Zou, Y.-C., Wu, X.-F., & Zhang, B. 2013, *New Astronomy Review*, 57, 141
- Gao, H., & Mészáros, P. 2015, *Advances in Astronomy*, 2015, 192383
- Gavazzi, G., Fumagalli, M., Cucciati, O., & Boselli, A. 2010, *A&A*, 517, A73
- Gehrels, N., Norris, J. P., Barthelmy, S. D., et al. 2006, *Nature*, 444, 1044.
- Gehrels, N., & Razaque, S. 2013, *Frontiers of Physics*, 8, 661.
- Gendre, B., Klotz, A., Palazzi, E., et al. 2010, *MNRAS*, 405, 2372
- Gendre, B., Atteia, J. L., Boër, M., et al. 2012, *ApJ*, 748, 59
- Giacomazzo, B., Rezzolla, L. and Baiotti, L. 2011, *Phys. Rev. D*, 83, 044014
- Goad, M. R., Osborne, J. P., Beardmore, A. P., & Evans, P. A. 2018, *GRB Coordinates Network, Circular Service*, No. 22650, #1 (2018/April-0), 22650, 1
- Gomboc, A., Kobayashi, S., Guidorzi, C., et al. 2008, *ApJ*, 687, 443
- Gomboc, A., Kobayashi, S., Mundell, C. G., et al. 2009, *American Institute of Physics Conference Series*, 1133, 145
- Granot, J., & Sari, R. 2002, *ApJ*, 568, 820
- Greiner, J., Bornemann, W., Clemens, C., et al. 2008, *PASP*, 120, 405
- Gruber, D., Krühler, T., Foley, S., et al. 2011, *A&A*, 528, A15
- Guidorzi, C., Martone, R., Kobayashi, S., et al. 2018, *GRB Coordinates Network, Circular Service*, No. 22648, #1 (2018/April-0), 22648, 1
- Hjorth, J., Sollerman, J., Møller, P., et al. 2003, *Nature*, 423, 847
- Hogg, D. W., Pahre, M. A., McCarthy, J. K., et al. 1997, *MNRAS*, 288, 404.
- Horiuchi, T., Hanayama, H., Honma, M., et al. 2018, *GRB Coordinates Network, Circular Service*, No. 22670, #1 (2018/April-0), 22670, 1
- Japelj, J., Kopač, D., Kobayashi, S., et al. 2014, *ApJ*, 785, 84
- Jelínek, M., Prouza, M., Kubánek, P., et al. 2006, *Nuovo Cimento B Serie*, 121, 1495
- Jin, Z.-P., Covino, S., Della Valle, M., et al. 2013, *ApJ*, 774, 114
- Kann, D. A., Klose, S., Zhang, B., et al. 2010, *ApJ*, 720, 1513
- Kippen, R. et al. 1999, *GRB Coordinates Network*, 224, 1
- Klotz, A., Gendre, B., Stratta, G., et al. 2006, *A&A*, 451, L39
- Klotz, A., Boë2006ApJ...642..354Zr, M., Eysseric, J., et al. 2008, *PASP*, 120, 1298
- Klotz, A., Atteia, J. L., Boer, M., Eymar, L., & Gendre, B. 2018, *GRB Coordinates Network, Circular Service*, No. 22671, #1 (2018/April-0), 22671, 1
- Kobayashi, S. 2000, *ApJ*, 545, 807
- Kobayashi, S., & Zhang, B. 2003, *ApJ*, 582, L75
- Kobayashi, S., Zhang, B., Mészáros, P., & Burrows, D. 2007, *ApJ*, 655, 391
- Kouveliotou, C., Meegan, C. A., Fishman, G. J., Bhat, N. P., Briggs, M. S., Koshut, T. M., Paciesas, W. S., & Pendleton, G. N. 1993, *ApJ*, 413, L101
- Kumar, P., & Zhang, B. 2015, *Phys. Rep.*, 561, 1
- Lang, D., Hogg, D. W., Mierle, K., Blanton, M., & Roweis, S. 2010, *AJ*, 139, 1782
- Perley, D. A., Cenko, S. B., Corsi, A., et al. 2014, *ApJ*, 781, 37
- Lee, W. H., & Ramirez-Ruiz, E. 2007, *New Journal of Physics*, 9, 17
- Levan, A. J., Cenko, S. B., Perley, D. A., & Tanvir, N. R. 2013, *GRB Coordinates Network, Circular Service*, No. 14455, #1 (2013), 14455, 1
- Littlejohns, O. M., Butler, N. R., Cucchiara, A., et al. 2015, *MNRAS*, 449, 2919
- Liu, Z., Melandri, A., D'Avanzo, P., et al. 2018, *GRB Coordinates Network, Circular Service*, No. 22655, #1 (2018/April-0), 22655, 1
- Lloyd-Ronning, N. 2018, *Galaxies*, 6, 468
- Malesani, D., Heintz, K. E., Stone, M., & Stone, J. 2018, *GRB Coordinates Network, Circular Service*, No. 22660, #1 (2018/April-0), 22660, 1
- Markwardt, C., Barthelmy, S., Barbier, L., et al. 2005, *GRB Coordinates Network*, 3467, 1
- Markwardt, C. B., Barthelmy, S. D., Baumgartner, W. H., et al. 2011, *GRB Coordinates Network, Circular Service*, No. 11646, #1 (2011), 11646, 1
- Mészáros, P., & Rees, M. J. 1993, *ApJ*, 405, 278
- Mészáros, P., Rees, M. J. 1997, *Optical and Long-Wavelength Afterglow from Gamma-Ray Bursts. The Astrophysical Journal* 476, 232.
- Mészáros, P., & Rees, M. J. 1999, *MNRAS*, 306, L39
- Misra, K. et al. 2018, *GRB Coordinates Network*, 22663, 1
- Mundell, C. G., Kopač, D., Arnold, D. M., et al. 2013, *Nature*, 504, 119
- Narayan, R., Paczynski, B. and Piran, T. 1992, *ApJ*, 395, L83
- Narayana Bhat, P., Meegan, C. A., von Kienlin, A., et al. 2016, *ApJS*, 223, 28
- Nicuesa Guelbenzu, A., Klose, S., Krühler, T., et al. 2012, *A&A*, 538, L7
- Nicuesa Guelbenzu, A., Klose, S., Rossi, A., et al. 2011, *A&A*, 531, L6
- Norris, J. P., Marani, G. F., & Bonnell, J. T. 2000, *ApJ*, 534, 248
- Norris, J. P. 2002, *ApJ*, 579, 386
- Osborne, J. P., Burrows, D. N., Kennea, J. A., et al. 2018, *GRB Coordinates Network, Circular Service*, No. 22649, #1 (2018/April-0), 22649, 1
- Paczynski, B., & Rhoads, J. E. 1993, *ApJ*, 418, L5
- de Palma, F., Bissaldi, E., Tajima, H., et al. 2009, *GRB Coordinates Network*, 9872, 1
- Palmer, D. M., Barthelmy, S. D., Cummings, J. R., et al. 2018, *GRB Coordinates Network, Circular Service*, No. 22658, #1 (2018/April-0), 22658, 1
- Pandey, S. B., Swenson, C. A., Perley, D. A., et al. 2010, *ApJ*, 714, 799
- Pelangeon, A. & Atteia, J. L. 2006, *GRB Coordinates Network*, 4544, 1
- Peng, F., Königl, A., & Granot, J. 2005, *ApJ*, 626, 966
- Perley, D. A., Bloom, J. S., Butler, N. R., et al. 2008, *ApJ*, 672, 449
- Planck Collaboration, Ade, P. A. R., Aghanim, N., et al. 2014, *A&A*, 571, A1
- Poole, T. S., Breeveld, A. A., Page, M. J., et al. 2008, *MNRAS*, 383, 627
- Piran, T. 1999, *Phys. Rep.*, 314, 575
- Rees, M. J., & Mészáros, P. 1998, *ApJ*, 496, L1
- Rosswog, S. and Ramirez-Ruiz, E. 2002, *MNRAS*, 336, L7
- Ruffert, M. and Janka, H. T. 1998, *A&A*, 338, 535
- Sakamoto, W., et al. 2005, *GRB Coordinates Network*, 3938, 1
- Sakamoto, T., Barthelmy, S. D., Baumgartner, W. H., et al. 2009, *GRB Coordinates Network*, 9231, 1
- Sari, R., Piran, T., & Narayan, R. 1998, *ApJ*, 497, L17
- Sari, R., & Piran, T. 1999, *ApJ*, 520, 641
- Sari, R., Piran, T., & Halpern, J. P. 1999, *ApJ*, 519, L17
- Schady, P. 2018, *GRB Coordinates Network, Circular Service*, No. 22662, #1 (2018/April-0), 22662, 1
- Schady, P., & Chen, T.-W. 2018, *GRB Coordinates Network, Circular Service*, No. 22666, #1 (2018/April-0), 22666, 1
- Shao, L., & Dai, Z. G. 2005, *ApJ*, 633, 1027
- Siegel, M. H., & D'Elia, V. 2018, *GRB Coordinates Network, Circular Service*, No. 22665, #1 (2018/April-0), 22665, 1
- Sota, A., Hu, Y., Tello, J. C., Carrasco, I., & Castro-Tirado, A. J. 2018, *GRB Coordinates Network, Circular Service*, No. 22657, #1 (2018/April-0), 22657, 1

- Steele, I. A., Mundell, C. G., Smith, R. J., et al. 2009, *Nature*, 462, 767
- Steidel, C. C., & Hamilton, D. 1993, *AJ*, 105, 2017
- Stratta, G., D'Avanzo, P., Piranomonte, S., et al. 2007, *A&A*, 474, 827
- Stratta, G., D'Avanzo, P., Piranomonte, S., et al. 2008, *American Institute of Physics Conference Series*, 1000, 297
- Stratta, G., Pozanenko, A., Atteia, J.-L., et al. 2009, *A&A*, 503, 783
- Troja, E., King, A. R., O'Brien, P. T., Lyons, N., & Cusumano, G. 2008, *MNRAS*, 385, L10
- Troja, E., Sakamoto, T., Cenko, S. B., et al. 2016, *ApJ*, 827, 102
- Troja, E., Butler, N., Watson, A. M., et al. 2018, *GRB Coordinates Network*, Circular Service, No. 22652, #1 (2018/April-0), 22652, 1
- Troja, E., Lipunov, V. M., Mundell, C. G., et al. 2017, *Nature*, 547, 425
- Troja, E., Butler, N., Watson, A. M., et al. 2018, *GRB Coordinates Network*, Circular Service, No. 22664, #1 (2018/April-0), 22664, 1
- Vestrand, W. T., Wren, J. A., Panaitescu, A., et al. 2014, *Science*, 343, 38
- Vreeswijk, P. M., Smette, A., Malesani, D., et al. 2008, *GRB Coordinates Network*, 7444, 1
- Watson, A. M., Richer, M. G., Bloom, J. S., et al. 2012, *Proc. SPIE*, 8444, 84445L
- Wei, D. M. 2003, *A&A*, 402, L9
- Wei, D. M., Yan, T., & Fan, Y. Z. 2006, *ApJ*, 636, L69
- Yasuda, N., Fukugita, M., Narayanan, V. K., et al. 2001, *AJ*, 122, 1104
- Yu, Y. W., Wang, X. Y., & Dai, Z. G. 2009, *ApJ*, 692, 1662
- Zhang, B., & Mészáros, P. 2002, *ApJ*, 566, 712
- Zhang, B. and Mészáros, P. 2004, *International Journal of Modern Physics A*, 19, 2385
- Zhang, B., Fan, Y. Z., Dyks, J., et al. 2006, *ApJ*, 642, 354
- Zhang, B.-B., Zhang, B., Castro-Tirado, A. J., et al. 2018, *Nature Astronomy*, 2, 69
- Zheng, W. & Filippenko, A. V., 2018, *GRB Coordinates Network*, 22647, 1

TABLE 1  
UVOT OBSERVATIONS OF GRB 180418A

Filter	$t_i$ (s)	$t_f$ (s)	AB	SNR
<i>v</i>	3242.6	4834.19	$> 20.25$	—
<i>b</i>	4063.89	4263.66	$20.43 \pm 0.30$	3.687
<i>u</i>	3858.83	4058.61	$20.52 \pm 0.20$	5.675
<i>uvw1</i>	3654.22	3854.01	$20.77 \pm 0.25$	4.438
<i>uvw2</i>	3449.18	3648.95	$20.85 \pm 0.30$	3.734
<i>uvw2</i>	4475.76	4675.53	$> 20.90$	—
White	3086.17	3235.93	$19.99 \pm 0.13$	9.123
White	4270.14	4469.9	$20.40 \pm 0.15$	8.060

TABLE 2  
TAROT OBSERVATIONS OF GRB 180418A

$t_i$ (s)	$t_f$ (s)	$r$
28.0	36.0	$14.30 \pm 0.04$
36.0	43.0	$14.24 \pm 0.03$
43.0	51.0	$14.40 \pm 0.03$
51.0	58.0	$14.61 \pm 0.04$
58.0	66.0	$14.98 \pm 0.05$
66.0	73.0	$15.42 \pm 0.06$
73.0	81.0	$15.52 \pm 0.09$
81.0	88.0	$15.83 \pm 0.15$
100.0	130.0	$15.96 \pm 0.06$
141.0	171.0	$16.50 \pm 0.11$
181.0	211.0	$16.58 \pm 0.13$
221.0	251.0	$17.10 \pm 0.31$
262.0	292.0	$16.90 \pm 0.25$
302.0	392.0	$17.00 \pm 0.29$

TABLE 3  
RATIR OBSERVATIONS OF GRB 180418A

$t_i$ (s)	$t_f$ (s)	$t_{\text{exp}}$ (s)	$r$	$i$
120.6	200.6	80	$16.39 \pm 0.01$	$16.29 \pm 0.01$
230.6	310.6	80	$17.21 \pm 0.01$	$16.96 \pm 0.02$
322.4	402.4	80	$17.56 \pm 0.01$	$17.40 \pm 0.01$
414.3	494.3	80	$17.85 \pm 0.02$	$17.93 \pm 0.03$
521.6	601.6	80	$18.13 \pm 0.04$	$18.53 \pm 0.06$
616.2	696.2	80	$18.17 \pm 0.02$	...
617.1	697.1	80	...	$18.04 \pm 0.03$
714.1	794.1	80	$18.25 \pm 0.04$	$18.27 \pm 0.04$
812.1	892.1	80	$18.43 \pm 0.02$	$19.33 \pm 0.05$
900.7	980.7	80	$18.71 \pm 0.05$	$18.89 \pm 0.07$
999.6	1079.6	80	$18.65 \pm 0.06$	$18.50 \pm 0.07$
1087.7	1167.7	80	$18.66 \pm 0.03$	$18.51 \pm 0.04$
1199.0	1279.0	80	$18.86 \pm 0.03$	...
1199.1	1279.0	80	...	$18.79 \pm 0.04$
1287.2	1367.2	80	...	$18.75 \pm 0.04$
1287.6	1367.6	80	$18.84 \pm 0.03$	...
1380.3	1460.3	80	$18.81 \pm 0.03$	$18.83 \pm 0.05$
1472.1	1552.1	80	...	$18.77 \pm 0.05$
1570.0	1650.0	80	$19.16 \pm 0.06$	$18.94 \pm 0.06$
1683.4	1763.3	80	$19.17 \pm 0.04$	...
1684.3	1764.3	80	...	$19.17 \pm 0.05$
1777.3	1857.3	80	$19.22 \pm 0.06$	$19.01 \pm 0.06$
1883.6	1963.6	80	$19.08 \pm 0.04$	$18.93 \pm 0.04$
1975.8	2055.8	80	$19.36 \pm 0.05$	$19.26 \pm 0.06$
2064.0	2144.0	80	$19.11 \pm 0.08$	$19.06 \pm 0.08$
2164.6	2244.6	80	...	$19.21 \pm 0.07$
2164.9	2244.9	80	$19.18 \pm 0.05$	...
2284.4	2364.4	80	$19.46 \pm 0.07$	$19.16 \pm 0.07$
2377.5	2457.5	80	$19.34 \pm 0.05$	$19.53 \pm 0.07$
2466.0	2546.0	80	$19.74 \pm 0.14$	$19.51 \pm 0.15$
2558.5	2638.5	80	$19.53 \pm 0.06$	...
2559.5	2639.5	80	...	$19.35 \pm 0.06$
2655.9	2735.9	80	$19.53 \pm 0.08$	$19.20 \pm 0.07$
2755.1	2835.1	80	$19.97 \pm 0.07$	$19.45 \pm 0.06$
2842.3	2922.3	80	$19.73 \pm 0.08$	$19.49 \pm 0.08$
2934.2	3014.2	80	$19.63 \pm 0.06$	$19.50 \pm 0.08$
3023.6	3103.6	80	$19.84 \pm 0.10$	$19.64 \pm 0.10$
3134.3	3214.3	80	$19.92 \pm 0.09$	...
3135.3	3215.3	80	...	$19.64 \pm 0.08$
3247.5	3327.5	80	$19.90 \pm 0.08$	$19.88 \pm 0.09$
3341.3	3421.3	80	$19.91 \pm 0.11$	$19.73 \pm 0.13$
3428.6	3508.6	80	$19.67 \pm 0.07$	$19.67 \pm 0.08$
3521.2	3601.2	80	$19.96 \pm 0.12$	$19.77 \pm 0.12$
3608.5	3688.5	80	$19.80 \pm 0.10$	$20.13 \pm 0.14$
3714.2	3794.2	80	$19.84 \pm 0.09$	$19.80 \pm 0.10$
3812.2	3892.2	80	$19.87 \pm 0.12$	$19.80 \pm 0.13$
3910.9	3990.9	80	$20.01 \pm 0.12$	$19.81 \pm 0.10$
4090.6	4170.6	80	$20.05 \pm 0.13$	$19.69 \pm 0.10$
4207.0	4287.0	80	$20.34 \pm 0.15$	$19.70 \pm 0.09$
4387.7	4467.7	80	$20.30 \pm 0.13$	$19.99 \pm 0.10$
4479.2	4559.2	80	$20.25 \pm 0.12$	$20.06 \pm 0.12$
4567.9	4647.9	80	$20.34 \pm 0.13$	$19.97 \pm 0.11$
4666.5	4746.5	80	$20.12 \pm 0.11$	$20.08 \pm 0.11$
4778.2	4858.2	80	$20.16 \pm 0.11$	$20.01 \pm 0.10$
4778.2	4858.2	80	$20.16 \pm 0.11$	$20.20 \pm 0.04$
4778.2	6292.3	1280	$20.33 \pm 0.04$	$20.01 \pm 0.10$
4778.2	6292.3	1280	$20.33 \pm 0.04$	$20.20 \pm 0.04$
4888.0	4968.1	80	$19.96 \pm 0.10$	...
4888.1	4968.1	80	...	$19.89 \pm 0.11$
4976.1	5056.1	80	$20.28 \pm 0.15$	...
5068.0	5148.0	80	$20.30 \pm 0.13$	$20.29 \pm 0.13$
5156.0	5236.0	80	$20.36 \pm 0.13$	$20.34 \pm 0.14$
5247.9	5327.9	80	$20.32 \pm 0.13$	$20.04 \pm 0.12$
5348.4	5428.4	80	$19.92 \pm 0.09$	$20.16 \pm 0.13$
5447.4	5527.4	80	$20.48 \pm 0.16$	$20.35 \pm 0.14$
5630.6	5710.6	80	$20.47 \pm 0.15$	$20.21 \pm 0.14$
5728.5	5808.5	80	$20.23 \pm 0.13$	$20.29 \pm 0.15$
5826.9	5906.9	80	$20.34 \pm 0.14$	$20.24 \pm 0.13$
6113.6	6193.6	80	$20.40 \pm 0.15$	$20.34 \pm 0.17$
6212.3	6292.3	80	$20.43 \pm 0.16$	...
6324.4	6404.4	80	$20.53 \pm 0.15$	$20.30 \pm 0.12$
6324.4	6404.4	80	$20.53 \pm 0.15$	$20.51 \pm 0.05$
6324.4	7883.8	1280	$20.72 \pm 0.06$	$20.30 \pm 0.12$
6324.4	7883.8	1280	$20.72 \pm 0.06$	$20.51 \pm 0.05$
6435.7	6515.7	80	...	$20.24 \pm 0.13$
6523.2	6603.2	80	$20.44 \pm 0.14$	$20.20 \pm 0.12$



TABLE 3 — *Continued*

$t_i$ (s)	$t_f$ (s)	$t_{exp}$ (s)	$r$	$i$
6623.3	6703.4	80	$20.42 \pm 0.14$	$20.67 \pm 0.17$
6732.1	6812.1	80	$20.61 \pm 0.16$	$20.99 \pm 0.24$
6825.8	6905.8	80	$20.43 \pm 0.14$	$20.25 \pm 0.14$
6923.6	7003.6	80	...	$20.46 \pm 0.17$
7111.3	7191.3	80	...	$20.48 \pm 0.17$
7318.6	7398.6	80	...	$20.53 \pm 0.18$
7418.1	7498.1	80	...	$20.52 \pm 0.15$
8362.3	9887.7	1280	$21.56 \pm 0.15$	...
8362.4	9887.7	1280	...	$20.85 \pm 0.08$
8542.3	8622.3	80	...	$20.64 \pm 0.25$
9940.3	11481.0	1280	...	$20.96 \pm 0.10$
11513.1	13094.9	1280	...	$21.22 \pm 0.13$

TABLE 4  
FITTING PARAMETERS OF GRB 180418A

Parameter		Value
Reverse shock		
Electron index	$p$	$2.35 \pm 0.03$
	$t_\gamma$	$35 \pm 1$ s
$t < t_\gamma$	$\alpha_{\text{reverse,R}}$	$-5.56 \pm 0.01$
$t > t_\gamma$	$\alpha_{\text{reverse,D}}$	$2.02 \pm 0.01$
Forward shock		
Electron index	$p$	$2.35 \pm 0.03$
Optical	$\alpha_{\text{forward,optical}}$	$1.01 \pm 0.01$
X-rays	$\alpha_{\text{forward,X}}$	$1.04 \pm 0.05$
	$\beta$	$0.80 \pm 0.04$

NOTE. — The variable  $t_\gamma$  is the time when is reached a maximum for reverse shock component. The temporal indexes  $\alpha$  are labeled with suffixes for reverse and forward and with  $R$  or  $D$  to refer to the rise and decay phase of the reverse component.

TABLE 5  
PARAMETERS FOUND OF THE EARLY AND LATE AFTERGLOW OF GRB 180418A

Parameter	Symbol	Value
ISM density	$n$	$0.15 \text{cm}^{-3}$
Lorentz Factor	$\Gamma$	160
Critic Lorentz factor	$\Gamma_c$	430
Magnetization rate	$R_B = (B_r/B_f)$	14
	$\epsilon_{B,f}$	$10^{-3}$
	$\epsilon_{B,r}$	0.2
	$\epsilon_e$	0.1
Isotropic energy	$E_{\text{iso}}$	$0.77 \times 10^{51}$ erg
Redshift	$z$	0.5
Optical luminosity	$L_{\text{opt},7}$	$1.51 \times 10^{42} \text{erg s}^{-1}$
Opening angle	$\theta_j$	$> 7^\circ$

NOTE. — Most of this parameters are calculated using the work of Fraija et al. (2017) and using the model of Kobayashi (2000). The value of the redshift  $z=0.5$  is a estimation according with the average value in SGRBs and, from it, we calculate the isotropic kinetic energy  $E_{\text{iso}}$ ,  $L_{\text{opt},7}$  and the limit value of  $\theta_j$ .

TABLE 6  
GRBs WITH SIGNATURE OF A REVERSE SHOCK.

GRB	$z$	$T_{90}$	Evidence	Reference
GRB 990123	1.60	63.3	B	1, 2, 3
GRB 021004	2.33	100.0	A	4, 5
GRB 021211	0.80	2.67	B	6
GRB 050525A	0.61	8.8	C	7, 8, 9, 10
GRB 050904	6.9	225.0	C	11,12
GRB 060111B	1-2	59	C	13, 14
GRB 060117	0.45	16.0	C	15, 16, 17
GRB 060908	1.88	19.30	A	18
GRB 061126	1.56	191	B	19, 20
GRB 080319B	0.94	$>50$	A	21, 22
GRB 081007	0.53	8.0	B	23, 24
GRB 090102	1.55	27.0	A	18, 25, 26
GRB 090424	0.54	48.0	A	23,27
GRB 090902B	1.82	21.0	C	28, 29, 30
GRB 091024	1.1	1020	C	31, 32
GRB 110205A	2.11	257	C	33, 34, 35
GRB 130427A	0.34	163	B	36, 37, 38
GRB 160625B	1.41	35	B	39, 40
GRB 180418A	$< 1.31$	1.5	B	This work

REFERENCES. — (1) Mészáros & Rees (1999); (2) Bloom et al. (1999); (3) Kippen et al. (1999); (4) Castro-Tirado et al. (2010), (5) Kobayashi & Zhang (2003), (6) Wei (2003), (7) Shao & Dai (2005), (8) Cummings et al. (2005), (9) Foley et al. (2005), (10) Markwardt et al. (2005), (11) Sakamoto et al. (20005), (12) Wei et al. (2006), (13) Klotz et al. (2006), (14) Stratta et al. (2009), (15) Jelínek et al. (2006), (16) Pelangeon & Atteia (2006), (17) Cummings et al. (2006), (18) Japelj et al. (2014), (19) Gomboc et al. (2008), (20) Perley et al. (2008), (21) Yu et al. (2009), (22) Vreeswijk et al. (2008), (23) Jin et al. (2013), (24) de Ugarte Postigo et al. (2011), (25) de Ugarte Postigo et al. (2009), (26) Gendre et al. (2010), (27) Sakamoto et al. (2009), (28) Pandey et al. (2010), (29) Cucchiara et al. (2009), (30) de Palma et al. (2009), (31) Gruber et al. (2011), (32) Cucchiara et al. (2011), (33) da Silva et al. (2011), (34) Markwardt et al. (2011), (35) Gendre et al. (2012), (36) Perley et al. (2014), (37) Barthelmy et al. (2013), (38) Levan et al. (2013), (39) Troja et al. (2017), (40) Zhang et al. (2018)

A Confirmed.

B Strongly confirmed.

C There are another possibilities but due to the lack of good early-time photometric coverage.

TABLE 7  
CANDIDATE GALAXIES TO BE THE HOST GALAXY OF GRB 180418A

Label	SDSS ID	RA	DEC	$r$	$i$	$\delta R$ ["]	$P(< \delta R)$
G1	1237667551421006080	170.1150	24.9451	$21.1390 \pm 0.0274$	$20.8640 \pm 0.0240$	48.18	0.997
G2	1237667551421006592	170.1097	24.9475	$20.0264 \pm 0.0115$	$19.5144 \pm 0.0084$	64.84	0.986
G3	1237667551421006592	170.1216	24.9242	$22.2155 \pm 0.0714$	$21.9499 \pm 0.0613$	32.11	0.996
G4	1237667551421006848	170.1256	24.9331	$22.7085 \pm 0.1149$	$22.5791 \pm 0.1089$	13.39	0.674
G5	1237667551421006592	170.1400	24.9250	$20.2362 \pm 0.0141$	$19.7060 \pm 0.0099$	66.93	1.000
G6	1237667551421006592	170.1185	24.9224	$22.1486 \pm 0.0662$	$21.7405 \pm 0.0509$	39.83	0.999
S1	...	170.1241	24.9319	$23.9651 \pm 0.0000$	$23.7360 \pm 0.3158$	9.45	0.690

### 4.3 Photometric Observations of Supernova 2013cq Associated with GRB 130427A

The objective of this work was to analyse the late photometry of GRB 130427A with the RATIR instrument on the 1.5-m Harold L. Johnson telescope placed at the Observatorio Astronómico Nacional on Sierra San Pedro Mártir. Our homogenous *griZYJH* photometry extends from the night of burst to one year later. We fit a model for the afterglow and the host galaxy. There is a significant positive residual which matches the behavior of SN 1998bw in the *griZ* filters; we suggest that this is a photometric confirmation of the supernova SN 2013cq associated with the GRB.

For this work we fit the data on the first night with a simple power-law component and the data on later nights with power-law and host galaxy components. This work complements the papers of [Perley et al. \(2014\)](#) and [Melandri et al. \(2014\)](#) on an inhomogeneous data set. In comparison, [Perley et al. \(2014\)](#) and [Melandri et al. \(2014\)](#) have better temporal coverage, but suffer from possible systematic errors when comparing observations with different instruments. Thus, they were better able to study the afterglow over the first couple of days and show the existence of a temporal break at about 0.7 days. Our data, on the other hand, are better suited to looking for deviations from simple power-law model at later times.

Also, we showed that the light curve GRB130427A in Y-band light curve is consistent with the analytical synchrotron forward shock model in the slow cooling regime shown in [Gao et al. \(2013\)](#) with the temporal index of the power-law components which changes from 0.97 at  $t < 0.7$  day to 1.36 at  $t > 0.7$  day, in agreement with the values and temporal break around 0.7 days determined by [Maselli et al. \(2014\)](#) and [Perley et al. \(2014\)](#).

The color and absolute magnitude of the host suggest that it is a blue, star-forming galaxy.

Positive residuals to the fits in *griZYJ* between about 7 and 40 days show that we are seeing the photometric signature of SN 2013cq, previously detected spectroscopically by [de Ugarte Postigo et al. \(2013\)](#) and [Xu et al. \(2013\)](#) and hinted at photometrically by [Watson et al. \(2013\)](#). The absolute magnitude and broad-band spectrum of the supernova are consistent with those of the prototype SN 1998bw and suggest similar progenitors.

This paper is published in ApJ ([Becerra et al. 2017](#)) and is attached below.



## Photometric Observations of Supernova 2013cq Associated with GRB 130427A

R. L. Becerra<sup>1</sup>, A. M. Watson<sup>1</sup>, W. H. Lee<sup>1</sup>, N. Fraija<sup>1</sup>, N. R. Butler<sup>2</sup>, J. S. Bloom<sup>3</sup>, J. I. Capone<sup>4</sup>, A. Cucchiara<sup>5</sup>, J. A. de Diego<sup>1</sup>, O. D. Fox<sup>6</sup>, N. Gehrels<sup>7</sup>, L. N. Georgiev<sup>1</sup>, J. J. González<sup>1</sup>, A. S. Kutuyev<sup>7</sup>, O. M. Littlejohns<sup>2</sup>, J. X. Prochaska<sup>8</sup>, E. Ramirez-Ruiz<sup>8</sup>,

M. G. Richer<sup>9</sup>, C. G. Román-Zúñiga<sup>9</sup>, V. L. Toy<sup>4</sup>, and E. Troja<sup>4,7</sup>

<sup>1</sup>Instituto de Astronomía, Universidad Nacional Autónoma de México, Apartado Postal 70-264, 04510 México, D. F., México

<sup>2</sup>School of Earth and Space Exploration, Arizona State University, Tempe, AZ 85287, USA

<sup>3</sup>Department of Astronomy, University of California, Berkeley, CA 94720-3411, USA

<sup>4</sup>Department of Astronomy, University of Maryland, College Park, MD 20742, USA

<sup>5</sup>NASA Postdoctoral Program Fellow, Goddard Space Flight Center, Greenbelt, MD 20771, USA

<sup>6</sup>Space Telescope Science Institute, 3700 San Martin Drive, Baltimore, MD 21218, USA

<sup>7</sup>NASA, Goddard Space Flight Center, Greenbelt, MD 20771, USA

<sup>8</sup>Department of Astronomy and Astrophysics, UCO/Lick Observatory, University of California, 1156 High Street, Santa Cruz, CA 95064, USA

<sup>9</sup>Instituto de Astronomía, Universidad Nacional Autónoma de México, Apartado Postal 106, 22800 Ensenada, Baja California, México

Received 2016 April 25; revised 2017 February 13; accepted 2017 February 14; published 2017 March 9

### Abstract

We observed the afterglow of GRB 130427A with the Reionization and Transients Infrared Camera (RATIR) instrument on the 1.5 m Harold L. Johnson telescope of the Observatorio Astronómico Nacional in Sierra San Pedro Mártir. Our homogenous *griZYJH* photometry extends from the night of the burst to three years later. We fit a model for the afterglow. There is a significant positive residual that matches the behavior of SN 1998bw in the *griZ* filters; we suggest that this is a photometric signature of the supernova SN 2013cq associated with the Gamma-ray burst. The peak absolute magnitude of the supernova is  $M_r = -18.43 \pm 0.11$ .

**Key words:** gamma-ray burst: individual (GRB 130427A) – supernovae: individual (2013cq)

### 1. Introduction

Gamma-ray bursts (GRBs) are the most energetic events in the universe and are produced at cosmological distances. They can be classified according to their duration  $T_{90}$ , the time interval in the observer's frame over which 90% of the total background-subtracted counts are observed (Koshut et al. 1995). This parameter has long pointed to a bi-modal distribution (Kouveliotou et al. 1993).

Long GRBs ( $T_{90} > 2$  s) are today thought to be the result of the core-collapse of a star (Woosley 1993; MacFadyen & Woosley 1999; Hjorth & Bloom 2012) with an initial mass of more than  $10 M_{\odot}$  (see Woosley & Bloom 2006, for a review), while short GRBs ( $T_{90} < 2$  s) are thought to be the result of mergers between two compact objects (Lattimer & Schramm 1976; Eichler et al. 1989; Paczynski 1989, 1991; Narayan et al. 1992) like black holes or neutron stars (see Lee & Ramirez-Ruiz 2007; Nakar 2007, for reviews).

Woosley (1993) specifically proposed a way in which the core-collapse of massive stars could lead to a long GRB, and thus be possibly associated with a supernova (SN; Woosley & Bloom 2006; Modjaz 2011; Bersier 2012; Hjorth 2013). In this scenario, the optical emission from the SN would appear a few days after the GRB, when the ejecta becomes optically thin. This leads to two ways to identify the presence of an SN associated with a GRB: (1) by the appearance of the broad spectral lines that are characteristic of SN a few days after the burst; and (2) through a rebrightening in the light curve of the GRB after a few days due to the broadband emission of the SN. The identification of a SN associated with GRB 980425 (Galama et al. 1998) showed that at least some GRBs are truly linked to the core-collapse of massive stars.

Subsequently, other SNe have also been associated with long GRBs. Confirmed spectroscopic cases are listed in Table 1. Most or perhaps all of these SNe are Type Ic. Usually, the hosts of GRB-SNe are blue, star-forming galaxies (Fynbo et al. 2000;

Foley et al. 2006; Fruchter et al. 2006; Hammer et al. 2006; Niino 2013) and the events occur within a low-metallicity environment (Modjaz et al. 2008).

Simply taking into account the rates of SNe and GRBs, however, it is apparent that not all core-collapse SNe produce long GRBs, and special conditions are required in order to successfully power a burst. These probably involve rotation, magnetic fields, chemical composition, binarity, or a combination of the above, and are not yet fully resolved. Thus, precise observations of a significant sample of GRBs associated with SNe are fundamental in order to determine the evolutionary pathways that can lead to such a link. Given that the current sample is extremely limited, studying single events like SN 2013cq associated with GRB 130427A in great detail offers the opportunity to provide unique additional insights and to eventually lead the way to a statistically significant sample, and this is the main motivation for the present paper.

GRB 130427A is one of the brightest GRBs of the last few years, and had  $E_{\gamma, \text{iso}} = 1.40 \times 10^{54}$  erg in total isotropic energy release (Ackermann et al. 2014) and  $E_{\gamma, \text{peak}} = 1028 \pm 8$  keV (Maselli et al. 2014). It was detected at high energies by several satellite instruments and led to a flurry of ground-based observations. In total, there have been 91 GCN Circulars related to GRB 130427A. Its redshift was measured to be  $z = 0.34$  (Levan et al. 2013). RAPTOR (the Rapid Telescope for Optical Response) observed a bright optical flash with a magnitude of  $7.03 \pm 0.03$  in the time interval from 9.31 to 19.31 s after the GBM trigger (Vestrand et al. 2014). The bright optical flash at early times was modeled with synchrotron emission from reverse shocks (Vestrand et al. 2014; Fraija et al. 2016). Perley et al. (2014) show multi-wavelength optical/infrared photometry of the afterglow of GRB 130427A, and explain the afterglow through synchrotron radiation and suggest a massive-star progenitor. Spectroscopy with the 10.4 m GTC telescope reported by Xu et al.

**Table 1**  
GRBs with Associated SN

GRB	SN	SN Type	$z$	Evidence <sup>a</sup>	References
GRB 980425	SN 1998bw	Ic	0.0085	A	1
GRB 011121	SN 2001ke	IIn?/Ic? <sup>b</sup>	0.362	B	2, 3, 4
GRB 021211	SN 2002lt	Ic	1.006	B	5
GRB 030329	SN 2003dh	Ic	0.1687	A	6, 7
GRB 031203	SN 2003lw	Ic	0.105	A	8, 9, 10
GRB 050525A	SN 2005nc	Ic	0.606	B	11
GRB 060218	SN 2006aj	Ic	0.0335	A	12, 13, 14, 15, 16
GRB 081007	SN 2008hw	Ic	0.530	B	17, 18, 19
GRB 091127	SN 2009nz	Ic	0.49	A	20, 21
GRB 100316D	SN 2010bh	Ic	0.059	A	22, 23, 24, 25, 26
GRB 120422A	SN 2012bz	Ic	0.283	A	27, 28
GRB 130427A	SN 2013cq	Ic	0.34	A	29, 30, 31
GRB 130702A	SN 2013dx	Ic	0.145	A	32, 33
GRB 140606B	iPTF14bfu	Ic	0.384	A	34

**Notes.**

<sup>a</sup> Evidence for the GRB-SN association, according to the authors, with A meaning strong spectroscopic evidence and B meaning a clear light curve bump together with some spectroscopic evidence resembling a SN.

<sup>b</sup> SN 2001ke has no clear spectroscopic classification. Garnavich et al. (2003) suggest that it is a Type IIn but Bloom et al. (2002) claim it is indeed consistent with a 1998bw-like Type Ic.

**References.** (1) Galama et al. (1998), (2) Bloom et al. (2002), (3) Garnavich et al. (2003), (4) Greiner et al. (2003), (5) Della Valle et al. (2003), (6) Stanek et al. (2003), (7) Matheson et al. (2003), (8) Malesani et al. (2004), (9) Gal-Yam et al. (2004), (10) Thomsen et al. (2004), (11) Della Valle et al. (2006), (12) Campana et al. (2006), (13) Modjaz et al. (2008), (14) Mirabal et al. (2006), (15) Ferrero et al. (2006), (16) Pian et al. (2006), (17) Berger et al. (2008), (18) Della Valle et al. (2008), (19) Soderberg et al. (2008), (20) Cobb et al. (2010), (21) Berger et al. (2011), (22) Starling et al. (2011), (23) Bufano et al. (2012), (24) Olivares et al. (2012), (25) Cano et al. (2011), (26) Chornock et al. (2010), (27) Melandri et al. (2012), (28) Schulze et al. (2014), (29) de Ugarte Postigo et al. (2013), (30) Xu et al. (2013a), (31) This work; (32) Toy et al. (2015), (33) D'Elia et al. (2015), and (34) Cano et al. (2015).

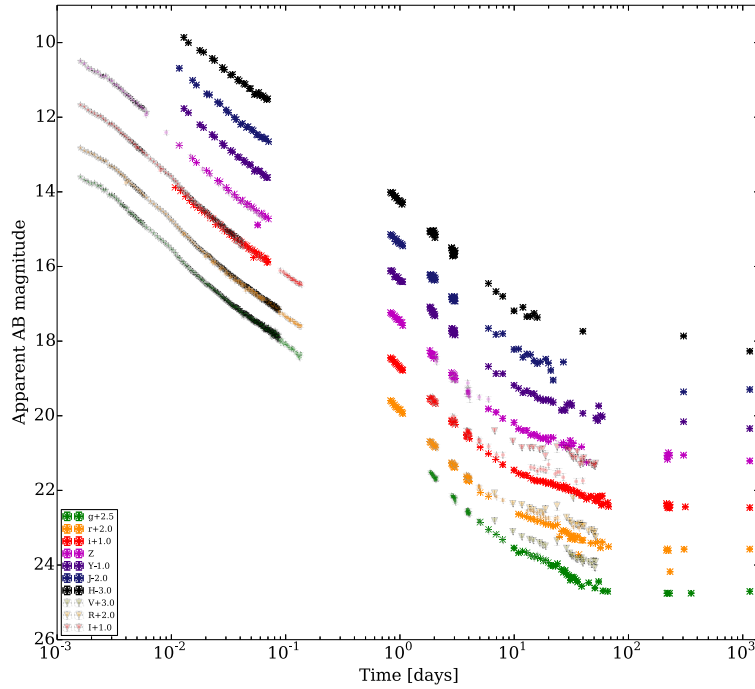


**Figure 1.** *griZYJH* light curves for GRB 130427A from RATIR (lines), RAPTOR (Maselli et al. 2014; stars), Palomar P60 (Perley et al. 2014; points) and VLT (Melandri et al. 2014; triangles). The RATIR photometry shown here is our aperture photometry of the afterglow and host galaxy.

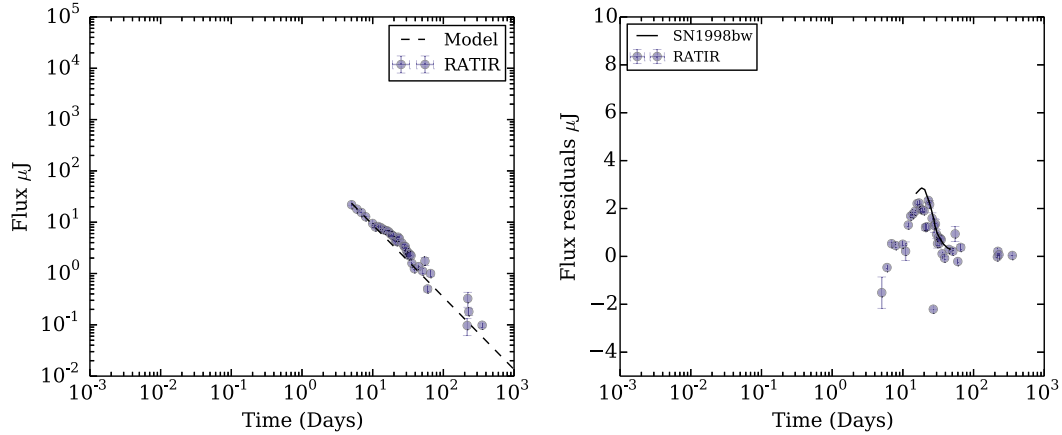


**Figure 2.** Left: the host-subtracted data (points) and power-law model (dashed line) in the  $g$  filter of RATIR (points). Right: flux density residuals in  $g$  (points) and the flux density of SN 1998bw in  $U$  shifted to  $z = 0.34$  (continuous line).

**Table 2**  
Host Galaxy Magnitudes for GRB 130427A

Filter	$m_{\text{RATIR}}$	Exposure (hr)	$m_{\text{SDSS}}$
$g$	$22.20 \pm 0.04$	10.6	$22.14 \pm 0.12$
$r$	$21.57 \pm 0.04$	6.5	$21.41 \pm 0.10$
$i$	$21.46 \pm 0.03$	17.8	$21.53 \pm 0.23$
$Z$	$21.29 \pm 0.05$	8.3	...
$Y$	$21.34 \pm 0.07$	8.2	...
$J$	$21.30 \pm 0.09$	8.0	...
$H$	$21.27 \pm 0.13$	7.9	...

**Table 3**  
Fit Parameters

Parameter	Band	Value
$\alpha_E$	...	$0.97 \pm 0.04$
$A_E$	$i$	$303 \pm 28 \mu\text{Jy}$
$A_E$	$Z$	$348 \pm 38 \mu\text{Jy}$
$A_E$	$Y$	$373 \pm 38 \mu\text{Jy}$
$A_E$	$J$	$364 \pm 37 \mu\text{Jy}$
$A_E$	$H$	$373 \pm 27 \mu\text{Jy}$
$\alpha_L$	...	$1.41 \pm 0.04$
$A_L$	$g$	$228 \pm 12 \mu\text{Jy}$
$A_L$	$r$	$268 \pm 10 \mu\text{Jy}$
$A_L$	$i$	$315 \pm 20 \mu\text{Jy}$
$A_L$	$Z$	$388 \pm 37 \mu\text{Jy}$
$A_L$	$Y$	$436 \pm 18 \mu\text{Jy}$
$A_L$	$J$	$426 \pm 11 \mu\text{Jy}$
$A_L$	$H$	$489 \pm 116 \mu\text{Jy}$

(2013a) showed a broad-lined Ic SN 2013cq associated with GRB 130427A.

This paper presents a detailed set of calibrated and uniform photometry of the bright GRB 130427A with the Reionization and Transients Infrared Camera (RATIR) instrument in the  $grIZYJH$  filters. The major advantages of our work compared to earlier papers (Xu et al. 2013a; Melandri et al. 2014; Perley et al. 2014) is that our photometry is generally deeper, has

better temporal sampling, and we subtract the host galaxy using deep late-epoch images. Furthermore, our data were all obtained with the same instrument, using the same observing strategy, and were all processed in the same way. This means that our data are naturally homogeneous. The paper is organized as follows: in Section 2 we present the observations; in Section 3 we fit the data using segments of a power-law according to the fireball model; in Section 4 we search for the signature of SN 2013cq in the difference between the host-subtracted measurements and the power-law afterglow model; and in Section 5 we discuss the results and summarize our conclusions.

## 2. Observations

### 2.1. Fermi and Swift

The Gamma-Ray Burst Monitor (GBM) instrument on the *Fermi* satellite triggered on GRB 130427A at 07:47:06.42 UTC on 2013 April 27 (von Kienlin 2013). Subsequently, the Burst Alert Telescope (BAT) on the *Swift* satellite triggered on the GRB at 07:47:57.51 UTC (Maselli et al. 2014). The duration measured with BAT was  $T_{90} = 163$  s (Barthelmy et al. 2013), making GRB 130427A a long GRB.

### 2.2. Ratir

The RATIR is a four-channel simultaneous optical and near-infrared imager mounted on the 1.5 m Harold L. Johnson Telescope at the Observatorio Astronómico Nacional in Sierra San Pedro Mártir in Baja California, Mexico. RATIR responds autonomously to GRB triggers from the *Swift* satellite and obtains simultaneous photometry in  $riZJ$  or  $riYH$  (Butler et al. 2012; Watson et al. 2012; Littlejohns et al. 2015). In manually programmed follow-up observations, the  $g$  filter can be substituted for  $r$ .

RATIR began to observe the field of GRB 130427A 15.5 minutes after the BAT trigger, and continued to observe it intensively over the subsequent weeks. On the first night, the  $r$  detector failed, so we only have data in  $iZYH$ . On subsequent nights, we have data in  $riZYH$ . After one week, we began to

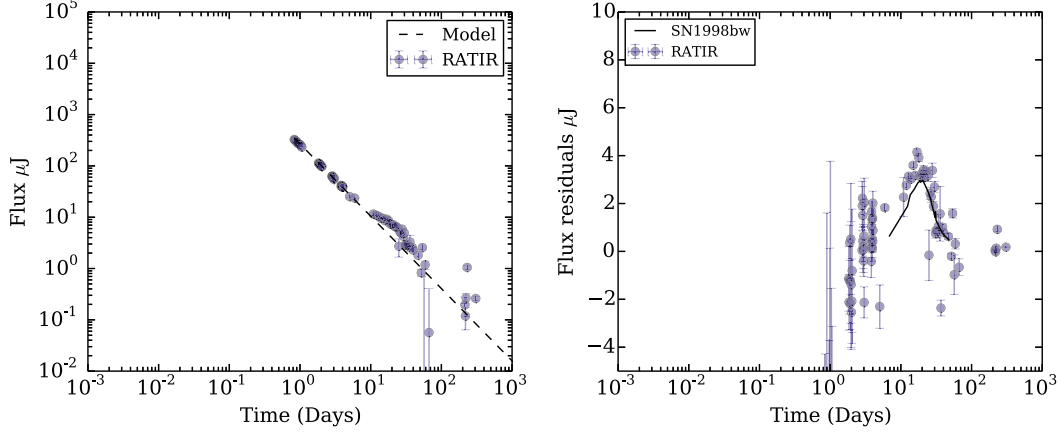


**Figure 3.** Left: the host-subtracted data (points) and power-law model (dashed line) in the  $r$  filter of RATIR (points). Right: flux density residuals in  $r$  (points) and the flux density of SN 1998bw in  $B$  shifted to  $z = 0.34$  (continuous line).

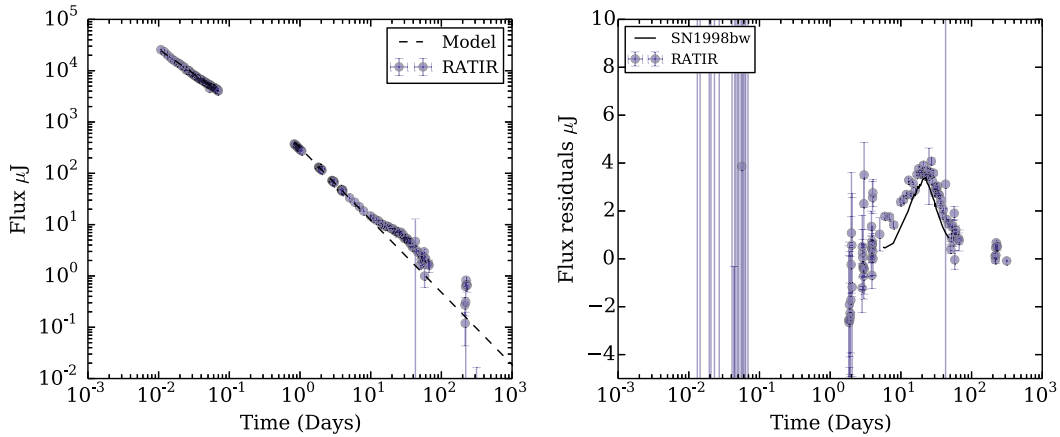


**Figure 4.** Left: the host-subtracted data (points) and power-law model (dashed line) in the  $i$  filter of RATIR (points). Right: flux density residuals in  $i$  (points) and the flux density of SN 1998bw in  $V$  shifted to  $z = 0.34$  (continuous line).

observe in  $g$  as well. We reobserved the field on several nights in 2014 and 2016 mainly to place constraints on the host galaxy.

Our reduction pipeline performs bias subtraction and flat-field correction, followed by astrometric calibration using the `astrometry.net` software (Lang et al. 2010), iterative sky-subtraction, coaddition using `SWARP`, and source detection using `SEXTRACTOR` (Littlejohns et al. 2015). We calibrate against `SDSS` and `2MASS` (Littlejohns et al. 2015). The systematic calibration error is about 1%.

The individual exposures were 80 s in  $gri$  and 67 s in  $ZYJH$  filters (with the infrared exposures being shorter because of their longer read-out overhead). On the first night, we consider the exposures individually. For the second to the fifth night, we combined sets of 16 exposures taken over about 30 minutes to improve the signal-to-noise ratio. For the remaining nights in

2013, we combined all of the exposures for each night, for 2014, we combined several nights, and for 2016, we combined all of the exposures. The image quality in the final images was typically 2 arcsec FWHM.

We obtained aperture photometry using a 3 arcsec diameter aperture. Table 6 gives our aperture photometry. For each image it gives the start and end time,  $t_0$  and  $t_f$ , the total exposure time  $t_e$ , the magnitude, the  $1\sigma$  total uncertainty (including both statistical and systematic contributions), and the filter. These magnitudes are not corrected for Galactic extinction.

We also obtained point-spread function (PSF)-fitting photometry of the afterglow and supernova in our 2013 and 2014 images after subtracting the host galaxy using our 2016 image. For each image, we estimated the PSF by co-aligning and summing images of stars (as categorized by the `SDSS`) within



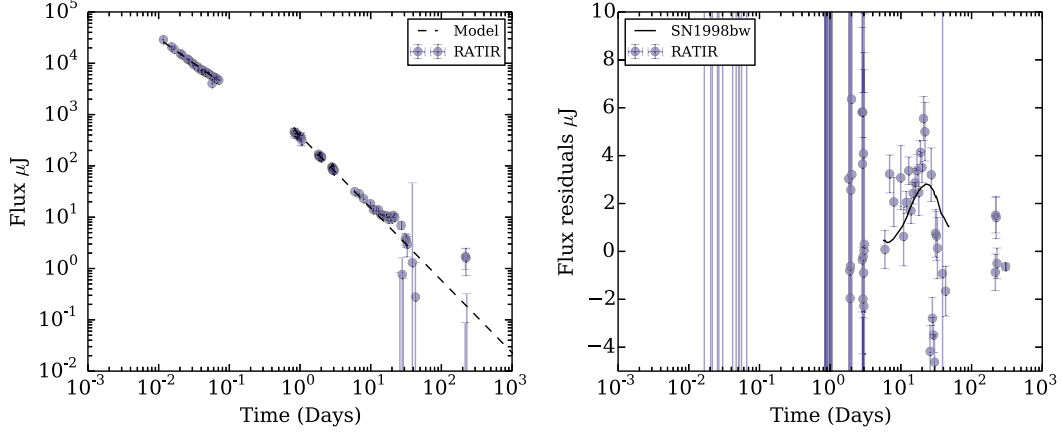


**Figure 5.** Left: the host-subtracted data (points) and power-law model (dashed line) in the Z filter of RATIR (points). Right: Flux density residuals in Z (points) and the flux density of SN 1998bw in R shifted to  $z = 0.34$  (continuous line).

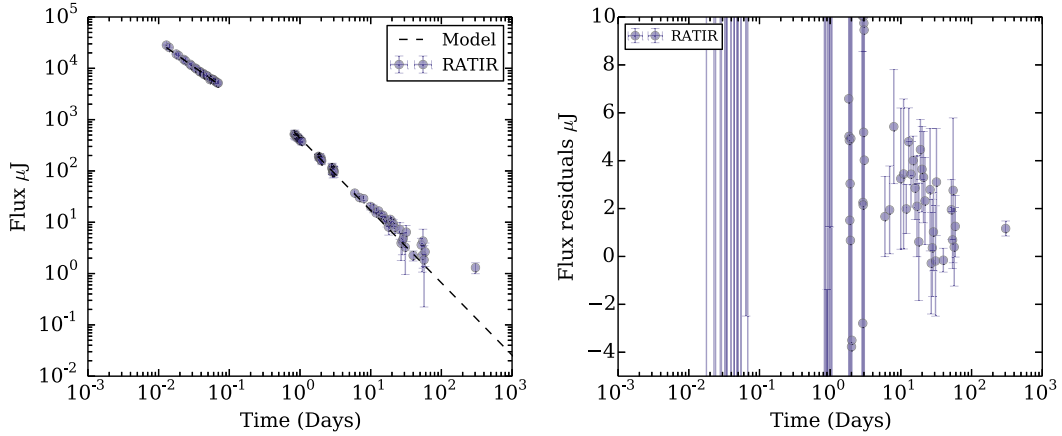


**Figure 6.** Left: the host-subtracted data (points) power-law model (dashed line) in the Y filter of RATIR. Right: flux density residuals in Y (points).

3 arcmin of the GRB. We subtracted the 2016 image from the earlier images using HOTPANTS (Becker 2015) and fitted the PSF to the residual. Even though our image quality is typically 2 arcsec FWHM, we cannot reliably perform PSF-fitting on the unsubtracted images because the galaxy is offset about 0.8 arcsec to the southeast of the afterglow (Levan et al. 2014). Table 6 also gives our PSF-fitting photometry. The main advantage of PSF-fitting is that the statistical uncertainties are reduced typically by about 20%. Figure 1 shows the RATIR optical and near-infrared light curves.

### 3. Models

The standard fireball model for GRBs (Kumar & Zhang 2015) distinguishes two stages: the *prompt emission* and the *afterglow*. The prompt emission is simultaneous with emission in gamma-rays and is produced by internal shocks in

the jet driven by the central engine. The afterglow is produced by the external shock between the jet and the circumstellar environment (e.g., Kumar & Piran 2000; Fraija 2015).

The emission region of the radiation determines the form and behavior of the spectrum and light curve for a GRB (e.g., Fraija et al. 2016), and can be different for each filter. Optical radiation has three possible origins: internal shocks in the jet, the forward external shock, and the reverse external shock (Sari & Piran 1999).

The afterglow phase can be explained by assuming a power-law energy distribution of shocked relativistic electrons,  $N(E) \propto E^{-p}$ , which leads to the observed flux being a series of power-law segments as a function of time  $t$  and frequency  $\nu$  as  $F_\nu^{\text{syn}} \propto t^{-\alpha} \nu^{-\beta}$  (Sari & Piran 1998).

RATIR began to observe after the end of the prompt emission, so we only have photometry for the afterglow. We divided these

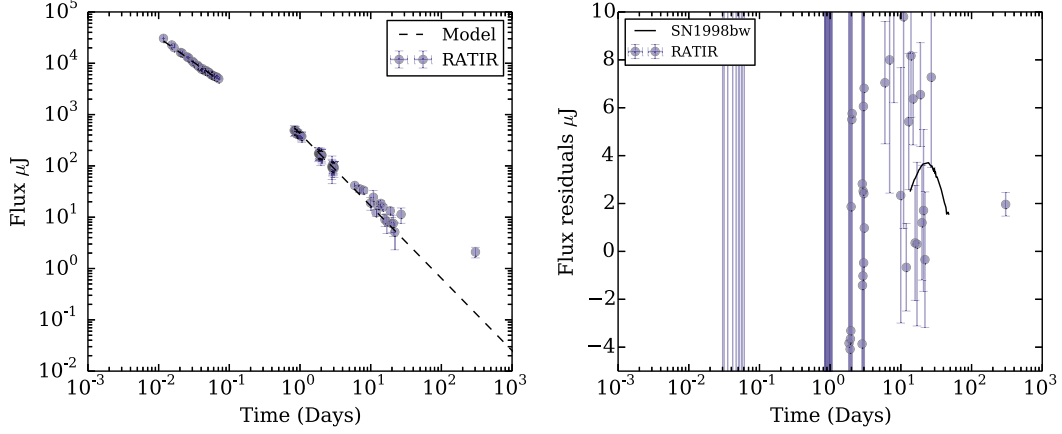


**Figure 7.** Left: the host-subtracted data (points) and power-law model (dashed line) in the  $J$  filter of RATIR. Right: flux density residuals in  $J$  (points) and the flux density of SN 1998bw in  $J$  shifted to  $z = 0.34$  (continuous line).

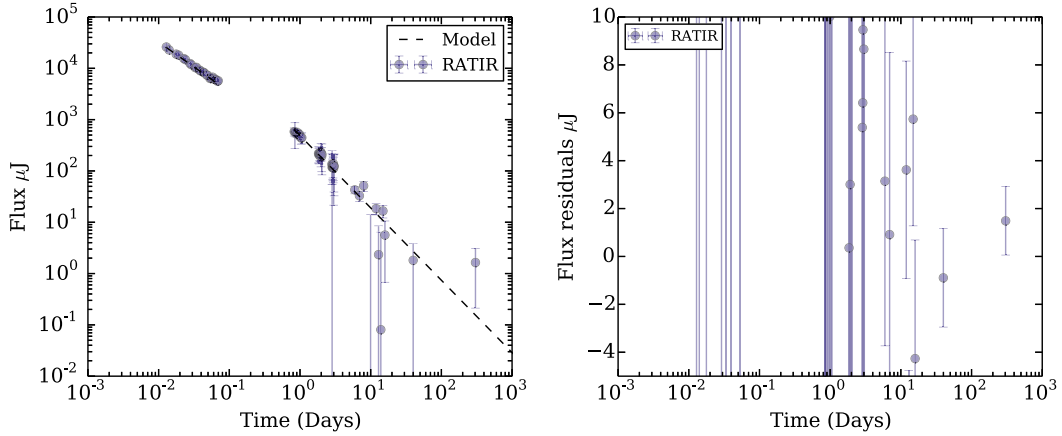


**Figure 8.** Left: the host-subtracted data (points) and power-law model (dashed line) in the  $H$  filter of RATIR. Right: flux density residuals in  $H$  (points).

**Table 4**  
Correspondence between RATIR Filters at  $z = 0.34$  and Johnson-Cousins Filters at  $z \approx 0$

Filter	$\bar{\lambda}$ (nm) $z = 0$	$\bar{\lambda}$ (nm) $z = 0.34$	Filter	$\bar{\lambda}$ (nm) $z = 0$
$g$	470	351	$U$	360
$r$	618	461	$B$	440
$i$	760	567	$V$	550
$Z$	878	655	$R$	640
$Y$	1020	761	$I$	759
$J$	1250	932	...	...
$H$	1635	1220	$J$	1260

data into two epochs: the *early* afterglow for time  $t < 0.1$  days (the first night) and the *late* afterglow for the  $t > 0.7$  day (the second and subsequent nights). This division was guided by the

analysis of Perley et al. (2014), who reported a change in the slope of the light curve at  $t = 0.7$  days. We have no data between  $t = 0.1$  and  $t = 0.7$  days.

### 3.1. Host Galaxy

Vonova et al. (2013) suggested that SDSS DR12 galaxy object 1237667431180861948 was the host galaxy of the GRB. This was subsequently confirmed by the close agreement in redshift between absorption lines in the GRB spectrum (Flores et al. 2013; Levan et al. 2013; Xu et al. 2013b) and emission lines from the galaxy (Xu et al. 2013a).

Levan et al. (2014) obtained *HST* images of the afterglow and host galaxy. They suggested that the host is a moderately star-forming, possibly interacting, disk galaxy, and the GRB occurred about 0.8 arcsec (4 kpc) from the nucleus.

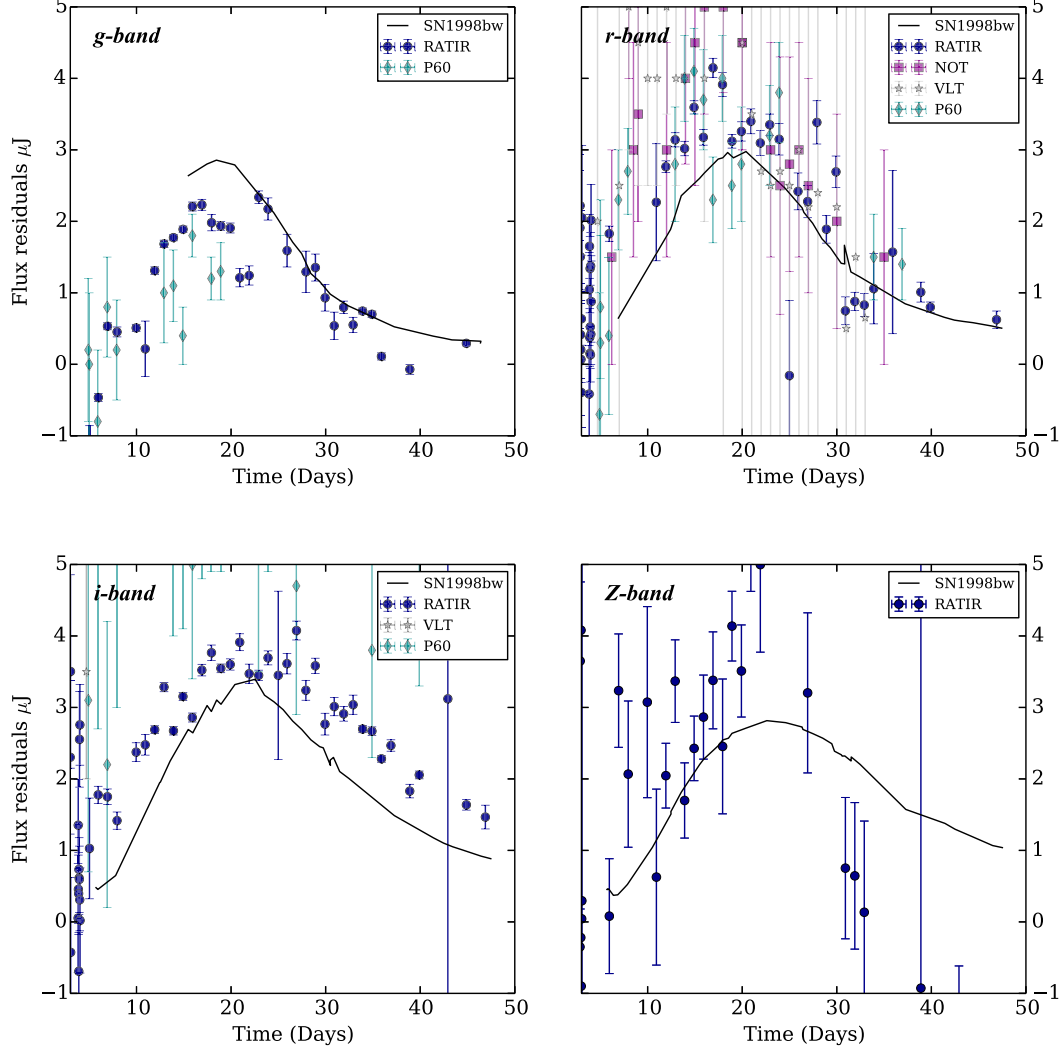


**Figure 9.** Light curves of SN 2013cq associated with GRB 130427A in the *griz* bands. RATIR from this work (points), P60 from Perley et al. (2014; diamonds), NOT from (Xu et al. 2013a; squares), and VLT from (Melandri et al. 2014; stars). The line shows that the light curves for SN 1998bw are shifted to  $z = 0.34$ .

Table 2 reports our RATIR *grizYJH* aperture magnitudes from 2016 and magnitudes from the SDSS DR12 image using the same apertures and calibrating stars. The magnitudes from our image are consistent with the magnitudes from the SDSS image, but have lower uncertainties.

We can estimate the rest-frame  $g - i$  color and  $M_i$  magnitude from our observed  $r - Y$  color and  $Y$  magnitude (see Table 4 for the correspondence between rest-frame and observed bands) assuming a  $\Lambda$ CDM model with a  $H_0 = 67.8 \text{ km Mpc}^{-1} \text{ s}^{-1}$  (Planck Collaboration et al. 2014). We obtain a rest-frame  $g - i = 0.23 \pm 0.08$  and a rest-frame  $M_i = -19.91 \pm 0.07$ . These properties place it among the most extremely blue galaxies in the  $z \approx 0$  sample of Gavazzi et al. (2010).

### 3.2. Early Afterglow ( $t < 0.7$ days)

To characterize the early afterglow data ( $t < 0.7$  days), we used the *iZYJH* aperture photometry from Table 6, as the contribution of the host galaxy can be neglected at early times. We fitted the flux densities with a power-law model  $F = A_E t^{-\alpha_E}$ , in which  $F$  is the flux density in the filter,  $A_E$  is a constant,  $t$  is the time since the BAT trigger (in days), and  $\alpha_E$  is the temporal index, assumed to be the same for all filters. The model has six free parameters: the five values of  $A_E$  and the one value of the index  $\alpha_E$ .

We minimized the value of  $\chi^2$  to find the best-fit parameters. The final fit has a  $\chi^2/n = 1.64$  with  $n = 100$  degrees of freedom. The best-fit parameters are given in Table 3. The

**Table 5**  
Peak Flux Densities and Absolute Magnitudes for SN 2013cq  
and SN 1998bw Shifted to  $z = 0.34$

Band	SN 2013cq		SN 1998bw at $z = 0.34$	
	$F_\nu$ ( $\mu\text{Jy}$ )	$M$	$F_\nu$ ( $\mu\text{Jy}$ )	$M$
<i>g</i>	$+1.77 \pm 0.12$	$-17.97 \pm 0.07$	$2.58 \pm 0.07$	$-18.38 \pm 0.03$
<i>r</i>	$+2.70 \pm 0.28$	$-18.43 \pm 0.11$	$2.82 \pm 0.08$	$-18.48 \pm 0.03$
<i>i</i>	$+3.59 \pm 0.23$	$-18.74 \pm 0.07$	$3.15 \pm 0.09$	$-18.60 \pm 0.03$
<i>Z</i>	$+2.80 \pm 0.87$	$-18.47 \pm 0.33$	$2.70 \pm 0.07$	$-18.43 \pm 0.03$
<i>Y</i>	$+3.30 \pm 1.86$	$-18.65 \pm 0.61$	...	...
<i>J</i>	$+2.28 \pm 2.69$	$-18.24 \pm 0.28$	$3.57 \pm 0.10$	$-18.74 \pm 0.03$
<i>H</i>	...	...	...	...

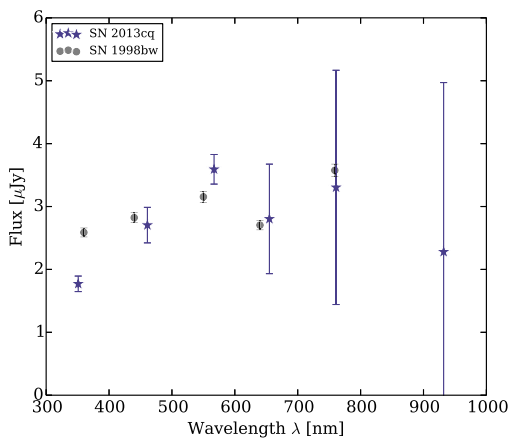


**Figure 10.** Broadband rest-frame SED of SN 2013cq (stars) and SN 1998bw (circles) by averaging their fluxes from days 18 to 26. The wavelength is in the rest-frame, but the flux density is observed for SN 2013cq and shifted to  $z = 0.34$  for SN 1998bw.

errors were calculated using the standard deviation of the best-fit parameters after Gaussian perturbations around the flux values observed over 10,000 trials. Table 7 shows the residuals to the fit in the sense of data minus model in units of  $\mu\text{Jy}$ .

### 3.3. Late Afterglow ( $t > 0.7$ days)

To characterize the late afterglow ( $t > 0.7$  days), we use the *grizY HJ* flux densities from our PSF-fitting photometry of the subtracted images from Table 6. We fitted with a model  $F = A_L t^{-\alpha_L}$ , in which  $F$  is the flux density in each filter,  $A_L$  is a constant,  $t$  is the time since the BAT trigger (in days) and  $\alpha_L$  is the temporal index, assumed to be the same for all filters. The model has eight free parameters: the seven values of  $A_L$  and the one value of the index  $\alpha_L$ .

Again, we minimized the value of  $\chi^2$  to find the best-fit parameters. To avoid the worst contamination from the SN, we fitted only the data points from 0.7 to 7 days and from 40 days onward. The final fit has a  $\chi^2/n = 1.05$  with  $n = 327$  degrees of freedom. The best-fit parameters are given in Table 3. The errors were calculated using the standard deviation of the best-fit parameters with Gaussian perturbations to the flux value and 10,000 trials. Figures 2–8 show the data and the best fit.

Table 8 shows the residuals to the fit in the sense of data minus model in units of  $\mu\text{Jy}$ .

## 4. Results

### 4.1. SN Component

The host-subtracted measurements minus the the best-fit afterglow models (Table 8), henceforth residuals, are show in Figures 2–8. These residuals show a rise and fall from about 7 to about 40 days, confirming the suggestion of Watson et al. (2013). We propose that this is the photometric signature of SN 2013cq.

To compare our data to SN 1988bw at a redshift of  $z = 0.0085$  (Tinney et al. 1998), we need to account for the effects of redshift on the luminosity distance, observed band, and time dilation. For the luminosity distance, we used a  $\Lambda\text{CDM}$  model with a  $H_0 = 67.8 \text{ km Mpc}^{-1} \text{ s}^{-1}$  (Planck Collaboration et al. 2014). The effect of redshift on the filters is shown in Table 4. In this table, the first and second column give the RATIR filter and its central wavelength  $\bar{\lambda}$  at  $z = 0$ , the third column gives the central wavelength  $\bar{\lambda}$  in the rest-frame of SN 2013cq at  $z = 0.34$ , and the fourth and fifth give the corresponding Johnson–Cousins filters and their central wavelengths at  $z = 0$ . Fortunately, there is a good correspondence between the RATIR *grizY H* filters at  $z = 0.34$  and the Johnson *UBVRIZ* filters at  $z \approx 0$ . The time dilation correction is a factor of  $(1 + 0.34)/(1 + 0.0085) = 1.33$ .

Figure 9 compares our photometry of SN 2013cq with that of SN 1998bw shifted to  $z = 0.34$  (Galama et al. 1998; Foley et al. 2006; Clocchiatti et al. 2011), both bands in the rest-frame. Qualitatively, the agreement is good, especially in the bluer *griz* filters, although compared with SN 1998bw, SN 2013cq is fainter in the *g*-band while it is brighter in the *riz* filters.

The peak times, calculated by adjusting third-degree polynomials to the residuals (between 7 and 40 days), are 17.66, 17.33, and 22.00 days, with  $\chi^2/\text{dof}$  of 0.62, 0.92, and 0.06, respectively, for the *g*, *r*, and *i* bands, and are consistent with Xu et al. (2013a). A similar fit to the *Z* band did not produce a convincing fit (the reduced  $\chi^2/\text{dof}$  was 5.44), so we do not have confidence in the peak time for that band.

Moreover, Figure 9 also compares our residuals with the P60 (Perley et al. 2014), NOT (Xu et al. 2013a), and VLT (Melandri et al. 2014) photometry. This shows the superior temporal coverage of the RATIR data (we have photometry for every night from nights 5 to 40) and the lower noise. For example, the errors (associated with the observations) in our residuals, calculated around the SN peak in the *r*-band (between 18 and 26 days after the GRB trigger) are around  $0.48 \mu\text{Jy}$ , while Perley et al. (2014), Xu et al. (2013a), and Melandri et al. (2014) give estimated errors of 1.7, 1.5, and  $0.7 \mu\text{Jy}$  for their photometry with P60, NOT, and VLT, respectively.

We determined the peak flux density and magnitudes of SN 2013cq and SN 1998bw shifted to  $z = 0.34$ , by averaging the residuals from days 18 to 26. These are given in Table 5. The SEDs at the peak flux of both supernovae are shown in Figure 10. Within our considerable uncertainties, the broadband SED of SN 2013cq is compatible with that of SN 1998bw for 300–800 nm and suggest similarities in the ejected  $^{56}\text{Ni}$  masses and kinetic energies between both SNe. For SN 2013cq the rest-frame  $M_r$  magnitude (from our observed *Z* magnitude)

**Table 6**  
Photometry of GRB 130427A

$t_0$ (day)	$t_0$ (s)	$t_r$ (s)	$t_f$ (s)	Filter	$m$ (AB) (Aperture)	Flux ( $\mu$ Jy) (PSF)
0.01	930	80	0.01	<i>i</i>	12.88 $\pm$ 0.02	...
0.01	1009	67	0.01	<i>Z</i>	12.75 $\pm$ 0.02	...
0.01	1012	67	0.01	<i>J</i>	12.69 $\pm$ 0.02	...
0.01	1037	80	0.01	<i>i</i>	12.97 $\pm$ 0.02	...
0.01	1111	67	0.01	<i>H</i>	12.86 $\pm$ 0.02	...
0.01	1114	67	0.01	<i>Y</i>	12.77 $\pm$ 0.02	...
0.01	1141	80	0.01	<i>i</i>	13.12 $\pm$ 0.02	...
0.01	1216	67	0.01	<i>Y</i>	12.88 $\pm$ 0.02	...
0.01	1216	67	0.01	<i>H</i>	13.00 $\pm$ 0.02	...
0.01	1249	80	0.02	<i>i</i>	13.24 $\pm$ 0.02	...
0.02	1323	67	0.02	<i>Z</i>	13.10 $\pm$ 0.02	...
0.02	1326	67	0.02	<i>J</i>	13.01 $\pm$ 0.02	...
0.02	1348	80	0.02	<i>i</i>	13.35 $\pm$ 0.02	...
0.02	1429	67	0.02	<i>J</i>	13.14 $\pm$ 0.02	...
0.02	1432	67	0.02	<i>Z</i>	13.22 $\pm$ 0.02	...
0.02	1458	80	0.02	<i>i</i>	13.42 $\pm$ 0.02	...
0.02	1532	67	0.02	<i>H</i>	13.21 $\pm$ 0.03	...
0.02	1534	67	0.02	<i>Y</i>	13.20 $\pm$ 0.02	...
0.02	1579	80	0.02	<i>i</i>	13.51 $\pm$ 0.02	...
0.02	1653	67	0.02	<i>H</i>	13.26 $\pm$ 0.02	...
0.02	1653	67	0.02	<i>Y</i>	13.28 $\pm$ 0.02	...
0.02	1684	80	0.02	<i>i</i>	13.55 $\pm$ 0.02	...
0.02	1762	67	0.02	<i>Z</i>	13.43 $\pm$ 0.02	...
0.02	1764	67	0.02	<i>J</i>	13.37 $\pm$ 0.02	...
0.02	1778	80	0.02	<i>i</i>	13.61 $\pm$ 0.02	...
0.02	1858	67	0.02	<i>J</i>	13.40 $\pm$ 0.02	...
0.02	1859	67	0.02	<i>Z</i>	13.50 $\pm$ 0.02	...
0.02	1888	80	0.02	<i>i</i>	13.70 $\pm$ 0.02	...
0.02	1962	67	0.02	<i>Y</i>	13.47 $\pm$ 0.02	...
0.02	1964	67	0.02	<i>H</i>	13.43 $\pm$ 0.03	...
0.02	1993	80	0.02	<i>i</i>	13.72 $\pm$ 0.02	...
0.02	2067	67	0.02	<i>Y</i>	13.53 $\pm$ 0.02	...
0.02	2068	67	0.02	<i>H</i>	13.48 $\pm$ 0.03	...
0.02	2121	80	0.03	<i>i</i>	13.87 $\pm$ 0.02	...
0.03	2196	67	0.03	<i>J</i>	13.59 $\pm$ 0.02	...
0.03	2196	67	0.03	<i>Z</i>	13.69 $\pm$ 0.02	...
0.03	2224	80	0.03	<i>i</i>	13.87 $\pm$ 0.02	...
0.03	2298	67	0.03	<i>J</i>	13.64 $\pm$ 0.02	...
0.03	2300	67	0.03	<i>Z</i>	13.73 $\pm$ 0.02	...
0.03	2329	80	0.03	<i>i</i>	13.89 $\pm$ 0.02	...
0.03	2408	67	0.03	<i>H</i>	13.67 $\pm$ 0.02	...
0.03	2408	67	0.03	<i>Y</i>	13.70 $\pm$ 0.02	...
0.03	2422	80	0.03	<i>i</i>	13.98 $\pm$ 0.02	...
0.03	2502	67	0.03	<i>Y</i>	13.76 $\pm$ 0.02	...
0.03	2506	67	0.03	<i>H</i>	13.72 $\pm$ 0.02	...
0.03	2531	80	0.03	<i>i</i>	14.03 $\pm$ 0.02	...
0.03	2605	67	0.03	<i>J</i>	13.81 $\pm$ 0.02	...
0.03	2607	67	0.03	<i>Z</i>	13.88 $\pm$ 0.02	...
0.03	2655	80	0.03	<i>i</i>	14.07 $\pm$ 0.02	...
0.03	2729	67	0.03	<i>J</i>	13.88 $\pm$ 0.02	...
0.03	2732	67	0.03	<i>Z</i>	13.97 $\pm$ 0.02	...
0.03	2780	80	0.03	<i>i</i>	14.15 $\pm$ 0.02	...
0.03	2855	67	0.03	<i>Y</i>	13.89 $\pm$ 0.02	...
0.03	2856	67	0.03	<i>H</i>	13.87 $\pm$ 0.03	...
0.03	2885	80	0.03	<i>i</i>	14.14 $\pm$ 0.02	...
0.03	2960	67	0.04	<i>Y</i>	13.93 $\pm$ 0.02	...
0.03	2961	67	0.04	<i>H</i>	13.85 $\pm$ 0.03	...
0.03	2990	80	0.04	<i>i</i>	14.19 $\pm$ 0.02	...
0.04	3067	67	0.04	<i>Z</i>	14.06 $\pm$ 0.02	...
0.04	3069	67	0.04	<i>J</i>	14.00 $\pm$ 0.02	...
0.04	3108	80	0.04	<i>i</i>	14.25 $\pm$ 0.02	...
0.04	3186	67	0.04	<i>J</i>	14.06 $\pm$ 0.02	...
0.04	3186	67	0.04	<i>Z</i>	14.15 $\pm$ 0.02	...

**Table 6**  
(Continued)

$t_0$ (day)	$t_0$ (s)	$t_e$ (s)	$t_f$ (s)	Filter	$m$ (AB) (Aperture)	Flux ( $\mu$ Jy) (PSF)
0.04	3214	80	0.04	<i>i</i>	14.28 $\pm$ 0.02	...
0.04	3292	67	0.04	<i>Y</i>	14.06 $\pm$ 0.02	...
0.04	3293	67	0.04	<i>H</i>	13.99 $\pm$ 0.03	...
0.04	3307	80	0.04	<i>i</i>	14.31 $\pm$ 0.02	...
0.04	3387	67	0.04	<i>H</i>	14.03 $\pm$ 0.03	...
0.04	3389	67	0.04	<i>Y</i>	14.08 $\pm$ 0.02	...
0.04	3418	80	0.04	<i>i</i>	14.32 $\pm$ 0.02	...
0.04	3493	67	0.04	<i>J</i>	14.19 $\pm$ 0.02	...
0.04	3493	67	0.04	<i>Z</i>	14.24 $\pm$ 0.02	...
0.04	3535	80	0.04	<i>i</i>	14.35 $\pm$ 0.02	...
0.04	3610	67	0.04	<i>Z</i>	14.22 $\pm$ 0.02	...
0.04	3611	67	0.04	<i>J</i>	14.17 $\pm$ 0.02	...
0.04	3640	80	0.04	<i>i</i>	14.40 $\pm$ 0.02	...
0.04	3719	67	0.04	<i>H</i>	14.09 $\pm$ 0.03	...
0.04	3721	67	0.04	<i>Y</i>	14.16 $\pm$ 0.02	...
0.04	3736	80	0.04	<i>i</i>	14.41 $\pm$ 0.02	...
0.04	3814	67	0.04	<i>Y</i>	14.21 $\pm$ 0.02	...
0.04	3815	67	0.04	<i>H</i>	14.12 $\pm$ 0.03	...
0.04	3843	80	0.05	<i>i</i>	14.44 $\pm$ 0.02	...
0.05	3918	67	0.05	<i>J</i>	14.28 $\pm$ 0.03	...
0.05	3919	67	0.05	<i>Z</i>	14.33 $\pm$ 0.02	...
0.05	3964	80	0.05	<i>i</i>	14.45 $\pm$ 0.02	...
0.05	4038	67	0.05	<i>J</i>	14.25 $\pm$ 0.02	...
0.05	4038	67	0.05	<i>Z</i>	14.32 $\pm$ 0.02	...
0.05	4145	67	0.05	<i>H</i>	14.23 $\pm$ 0.03	...
0.05	4146	67	0.05	<i>Y</i>	14.26 $\pm$ 0.02	...
0.05	4172	80	0.05	<i>i</i>	14.51 $\pm$ 0.02	...
0.05	4247	67	0.05	<i>H</i>	14.24 $\pm$ 0.03	...
0.05	4248	67	0.05	<i>Y</i>	14.28 $\pm$ 0.02	...
0.05	4295	80	0.05	<i>i</i>	14.55 $\pm$ 0.02	...
0.05	4371	67	0.05	<i>J</i>	14.33 $\pm$ 0.02	...
0.05	4371	67	0.05	<i>Z</i>	14.40 $\pm$ 0.02	...
0.05	4415	80	0.05	<i>i</i>	14.56 $\pm$ 0.02	...
0.05	4493	67	0.05	<i>J</i>	14.36 $\pm$ 0.02	...
0.05	4493	67	0.05	<i>Z</i>	14.44 $\pm$ 0.02	...
0.05	4523	80	0.05	<i>i</i>	14.76 $\pm$ 0.03	...
0.05	4598	67	0.05	<i>H</i>	14.39 $\pm$ 0.07	...
0.05	4598	67	0.05	<i>Y</i>	14.45 $\pm$ 0.03	...
0.05	4643	80	0.05	<i>i</i>	14.59 $\pm$ 0.02	...
0.05	4718	67	0.06	<i>Y</i>	14.40 $\pm$ 0.02	...
0.05	4719	67	0.06	<i>H</i>	14.38 $\pm$ 0.03	...
0.05	4742	80	0.06	<i>i</i>	14.64 $\pm$ 0.02	...
0.06	4821	67	0.06	<i>J</i>	14.46 $\pm$ 0.02	...
0.06	4822	67	0.06	<i>Z</i>	14.51 $\pm$ 0.02	...
0.06	4847	80	0.06	<i>i</i>	14.66 $\pm$ 0.02	...
0.06	4922	67	0.06	<i>J</i>	14.48 $\pm$ 0.02	...
0.06	4923	67	0.06	<i>Z</i>	14.89 $\pm$ 0.02	...
0.06	4954	80	0.06	<i>i</i>	14.68 $\pm$ 0.02	...
0.06	5028	67	0.06	<i>H</i>	14.33 $\pm$ 0.05	...
0.06	5032	67	0.06	<i>Y</i>	14.44 $\pm$ 0.03	...
0.06	5059	80	0.06	<i>i</i>	14.70 $\pm$ 0.02	...
0.06	5134	67	0.06	<i>H</i>	14.42 $\pm$ 0.03	...
0.06	5135	67	0.06	<i>Y</i>	14.45 $\pm$ 0.02	...
0.06	5186	80	0.06	<i>i</i>	14.75 $\pm$ 0.03	...
0.06	5260	67	0.06	<i>J</i>	14.53 $\pm$ 0.02	...
0.06	5262	67	0.06	<i>Z</i>	14.57 $\pm$ 0.02	...
0.06	5288	80	0.06	<i>i</i>	14.71 $\pm$ 0.02	...
0.06	5362	67	0.06	<i>J</i>	14.54 $\pm$ 0.02	...
0.06	5362	67	0.06	<i>Z</i>	14.59 $\pm$ 0.02	...
0.06	5395	80	0.06	<i>i</i>	14.76 $\pm$ 0.02	...
0.06	5470	67	0.06	<i>H</i>	14.43 $\pm$ 0.04	...
0.06	5470	67	0.06	<i>Y</i>	14.52 $\pm$ 0.02	...
0.06	5506	80	0.06	<i>i</i>	14.79 $\pm$ 0.02	...

**Table 6**  
(Continued)

$t_0$ (day)	$t_0$ (s)	$t_e$ (s)	$t_f$ (s)	Filter	$m$ (AB) (Aperture)	Flux ( $\mu$ Jy) (PSF)
0.06	5586	67	0.07	<i>H</i>	14.47 $\pm$ 0.03	...
0.06	5586	67	0.07	<i>Y</i>	14.56 $\pm$ 0.02	...
0.06	5615	80	0.07	<i>i</i>	14.78 $\pm$ 0.02	...
0.07	5690	67	0.07	<i>J</i>	14.58 $\pm$ 0.02	...
0.07	5694	67	0.07	<i>Z</i>	14.69 $\pm$ 0.02	...
0.07	5715	80	0.07	<i>i</i>	14.79 $\pm$ 0.02	...
0.07	5789	67	0.07	<i>J</i>	14.58 $\pm$ 0.02	...
0.07	5790	67	0.07	<i>Z</i>	14.65 $\pm$ 0.02	...
0.07	5823	80	0.07	<i>i</i>	14.80 $\pm$ 0.02	...
0.07	5897	67	0.07	<i>H</i>	14.53 $\pm$ 0.02	...
0.07	5898	67	0.07	<i>Y</i>	14.62 $\pm$ 0.02	...
0.07	5943	80	0.07	<i>i</i>	14.89 $\pm$ 0.03	...
0.07	6018	67	0.07	<i>Y</i>	14.61 $\pm$ 0.02	...
0.07	6020	67	0.07	<i>H</i>	14.51 $\pm$ 0.03	...
0.07	6051	80	0.07	<i>i</i>	14.86 $\pm$ 0.02	...
0.07	6124	67	0.07	<i>J</i>	14.66 $\pm$ 0.02	...
0.07	6125	67	0.07	<i>Z</i>	14.73 $\pm$ 0.02	...
0.83	71485	1280	0.85	<i>i</i>	17.45 $\pm$ 0.42	374.99 $\pm$ 12.58
0.83	71485	1280	0.85	<i>r</i>	17.59 $\pm$ 0.42	327.32 $\pm$ 13.34
0.83	71489	536	0.85	<i>Y</i>	17.12 $\pm$ 0.42	519.07 $\pm$ 89.32
0.83	71489	536	0.85	<i>Z</i>	17.23 $\pm$ 0.42	459.20 $\pm$ 82.36
0.83	71490	536	0.85	<i>H</i>	17.01 $\pm$ 0.42	584.25 $\pm$ 104.51
0.83	71490	536	0.85	<i>J</i>	17.14 $\pm$ 0.42	489.86 $\pm$ 118.33
0.85	73170	1280	0.87	<i>i</i>	17.48 $\pm$ 0.42	360.45 $\pm$ 12.42
0.85	73170	1280	0.87	<i>r</i>	17.61 $\pm$ 0.42	319.00 $\pm$ 16.78
0.85	73171	536	0.87	<i>Y</i>	17.11 $\pm$ 0.42	519.29 $\pm$ 106.76
0.85	73171	536	0.87	<i>Z</i>	17.26 $\pm$ 0.42	444.71 $\pm$ 97.80
0.85	73173	536	0.87	<i>H</i>	17.04 $\pm$ 0.42	572.18 $\pm$ 298.77
0.85	73173	536	0.87	<i>J</i>	17.16 $\pm$ 0.42	482.33 $\pm$ 99.53
0.87	74870	1280	0.89	<i>i</i>	17.50 $\pm$ 0.42	361.40 $\pm$ 11.22
0.87	74870	1280	0.89	<i>r</i>	17.66 $\pm$ 0.42	307.57 $\pm$ 6.73
0.87	74872	536	0.89	<i>H</i>	17.02 $\pm$ 0.42	556.82 $\pm$ 94.64
0.87	74872	536	0.89	<i>J</i>	17.19 $\pm$ 0.42	492.18 $\pm$ 98.82
0.87	74873	536	0.89	<i>Y</i>	17.14 $\pm$ 0.42	492.73 $\pm$ 91.88
0.87	74873	536	0.89	<i>Z</i>	17.29 $\pm$ 0.42	434.49 $\pm$ 62.79
0.90	77485	1280	0.92	<i>r</i>	17.71 $\pm$ 0.42	297.70 $\pm$ 17.58
0.90	77485	1280	0.92	<i>i</i>	17.56 $\pm$ 0.42	335.92 $\pm$ 15.12
0.90	77490	536	0.92	<i>Y</i>	17.27 $\pm$ 0.42	451.80 $\pm$ 55.35
0.90	77490	536	0.92	<i>Z</i>	17.32 $\pm$ 0.42	413.81 $\pm$ 67.52
0.90	77491	536	0.92	<i>H</i>	17.14 $\pm$ 0.42	520.21 $\pm$ 61.26
0.90	77491	536	0.92	<i>J</i>	17.25 $\pm$ 0.42	456.95 $\pm$ 65.92
0.92	79150	1280	0.93	<i>i</i>	17.59 $\pm$ 0.42	329.32 $\pm$ 11.05
0.92	79150	1280	0.93	<i>r</i>	17.76 $\pm$ 0.42	281.54 $\pm$ 8.12
0.92	79151	536	0.93	<i>Y</i>	17.28 $\pm$ 0.42	466.42 $\pm$ 62.22
0.92	79151	536	0.93	<i>Z</i>	17.36 $\pm$ 0.42	399.12 $\pm$ 62.30
0.92	79151	536	0.93	<i>H</i>	17.11 $\pm$ 0.42	539.28 $\pm$ 76.97
0.92	79151	536	0.93	<i>J</i>	17.33 $\pm$ 0.42	412.45 $\pm$ 54.73
0.94	80826	1280	0.95	<i>i</i>	17.62 $\pm$ 0.42	314.80 $\pm$ 10.13
0.94	80826	1280	0.95	<i>r</i>	17.77 $\pm$ 0.42	275.47 $\pm$ 8.21
0.94	80827	536	0.95	<i>Y</i>	17.26 $\pm$ 0.42	441.59 $\pm$ 64.98
0.94	80827	536	0.95	<i>Z</i>	17.41 $\pm$ 0.42	391.78 $\pm$ 29.23
0.94	80828	536	0.95	<i>H</i>	17.17 $\pm$ 0.42	551.47 $\pm$ 69.19
0.94	80828	536	0.95	<i>J</i>	17.26 $\pm$ 0.42	437.22 $\pm$ 73.40
0.97	83586	1280	0.99	<i>i</i>	17.65 $\pm$ 0.42	306.26 $\pm$ 11.71
0.97	83586	1280	0.99	<i>r</i>	17.81 $\pm$ 0.42	267.65 $\pm$ 10.62
0.97	83593	536	0.99	<i>H</i>	17.23 $\pm$ 0.42	504.95 $\pm$ 57.64
0.97	83593	536	0.99	<i>J</i>	17.35 $\pm$ 0.42	411.12 $\pm$ 57.56
0.97	83632	536	0.99	<i>Y</i>	17.30 $\pm$ 0.42	427.96 $\pm$ 57.65
0.97	83632	536	0.99	<i>Z</i>	17.42 $\pm$ 0.42	380.83 $\pm$ 41.56
0.99	85331	1280	1.01	<i>i</i>	17.69 $\pm$ 0.42	295.68 $\pm$ 8.70
0.99	85331	1280	1.01	<i>r</i>	17.84 $\pm$ 0.42	260.68 $\pm$ 13.34
0.99	85333	536	1.01	<i>Y</i>	17.37 $\pm$ 0.42	401.37 $\pm$ 43.58
0.99	85333	536	1.01	<i>Z</i>	17.43 $\pm$ 0.42	372.94 $\pm$ 56.57

**Table 6**  
(Continued)

$t_0$ (day)	$t_0$ (s)	$t_e$ (s)	$t_f$ (s)	Filter	$m$ (AB) (Aperture)	Flux ( $\mu$ Jy) (PSF)
0.99	85333	536	1.01	<i>H</i>	17.23 $\pm$ 0.42	507.92 $\pm$ 63.59
0.99	85333	536	1.01	<i>J</i>	17.38 $\pm$ 0.42	395.39 $\pm$ 53.28
1.01	87061	1280	1.03	<i>r</i>	17.84 $\pm$ 0.42	258.40 $\pm$ 11.61
1.01	87061	1280	1.03	<i>i</i>	17.73 $\pm$ 0.42	285.60 $\pm$ 10.05
1.01	87064	536	1.03	<i>Y</i>	17.40 $\pm$ 0.42	401.01 $\pm$ 52.93
1.01	87064	536	1.03	<i>Z</i>	17.49 $\pm$ 0.42	362.49 $\pm$ 54.65
1.01	87066	536	1.03	<i>H</i>	17.25 $\pm$ 0.42	466.24 $\pm$ 60.97
1.01	87066	536	1.03	<i>J</i>	17.38 $\pm$ 0.42	400.08 $\pm$ 54.92
1.04	89861	1280	1.06	<i>i</i>	17.76 $\pm$ 0.42	278.74 $\pm$ 9.38
1.04	89861	1280	1.06	<i>r</i>	17.90 $\pm$ 0.42	243.80 $\pm$ 9.30
1.04	89867	536	1.06	<i>Y</i>	17.41 $\pm$ 0.42	382.43 $\pm$ 51.77
1.04	89867	536	1.06	<i>Z</i>	17.50 $\pm$ 0.42	348.99 $\pm$ 96.74
1.04	89871	536	1.06	<i>H</i>	17.33 $\pm$ 0.42	437.23 $\pm$ 106.18
1.04	89871	536	1.06	<i>J</i>	17.41 $\pm$ 0.42	380.89 $\pm$ 75.30
1.06	91596	1280	1.08	<i>i</i>	17.78 $\pm$ 0.42	271.33 $\pm$ 9.76
1.06	91596	1280	1.08	<i>r</i>	17.94 $\pm$ 0.42	231.70 $\pm$ 13.04
1.06	91600	536	1.08	<i>H</i>	17.28 $\pm$ 0.42	445.08 $\pm$ 108.89
1.06	91600	536	1.08	<i>J</i>	17.45 $\pm$ 0.42	375.58 $\pm$ 86.51
1.06	91600	536	1.08	<i>Y</i>	17.41 $\pm$ 0.42	376.09 $\pm$ 57.58
1.06	91600	536	1.08	<i>Z</i>	17.58 $\pm$ 0.42	317.29 $\pm$ 72.73
1.83	157967	1280	1.85	<i>r</i>	18.70 $\pm$ 0.42	113.69 $\pm$ 1.72
1.83	157967	1280	1.85	<i>i</i>	18.53 $\pm$ 0.42	132.35 $\pm$ 3.46
1.83	157972	536	1.85	<i>H</i>	18.05 $\pm$ 0.43	219.71 $\pm$ 76.44
1.83	157972	536	1.85	<i>J</i>	18.23 $\pm$ 0.43	173.86 $\pm$ 53.15
1.83	157972	536	1.85	<i>Y</i>	18.08 $\pm$ 0.42	192.81 $\pm$ 23.85
1.83	157972	536	1.85	<i>Z</i>	18.25 $\pm$ 0.42	169.00 $\pm$ 20.03
1.85	159663	1280	1.87	<i>r</i>	18.70 $\pm$ 0.42	110.99 $\pm$ 1.53
1.85	159663	1280	1.87	<i>i</i>	18.55 $\pm$ 0.42	130.24 $\pm$ 3.16
1.85	159666	536	1.87	<i>H</i>	18.06 $\pm$ 0.43	206.18 $\pm$ 67.93
1.85	159666	536	1.87	<i>J</i>	18.21 $\pm$ 0.43	175.43 $\pm$ 44.56
1.85	159668	536	1.87	<i>Y</i>	18.12 $\pm$ 0.42	188.45 $\pm$ 27.83
1.85	159668	536	1.87	<i>Z</i>	18.34 $\pm$ 0.42	158.21 $\pm$ 15.76
1.87	161334	1280	1.89	<i>i</i>	18.55 $\pm$ 0.42	129.04 $\pm$ 2.97
1.87	161334	1280	1.89	<i>r</i>	18.72 $\pm$ 0.42	110.25 $\pm$ 1.77
1.87	161335	536	1.89	<i>Y</i>	18.11 $\pm$ 0.42	185.62 $\pm$ 27.80
1.87	161335	536	1.89	<i>Z</i>	18.34 $\pm$ 0.42	153.69 $\pm$ 17.65
1.87	161337	536	1.89	<i>H</i>	18.08 $\pm$ 0.43	215.43 $\pm$ 78.45
1.87	161337	536	1.89	<i>J</i>	18.23 $\pm$ 0.43	169.34 $\pm$ 41.59
1.89	163694	1280	1.91	<i>i</i>	18.57 $\pm$ 0.42	125.75 $\pm$ 1.90
1.89	163694	1280	1.91	<i>r</i>	18.72 $\pm$ 0.42	109.57 $\pm$ 1.17
1.89	163700	536	1.91	<i>Y</i>	18.19 $\pm$ 0.42	178.61 $\pm$ 17.89
1.89	163700	536	1.91	<i>Z</i>	18.35 $\pm$ 0.42	157.04 $\pm$ 13.47
1.89	163702	536	1.91	<i>H</i>	18.06 $\pm$ 0.43	219.76 $\pm$ 61.30
1.89	163702	536	1.91	<i>J</i>	18.34 $\pm$ 0.42	163.73 $\pm$ 28.56
1.91	165405	1280	1.93	<i>i</i>	18.60 $\pm$ 0.42	124.18 $\pm$ 2.92
1.91	165405	1280	1.93	<i>r</i>	18.77 $\pm$ 0.42	105.43 $\pm$ 1.43
1.91	165407	536	1.93	<i>Y</i>	18.20 $\pm$ 0.42	177.57 $\pm$ 18.95
1.91	165407	536	1.93	<i>Z</i>	18.36 $\pm$ 0.42	153.59 $\pm$ 12.91
1.91	165408	536	1.93	<i>H</i>	18.14 $\pm$ 0.43	198.83 $\pm$ 46.64
1.91	165408	536	1.93	<i>J</i>	18.30 $\pm$ 0.42	166.47 $\pm$ 29.66
1.93	167079	1280	1.95	<i>i</i>	18.60 $\pm$ 0.42	122.24 $\pm$ 2.87
1.93	167079	1280	1.95	<i>r</i>	18.76 $\pm$ 0.42	104.86 $\pm$ 2.11
1.93	167081	536	1.95	<i>H</i>	18.06 $\pm$ 0.42	209.93 $\pm$ 56.56
1.93	167081	536	1.95	<i>J</i>	18.28 $\pm$ 0.42	164.50 $\pm$ 26.93
1.93	167081	536	1.95	<i>Y</i>	18.23 $\pm$ 0.42	172.74 $\pm$ 18.35
1.93	167081	536	1.95	<i>Z</i>	18.39 $\pm$ 0.42	152.73 $\pm$ 12.78
1.96	169250	536	1.98	<i>H</i>	18.04 $\pm$ 0.42	209.45 $\pm$ 45.11
1.96	169250	536	1.98	<i>J</i>	18.34 $\pm$ 0.42	161.81 $\pm$ 61.05
1.96	169286	1280	1.98	<i>r</i>	18.78 $\pm$ 0.42	104.67 $\pm$ 2.68
1.96	169286	1280	1.98	<i>i</i>	18.62 $\pm$ 0.42	120.64 $\pm$ 2.56
1.96	169310	469	1.98	<i>Y</i>	18.29 $\pm$ 0.42	173.81 $\pm$ 21.84
1.96	169310	604	1.98	<i>Z</i>	18.36 $\pm$ 0.42	153.08 $\pm$ 13.55
1.98	170985	1280	2.00	<i>i</i>	18.63 $\pm$ 0.42	120.42 $\pm$ 2.36



**Table 6**  
(Continued)

$t_0$ (day)	$t_0$ (s)	$t_e$ (s)	$t_f$ (s)	Filter	$m$ (AB) (Aperture)	Flux ( $\mu$ Jy) (PSF)
1.98	170985	1280	2.00	<i>r</i>	18.80 ± 0.42	101.31 ± 2.98
1.98	170986	536	2.00	<i>H</i>	18.04 ± 0.43	230.80 ± 110.74
1.98	170986	536	2.00	<i>J</i>	18.23 ± 0.42	164.63 ± 30.78
1.98	171108	536	2.00	<i>Y</i>	18.21 ± 0.42	180.27 ± 22.90
1.98	171108	536	2.00	<i>Z</i>	18.45 ± 0.42	142.52 ± 16.11
2.00	172728	1280	2.02	<i>r</i>	18.82 ± 0.42	98.70 ± 1.90
2.00	172728	1280	2.02	<i>i</i>	18.62 ± 0.42	120.02 ± 2.87
2.00	172735	536	2.02	<i>H</i>	18.10 ± 0.43	219.87 ± 63.24
2.00	172735	536	2.02	<i>J</i>	18.37 ± 0.43	154.87 ± 31.02
2.00	173091	536	2.03	<i>Y</i>	18.28 ± 0.42	159.93 ± 21.83
2.00	173091	536	2.03	<i>Z</i>	18.37 ± 0.42	152.26 ± 18.02
2.02	174940	1280	2.04	<i>r</i>	18.83 ± 0.42	97.36 ± 2.12
2.02	174940	1280	2.04	<i>i</i>	18.65 ± 0.42	117.40 ± 2.51
2.02	174946	536	2.04	<i>H</i>	18.23 ± 0.43	191.66 ± 95.17
2.02	174946	536	2.04	<i>J</i>	18.31 ± 0.43	163.10 ± 44.53
2.03	175056	536	2.05	<i>Y</i>	18.32 ± 0.42	157.62 ± 25.69
2.03	175056	536	2.05	<i>Z</i>	18.41 ± 0.42	146.81 ± 18.00
2.04	176669	1280	2.06	<i>i</i>	18.68 ± 0.42	114.04 ± 4.09
2.04	176669	1280	2.06	<i>r</i>	18.85 ± 0.42	97.26 ± 2.93
2.04	176673	536	2.06	<i>H</i>	18.14 ± 0.43	209.82 ± 125.97
2.04	176673	536	2.06	<i>J</i>	18.35 ± 0.43	161.18 ± 52.20
2.83	244162	1280	2.85	<i>i</i>	19.15 ± 0.42	71.80 ± 1.38
2.83	244162	1280	2.85	<i>r</i>	19.28 ± 0.42	62.18 ± 0.91
2.83	244168	536	2.85	<i>H</i>	18.49 ± 0.43	135.44 ± 80.88
2.83	244168	536	2.85	<i>J</i>	18.81 ± 0.43	94.62 ± 40.25
2.83	244171	536	2.85	<i>Y</i>	18.72 ± 0.43	114.77 ± 24.01
2.83	244171	536	2.85	<i>Z</i>	18.84 ± 0.42	95.64 ± 8.66
2.85	245865	1280	2.86	<i>i</i>	19.13 ± 0.42	72.81 ± 1.67
2.85	245865	1280	2.86	<i>r</i>	19.26 ± 0.42	63.45 ± 1.38
2.85	245867	469	2.86	<i>H</i>	18.51 ± 0.43	117.37 ± 133.41
2.85	245867	536	2.86	<i>Y</i>	18.67 ± 0.43	109.85 ± 23.93
2.85	245867	536	2.86	<i>Z</i>	18.92 ± 0.42	88.60 ± 9.96
2.85	245867	604	2.86	<i>J</i>	18.81 ± 0.43	100.35 ± 55.57
2.87	247553	1280	2.88	<i>i</i>	19.14 ± 0.42	71.86 ± 1.42
2.87	247553	1280	2.88	<i>r</i>	19.28 ± 0.42	63.17 ± 0.93
2.87	247555	536	2.88	<i>Y</i>	18.66 ± 0.43	116.44 ± 25.16
2.87	247555	536	2.88	<i>Z</i>	18.91 ± 0.42	91.74 ± 8.23
2.87	247556	536	2.88	<i>H</i>	18.56 ± 0.43	130.53 ± 76.23
2.87	247556	536	2.88	<i>J</i>	18.86 ± 0.43	95.17 ± 31.71
2.89	249656	536	2.91	<i>H</i>	18.72 ± 0.43	116.01 ± 48.13
2.89	249656	536	2.91	<i>J</i>	18.89 ± 0.43	88.72 ± 22.27
2.89	249656	536	2.91	<i>Y</i>	18.81 ± 0.43	94.88 ± 11.61
2.89	249656	536	2.91	<i>Z</i>	18.86 ± 0.42	92.86 ± 5.93
2.89	249693	1280	2.91	<i>i</i>	19.16 ± 0.42	70.79 ± 1.21
2.89	249693	1280	2.91	<i>r</i>	19.31 ± 0.42	61.72 ± 1.09
2.91	251349	1280	2.93	<i>i</i>	19.16 ± 0.42	69.79 ± 1.31
2.91	251349	1280	2.93	<i>r</i>	19.32 ± 0.42	60.07 ± 1.05
2.91	251350	536	2.93	<i>Y</i>	18.76 ± 0.43	99.00 ± 15.22
2.91	251350	536	2.93	<i>Z</i>	18.94 ± 0.42	84.23 ± 7.06
2.91	251352	536	2.93	<i>H</i>	18.70 ± 0.43	118.01 ± 54.31
2.91	251352	536	2.93	<i>J</i>	18.88 ± 0.43	93.52 ± 23.21
2.93	253022	1280	2.95	<i>i</i>	19.18 ± 0.42	69.02 ± 1.33
2.93	253022	1280	2.95	<i>r</i>	19.33 ± 0.42	59.30 ± 1.37
2.93	253024	536	2.95	<i>Y</i>	18.77 ± 0.43	97.99 ± 25.24
2.93	253024	536	2.95	<i>Z</i>	18.94 ± 0.42	85.20 ± 7.17
2.93	253024	536	2.95	<i>H</i>	18.60 ± 0.43	130.78 ± 58.04
2.93	253024	536	2.95	<i>J</i>	18.86 ± 0.43	96.18 ± 22.58
2.95	255197	536	2.97	<i>Y</i>	18.70 ± 0.43	104.72 ± 17.90
2.95	255197	536	2.97	<i>Z</i>	18.89 ± 0.42	88.48 ± 7.17
2.95	255199	536	2.97	<i>H</i>	18.70 ± 0.43	120.87 ± 62.41
2.95	255199	536	2.97	<i>J</i>	18.85 ± 0.43	98.59 ± 21.59
2.95	255236	1280	2.97	<i>r</i>	19.36 ± 0.42	58.44 ± 1.39
2.95	255236	1280	2.97	<i>i</i>	19.18 ± 0.42	68.25 ± 1.39

**Table 6**  
(Continued)

$t_0$ (day)	$t_0$ (s)	$t_e$ (s)	$t_f$ (s)	Filter	$m$ (AB) (Aperture)	Flux ( $\mu$ Jy) (PSF)
2.97	256928	1280	2.99	<i>r</i>	19.38 $\pm$ 0.42	57.44 $\pm$ 1.10
2.97	256930	1280	2.99	<i>i</i>	19.19 $\pm$ 0.42	67.23 $\pm$ 1.40
2.97	256934	536	2.99	<i>H</i>	18.66 $\pm$ 0.43	137.34 $\pm$ 72.34
2.97	256934	536	2.99	<i>J</i>	18.92 $\pm$ 0.43	91.18 $\pm$ 22.10
2.97	256936	536	2.99	<i>Y</i>	18.77 $\pm$ 0.43	98.98 $\pm$ 17.71
2.97	256936	536	2.99	<i>Z</i>	19.03 $\pm$ 0.42	82.69 $\pm$ 8.79
2.99	258662	1280	3.01	<i>i</i>	19.17 $\pm$ 0.42	69.61 $\pm$ 1.43
2.99	258662	1280	3.01	<i>r</i>	19.37 $\pm$ 0.42	57.93 $\pm$ 1.33
2.99	258663	536	3.01	<i>Y</i>	18.74 $\pm$ 0.43	102.65 $\pm$ 22.76
2.99	258663	536	3.01	<i>Z</i>	18.96 $\pm$ 0.42	80.52 $\pm$ 9.23
2.99	258664	536	3.01	<i>H</i>	18.68 $\pm$ 0.43	112.91 $\pm$ 91.56
2.99	258664	536	3.01	<i>J</i>	18.80 $\pm$ 0.43	93.21 $\pm$ 27.34
3.02	260909	536	3.04	<i>Y</i>	18.72 $\pm$ 0.43	101.24 $\pm$ 20.76
3.02	260909	536	3.04	<i>Z</i>	18.93 $\pm$ 0.42	81.85 $\pm$ 8.58
3.02	260910	536	3.04	<i>H</i>	18.67 $\pm$ 0.43	123.48 $\pm$ 84.77
3.02	260910	536	3.04	<i>J</i>	18.83 $\pm$ 0.43	96.51 $\pm$ 26.43
3.02	260945	1280	3.04	<i>r</i>	19.40 $\pm$ 0.42	54.45 $\pm$ 1.09
3.02	260945	1280	3.04	<i>i</i>	19.19 $\pm$ 0.42	69.98 $\pm$ 1.71
3.04	262654	1280	3.06	<i>i</i>	19.23 $\pm$ 0.42	65.45 $\pm$ 1.41
3.04	262654	1280	3.06	<i>r</i>	19.36 $\pm$ 0.42	58.12 $\pm$ 1.37
3.04	262658	536	3.06	<i>H</i>	18.57 $\pm$ 0.43	123.33 $\pm$ 90.72
3.04	262658	536	3.06	<i>J</i>	18.93 $\pm$ 0.43	89.83 $\pm$ 30.08
3.04	262659	536	3.06	<i>Y</i>	18.84 $\pm$ 0.43	94.95 $\pm$ 20.75
3.04	262659	536	3.06	<i>Z</i>	19.01 $\pm$ 0.43	81.33 $\pm$ 9.88
3.82	330101	1280	3.84	<i>r</i>	19.70 $\pm$ 0.42	40.20 $\pm$ 1.12
3.82	330102	1280	3.84	<i>i</i>	19.53 $\pm$ 0.42	47.78 $\pm$ 1.20
3.84	331631	1280	3.86	<i>r</i>	19.65 $\pm$ 0.42	41.40 $\pm$ 0.96
3.84	331631	1280	3.86	<i>i</i>	19.50 $\pm$ 0.42	48.77 $\pm$ 1.08
3.86	333148	1280	3.87	<i>r</i>	19.63 $\pm$ 0.42	41.75 $\pm$ 0.89
3.86	333148	1280	3.87	<i>i</i>	19.54 $\pm$ 0.42	47.57 $\pm$ 0.92
3.88	335229	1280	3.90	<i>r</i>	19.69 $\pm$ 0.42	40.12 $\pm$ 0.84
3.88	335229	1280	3.90	<i>i</i>	19.54 $\pm$ 0.42	47.09 $\pm$ 1.01
3.90	336754	1280	3.92	<i>r</i>	19.69 $\pm$ 0.42	39.64 $\pm$ 1.01
3.90	336754	1280	3.92	<i>i</i>	19.54 $\pm$ 0.42	45.71 $\pm$ 0.98
3.92	338278	1280	3.93	<i>r</i>	19.72 $\pm$ 0.42	40.58 $\pm$ 0.89
3.92	338279	1280	3.93	<i>i</i>	19.54 $\pm$ 0.42	46.84 $\pm$ 1.07
3.94	340206	1280	3.95	<i>r</i>	19.70 $\pm$ 0.42	39.45 $\pm$ 1.02
3.94	340206	1280	3.95	<i>i</i>	19.54 $\pm$ 0.42	46.35 $\pm$ 1.00
3.96	341738	1280	3.97	<i>r</i>	19.74 $\pm$ 0.42	38.82 $\pm$ 0.82
3.96	341738	1280	3.97	<i>i</i>	19.56 $\pm$ 0.42	46.04 $\pm$ 0.90
3.97	343270	1280	3.99	<i>r</i>	19.70 $\pm$ 0.42	39.81 $\pm$ 0.91
3.97	343271	1280	3.99	<i>i</i>	19.53 $\pm$ 0.42	47.72 $\pm$ 1.11
4.00	345316	1280	4.01	<i>r</i>	19.73 $\pm$ 0.42	38.54 $\pm$ 0.86
4.00	345316	1280	4.01	<i>i</i>	19.57 $\pm$ 0.42	45.09 $\pm$ 0.87
4.01	346882	1280	4.03	<i>r</i>	19.72 $\pm$ 0.42	39.89 $\pm$ 0.94
4.01	346882	1280	4.03	<i>i</i>	19.56 $\pm$ 0.42	47.26 $\pm$ 1.00
4.03	348470	1280	4.05	<i>r</i>	19.75 $\pm$ 0.42	38.51 $\pm$ 1.01
4.03	348471	1280	4.05	<i>i</i>	19.62 $\pm$ 0.42	44.24 $\pm$ 1.18
5.03	434444	1280	5.05	<i>g</i>	20.35 $\pm$ 0.42	21.96 $\pm$ 1.09
5.03	434467	2320	5.08	<i>r</i>	20.06 $\pm$ 0.42	25.27 $\pm$ 1.34
5.03	434468	3839	5.08	<i>i</i>	19.84 $\pm$ 0.42	33.42 $\pm$ 1.14
5.94	513072	5119	6.11	<i>r</i>	20.16 $\pm$ 0.42	23.64 $\pm$ 0.55
5.95	513912	10240	6.14	<i>i</i>	20.02 $\pm$ 0.42	27.34 $\pm$ 0.56
5.95	513920	4228	6.14	<i>Y</i>	19.68 $\pm$ 0.42	36.96 $\pm$ 2.04
5.95	513920	4295	6.14	<i>Z</i>	19.82 $\pm$ 0.42	31.53 $\pm$ 1.24
5.95	513921	4295	6.14	<i>H</i>	19.45 $\pm$ 0.43	42.74 $\pm$ 7.19
5.95	513921	4295	6.14	<i>J</i>	19.66 $\pm$ 0.42	41.53 $\pm$ 2.91
5.97	515483	5119	6.12	<i>g</i>	20.54 $\pm$ 0.42	17.98 $\pm$ 0.50
6.93	598530	12400	7.13	<i>i</i>	20.16 $\pm$ 0.42	22.37 $\pm$ 0.55
6.93	598765	11759	7.13	<i>g</i>	20.67 $\pm$ 0.42	15.46 $\pm$ 0.49
6.93	598772	4832	7.13	<i>Y</i>	19.87 $\pm$ 0.43	30.39 $\pm$ 2.19
6.93	598772	5033	7.13	<i>Z</i>	19.90 $\pm$ 0.42	28.59 $\pm$ 1.23
6.93	598776	4966	7.13	<i>H</i>	19.67 $\pm$ 0.43	32.84 $\pm$ 7.91

**Table 6**  
(Continued)

$t_0$ (day)	$t_0$ (s)	$t_e$ (s)	$t_f$ (s)	Filter	$m$ (AB) (Aperture)	Flux ( $\mu$ Jy) (PSF)
6.93	598776	5033	7.13	<i>J</i>	19.82 $\pm$ 0.43	35.80 $\pm$ 5.87
7.94	686416	9040	8.14	<i>g</i>	20.82 $\pm$ 0.42	12.77 $\pm$ 0.51
7.94	686416	9679	8.14	<i>i</i>	20.31 $\pm$ 0.42	18.42 $\pm$ 0.56
7.95	686463	3557	8.14	<i>Z</i>	20.07 $\pm$ 0.43	22.98 $\pm$ 1.38
7.95	686463	3557	8.14	<i>J</i>	19.80 $\pm$ 0.43	33.50 $\pm$ 4.67
7.95	686463	4093	8.14	<i>Y</i>	19.87 $\pm$ 0.43	28.88 $\pm$ 2.74
7.95	686463	4698	8.14	<i>H</i>	19.80 $\pm$ 0.43	51.25 $\pm$ 11.57
9.96	860894	5999	10.08	<i>g</i>	21.04 $\pm$ 0.42	9.46 $\pm$ 0.49
9.96	860894	5999	10.08	<i>i</i>	20.46 $\pm$ 0.42	14.73 $\pm$ 0.57
9.96	860902	2483	10.08	<i>J</i>	20.22 $\pm$ 0.43	19.00 $\pm$ 5.64
9.96	860902	2550	10.08	<i>H</i>	20.19 $\pm$ 0.44	-1.10 $\pm$ 15.50
9.96	860904	2483	10.08	<i>Z</i>	20.18 $\pm$ 0.43	18.27 $\pm$ 1.70
9.96	860904	2550	10.08	<i>Y</i>	20.18 $\pm$ 0.43	20.30 $\pm$ 3.31
10.91	943033	1120	10.93	<i>r</i>	20.64 $\pm$ 0.43	11.51 $\pm$ 1.26
10.93	943968	3892	11.15	<i>Z</i>	20.35 $\pm$ 0.43	13.97 $\pm$ 1.59
10.93	943968	3959	11.15	<i>Y</i>	20.27 $\pm$ 0.43	18.42 $\pm$ 3.49
10.93	944062	9840	11.15	<i>i</i>	20.54 $\pm$ 0.42	13.32 $\pm$ 0.58
10.93	944113	2480	11.15	<i>g</i>	21.17 $\pm$ 0.43	8.07 $\pm$ 0.83
10.93	944130	4093	11.15	<i>J</i>	20.21 $\pm$ 0.44	24.43 $\pm$ 9.14
11.93	1030399	4832	12.13	<i>Y</i>	20.38 $\pm$ 0.43	15.22 $\pm$ 1.38
11.93	1030399	4832	12.13	<i>Z</i>	20.40 $\pm$ 0.42	13.84 $\pm$ 0.89
11.93	1030400	4832	12.13	<i>H</i>	20.09 $\pm$ 0.43	18.47 $\pm$ 4.85
11.93	1030400	4832	12.13	<i>J</i>	20.43 $\pm$ 0.43	12.27 $\pm$ 2.19
11.93	1030435	6399	12.13	<i>r</i>	20.68 $\pm$ 0.42	10.92 $\pm$ 0.52
11.93	1030435	5119	12.09	<i>g</i>	21.12 $\pm$ 0.42	8.26 $\pm$ 0.49
11.93	1030435	11519	12.13	<i>i</i>	20.58 $\pm$ 0.42	12.27 $\pm$ 0.49
12.91	1115381	5119	13.09	<i>r</i>	20.71 $\pm$ 0.42	10.44 $\pm$ 0.54
12.91	1115381	10240	13.09	<i>i</i>	20.60 $\pm$ 0.42	11.86 $\pm$ 0.50
12.91	1115386	4295	13.09	<i>Y</i>	20.33 $\pm$ 0.43	16.63 $\pm$ 1.77
12.91	1115386	4295	13.09	<i>Z</i>	20.39 $\pm$ 0.43	13.92 $\pm$ 1.02
12.91	1115413	5119	13.05	<i>g</i>	21.17 $\pm$ 0.42	7.90 $\pm$ 0.49
12.91	1115428	4295	13.09	<i>H</i>	20.34 $\pm$ 0.44	2.34 $\pm$ 6.49
12.91	1115428	4295	13.09	<i>J</i>	20.34 $\pm$ 0.43	16.98 $\pm$ 3.20
13.91	1201686	5119	14.04	<i>g</i>	21.24 $\pm$ 0.42	7.36 $\pm$ 0.48
13.91	1201710	5119	14.08	<i>r</i>	20.76 $\pm$ 0.42	9.59 $\pm$ 0.54
13.91	1201710	10160	14.08	<i>i</i>	20.67 $\pm$ 0.42	10.39 $\pm$ 0.50
13.91	1201715	4228	14.08	<i>Y</i>	20.40 $\pm$ 0.43	14.09 $\pm$ 1.74
13.91	1201715	4295	14.08	<i>Z</i>	20.52 $\pm$ 0.43	11.19 $\pm$ 0.97
13.91	1201716	4295	14.08	<i>H</i>	20.33 $\pm$ 0.44	0.08 $\pm$ 6.63
13.91	1201716	4295	14.08	<i>J</i>	20.36 $\pm$ 0.43	18.58 $\pm$ 2.92
14.90	1287710	5119	15.05	<i>r</i>	20.78 $\pm$ 0.42	9.55 $\pm$ 0.53
14.91	1288530	10240	15.08	<i>i</i>	20.72 $\pm$ 0.42	10.15 $\pm$ 0.49
14.91	1288579	4295	15.08	<i>H</i>	20.26 $\pm$ 0.43	16.57 $\pm$ 4.77
14.91	1288579	4295	15.08	<i>J</i>	20.53 $\pm$ 0.43	15.81 $\pm$ 2.29
14.91	1288581	4295	15.08	<i>Y</i>	20.41 $\pm$ 0.43	13.66 $\pm$ 1.38
14.91	1288581	4295	15.08	<i>Z</i>	20.49 $\pm$ 0.43	11.03 $\pm$ 0.89
14.92	1289370	5119	15.07	<i>g</i>	21.26 $\pm$ 0.42	6.95 $\pm$ 0.49
15.89	1373149	5119	16.03	<i>r</i>	20.83 $\pm$ 0.42	8.62 $\pm$ 0.55
15.90	1373982	10240	16.06	<i>i</i>	20.75 $\pm$ 0.42	9.25 $\pm$ 0.50
15.90	1374029	4295	16.06	<i>Y</i>	20.52 $\pm$ 0.43	11.67 $\pm$ 1.67
15.90	1374029	4295	16.06	<i>Z</i>	20.54 $\pm$ 0.43	10.73 $\pm$ 1.03
15.90	1374030	4295	16.06	<i>H</i>	20.36 $\pm$ 0.44	5.63 $\pm$ 5.26
15.90	1374030	4295	16.06	<i>J</i>	20.60 $\pm$ 0.43	8.97 $\pm$ 2.75
15.91	1374818	5119	16.05	<i>g</i>	21.29 $\pm$ 0.42	6.83 $\pm$ 0.50
16.91	1460973	4480	17.04	<i>r</i>	20.81 $\pm$ 0.42	9.13 $\pm$ 0.57
16.91	1460973	8319	17.04	<i>i</i>	20.75 $\pm$ 0.42	9.38 $\pm$ 0.52
16.91	1460979	3489	17.04	<i>Y</i>	20.55 $\pm$ 0.43	10.18 $\pm$ 2.47
16.91	1460979	3489	17.04	<i>Z</i>	20.60 $\pm$ 0.43	10.59 $\pm$ 1.12
16.91	1460981	3489	17.04	<i>J</i>	20.55 $\pm$ 0.44	8.21 $\pm$ 3.78
16.91	1461359	3839	17.02	<i>g</i>	21.33 $\pm$ 0.42	6.47 $\pm$ 0.52
17.91	1547770	3839	18.06	<i>r</i>	20.87 $\pm$ 0.42	8.51 $\pm$ 0.61
17.93	1548872	7680	18.09	<i>i</i>	20.75 $\pm$ 0.42	9.16 $\pm$ 0.55
17.93	1548882	3221	18.09	<i>Y</i>	20.59 $\pm$ 0.43	8.06 $\pm$ 2.81

**Table 6**  
(Continued)

$t_0$ (day)	$t_0$ (s)	$t_e$ (s)	$t_f$ (s)	Filter	$m$ (AB) (Aperture)	Flux ( $\mu$ Jy) (PSF)
17.93	1548882	3221	18.09	Z	20.61 $\pm$ 0.43	9.09 $\pm$ 1.38
17.94	1549668	3839	18.08	g	21.39 $\pm$ 0.42	5.89 $\pm$ 0.55
18.92	1634492	6399	19.11	r	20.91 $\pm$ 0.42	7.38 $\pm$ 0.54
18.92	1634492	11359	19.11	i	20.79 $\pm$ 0.42	8.55 $\pm$ 0.50
18.92	1634525	4959	19.07	g	21.38 $\pm$ 0.42	5.56 $\pm$ 0.50
18.92	1634538	4765	19.10	J	20.48 $\pm$ 0.43	13.30 $\pm$ 2.52
18.92	1634542	4765	19.10	Y	20.57 $\pm$ 0.43	11.37 $\pm$ 1.61
18.92	1634542	4765	19.10	Z	20.59 $\pm$ 0.43	10.29 $\pm$ 0.93
19.91	1720548	6079	20.09	r	20.91 $\pm$ 0.42	7.22 $\pm$ 0.57
19.91	1720548	11120	20.09	i	20.82 $\pm$ 0.42	8.25 $\pm$ 0.52
19.91	1720583	5119	20.05	g	21.43 $\pm$ 0.42	5.28 $\pm$ 0.51
19.91	1720594	4563	20.09	J	20.59 $\pm$ 0.43	7.48 $\pm$ 2.76
19.91	1720597	4429	20.09	Y	20.57 $\pm$ 0.43	10.06 $\pm$ 2.14
19.91	1720597	4496	20.09	Z	20.70 $\pm$ 0.43	9.23 $\pm$ 1.08
20.91	1807055	6399	21.10	r	20.91 $\pm$ 0.42	7.10 $\pm$ 0.61
20.91	1807055	11439	21.10	i	20.79 $\pm$ 0.42	8.25 $\pm$ 0.56
20.92	1807079	5039	21.06	g	21.52 $\pm$ 0.43	4.36 $\pm$ 0.57
20.92	1807103	4765	21.10	J	20.78 $\pm$ 0.44	7.57 $\pm$ 3.74
20.92	1807104	4765	21.10	Z	20.58 $\pm$ 0.43	10.89 $\pm$ 1.36
20.92	1807104	4832	21.10	Y	20.60 $\pm$ 0.43	9.30 $\pm$ 2.26
21.92	1893510	6399	22.10	r	20.96 $\pm$ 0.42	6.56 $\pm$ 0.62
21.92	1893511	11519	22.10	i	20.84 $\pm$ 0.42	7.54 $\pm$ 0.57
21.92	1893520	5119	22.06	g	21.51 $\pm$ 0.43	4.19 $\pm$ 0.57
21.92	1893559	4832	22.09	J	21.04 $\pm$ 0.45	5.14 $\pm$ 3.19
21.92	1893561	4832	22.09	Z	20.59 $\pm$ 0.43	10.00 $\pm$ 1.58
21.92	1893561	4832	22.09	Y	20.64 $\pm$ 0.43	7.93 $\pm$ 2.18
22.91	1979266	5119	23.04	r	20.94 $\pm$ 0.42	6.60 $\pm$ 0.59
22.92	1980062	10240	23.07	i	20.87 $\pm$ 0.42	7.27 $\pm$ 0.51
22.93	1980833	5119	23.06	g	21.53 $\pm$ 0.43	5.10 $\pm$ 0.53
23.91	2065542	4959	24.04	g	21.46 $\pm$ 0.43	4.78 $\pm$ 0.59
23.91	2065553	6399	24.08	r	20.91 $\pm$ 0.42	6.21 $\pm$ 0.66
23.91	2065553	11519	24.08	i	20.86 $\pm$ 0.42	7.29 $\pm$ 0.54
24.99	2159267	1200	25.01	r	21.24 $\pm$ 0.44	2.72 $\pm$ 1.41
24.99	2159267	1200	25.01	i	20.92 $\pm$ 0.43	6.83 $\pm$ 1.54
25.90	2237953	4879	26.05	r	21.10 $\pm$ 0.43	5.15 $\pm$ 0.70
25.91	2238775	10000	26.08	i	20.91 $\pm$ 0.42	6.82 $\pm$ 0.58
25.91	2238821	4161	26.08	Y	20.85 $\pm$ 0.44	7.22 $\pm$ 2.92
25.91	2238821	4228	26.08	Z	20.78 $\pm$ 0.43	-0.23 $\pm$ 1.43
25.92	2239618	5039	26.07	g	21.61 $\pm$ 0.43	3.91 $\pm$ 0.67
26.91	2325407	3839	27.01	g	21.69 $\pm$ 0.43	0.00 $\pm$ 0.44
26.92	2325639	5119	27.06	r	21.07 $\pm$ 0.43	4.87 $\pm$ 0.67
26.92	2325639	8960	27.06	i	20.86 $\pm$ 0.42	7.12 $\pm$ 0.57
26.92	2325685	3758	27.06	J	20.56 $\pm$ 0.44	11.38 $\pm$ 4.12
26.92	2325688	3758	27.06	Z	20.72 $\pm$ 0.43	6.95 $\pm$ 1.48
26.92	2325688	3758	27.06	Y	20.84 $\pm$ 0.44	3.92 $\pm$ 2.48
27.90	2410506	5119	28.04	r	21.09 $\pm$ 0.43	5.85 $\pm$ 0.74
27.91	2411320	10240	28.07	i	20.96 $\pm$ 0.42	6.13 $\pm$ 0.58
27.91	2411368	4295	28.07	Z	20.84 $\pm$ 0.43	0.76 $\pm$ 1.29
27.91	2411368	4295	28.07	Y	20.86 $\pm$ 0.44	4.35 $\pm$ 2.39
27.92	2412156	5119	28.06	g	21.64 $\pm$ 0.43	3.39 $\pm$ 0.73
28.90	2496872	4959	29.04	r	21.13 $\pm$ 0.43	4.23 $\pm$ 0.63
28.91	2497696	10080	29.07	i	20.91 $\pm$ 0.42	6.33 $\pm$ 0.55
28.91	2497747	4228	29.07	Y	20.70 $\pm$ 0.43	4.82 $\pm$ 1.99
28.91	2497747	4228	29.07	Z	20.79 $\pm$ 0.43	-0.11 $\pm$ 1.18
28.92	2498536	5119	29.06	g	21.75 $\pm$ 0.43	3.35 $\pm$ 0.63
29.92	2584960	3520	30.02	r	21.15 $\pm$ 0.43	4.92 $\pm$ 0.66
29.93	2586106	7119	30.06	i	21.00 $\pm$ 0.42	5.39 $\pm$ 0.59
29.93	2586153	3020	30.06	Z	20.81 $\pm$ 0.43	-1.40 $\pm$ 1.53
29.94	2586921	3440	30.05	g	21.78 $\pm$ 0.43	2.83 $\pm$ 0.63
30.91	2670326	3199	31.00	g	21.90 $\pm$ 0.43	2.35 $\pm$ 0.63
30.91	2670536	4879	31.05	r	21.30 $\pm$ 0.43	2.88 $\pm$ 0.63
30.91	2670536	8080	31.05	i	20.97 $\pm$ 0.42	5.52 $\pm$ 0.57
30.91	2670583	3355	31.05	Y	20.66 $\pm$ 0.43	3.27 $\pm$ 2.66

**Table 6**  
(Continued)

$t_0$ (day)	$t_0$ (s)	$t_e$ (s)	$t_f$ (s)	Filter	$m$ (AB) (Aperture)	Flux ( $\mu$ Jy) (PSF)
30.91	2670583	3422	31.05	Z	20.66 $\pm$ 0.43	3.83 $\pm$ 1.43
31.90	2756306	3680	32.00	g	21.82 $\pm$ 0.43	2.53 $\pm$ 0.53
31.90	2756574	5119	32.05	r	21.22 $\pm$ 0.42	2.92 $\pm$ 0.57
31.90	2756574	8800	32.05	i	21.00 $\pm$ 0.42	5.30 $\pm$ 0.54
31.91	2756622	3691	32.05	Y	20.73 $\pm$ 0.43	6.41 $\pm$ 2.60
31.91	2756622	3691	32.05	Z	20.81 $\pm$ 0.43	3.59 $\pm$ 1.38
32.90	2842792	3440	33.00	g	21.83 $\pm$ 0.43	2.21 $\pm$ 0.54
32.91	2843068	4879	33.05	r	21.22 $\pm$ 0.43	2.78 $\pm$ 0.60
32.91	2843068	8319	33.05	i	21.01 $\pm$ 0.42	5.33 $\pm$ 0.57
32.91	2843117	3557	33.05	Z	20.74 $\pm$ 0.43	2.95 $\pm$ 1.64
33.90	2929382	3839	34.01	g	21.86 $\pm$ 0.43	2.34 $\pm$ 0.48
33.91	2929674	4800	34.05	r	21.32 $\pm$ 0.43	2.93 $\pm$ 0.93
33.91	2929674	8960	34.05	i	21.02 $\pm$ 0.42	4.89 $\pm$ 0.49
34.89	3014902	3839	35.00	g	21.91 $\pm$ 0.43	2.23 $\pm$ 0.48
34.90	3015214	8960	35.05	i	21.06 $\pm$ 0.42	4.78 $\pm$ 0.50
35.90	3101699	3839	36.00	g	21.95 $\pm$ 0.43	1.58 $\pm$ 0.49
35.90	3101980	8960	36.05	i	21.06 $\pm$ 0.42	4.31 $\pm$ 0.49
35.90	3102033	2160	36.05	r	21.23 $\pm$ 0.44	3.30 $\pm$ 1.50
36.89	3187381	3520	37.00	r	21.71 $\pm$ 0.43	-0.70 $\pm$ 0.77
36.90	3188503	8080	37.04	i	21.08 $\pm$ 0.42	4.42 $\pm$ 0.52
38.88	3359533	3839	38.98	r	21.33 $\pm$ 0.43	2.55 $\pm$ 0.58
38.89	3360354	7680	39.01	i	21.13 $\pm$ 0.42	3.64 $\pm$ 0.53
38.89	3360403	3221	39.01	Z	20.83 $\pm$ 0.43	1.30 $\pm$ 45.53
38.90	3361179	3839	39.00	g	22.07 $\pm$ 0.43	1.24 $\pm$ 0.51
39.90	3446958	7680	40.01	r	21.34 $\pm$ 0.42	2.29 $\pm$ 0.51
39.90	3446958	7680	40.01	i	21.14 $\pm$ 0.42	3.80 $\pm$ 0.49
39.90	3447005	6442	40.01	H	20.73 $\pm$ 0.43	1.81 $\pm$ 2.42
39.90	3447006	6442	40.01	Y	20.93 $\pm$ 0.43	2.26 $\pm$ 0.94
42.92	3708410	2640	42.99	i	21.23 $\pm$ 0.43	4.70 $\pm$ 8.51
42.92	3708417	2214	42.99	Z	21.25 $\pm$ 0.44	0.28 $\pm$ 1.40
44.88	3877978	6399	44.98	g	21.98 $\pm$ 0.43	1.37 $\pm$ 0.48
44.88	3877978	6399	44.98	i	21.18 $\pm$ 0.42	3.12 $\pm$ 0.51
46.89	4051373	6560	47.00	r	21.41 $\pm$ 0.43	1.81 $\pm$ 0.56
46.89	4051373	6319	47.00	i	21.15 $\pm$ 0.43	2.86 $\pm$ 0.61
50.87	4395336	3680	50.93	g	22.11 $\pm$ 0.43	1.12 $\pm$ 0.56
50.87	4395336	3680	50.93	i	21.28 $\pm$ 0.43	1.64 $\pm$ 0.63
51.88	4482266	5119	51.96	r	21.41 $\pm$ 0.43	0.83 $\pm$ 0.56
51.88	4482267	5119	51.96	i	21.20 $\pm$ 0.43	2.08 $\pm$ 0.58
51.88	4482314	4295	51.96	Y	21.06 $\pm$ 0.43	3.62 $\pm$ 1.61
52.90	4570263	2560	52.94	i	21.23 $\pm$ 0.43	2.51 $\pm$ 0.74
53.88	4655540	3839	53.94	r	21.36 $\pm$ 0.43	2.56 $\pm$ 0.63
53.88	4655540	3839	53.94	i	21.16 $\pm$ 0.43	2.54 $\pm$ 0.64
53.88	4655589	3221	53.94	Y	21.13 $\pm$ 0.44	2.27 $\pm$ 1.56
54.88	4741565	4800	54.96	g	21.94 $\pm$ 0.44	1.75 $\pm$ 0.75
54.88	4741565	5119	54.96	i	21.29 $\pm$ 0.43	1.82 $\pm$ 0.62
54.88	4741615	2147	54.96	Y	20.74 $\pm$ 0.44	4.30 $\pm$ 3.39
56.88	4914230	5119	56.96	r	21.54 $\pm$ 0.43	-0.07 $\pm$ 1.27
56.88	4914230	5119	56.96	i	21.16 $\pm$ 0.43	2.96 $\pm$ 0.72
56.88	4914278	4295	56.96	Y	20.99 $\pm$ 0.43	1.86 $\pm$ 1.99
57.87	4999923	3839	57.93	i	21.40 $\pm$ 0.43	0.99 $\pm$ 0.83
58.87	5086058	3839	58.92	r	21.39 $\pm$ 0.43	1.18 $\pm$ 0.66
58.87	5086058	3839	58.92	i	21.15 $\pm$ 0.43	2.11 $\pm$ 0.68
58.87	5086106	3221	58.92	Y	21.03 $\pm$ 0.43	2.65 $\pm$ 1.64
59.87	5172391	3839	59.92	g	22.19 $\pm$ 0.43	0.50 $\pm$ 0.50
59.87	5172391	3839	59.92	i	21.36 $\pm$ 0.43	2.19 $\pm$ 0.61
65.86	5690438	2560	65.90	i	21.33 $\pm$ 0.43	1.71 $\pm$ 0.67
65.86	5690438	2560	65.90	g	22.20 $\pm$ 0.43	1.00 $\pm$ 0.55
66.86	5776448	2480	66.90	i	21.43 $\pm$ 0.43	1.61 $\pm$ 0.88
66.86	5776448	2560	66.90	r	21.51 $\pm$ 0.43	0.06 $\pm$ 0.79
215.15	18588991	8479	215.29	r	21.60 $\pm$ 0.43	0.20 $\pm$ 0.52
215.15	18588991	8479	215.29	i	21.35 $\pm$ 0.42	0.27 $\pm$ 0.55
217.15	18761668	8880	217.30	g	22.26 $\pm$ 0.43	0.10 $\pm$ 0.47
217.15	18761668	8880	217.30	i	21.40 $\pm$ 0.42	0.12 $\pm$ 0.52

**Table 6**  
(Continued)

$t_0$ (day)	$t_0$ (s)	$t_e$ (s)	$t_f$ (s)	Filter	$m$ (AB) (Aperture)	Flux ( $\mu$ Jy) (PSF)
217.15	18761678	3691	217.30	Z	$21.07 \pm 0.43$	$-0.67 \pm 1.20$
219.14	18933938	4093	219.30	Z	$21.17 \pm 0.43$	$1.71 \pm 1.18$
219.14	18933983	9920	219.31	r	$21.57 \pm 0.42$	$0.12 \pm 0.49$
219.14	18933983	9920	219.31	i	$21.41 \pm 0.42$	$0.63 \pm 0.51$
221.11	19104115	6319	221.23	g	$22.25 \pm 0.43$	$0.33 \pm 0.54$
221.11	19104115	6560	221.23	i	$21.46 \pm 0.43$	$0.31 \pm 0.79$
223.14	19279069	10240	223.30	r	$21.61 \pm 0.42$	$0.27 \pm 0.50$
223.14	19279069	10240	223.30	i	$21.45 \pm 0.42$	$0.83 \pm 0.53$
223.14	19279078	4295	223.30	Z	$20.99 \pm 0.43$	$1.61 \pm 1.32$
229.14	19797449	4765	229.32	Z	$21.06 \pm 0.43$	$-0.32 \pm 1.08$
229.14	19797488	11040	229.32	g	$22.26 \pm 0.43$	$0.18 \pm 0.47$
229.14	19797488	11439	229.32	i	$21.47 \pm 0.42$	$0.67 \pm 0.50$
231.13	19969644	10479	231.33	i	$21.38 \pm 0.43$	$0.65 \pm 0.61$
231.13	19969803	10240	231.33	r	$22.18 \pm 0.43$	$1.05 \pm 0.54$
303.53	26224942	28254	384.70	Y	$21.16 \pm 0.43$	$1.31 \pm 0.75$
303.53	26224942	28389	384.70	Z	$21.06 \pm 0.43$	$-0.51 \pm 0.59$
303.53	26224983	27986	384.70	J	$21.36 \pm 0.43$	$2.10 \pm 0.93$
303.53	26224983	28694	384.70	H	$20.86 \pm 0.44$	$1.64 \pm 1.79$
306.52	26483726	79599	395.67	r	$21.58 \pm 0.42$	$0.26 \pm 0.46$
314.00	27129366	145272	418.10	i	$21.44 \pm 0.42$	$0.01 \pm 0.45$
353.44	30537092	53200	378.66	g	$22.25 \pm 0.42$	$0.10 \pm 0.45$
1152.86	99607079	23439	1192.87	r	$21.57 \pm 0.42$	$0.00 \pm 0.44$
1153.36	99650438	63920	1194.37	i	$21.46 \pm 0.42$	$-0.00 \pm 0.48$
1153.36	99650451	28456	1194.37	H	$21.27 \pm 0.44$	$5.55 \pm 54.54$
1153.36	99650451	28657	1194.37	J	$21.30 \pm 0.43$	$0.11 \pm 1.62$
1153.36	99650553	29463	1194.37	Y	$21.34 \pm 0.43$	$0.00 \pm 0.96$
1153.36	99650553	29865	1194.37	Z	$21.21 \pm 0.43$	$0.05 \pm 0.73$
1153.85	99692829	38160	1193.88	g	$22.21 \pm 0.42$	$0.00 \pm 0.44$

is  $M_r = -18.43 \pm 0.11$  for SN 2013cq, which is close to the measured  $M_r = -18.48 \pm 0.08$  for SN 1998bw.

### 5. Summary

We have presented *grizYJH* photometry of the afterglow of GRB 130427A with the RATIR instrument, from the night of the burst to three years later. Comparing our work to previous photometric studies (Xu et al. 2013a; Melandri et al. 2014; Perley et al. 2014), we have better temporal sampling, deeper photometry, and we subtract a deep late-epoch image to remove the host galaxy.

Perley et al. (2014) were better able to study the afterglow over the first couple of days and show the existence of a temporal break at about 0.7 days. Our data, on the other hand, are better suited to looking for deviations from a simple power-law model at later times associated with a supernova.

We fit the early afterglow (up to 0.7 days) and late afterglow (after 0.7 days) with power-laws. Prior to fitting for the late afterglow, we subtracted a late image to remove the contamination from the host galaxy. The temporal index of the power-law components changes from 0.97 during the early afterglow to 1.41 during the late afterglow, in agreement with the values and temporal break around 0.7 days determined by Maselli et al. (2014) and Perley et al. (2014).

Positive residuals to the fits in *griz* between about 7 and 40 days show that we are seeing the photometric signature of SN 2013cq, previously detected spectroscopically by de Ugarte Postigo et al. (2013) and Xu et al. (2013a) and photometrically by Perley et al. (2014), Xu et al. (2013a), and Melandri et al.

(2014). The absolute magnitude and broadband SED of the supernova are consistent with those of the prototype SN 1998bw and suggest similar progenitors. The peak times agree with those reported by Xu et al. (2013a) and are detailed for *griz* bands. The absolute magnitudes calculated match with SN 1998bw for *riz* bands. Our better temporal coverage and deeper photometry give us an improved light curve compared to previous work (Xu et al. 2013a; Melandri et al. 2014; Perley et al. 2014). Photometric data obtained three years after the GRB 130427A suggest that the host galaxy is extremely blue compared to local samples.

GRB 130427A is among the handful of events with a confirmed GRB/SN association. In addition it is a high-luminosity event, differing from sub-luminous, very local ones such as GRB 980425/SN 1998bw. The combination is thus unique, and the detailed, homogeneous photometry are presented here with the aim of enlarging the sample for which detailed inferences can be made, eventually in a more statistically significant way when combined with other bursts.

We thank the staff of the Observatorio Astronómico Nacional in Sierra San Pedro Mártir. We thank the anonymous referee for a very helpful report. We thank Fabio De Colle for useful comments on earlier drafts. RATIR is a collaboration between the University of California, the Universidad Nacional Autónoma de México, NASA Goddard Space Flight Center, and Arizona State University, benefiting from the loan of an H2RG detector and hardware and software support from Teledyne Scientific and Imaging. RATIR, the automation of the Harold L.

**Table 7**  
Residuals between Observations and the Power-law Model for RATIR Data for Early Afterglow (Before 0.7 days)

$t_0$ (s)	Filter				
	$i$ ( $\mu\text{Jy}$ )	$Z$ ( $\mu\text{Jy}$ )	$Y$ ( $\mu\text{Jy}$ )	$J$ ( $\mu\text{Jy}$ )	$H$ ( $\mu\text{Jy}$ )
929	1099.93 $\pm$ 539.14	...	...	...	...
1009	...	2805.23 $\pm$ 601.42	...	...	...
1012	...	...	...	3354.17 $\pm$ 649.69	...
1037	1373.25 $\pm$ 518.59	...	...	...	...
1111	...	...	...	...	591.10 $\pm$ 605.02
1114	...	...	2951.70 $\pm$ 651.46	...	...
1140	314.13 $\pm$ 467.87	...	...	...	...
1216	...	...	-497.04 $\pm$ 535.12	...	2238.44 $\pm$ 567.07
1249	-34.68 $\pm$ 385.64	...	...	...	...
1323	...	832.70 $\pm$ 441.93	...	...	...
1326	...	...	...	1761.38 $\pm$ 465.51	...
1348	-541.16 $\pm$ 341.65	...	...	...	...
1429	...	...	...	705.36 $\pm$ 425.84	...
1432	...	207.34 $\pm$ 388.42	...	...	...
1457	-341.40 $\pm$ 325.81	...	...	...	...
1532	...	...	...	...	271.86 $\pm$ 473.29
1534	...	...	398.85 $\pm$ 421.20	...	...
1579	-344.62 $\pm$ 303.13	...	...	...	...
1653	...	...	760.35 $\pm$ 424.83	...	413.36 $\pm$ 387.92
1683	-10.17 $\pm$ 294.07	...	...	...	...
1762	...	237.31 $\pm$ 321.87	...	...	...
1764	...	...	...	362.12 $\pm$ 345.01	...
1778	-26.80 $\pm$ 276.89	...	...	...	...
1858	...	...	...	702.49 $\pm$ 330.55	...
1859	...	98.84 $\pm$ 303.47	...	...	...
1887	-345.25 $\pm$ 280.13	...	...	...	...
1962	...	...	260.62 $\pm$ 336.24	...	...
1964	...	...	...	...	843.22 $\pm$ 386.70
1993	63.20 $\pm$ 253.56	...	...	...	...
2067	...	...	116.67 $\pm$ 309.69	...	...
2068	...	...	...	...	810.12 $\pm$ 362.53
2120	-776.28 $\pm$ 223.10	...	...	...	...
2196	...	1021.73 $\pm$ 282.60	...	-721.88 $\pm$ 256.29	...
2223	-304.10 $\pm$ 218.44	...	...	...	...
2298	...	...	...	416.47 $\pm$ 272.67	...
2300	...	-45.74 $\pm$ 248.32	...	...	...
2328	11.83 $\pm$ 217.43	...	...	...	...
2408	...	...	365.80 $\pm$ 287.64	...	-10.21 $\pm$ 276.78
2422	-416.26 $\pm$ 212.59	...	...	...	...
2502	...	...	-192.37 $\pm$ 258.31	...	...
2506	...	...	...	...	191.98 $\pm$ 266.82
2531	-446.33 $\pm$ 184.76	...	...	...	...
2605	...	...	...	26.02 $\pm$ 236.63	...
2607	...	-175.13 $\pm$ 217.63	...	...	...
2654	-305.91 $\pm$ 178.58	...	...	...	...
2729	...	...	...	-206.29 $\pm$ 217.49	...
2732	...	-567.47 $\pm$ 204.66	...	...	...
2780	-522.44 $\pm$ 193.74	...	...	...	...
2855	...	...	-77.25 $\pm$ 243.18	...	...
2856	...	...	...	...	106.19 $\pm$ 273.15
2884	-204.39 $\pm$ 164.74	...	...	...	...
2960	...	...	-147.92 $\pm$ 218.22	...	...
2961	...	...	...	...	605.39 $\pm$ 291.40
2990	-278.80 $\pm$ 162.89	...	...	...	...
3067	...	-239.20 $\pm$ 178.90	...	...	...
3069	...	...	...	-166.34 $\pm$ 196.09	...
3108	-360.19 $\pm$ 150.44	...	...	...	...
3186	...	77.07 $\pm$ 182.57	...	-1002.49 $\pm$ 167.46	...
3213	-362.91 $\pm$ 150.66	...	...	...	...
3292	...	...	-227.89 $\pm$ 191.97	...	...
3293	...	...	...	...	329.50 $\pm$ 284.11
3307	-333.22 $\pm$ 144.97	...	...	...	...
3387	...	...	...	...	247.13 $\pm$ 256.03
3389	...	...	-131.45 $\pm$ 190.18	...	...
3418	-168.13 $\pm$ 156.71	...	...	...	...
3493	...	-169.05 $\pm$ 185.52	...	-868.70 $\pm$ 156.80	...
3535	-105.29 $\pm$ 140.17	...	...	...	...
3610	...	-128.75 $\pm$ 158.66	...	...	...
3611	...	...	...	-100.35 $\pm$ 168.94	...
3640	-217.72 $\pm$ 133.67	...	...	...	...

**Table 7**  
(Continued)

$t_0$ (s)	Filter				
	$i$ ( $\mu\text{Jy}$ )	$Z$ ( $\mu\text{Jy}$ )	$Y$ ( $\mu\text{Jy}$ )	$J$ ( $\mu\text{Jy}$ )	$H$ ( $\mu\text{Jy}$ )
3719	...	...	...	...	491.39 $\pm$ 228.38
3721	...	...	11.29 $\pm$ 175.04	...	...
3735	-143.56 $\pm$ 143.25	...	...	...	...
3814	...	...	-144.77 $\pm$ 170.13	...	...
3815	...	...	...	...	476.88 $\pm$ 207.06
3842	-116.80 $\pm$ 128.28	...	...	...	...
3918	...	...	...	-245.69 $\pm$ 183.08	...
3919	...	-282.94 $\pm$ 158.48	...	...	...
3963	-22.03 $\pm$ 123.97	...	...	...	...
4038	...	429.42 $\pm$ 154.41	...	-334.68 $\pm$ 144.00	...
4069	-204.18 $\pm$ 131.80	...	...	...	...
4145	...	...	...	...	294.22 $\pm$ 210.48
4146	...	...	88.92 $\pm$ 159.62	...	...
4171	-43.37 $\pm$ 129.77	...	...	...	...
4247	...	...	...	...	403.42 $\pm$ 206.94
4248	...	...	92.01 $\pm$ 155.91	...	...
4295	-68.97 $\pm$ 114.90	...	...	...	...
4371	...	430.77 $\pm$ 141.70	...	-268.65 $\pm$ 134.35	...
4414	20.95 $\pm$ 113.41	...	...	...	...
4493	...	405.50 $\pm$ 142.94	...	-305.07 $\pm$ 129.43	...
4523	-753.30 $\pm$ 142.08	...	...	...	...
4598	...	...	-62.47 $\pm$ 384.04	...	-379.43 $\pm$ 186.04
4642	128.93 $\pm$ 111.30	...	...	...	...
4718	...	...	68.32 $\pm$ 145.11	...	...
4719	...	...	...	...	193.53 $\pm$ 181.91
4742	13.53 $\pm$ 106.79	...	...	...	...
4821	...	...	...	-34.60 $\pm$ 133.02	...
4822	...	-10.51 $\pm$ 122.19	...	...	...
4846	3.86 $\pm$ 107.35	...	...	...	...
4922	...	...	...	16.76 $\pm$ 130.56	...
4923	...	-1574.14 $\pm$ 86.59	...	...	...
4953	12.21 $\pm$ 106.93	...	...	...	...
5028	...	...	...	...	826.11 $\pm$ 322.54
5032	...	...	216.10 $\pm$ 150.56	...	...
5059	33.37 $\pm$ 106.53	...	...	...	...
5134	...	...	...	...	422.64 $\pm$ 177.33
5135	...	...	270.93 $\pm$ 131.95	...	...
5186	-59.76 $\pm$ 133.88	...	...	...	...
5260	...	...	...	107.47 $\pm$ 126.22	...
5262	...	139.56 $\pm$ 115.97	...	...	...
5287	187.44 $\pm$ 103.88	...	...	...	...
5362	...	402.54 $\pm$ 128.18	...	-101.23 $\pm$ 111.83	...
5394	48.19 $\pm$ 97.91	...	...	...	...
5470	...	...	732.22 $\pm$ 209.78	...	207.25 $\pm$ 125.30
5506	22.50 $\pm$ 97.93	...	...	...	...
5586	...	...	605.06 $\pm$ 160.57	...	124.24 $\pm$ 126.73
5615	165.21 $\pm$ 94.75	...	...	...	...
5690	...	...	...	255.73 $\pm$ 118.96	...
5694	...	-29.63 $\pm$ 109.85	...	...	...
5715	176.93 $\pm$ 92.38	...	...	...	...
5789	...	...	...	338.34 $\pm$ 120.32	...
5790	...	224.85 $\pm$ 106.05	...	...	...
5823	203.43 $\pm$ 90.44	...	...	...	...
5897	...	...	...	...	557.04 $\pm$ 129.97
5898	...	...	112.54 $\pm$ 123.03	...	...
5942	-57.18 $\pm$ 99.26	...	...	...	...
6018	...	...	240.91 $\pm$ 114.64	...	...
6020	...	...	...	...	782.68 $\pm$ 182.53
6050	120.56 $\pm$ 87.90	...	...	...	...
6124	...	...	...	236.29 $\pm$ 108.81	...
6125	...	138.35 $\pm$ 99.38	...	...	...



**Table 8**  
Residuals between Observations and the Power-law Model for RATIR Data for Late Afterglow (After 0.7 days)

$t_0$ (day)	Filter						
	$g$ ( $\mu\text{Jy}$ )	$r$ ( $\mu\text{Jy}$ )	$i$ ( $\mu\text{Jy}$ )	$Z$ ( $\mu\text{Jy}$ )	$Y$ ( $\mu\text{Jy}$ )	$J$ ( $\mu\text{Jy}$ )	$H$ ( $\mu\text{Jy}$ )
0.83	...	$-23.90 \pm 3.62$	$-37.66 \pm 3.51$	$-48.43 \pm 9.07$	$-50.50 \pm 9.44$	$-66.74 \pm 10.87$	$-54.80 \pm 10.22$
0.85	...	$-20.88 \pm 4.07$	$-38.87 \pm 3.49$	$-46.55 \pm 9.88$	$-31.91 \pm 10.33$	$-56.30 \pm 9.97$	$-46.25 \pm 17.28$
0.87	...	$-21.47 \pm 2.53$	$-25.19 \pm 3.31$	$-41.10 \pm 7.91$	$-40.88 \pm 9.58$	$-29.30 \pm 9.93$	$-41.91 \pm 9.72$
0.90	...	$-15.79 \pm 4.17$	$-32.39 \pm 3.86$	$-39.28 \pm 8.21$	$-56.57 \pm 7.43$	$-39.85 \pm 8.11$	$-50.19 \pm 7.82$
0.92	...	$-22.70 \pm 2.79$	$-28.13 \pm 3.29$	$-40.63 \pm 7.88$	$-26.98 \pm 7.88$	$-69.72 \pm 7.39$	$-14.33 \pm 8.76$
0.94	...	$-19.90 \pm 2.81$	$-32.23 \pm 3.14$	$-35.16 \pm 5.39$	$-37.45 \pm 8.05$	$-30.91 \pm 8.56$	$14.00 \pm 8.31$
0.97	...	$-14.07 \pm 3.22$	$-24.73 \pm 3.38$	$-26.06 \pm 6.43$	$-28.58 \pm 7.58$	$-35.32 \pm 7.58$	$-7.64 \pm 7.58$
0.99	...	$-12.95 \pm 3.62$	$-25.80 \pm 2.90$	$-22.56 \pm 7.51$	$-42.19 \pm 6.59$	$-38.27 \pm 7.29$	$10.01 \pm 7.96$
1.01	...	$-7.59 \pm 3.37$	$-26.91 \pm 3.13$	$-21.96 \pm 7.38$	$-30.36 \pm 7.26$	$-21.45 \pm 7.40$	$-17.75 \pm 7.80$
1.04	...	$-10.58 \pm 3.01$	$-20.13 \pm 3.02$	$-18.67 \pm 9.83$	$-30.09 \pm 7.18$	$-22.21 \pm 8.67$	$-25.60 \pm 10.30$
1.06	...	$-15.91 \pm 3.58$	$-19.59 \pm 3.08$	$-40.60 \pm 8.52$	$-25.47 \pm 7.58$	$-16.84 \pm 9.29$	$-5.48 \pm 10.43$
1.83	...	$-1.14 \pm 1.17$	$-2.56 \pm 1.76$	$3.03 \pm 4.45$	$6.59 \pm 4.86$	$-8.12 \pm 7.28$	$10.77 \pm 8.73$
1.85	...	$-2.12 \pm 1.08$	$-2.66 \pm 1.67$	$-5.28 \pm 3.94$	$5.02 \pm 5.26$	$-3.83 \pm 6.66$	$0.36 \pm 8.23$
1.87	...	$-1.21 \pm 1.19$	$-1.91 \pm 1.62$	$-7.42 \pm 4.18$	$4.85 \pm 5.26$	$-7.31 \pm 6.44$	$12.60 \pm 8.85$
1.89	...	$0.36 \pm 0.86$	$-2.55 \pm 1.24$	$-0.80 \pm 3.64$	$1.51 \pm 4.21$	$-9.33 \pm 5.33$	$21.06 \pm 7.82$
1.91	...	$-2.19 \pm 1.04$	$-2.26 \pm 1.60$	$-1.96 \pm 3.56$	$3.04 \pm 4.33$	$-4.08 \pm 5.43$	$3.01 \pm 6.82$
1.93	...	$-1.24 \pm 1.32$	$-2.41 \pm 1.59$	$-0.62 \pm 3.54$	$0.67 \pm 4.26$	$-3.65 \pm 5.17$	$16.87 \pm 7.51$
1.96	...	$0.51 \pm 1.52$	$-1.73 \pm 1.48$	$2.56 \pm 3.65$	$4.93 \pm 4.65$	$-3.31 \pm 7.80$	$19.87 \pm 6.70$
1.98	...	$-1.38 \pm 1.62$	$-0.24 \pm 1.41$	$-5.77 \pm 3.98$	$13.89 \pm 4.77$	$1.87 \pm 5.53$	$43.92 \pm 10.52$
2.00	...	$-2.54 \pm 1.24$	$1.08 \pm 1.59$	$6.36 \pm 4.22$	$-3.77 \pm 4.65$	$-5.57 \pm 5.55$	$35.66 \pm 7.94$
2.02	...	$-2.07 \pm 1.33$	$0.57 \pm 1.47$	...	...	$5.51 \pm 6.66$	$10.72 \pm 9.75$
2.03	...	...	...	$3.21 \pm 4.22$	$-3.50 \pm 5.05$	...	...
2.04	...	$-0.80 \pm 1.60$	$-1.18 \pm 1.93$	...	...	$5.76 \pm 7.21$	$31.37 \pm 11.22$
2.83	...	$0.04 \pm 0.68$	$-1.22 \pm 1.01$	$5.82 \pm 2.89$	$13.99 \pm 4.88$	$-3.86 \pm 6.33$	$22.36 \pm 8.99$
2.85	...	$1.91 \pm 1.01$	$0.51 \pm 1.14$	$-0.35 \pm 3.12$	$10.05 \pm 4.87$	$2.82 \pm 7.44$	$5.39 \pm 11.54$
2.87	...	$2.22 \pm 0.70$	$0.25 \pm 0.99$	$3.65 \pm 2.81$	$17.59 \pm 5.00$	$-1.42 \pm 5.62$	$19.63 \pm 8.72$
2.89	...	$1.50 \pm 0.81$	$0.05 \pm 0.88$	$5.80 \pm 2.37$	$-2.79 \pm 3.37$	$-6.73 \pm 4.70$	$6.42 \pm 6.93$
2.91	...	$0.41 \pm 0.78$	$-0.30 \pm 0.93$	$-2.00 \pm 2.60$	$2.25 \pm 3.87$	$-1.02 \pm 4.80$	$9.47 \pm 7.36$
2.93	...	$0.20 \pm 0.96$	$-0.41 \pm 0.94$	$-0.22 \pm 2.62$	$2.15 \pm 5.01$	$2.52 \pm 4.73$	$23.24 \pm 7.61$
2.95	...	$0.07 \pm 0.97$	$-0.34 \pm 0.97$	$4.08 \pm 2.62$	$10.02 \pm 4.21$	$6.05 \pm 4.63$	$14.62 \pm 7.89$
2.97	...	$-0.39 \pm 0.81$	$-0.72 \pm 0.98$	$-0.90 \pm 2.91$	$5.18 \pm 4.19$	$-0.48 \pm 4.68$	$32.10 \pm 8.50$
2.99	...	$0.64 \pm 0.94$	$2.30 \pm 1.04$	$-2.29 \pm 2.99$	$9.74 \pm 4.75$	$2.42 \pm 5.21$	$8.66 \pm 9.56$
3.02	...	$-2.13 \pm 0.81$	$3.50 \pm 1.16$	$0.04 \pm 2.88$	$9.46 \pm 4.54$	$6.81 \pm 5.12$	$20.49 \pm 9.20$
3.04	...	$2.05 \pm 1.00$	$-0.43 \pm 1.02$	$0.30 \pm 3.10$	$4.02 \pm 4.53$	$0.98 \pm 5.47$	$21.31 \pm 9.52$
3.82	...	$-0.42 \pm 0.82$	$0.05 \pm 0.87$	...	...	...	...
3.84	...	$1.05 \pm 0.72$	$1.35 \pm 0.80$	...	...	...	...
3.86	...	$1.65 \pm 0.67$	$0.46 \pm 0.69$	...	...	...	...
3.88	...	$0.38 \pm 0.63$	$0.40 \pm 0.76$	...	...	...	...
3.90	...	$0.15 \pm 0.75$	$-0.69 \pm 0.74$	...	...	...	...
3.92	...	$1.34 \pm 0.67$	$0.73 \pm 0.80$	...	...	...	...
3.94	...	$0.52 \pm 0.76$	$0.61 \pm 0.75$	...	...	...	...
3.96	...	$0.13 \pm 0.62$	$0.59 \pm 0.68$	...	...	...	...
3.97	...	$1.37 \pm 0.69$	$2.55 \pm 0.82$	...	...	...	...
4.00	...	$0.42 \pm 0.65$	$0.31 \pm 0.66$	...	...	...	...
4.01	...	$2.02 \pm 0.71$	$2.76 \pm 0.75$	...	...	...	...
4.03	...	$0.88 \pm 0.75$	$0.02 \pm 0.86$	...	...	...	...
5.03	$-1.51 \pm 0.81$	$-2.30 \pm 0.95$	$1.03 \pm 0.84$	...	...	...	...
5.94	...	$1.83 \pm 0.33$	...	...	...	...	...
5.95	...	...	$1.78 \pm 0.35$	$0.08 \pm 0.90$	$1.67 \pm 1.29$	$7.04 \pm 1.60$	$3.14 \pm 2.62$
5.97	$-0.46 \pm 0.24$	...	...	...	...	...	...
6.93	$0.53 \pm 0.22$	...	$1.75 \pm 0.33$	$3.24 \pm 0.89$	$1.94 \pm 1.35$	$8.00 \pm 2.36$	$0.91 \pm 2.76$
7.94	$0.45 \pm 0.26$	...	$1.42 \pm 0.35$	...	...	...	...
7.95	...	...	...	$2.07 \pm 1.01$	$5.42 \pm 1.54$	$10.57 \pm 2.09$	$24.92 \pm 3.36$
9.96	$0.51 \pm 0.23$	...	$2.37 \pm 0.36$	$3.07 \pm 1.16$	$3.25 \pm 1.72$	$2.34 \pm 2.31$	$-20.23 \pm 3.90$
10.91	...	$2.27 \pm 0.90$	...	...	...	...	...
10.93	$0.22 \pm 0.62$	...	$2.48 \pm 0.38$	$0.63 \pm 1.11$	$3.45 \pm 1.77$	$9.80 \pm 2.97$	...
11.93	$1.31 \pm 0.23$	$2.76 \pm 0.29$	$2.69 \pm 0.23$	$2.05 \pm 0.67$	$1.99 \pm 1.01$	$-0.66 \pm 1.35$	$3.62 \pm 2.13$
12.91	$1.68 \pm 0.23$	$3.14 \pm 0.31$	$3.28 \pm 0.26$	$3.37 \pm 0.76$	$4.80 \pm 1.19$	$5.42 \pm 1.69$	$-10.94 \pm 2.49$
13.91	$1.77 \pm 0.21$	$3.02 \pm 0.32$	$2.67 \pm 0.24$	$1.70 \pm 0.73$	$3.44 \pm 1.17$	$8.17 \pm 1.60$	$-11.87 \pm 2.51$
14.90	...	$3.59 \pm 0.30$	...	...	...	...	...
14.91	...	...	$3.15 \pm 0.23$	$2.43 \pm 0.67$	$4.01 \pm 1.01$	$6.37 \pm 1.39$	$5.74 \pm 2.11$
14.92	$1.89 \pm 0.21$	...	...	...	...	...	...
15.89	...	$3.18 \pm 0.33$	...	...	...	...	...

**Table 8**  
(Continued)

$t_0$ (day)	Filter						
	$g$ ( $\mu\text{Jy}$ )	$r$ ( $\mu\text{Jy}$ )	$i$ ( $\mu\text{Jy}$ )	$Z$ ( $\mu\text{Jy}$ )	$Y$ ( $\mu\text{Jy}$ )	$J$ ( $\mu\text{Jy}$ )	$H$ ( $\mu\text{Jy}$ )
15.90	...	...	$2.86 \pm 0.25$	$2.86 \pm 0.77$	$2.85 \pm 1.14$	$0.35 \pm 1.55$	$-4.27 \pm 2.23$
15.91	$2.21 \pm 0.25$	...	...	...	...	...	...
16.91	$2.23 \pm 0.28$	$4.15 \pm 0.36$	$3.52 \pm 0.28$	$3.38 \pm 0.82$	$2.10 \pm 1.45$	$0.30 \pm 1.85$	...
17.91	...	$3.91 \pm 0.41$	...	...	...	...	...
17.93	...	...	$3.77 \pm 0.33$	$2.45 \pm 0.97$	$0.61 \pm 1.57$	...	...
17.94	$1.98 \pm 0.34$	...	...	...	...	...	...
18.92	$1.94 \pm 0.25$	$3.12 \pm 0.31$	$3.55 \pm 0.25$	$4.14 \pm 0.70$	$4.46 \pm 1.12$	$6.55 \pm 1.47$	...
19.91	$1.91 \pm 0.26$	$3.26 \pm 0.37$	$3.60 \pm 0.28$	$3.51 \pm 0.80$	$3.64 \pm 1.34$	$1.20 \pm 1.55$	...
20.91	...	$3.40 \pm 0.42$	$3.91 \pm 0.34$	...	...	...	...
20.92	$1.21 \pm 0.36$	...	...	$5.55 \pm 0.96$	$3.31 \pm 1.38$	$1.71 \pm 1.84$	...
21.92	$1.24 \pm 0.37$	$3.10 \pm 0.42$	$3.47 \pm 0.37$	$5.00 \pm 1.11$	$2.32 \pm 1.35$	$-0.34 \pm 1.68$	...
22.91	...	$3.35 \pm 0.39$	...	...	...	...	...
22.92	...	...	$3.45 \pm 0.27$	...	...	...	...
22.93	$2.34 \pm 0.30$	...	...	...	...	...	...
23.91	$2.17 \pm 0.39$	$3.15 \pm 0.47$	$3.69 \pm 0.31$	...	...	...	...
24.99	...	$-0.16 \pm 1.02$	$3.45 \pm 1.08$	...	...	...	...
25.90	...	$2.42 \pm 0.51$	...	...	...	...	...
25.91	...	...	$3.61 \pm 0.38$	$-4.18 \pm 1.03$	$2.79 \pm 1.60$	...	...
25.92	$1.59 \pm 0.48$	...	...	...	...	...	...
26.91	$-2.20 \pm 0.00$	...	...	...	...	...	...
26.92	...	$2.28 \pm 0.48$	$4.08 \pm 0.36$	$3.20 \pm 1.06$	$-0.28 \pm 1.46$	$7.28 \pm 1.94$	...
27.90	...	$3.38 \pm 0.55$	...	...	...	...	...
27.91	...	...	$3.24 \pm 0.37$	$-2.79 \pm 0.92$	$0.36 \pm 1.43$	...	...
27.92	$1.29 \pm 0.54$	...	...	...	...	...	...
28.90	...	$1.89 \pm 0.44$	...	...	...	...	...
28.91	...	...	$3.58 \pm 0.33$	$-3.49 \pm 0.86$	$1.02 \pm 1.28$	...	...
28.92	$1.35 \pm 0.43$	...	...	...	...	...	...
29.92	...	$2.69 \pm 0.47$	...	...	...	...	...
29.93	...	...	$2.77 \pm 0.39$	$-4.62 \pm 1.08$	...	...	...
29.94	$0.93 \pm 0.43$	...	...	...	...	...	...
30.91	$0.54 \pm 0.44$	$0.75 \pm 0.44$	$3.01 \pm 0.36$	$0.75 \pm 0.99$	$-0.19 \pm 1.52$	...	...
31.90	$0.80 \pm 0.30$	$0.88 \pm 0.36$	$2.91 \pm 0.32$	...	...	...	...
31.91	...	...	...	$0.64 \pm 1.01$	$3.11 \pm 1.50$	...	...
32.90	$0.55 \pm 0.33$	...	...	...	...	...	...
32.91	...	$0.83 \pm 0.40$	$3.04 \pm 0.37$	$0.13 \pm 1.13$	...	...	...
33.90	$0.75 \pm 0.21$	...	...	...	...	...	...
33.91	...	$1.06 \pm 0.70$	$2.70 \pm 0.23$	...	...	...	...
34.89	$0.70 \pm 0.21$	...	...	...	...	...	...
34.90	...	...	$2.67 \pm 0.24$	...	...	...	...
35.90	$0.11 \pm 0.22$	$1.57 \pm 1.07$	$2.28 \pm 0.22$	...	...	...	...
36.89	...	$-2.36 \pm 0.58$	...	...	...	...	...
36.90	...	...	$2.47 \pm 0.28$	...	...	...	...
38.88	...	$1.01 \pm 0.37$	...	...	...	...	...
38.89	...	...	$1.83 \pm 0.31$	$-0.93 \pm 6.74$	...	...	...
38.90	$-0.07 \pm 0.26$	...	...	...	...	...	...
39.90	...	$0.80 \pm 0.27$	$2.06 \pm 0.23$	...	$-0.16 \pm 0.71$	...	$-0.89 \pm 1.43$
42.92	...	...	$3.12 \pm 2.86$	$-1.66 \pm 1.02$	...	...	...
44.88	$0.29 \pm 0.19$	...	$1.64 \pm 0.27$	...	...	...	...
46.89	...	$0.62 \pm 0.35$	$1.47 \pm 0.41$	...	...	...	...
50.87	$0.22 \pm 0.34$	...	$0.40 \pm 0.43$	...	...	...	...
51.88	...	$-0.20 \pm 0.34$	$0.88 \pm 0.38$	...	$1.95 \pm 1.12$	...	...
52.90	...	...	$1.34 \pm 0.55$	...	...	...	...
53.88	...	$1.59 \pm 0.44$	$1.40 \pm 0.45$	...	$0.69 \pm 1.10$	...	...
54.88	$0.94 \pm 0.56$	...	$0.70 \pm 0.43$	...	$2.76 \pm 1.74$	...	...
56.88	...	$-0.97 \pm 0.91$	$1.91 \pm 0.53$	...	$0.39 \pm 1.28$	...	...
57.87	...	...	$-0.04 \pm 0.63$	...	...	...	...
58.87	...	$0.32 \pm 0.47$	$1.10 \pm 0.49$	...	$1.26 \pm 1.13$	...	...
59.87	$-0.21 \pm 0.25$	...	$1.20 \pm 0.42$	...	...	...	...
65.86	$0.38 \pm 0.34$	...	$0.85 \pm 0.49$	...	...	...	...
66.86	...	$-0.66 \pm 0.59$	$0.77 \pm 0.66$	...	...	...	...
215.15	...	$0.06 \pm 0.29$	$0.11 \pm 0.33$	...	...	...	...
217.15	$-0.02 \pm 0.19$	...	$-0.04 \pm 0.28$	$-0.87 \pm 0.87$	...	...	...
219.14	...	$-0.02 \pm 0.23$	$0.47 \pm 0.26$	$1.51 \pm 0.86$	...	...	...

**Table 8**  
(Continued)

$t_0$ (day)	Filter						
	$g$ ( $\mu\text{Jy}$ )	$r$ ( $\mu\text{Jy}$ )	$i$ ( $\mu\text{Jy}$ )	$Z$ ( $\mu\text{Jy}$ )	$Y$ ( $\mu\text{Jy}$ )	$J$ ( $\mu\text{Jy}$ )	$H$ ( $\mu\text{Jy}$ )
221.11	$0.21 \pm 0.32$	...	$0.16 \pm 0.59$	...	...	...	...
223.14	...	$0.13 \pm 0.25$	$0.67 \pm 0.30$	$1.42 \pm 0.94$	...	...	...
229.14	$0.07 \pm 0.17$	...	$0.53 \pm 0.25$	$-0.50 \pm 0.80$	...	...	...
231.13	...	$0.92 \pm 0.31$	$0.51 \pm 0.41$	...	...	...	...
303.53	...	...	...	$-0.64 \pm 0.39$	$1.17 \pm 0.56$	$1.96 \pm 0.70$	$1.49 \pm 1.20$
306.52	...	$0.18 \pm 0.15$	...	...	...	...	...
314.00	...	...	$-0.09 \pm 0.09$	...	...	...	...
353.44	$0.04 \pm 0.09$	...	...	...	...	...	...
1152.86	...	$-0.01 \pm 0.00$	...	...	...	...	...
1153.36	...	...	$-0.02 \pm 0.19$	$0.03 \pm 0.54$	$-0.02 \pm 0.72$	$0.09 \pm 1.12$	$5.53 \pm 7.37$
1153.85	$-0.01 \pm 0.00$	...	...	...	...	...	...

Johnson Telescope of the Observatorio Astronómico Nacional in Sierra San Pedro Mártir, and the operation of both are funded through NASA grants NNX09AH71G, NNX09AT02G, NNX10AI27G, and NNX12AE66G, CONACyT grants INFR-2009-01-122785 and CB-2008-101958, UNAM PAPIIT grants IG100414 and IA102917, UC MEXUS-CONACyT grant CN 09-283, and the Instituto de Astronomía of the Universidad Nacional Autónoma de México.

### References

- Ackermann, M., Ajello, M., Asano, K., et al. 2014, *Sci*, **343**, 42
- Barthelmy, S. D., Baumgartner, W. H., Cummings, J. R., et al. 2013, GCN, **14470**, 1
- Becker, A. 2015, HOTPANTS: High Order Transform of PSF AND Template Subtraction, Astrophysics Source Code Library, ascl:1504.004
- Berger, E., Chornock, R., Holmes, T. R., et al. 2011, *ApJ*, **743**, 204
- Berger, E., Fox, D. B., Cucchiara, A., & Cenko, S. B. 2008, GCN, **8335**, 1
- Bersier, D. 2012, arXiv:1206.6979
- Bloom, J. S., Kulkarni, S. R., Price, P. A., et al. 2002, *ApJL*, **572**, L45
- Bufano, F., Pian, E., Sollerman, J., et al. 2012, *ApJ*, **753**, 67
- Butler, N., Klein, C., Fox, O., et al. 2012, *Proc. SPIE*, **8446**, 844610
- Campana, S., Mangano, V., Blustin, A. J., et al. 2006, *Natur*, **442**, 1008
- Cano, Z., Bersier, D., Guidorzi, C., et al. 2011, *ApJ*, **740**, 41
- Cano, Z., de Ugarte Postigo, A., Perley, D., et al. 2015, *MNRAS*, **452**, 1535
- Chornock, R., Berger, E., Levesque, E. M., et al. 2010, arXiv:1004.2262
- Clocchiatti, A., Suntzeff, N. B., Covarrubias, R., & Candia, P. 2011, *AJ*, **141**, 163
- Cobb, B. E., Bloom, J. S., Perley, D. A., et al. 2010, *ApJL*, **718**, L150
- D'Elia, V., Pian, E., Melandri, A., et al. 2015, *A&A*, **577**, A116
- de Ugarte Postigo, A., Xu, D., Leloudas, G., et al. 2013, GCN, **14646**, 1
- Della Valle, M., Benetti, S., Mazzali, P., et al. 2008, *CBET*, **1602**, 1
- Della Valle, M., Malesani, D., Benetti, S., et al. 2003, *A&A*, **406**, L33
- Della Valle, M., Malesani, D., Bloom, J. S., et al. 2006, *ApJL*, **642**, L103
- Eichler, D., Livio, M., Piran, T., & Schramm, D. N. 1989, *Natur*, **340**, 126
- Ferrero, P., Kann, D. A., Zeh, A., et al. 2006, *A&A*, **457**, 857
- Flores, H., Covino, S., Xu, D., et al. 2013, GCN, **14491**, 1
- Foley, S., Watson, D., Gorosabel, J., et al. 2006, *A&A*, **447**, 891
- Fox, O. D., Kutryev, A. S., Rapchun, D. A., et al. 2012, *Proc. SPIE*, **8453**, 845310
- Fraija, N. 2015, *ApJ*, **804**, 105
- Fraija, N., Lee, W., & Veres, P. 2016, *ApJ*, **818**, 190
- Fraija, N., Lee, W., Veres, P., & Barniol Duran, R. 2016, *ApJ*, **831**, 22
- Fruchter, A. S., Levan, A. J., Strolger, L., et al. 2006, *Natur*, **441**, 463
- Fynbo, J. U., Holland, S., Andersen, M. I., et al. 2000, *ApJL*, **542**, L89
- Galama, T. J., Vreeswijk, P. M., van Paradijs, J., et al. 1998, *Natur*, **395**, 670
- Gal-Yam, A., Moon, D.-S., Fox, D. B., et al. 2004, *ApJL*, **609**, L59
- Garnavich, P. M., Stanek, K. Z., Wyrzykowski, L., et al. 2003, *ApJ*, **582**, 924
- Gavazzi, G., Fumagalli, M., Cucchiari, O., & Boselli, A. 2010, *A&A*, **517**, A73
- Greiner, J., Klose, S., Reinsch, K., et al. 2003, *Natur*, **426**, 157
- Hammer, F., Flores, H., Schaefer, D., et al. 2006, *A&A*, **454**, 103
- Hjorth, J. 2013, *RSPTA*, **371**, 20120275
- Hjorth, J., & Bloom, J. S. 2012, in *Gamma-Ray Bursts*, ed. C. Kouveliotou, R. A. M. J. Wijers, & S. Woosley (Cambridge: Cambridge Univ. Press)
- Koshut, T. M., Paciesas, W. S., Kouveliotou, C., et al. 1995, *BAAS*, **27**, 53.01
- Kouveliotou, C., Meegan, C. A., Fishman, G. J., et al. 1993, *ApJL*, **413**, L101
- Kumar, P., & Piran, T. 2000, *ApJ*, **532**, 286
- Kumar, P., & Zhang, B. 2015, *PhR*, **561**, 1
- Lang, D., Hogg, D. W., Mierle, K., Blanton, M., & Roweis, S. 2010, *AJ*, **139**, 1782
- Lattimer, J. M., & Schramm, D. N. 1976, *ApJ*, **210**, 549
- Lee, W. H., & Ramirez-Ruiz, E. 2007, *NJPh*, **9**, 17
- Levan, A. J., Cenko, S. B., Perley, D. A., & Tanvir, N. R. 2013, GCN, **14455**, 1
- Levan, A. J., Tanvir, N. R., Fruchter, A. S., et al. 2014, *ApJ*, **792**, 115
- Littlejohns, O. M., Butler, N. R., Cucchiara, A., et al. 2015, *MNRAS*, **449**, 2919
- MacFadyen, A. I., & Woosley, S. E. 1999, *ApJ*, **524**, 262
- Malesani, D., Tagliaferri, G., Chincarini, G., et al. 2004, *ApJL*, **609**, L5
- Maselli, A., Melandri, A., Nava, L., et al. 2014, *Sci*, **343**, 48
- Matheson, T., Garnavich, P. M., Stanek, K. Z., et al. 2003, *ApJ*, **599**, 394
- Melandri, A., Pian, E., D'Elia, V., et al. 2014, *A&A*, **567**, A29
- Melandri, A., Pian, E., Ferrero, P., et al. 2012, *A&A*, **547**, A82
- Mirabal, N., Halpern, J. P., An, D., Thorstensen, J. R., & Terndrup, D. M. 2006, *ApJL*, **643**, L99
- Modjaz, M. 2011, *AN*, **332**, 434
- Modjaz, M., Kewley, L., Kirshner, R. P., et al. 2008, *AJ*, **135**, 1136
- Nakar, E. 2007, *PhR*, **442**, 166
- Narayan, R., Paczynski, B., & Piran, T. 1992, *ApJL*, **395**, L83
- Niino, Y. 2013, in *EAS Publications Ser. 61 Gamma-ray Bursts: 15 Years of GRB Afterglows*, ed. A. J. Castro-Tirado et al. (Les Ulis: EDP Sciences), **427**
- Olivares, E. F., Greiner, J., Schady, P., et al. 2012, *A&A*, **539**, A76
- Paczynski, B. 1989, *ApJL*, **308**, L43
- Paczynski, B. 1991, *AcA*, **41**, 257
- Perley, D. A., Cenko, S. B., Corsi, A., et al. 2014, *ApJ*, **781**, 37
- Pian, E., Mazzali, P. A., Masetti, N., et al. 2006, *Natur*, **442**, 1011
- Planck Collaboration, Ade, P. A. R., Aghanim, N., et al. 2014, *A&A*, **571**, A1
- Sari, R., & Piran, T. 1998
- Sari, R., & Piran, T. 1999, *ApJ*, **520**, 641
- Schulze, S., Malesani, D., Cucchiara, A., et al. 2014, *A&A*, **566**, A102
- Soderberg, A., Berger, E., & Fox, D. 2008, GCN, **8662**, 1
- Stanek, K. Z., Matheson, T., Garnavich, P. M., et al. 2003, *ApJL*, **591**, L17
- Starling, R. L. C., Wiersema, K., Levan, A. J., et al. 2011, *MNRAS*, **411**, 2792
- Tam, P.-H. T., Tang, Q.-W., Hou, S.-J., Liu, R.-Y., & Wang, X.-Y. 2013, *ApJL*, **771**, L13
- Thomsen, B., Hjorth, J., Watson, D., et al. 2004, *A&A*, **419**, L21
- Tinney, C., Stathakis, R., Cannon, R., et al. 1998, *IAUC*, **6896**, 1
- Toy, V. L., Cenko, S. B., Silverman, J. M., et al. 2015, arXiv:1508.00575
- Vestrand, W. T., Wren, J. A., Panaitescu, A., et al. 2014, *Sci*, **343**, 38
- Vonova, A., Elenin, L., & Pozanenko, A. 2013, GCN, **14516**, 1
- von Kienlin, A. 2013, GCN, **14473**, 1
- Watson, A. M., Butler, N., Kutryev, A., et al. 2013, GCN, **14666**, 1
- Watson, A. M., Richer, M. G., Bloom, J. S., et al. 2012, *Proc. SPIE*, **8444**, 84445L
- Woosley, S. E. 1993, *ApJ*, **405**, 273
- Woosley, S. E., & Bloom, J. S. 2006, *ARA&A*, **44**, 507
- Xu, D., de Ugarte Postigo, A., Leloudas, G., et al. 2013a, *ApJ*, **776**, 98
- Xu, D., de Ugarte Postigo, A., Schulze, S., et al. 2013b, GCN, **14478**, 1



## Erratum: “Photometric Observations of Supernova 2013cq Associated with GRB 130427A (2017, APJ, 837, 116)”

R. L. Becerra<sup>1</sup>, A. M. Watson<sup>1</sup>, W. H. Lee<sup>1</sup>, N. Fraija<sup>1</sup>, N. R. Butler<sup>2</sup>, J. S. Bloom<sup>3</sup>, J. I. Capone<sup>4</sup>, A. Cucchiara<sup>5</sup>, J. A. de Diego<sup>1</sup>, O. D. Fox<sup>6</sup>, N. Gehrels<sup>7</sup>, L. N. Georgiev<sup>1</sup>, J. J. González<sup>1</sup>, A. S. Kutuyev<sup>7</sup>, O. M. Littlejohns<sup>2</sup>, J. X. Prochaska<sup>8</sup>, E. Ramirez-Ruiz<sup>8</sup>, M. G. Richer<sup>9</sup>, C. G. Román-Zúñiga<sup>9</sup>, V. L. Toy<sup>4</sup>, and E. Troja<sup>4,7</sup>

<sup>1</sup>Instituto de Astronomía, Universidad Nacional Autónoma de México, Apartado Postal 70-264, 04510 México, D. F., México

<sup>2</sup>School of Earth and Space Exploration, Arizona State University, Tempe, AZ 85287, USA

<sup>3</sup>Department of Astronomy, University of California, Berkeley, CA 94720-3411, USA

<sup>4</sup>Department of Astronomy, University of Maryland, College Park, MD 20742, USA

<sup>5</sup>NASA Postdoctoral Program Fellow, Goddard Space Flight Center, Greenbelt, MD 20771, USA

<sup>6</sup>Space Telescope Science Institute, 3700 San Martin Drive, Baltimore, MD 21218, USA

<sup>7</sup>NASA, Goddard Space Flight Center, Greenbelt, MD 20771, USA

<sup>8</sup>Department of Astronomy and Astrophysics, UCO/Lick Observatory, University of California, 1156 High Street, Santa Cruz, CA 95064, USA

<sup>9</sup>Instituto de Astronomía, Universidad Nacional Autónoma de México, Apartado Postal 106, 22800 Ensenada, Baja California, México

Received 2017 May 17; published 2017 June 14

Supporting material: machine-readable table

### Appendix

- (1) In of Table 6,  $t_f$  is stated as being in seconds, but the values are actually in days.
- (2) There is an error in our code to generate Table 6 that caused the column with the uncertainties in the aperture photometry to be incorrect. This error has no effect on the other columns in the table, on the figures, or on our analysis.

**Table 6**  
Photometry of GRB 130427A

$t_0$ (d)	$t_0$ (s)	$t_e$ (s)	$t_f$ (d)	Filter	$m$ (AB)	Flux ( $\mu$ Jy) (PSF)
0.01	930	80	0.01	<i>i</i>	12.88 $\pm$ 0.02	
0.01	1009	67	0.01	<i>Z</i>	12.75 $\pm$ 0.02	
0.01	1012	67	0.01	<i>J</i>	12.69 $\pm$ 0.02	
0.01	1037	80	0.01	<i>i</i>	12.97 $\pm$ 0.02	
0.01	1111	67	0.01	<i>H</i>	12.86 $\pm$ 0.02	
0.01	1114	67	0.01	<i>Y</i>	12.77 $\pm$ 0.02	
0.01	1141	80	0.01	<i>i</i>	13.12 $\pm$ 0.02	
0.01	1216	67	0.01	<i>Y</i>	12.88 $\pm$ 0.02	
0.01	1216	67	0.01	<i>H</i>	13.00 $\pm$ 0.02	
0.01	1249	80	0.02	<i>i</i>	13.24 $\pm$ 0.02	

**Note.** Table 6 is published in its entirety in the electronic edition of the *Astrophysical Journal*. A portion is shown here for guidance regarding its form and content.

(This table is available in its entirety in machine-readable form.)

## Chapter 5

# Conclusions

The main goal of this work was the study of the optical prompt emission and early optical afterglow emission from GRBs using the telescope COATLI. The data obtained during these months adds excellent photometry of several events to a current sample which is not very large as was discussed in § 4. Through this work, it was possible the understanding of the physical processes involved into the early phases of some gamma-ray burst. Moreover, we have compared with X-ray data in two cases (GRB 180205A and GRB 180418A) in order to explain the origin of each component.

Works presented in this thesis have been published in international journals. We can summarize the main results of each one:

- **GRB180205A**

We presented optical photometry of the afterglow of GRB 180205A with the COATLI telescope and interim instrument ([Watson et al. 2016](#)). COATLI received an automated alert at  $T + 206.3$  seconds, and its quick response allowed us to obtain photometry of the early afterglow from  $T + 217.0$  seconds, only 10.7 seconds after the alert.

We compared the optical light curve from COATLI with the X-rays light curve from XRT. We see an early X-ray flare from the start of the observations at  $T + 163$  seconds, with a peak at about  $T + 188$  seconds, and lasting until about  $T + 260$  seconds. The X-ray flare that does not have a detectable optical counterpart flare; the early optical light curve shows a plateau to about  $T + 454$  seconds. The flare and plateau are followed by a normal decay in both X-rays and the optical.

We compare the data to the predictions of models. We find that the normal decay of the afterglow is most convincingly explained as a forward shock against a surrounding homogeneous ISM rather than against a remnant stellar wind. The properties of the flare cannot be easily explained by reverse shock emission, neutron-proton decoupling, or a two-component jet. The flare is most consistently explained by late activity of the central engine; this can explain the fast rise and fall and the absence of an optical counterpart flare.

Our observations of GRB 180205A add photometric probes to the early evolution of optical light curves of GRB and let us analyze the transition from the prompt phase to the early afterglow comparing with the fireball model. While earlier observations give hints of the range of behavior in this transition, we think it is fair to say that observations have not yet really been able to provide strong guidance for theory due to the small sample of early data (dozens) compared with late afterglow detections (thousands). Over the next few years, we plan to use the COATLI telescope to conduct early follow-up observations of GRBs discovered by the *Neil Gehrels Swift Observatory*, and anticipate that these efforts will expand our empirical understanding of this important area.

- **GRB180418A**

We presented photometric data and analysis to GRB 180418A. The scientific results reported in this article are based on observations made by TAROT and RATIR instruments. We presented several arguments linking GRB 180418A to the class of SGRBs. We explain the early and late light curve from the standard fireball scenario with using a forward and reverse components. We find typical values to describe it.

In contrast with another previous SGRBs, the reverse shock component is present in GRB 180418A, with a peak emission at  $T + 35$  seconds.

From the total fit, we also calculated the microphysical parameters for GRB 180418A.

There is not a clear association with a host galaxy. The nearest galaxies to GRB 180418A have projected distances five times larger than the expected in these cases. Then, using a photometry of the fourth night after the trigger, we have an upper limit of  $r > 24$  and can constrain the angular distance in less than 3 arcseconds from GRB. The faintness of this hypothetical host galaxy is such that we do not detect it.

Assuming a typical redshift of  $z=0.5$  it is possible estimate the isotropic energy of GRB 180418A  $E_{\text{iso}}=0.77 \times 10^{51}$ erg, which is a typical value for SGRBs. We did not detect a temporal break in the afterglow light curve of the short GRB 180418A and therefore, we can give a lower limit for the angular jet of  $\theta_j > 7^\circ$  based in the non observation of a break up to time  $t < 10^5$ s, the photometric redshift of the host galaxy and the isotropic energy calculated.

Photometry presented in this work of GRB 180205A add to our understanding of the early stages of GRB, particularly of short GRBs, the first evidence and analysis of a reverse shock component for this kind of events.

- **GRB130427A** (Becerra et al. 2017)

We have presented homogeneous *griZYJH* photometry of the afterglow of GRB 130427A. We fit the data on the first night with a simple power-law component and the data on later nights with power-law and host galaxy components. Our data and analysis complements the work of Perley et al. (2014) and Melandri et al. (2014) on an inhomogeneous data set. Their data have better temporal coverage, but suffer from systematic possible errors when comparing observations with different instruments as is shown in Figures 2 to 5 in Becerra et al. (2017). Thus, they were better able to study the afterglow over the first couple of days and show the existence of a temporal break at about 0.7 days. Our data, on the other hand, are better suited to looking for deviations from simple power-law model at later times.

Using the values reported of GRB130427A and typical values of the microphysical parameters, we have shown that the Y-band light curve is consistent with the analytical synchrotron forward shock model in the slow cooling regime shown in Gao et al. (2013).

The temporal index of the power-law components changes from 0.97 at  $t < 0.7$  day to 1.36 at  $t > 0.7$  day, in agreement with the values and temporal break around 0.7 days determined by Maselli et al. (2014) and Perley et al. (2014).

The color and absolute magnitude of the host suggest that it is a blue, star-forming galaxy.

Positive residuals to the fits in *griZYJ* between about 7 and 40 days show that we are seeing the photometric signature of SN 2013cq, previously detected spectroscopically by de Ugarte

Postigo et al. (2013) and Xu et al. (2013) and hinted at photometrically by Watson et al. (2013). The absolute magnitude and broad-band spectrum of the supernova are consistent with those of the prototype SN 1998bw and suggest similar progenitors.

This thesis provides a little step in achieving a total understanding of GRBs. Specially, it would be necessary to combine the photometry with more studies, specially including polarization and numerical simulations to explain in detail the physics of the central engine and the prompt emission. Nevertheless, this dissertation helps to improve the total knowledge about the radiation mechanisms and therefore, it gives us clues of the progenitors and they bring us closer to realistic model of GRBs.

This thesis is a proof that to reach a better physical model of gamma-ray bursts, we need to work for increasing the sample of early events.



# References

- Abbott, B. P., Abbott, R., Abbott, T. D., et al. 2016, *Physical Review Letters*, 116, 061102
- Abbott, B. P., Abbott, R., Abbott, T. D., et al. 2017, *Physical Review Letters*, 119, 161101
- Abbott, B. P., Abbott, R., Abbott, T. D., et al. 2017, *ApJ*, 848, L12
- Abbott, B. P., Abbott, R., Abbott, T. D., et al. 2017, *ApJ*, 850, L39.
- Ackermann, M., Ajello, M., Asano, K., et al. 2014, *Science*, 343, 42
- Arnett, W. D. 1982, *ApJ*, 253, 785
- Band, D., Matteson, J., Ford, L., et al. 1993, *ApJ*, 413, 281
- Barthelmy, S. D., Baumgartner, W. H., Cummings, J. R., et al. 2013, *GRB Coordinates Network*, 14470, 1
- Becerra-Godínez, R. L., *Simulaciones y Rendimiento del Sistema Óptico OAXACA*, Master's thesis, Universidad Nacional Autonoma de México (2015).
- Becerra, R. L., Watson, A. M., Lee, W. H., et al. 2017, *ApJ*, 837, 116
- Becerra, R. L., Watson, A. M., Fraija, N., et al. 2019, *ApJ*, 872, 118
- Belczynski, K., Askar, A., Arca-Sedda, M., et al. 2018, *A&A*, 615, A91.
- Beloborodov, A. M. 2000, *ApJ*, 539, L25
- Beloborodov, A. M., 2003, *ApJ* 583, L19
- Berger, E., Fox, D. B., Cucchiara, A., & Cenko, S. B. 2008, *GRB Coordinates Network*, 8335, 1
- Berger, E., Chornock, R., Holmes, T. R., et al. 2011, *ApJ*, 743, 204
- Berger, E., Shin, M.-S., Mulchaey, J. S., & Jeltama, T. E. 2007, *ApJ*, 660, 496

- Berger, E. 2014, *Annual Review of Astronomy and Astrophysics*, 52, 43.
- Bertin, E., & Arnouts, S. 1996, *A&AS*, 117, 393
- Bessell, M. & Murphy, S. 2012, *Publications of the Astronomical Society of the Pacific*, 124, 140.
- Blandford, R. D., & McKee, C. F. 1976, *Physics of Fluids*, 19, 1130
- Bloom, J. S., Kulkarni, S. R., Djorgovski, S. G., et al. 1999, *Nature*, 401, 453
- Bloom, J. S., Kulkarni, S. R., Price, P. A., et al. 2002, *ApJ*, 572, L45
- Bloom, J. S., Kulkarni, S. R., & Djorgovski, S. G. 2002, *AJ*, 123, 1111
- Bloom, J. S., Prochaska, J. X., Pooley, D., et al. 2006, *ApJ*, 638, 354
- Bufano, F., Pian, E., Sollerman, J., et al. 2012, *ApJ*, 753, 67
- Burrows, D. N., Romano, P., Falcone, A., et al. 2005, *Science*, 309, 1833
- Butler, N., Klein, C., Fox, O., et al. 2012, *Proc. SPIE*, 8446, 844610
- Campana, S., Mangano, V., Blustin, A. J., et al. 2006, *Nature*, 442, 1008
- Cano, Z., Bersier, D., Guidorzi, C., et al. 2011, *ApJ*, 740, 41
- Cano, Z., de Ugarte Postigo, A., Perley, D., et al. 2015, *MNRAS*, 452, 1535
- Cardelli, J. A., Clayton, G. C., & Mathis, J. S. 1989, *ApJ*, 345, 245
- Sari, R., Piran, T. and Halpern, J. P. 1999, *ApJ* 519, 17
- Chevalier, R. A., & Li, Z.-Y. 2000, *ApJ*, 536, 195
- Chornock, R., Berger, E., Levesque, E. M., et al. 2010, *arXiv:1004.2262*
- Clocchiatti, A., Suntzeff, N. B., Covarrubias, R., & Candia, P. 2011, *AJ*, 141, 163
- Cobb, B. E., Bloom, J. S., Perley, D. A., et al. 2010, *ApJ*, 718, L150
- Dai, Z. G., Wang, X. Y., Wu, X. F., Zhang, B. 2006, *Science* 311, 1127
- de Ugarte Postigo, A., Xu, D., Leloudas, G., et al. 2013, *GRB Coordinates Network*, 14646, 1
- D'Elia, V., Pian, E., Melandri, A., et al. 2015, *A&A*, 577, A116
- Della Valle, M., Malesani, D., Benetti, S., et al. 2003, *A&A*, 406, L33
- Della Valle, M., Malesani, D., Bloom, J. S., et al. 2006, *ApJ*, 642, L103

- Della Valle, M., Benetti, S., Mazzali, P., et al. 2008, Central Bureau Electronic Telegrams, 1602, 1
- Denisenko, D. 2013, Publications de l'Observatoire Astronomique de Beograd, 92, 93
- Derishev, E. V., Kocharovsky, V. V. and Kocharovsky, V. V. 1999, ApJ 521, 640
- Dirirsa, F., Racusin, J., McEnery, J., & Desiante, R. 2016, GRB Coordinates Network, 19580, 1
- Drout, M. R., Soderberg, A. M., Gal-Yam, A., et al. 2011, ApJ, 741, 97
- Eichler, D., Livio, M., Piran, T., & Schramm, D. N. 1989, Nature, 340, 126
- van Eerten, H. 2018, International Journal of Modern Physics D, 27, 1842002?1842314.
- Evans, P. A., Beardmore, A. P., Page, K. L., et al. 2009, MNRAS, 397, 1177
- Ferrero, P., Kann, D. A., Zeh, A., et al. 2006, A&A, 457, 857
- Filgas, R., Greiner, J., Schady, P., et al. 2012, A&A, 546, A101
- Foley, S., Watson, D., Gorosabel, J., et al. 2006, A&A, 447, 891
- Fong, W., Berger, E., Margutti, R., et al. 2012, ApJ, 756, 189
- Fox, D. B., Frail, D. A., Price, P. A., et al. 2005, Nature, 437, 845
- Fox, O. D., Kutyrev, A. S., Rapchun, D. A., et al. 2012, Proc. SPIE, 8453, 84531O
- Filgas, R., Greiner, J., Schady, P., et al. 2012, A&A, 546, A101
- Fraija, N. 2015, ApJ, 804, 105
- Fraija, N., Lee, W. H., Veres, P., et al. 2016, ApJ, 831, 22.
- Fraija, N., Lee, W., & Veres, P. 2016, ApJ, 818, 190
- Fraija, N., Veres, P., Zhang, B. B., et al. 2017, ApJ, 848, 15
- Fraija, N., & Veres, P. 2018, ApJ, 859, 70
- Fraija, N. and Veres, P. 2018, Arxiv 1803.02978
- Fruchter, A.S. et al., 2006, Nature, 441, 463
- Fynbo, J. U., Holland, S., Andersen, M. I., et al. 2000, ApJ, 542, L89
- Gal-Yam, A., Moon, D.-S., Fox, D. B., et al. 2004, ApJ, 609, L59
- Galama, T. J., Vreeswijk, P. M., van Paradijs, J., et al. 1998, Nature, 395, 670

- Garnavich, P. M., Stanek, K. Z., Wyrzykowski, L., et al. 2003, *ApJ*, 582, 924
- Gao, H., Lei, W.-H., Zou, Y.-C., Wu, X.-F., & Zhang, B. 2013, *New Astronomy Reviews*, 57, 141
- Gehrels, N., Sarazin, C. L., O'Brien, P. T., et al. 2005, *Nature*, 437, 851
- Gehrels, N., Ramirez-Ruiz, E., & Fox, D. B. 2009, *ARA&A*, 47, 567
- Gehrels, N., & Mészáros, P. 2012, *Science*, 337, 932
- Gehrels, N., & Razzaque, S. 2013, *Frontiers of Physics*, 8, 661
- Gendre, B., Klotz, A., Stratta, G., et al. 2008, *SF2A-2008*, 223
- Goodman, J. 1986, *ApJ*, 308, L47
- Goodman, J., Dar, A., & Nussinov, S. 1987, *ApJ*, 314, L7
- Granot, J., & Sari, R. 2002, *ApJ*, 568, 820
- Granot, J. 2005, *ApJ* 631, 1022
- Greiner, J., Klose, S., Reinsch, K., et al. 2003, *Nature*, 426, 157
- Grupe, D., Nousek, J. A., Veres, P., Zhang, B.-B., & Gehrels, N. 2013, *ApJS*, 209, 20
- Guetta, D., Spada, M., & Waxman, E. 2001, *ApJ*, 557, 399
- Hammer, F., Flores, H., Schaerer, D., et al. 2006, *A&A*, 454, 103
- Hjorth, J., & Bloom, J. S. 2012, Chapter 9 in "Gamma-Ray Bursts", Cambridge Astrophysics Series 51, eds. C. Kouveliotou, R. A. M. J. Wijers and S. Woosley, Cambridge University Press (Cambridge), p. 169-190, 169
- Iwamoto, K., Nomoto, K., Mazzali, P. A., & et al. 2003, *Supernovae and Gamma-Ray Bursters*, 598, 243
- Hou, S. J., Geng, J. J., Wang, K., et al. 2014, *ApJ*, 785, 113
- Karpov, S., Beskin, G., Bondar, S., et al. 2016, *GRB Coordinates Network*, 19603, 1
- King, A., O'Brien, P. T., Goad, M. R., Osborne, J., Olsson, E. and Page, K. 2005, *ApJ* 630, L113
- Kobayashi, S., Zhang, B., Mészáros, P., Burrows, D. 2007, *ApJ* 655, 391
- Kobayashi, S., Piran, T., & Sari, R. 1999, *ApJ*, 513, 669
- Kobayashi, S., & Zhang, B. 2007, *ApJ*, 655, 973

- Koshut, T. M., Paciesas, W. S., Kouveliotou, C., et al. 1995, *Bulletin of the American Astronomical Society*, 27, #53.01
- Kouveliotou, C., Granot, J., Racusin, J. L., et al. 2013, *ApJ*, 779, L1
- Krimm, H. A. et al. 2018, *GRB Coordinates Network*, 22393, 1
- Kumar, P., & Piran, T. 2000, *ApJ*, 532, 286
- Kumar, P., & Zhang, B. 2015, *Phys. Rep.*, 561,
- Kouveliotou, C., Meegan, C. A., Fishman, G. J., Bhat, N. P., Briggs, M. S., Koshut, T. M., Paciesas, W. S., & Pendleton, G. N. 1993, *ApJ*, 413, L101
- Jakobsson, P., Levan, A., Fynbo, J. P. U., et al. 2006, *A&A*, 447, 897
- Janiuk, A., Bejger, M., Sukova, P., et al. 2017, *Galaxies*, 5, 15.
- Jóhannesson, G., Björnsson, G., & Gudmundsson, E. H. 2006, *ApJ*, 647, 1238
- Landolt, A. U. 1992, *AJ*, 104, 340
- Lang, D., Hogg, D. W., Mierle, K., Blanton, M., & Roweis, S. 2010, *AJ*, 139, 1782
- Laskar, T., Berger, E., Zauderer, B. A., et al. 2013, *ApJ*, 776, 119
- Lattimer, J. M., & Schramm, D. N. 1976, *ApJ*, 210, 549
- Le Floc'h, E., Papovich, C., Dole, H., et al. 2005, *ApJ*, 632, 169
- Lee, W. H., & Ramirez-Ruiz, E. 2007, *New Journal of Physics*, 9, 17
- Leibler, C. N., & Berger, E. 2010, *ApJ*, 725, 1202
- Levan, A. J., Cenko, S. B., Perley, D. A., & Tanvir, N. R. 2013, *GRB Coordinates Network*, 14455, 1
- Levan, A., Crowther, P., de Grijs, R., et al. 2016, *Space Sci. Rev.*, 202, 33.
- Li, C., Kauffmann, G., Jing, Y. P., et al. 2006, *MNRAS*, 368, 21
- Li, L.-X. 2006, *MNRAS*, 372, 1357
- Li, L., Wu, X.-F., Huang, Y.-F., et al. 2015, *ApJ*, 805, 13
- Liang, E.-W., Li, L., Gao, H., et al. 2013, *ApJ*, 774, 13
- Littlejohns, O. M., Butler, N. R., Cucchiara, A., et al. 2015, *MNRAS*, 449, 2919

- Lü, H.-J., Lü, J., Zhong, S.-Q., et al. 2017, *ApJ*, 849, 71.
- Lyutikov, M. 2017, arXiv:1705.01014
- MacFadyen, A., & Woosley, S. E. 1998, *Bulletin of the American Astronomical Society*, 30, 43.02
- MacFadyen, A. I., & Woosley, S. E. 1999, *ApJ*, 524, 262
- Magnier, E. A., Sweeney, W. E., Chambers, K. C., et al. 2016, arXiv:1612.05244
- Malesani, D., Tagliaferri, G., Chincarini, G., et al. 2004, *ApJ*, 609, L5
- Mandhai, S., Tanvir, N., Lamb, G., et al. 2018, *Galaxies*, 6, 130.
- Maselli, A., Beardmore, A. P., Lien, A. Y., et al. 2013, *GRB Coordinates Network*, 14448, 1
- Maselli, A., Melandri, A., Nava, L., et al. 2014, *Science*, 343, 48
- Matheson, T., Garnavich, P. M., Stanek, K. Z., et al. 2003, *ApJ*, 599, 394
- Mazaeva, E., Kusakin, A., Minaev, P., et al. 2016, *GRB Coordinates Network*, 19680, 1
- Mazaeva et al. 2018, *GRB Coordinates Network*, 22430, 1
- McBreen, B., Foley, S., & Hanlon, L. 2010, arXiv e-prints , arXiv:1003.4440.
- Melandri, A., Pian, E., Ferrero, P., et al. 2012, *A&A*, 547, A82
- Melandri, A., Pian, E., D’Elia, V., et al. 2014, *A&A*, 567, A29
- Mészáros, P., & Rees, M. J. 1997, *ApJ*, 476, 232
- Melandri, A., D’Avanzo, P., D’Elia, V., et al. 2016, *GRB Coordinates Network*, 19585, 1
- Metzger, M. R., et al. 1997, *Nature*, 387, 878
- Mirabal, N., Halpern, J. P., An, D., Thorstensen, J. R., & Terndrup, D. M. 2006, *ApJ*, 643, L99
- Modjaz, M., Stanek, K. Z., Garnavich, P. M., et al. 2006, *ApJ*, 645, L21
- Modjaz, M., Kewley, L., Kirshner, R. P., et al. 2008, *AJ*, 135, 1136
- Mooley, K. P., Deller, A. T., Gottlieb, O., et al. 2018, *Nature*, 561, 355.
- Moskvitin, A. 2016, *GRB Coordinates Network*, 19611, 1
- Nakar, E., & Piran, T. 2002, *ApJ*, 572, L139
- Nakar, E. 2007, *Advances in Space Research*, 40, 1224

- Nakar, E. 2007, *Phys. Rep.*, 442, 166
- Narayana Bhat, P., Meegan, C. A., von Kienlin, A., et al. 2016, *ApJS*, 223, 28
- Narayan, R., Paczynski, B., & Piran, T. 1992, *ApJ*, 395, L83
- Nomoto, K., Tominaga, N., Tanaka, M., et al. 2006, *Nuovo Cimento B Serie*, 121, 1207
- Oksanen, A. et al. 2018, *GRB Coordinates Network*, 22401, 1
- Olivares E., F., Greiner, J., Schady, P., et al. 2012, *A&A*, 539, A76
- Paczynski, B., 1986, *ApJ*, 308, L43
- Paczynski, B., 1991, *Acta Astron.*, 41, 257
- Paczynski, B., & Rhoads, J. E. 1993, *ApJ*, 418, L5
- Page, K. L. et al. 2018, *GRB Coordinates Network*, 22394, 1
- Panaitescu, A. 2008, *MNRAS*, 383, 1143
- Perley, D. A., Cenko, S. B., Corsi, A., et al. 2014, *ApJ*, 781, 37
- Perley, D. A. 2013, *GRB Coordinates Network*, 14451, 1
- Perley, D. A., & Tang, S. 2013, *GRB Coordinates Network*, 14615, 1
- Perley, D. A., Mazzali, P. A., Yan, L., et al. 2019, *MNRAS*, 484, 1031.
- Perna, R., Armitage, P. J., Zhang, B. 2006, *ApJ* 636, L29
- Piran, T. 1999, *Phys. Rep.*, 314, 575
- Piran, T., & Granot, J. 2001, *Gamma-ray Bursts in the Afterglow Era*, 300
- Piran, T. 2004, *Reviews of Modern Physics*, 76, 1143
- Pian, E., Mazzali, P. A., Masetti, N., et al. 2006, *Nature*, 442, 1011
- Planck Collaboration, Ade, P. A. R., Aghanim, N., et al. 2014, *A&A*, 571, A1
- Proga, D. and Zhang, B. 2006, *mnras* 370, L61
- Rees, M. J., & Meszaros, P. 1992, *MNRAS*, 258, 41P
- Rybicki, G. B., & Lightman, A. P. 1985, *Radiative processes in astrophysics..* G. B. Rybicki, A. P. Lightman. John Wiley

- Sari, R., Piran, T.,
- Sari, R., & Piran, T. 1999, *ApJ*, 520, 641 & Narayan, R. 1998, *ApJ*, 497, L17
- Savaglio, S., Glazebrook, K., & Le Borgne, D. 2009, *ApJ*, 691, 182
- Schlegel, D. J., Finkbeiner, D. P., & Davis, M. 1998, *ApJ*, 500, 525
- Schulze, S., Malesani, D., Cucchiara, A., et al. 2014, *A&A*, 566, A102
- Skibba, R. A., & Sheth, R. K. 2009, *MNRAS*, 392, 1080
- Soderberg, A. M., Kulkarni, S. R., Fox, D. B., et al. 2005, *ApJ*, 627, 877
- Soderberg, A., Berger, E., & Fox, D. 2008, *GRB Coordinates Network*, 8662, 1
- Sokolov, V. V., Castro-Tirado, A. J., Moskvitin, A. S., et al. 2013, *GRB Coordinates Network*, 14669, 1
- Sollerman, J., Jaunsen, A. O., Fynbo, J. P. U., et al. 2006, *A&A*, 454, 503
- Stanek, K. Z., Matheson, T., Garnavich, P. M., et al. 2003, *ApJ*, 591, L17
- Starling, R. L. C., Wiersema, K., Levan, A. J., et al. 2011, *MNRAS*, 411, 2792
- Tam, P.-H. T., Tang, Q.-W., Hou, S.-J., Liu, R.-Y., & Wang, X.-Y. 2013, *ApJ*, 771, L13
- Tanvir, N. et al. 2018, *GRB Coordinates Network*, 22384, 1
- Thomsen, B., Hjorth, J., Watson, D., et al. 2004, *A&A*, 419, L21
- Tinney, C., Stathakis, R., Cannon, R., et al. 1998, *IAU Circ.*, 6896, 1
- Tody, D. 1986, *Proc. SPIE*, 627, 733
- Tominaga, N., Maeda, K., Umeda, H., et al. 2007, *ApJ*, 657, L77
- Tonry, J. L., Stubbs, C. W., Lykke, K. R., et al. 2012, *ApJ*, 750, 99
- Toy, V. L., Cenko, S. B., Silverman, J. M., et al. 2016, *ApJ*, 818, 79.
- Troja, E., Butler, N., Watson, A. M., et al. 2016, *GRB Coordinates Network*, 19588, 1
- Troja, E., Ryan, G., Piro, L., et al. 2018, *Nature Communications*, 9, 4089.
- Uehara, T., Uemura, M., Kawabata, K. S., et al. 2010, *A&A*, 519, A56
- Usov, V. V. 1992, *Nature*, 357, 472



- van der Horst, A. J., Paragi, Z., de Bruyn, A. G., et al. 2014, *MNRAS*, 444, 3151
- Vestrand, W. T., Borozdin, K., Brumby, S., et al. 2003, *Bulletin of the American Astronomical Society*, 35, 16.01
- Vestrand, W. T., Wren, J. A., Panaitescu, A., et al. 2014, *Science*, 343, 38
- Vetere, L., Massaro, E., Costa, E., Soffitta, P., & Ventura, G. 2006, *A&A*, 447, 499
- von Kienlin, A. 2013, *GRB Coordinates Network*, 14473, 1
- Wainwright, C., Berger, E., & Penprase, B. E. 2007, *ApJ*, 657, 367
- Wang, X.-G., Zhang, B., Liang, E.-W., et al. 2015, *ApJS*, 219, 9
- Wang, Y., Aimuratov, Y., Moradi, R., et al. 2018, *Memorie della Societa Astronomica Italiana*, 89, 293.
- Watson, A. M., Richer, M. G., Bloom, J. S., et al. 2012, *Proc. SPIE*, 8444, 84445L
- Watson, A. M., Butler, N., Kuttyrev, A., et al. 2013, *GRB Coordinates Network*, 14666, 1
- Watson, A. M., Lee, W. H., Troja, E., et al. 2016, *Proc. SPIE*, 9910, 99100G
- Watson, A. M., Cuevas Cardona, S., Alvarez Nuñez, L. C., et al. 2016, *Proc. SPIE*, 9908, 99085O
- Wiersema K and Covino S. 2018, *GRB Coordinates Network*, 22388, 1
- Wiersema, K., Vaduvescu, O., Tanvir, N., Levan, A., & Hartoog, O. 2013, *GRB Coordinates Network*, 14617, 1
- Woosley, S. E., & Bloom, J. S. 2006, *ARA&A*, 44, 507
- Woosley, S. E. 1993, *ApJ*, 405, 273
- Woosley, S. E., & Bloom, J. S. 2006, *ARA&A*, 44, 507
- Xin, L. P. et al. 2018, *GRB Coordinates Network*, 22392, 1
- Xu, D., de Ugarte Postigo, A., Leloudas, G., et al. 2013, *ApJ*, 776, 98
- Zeh, A., Klose, S., & Hartmann, D. H. 2004, *ApJ*, 609, 952
- Zhang, B. 2014, *International Journal of Modern Physics D*, 23, 1430002
- Zhang, B.-B., Zhang, B., Castro-Tirado, A. J., et al. 2018, *Nature Astronomy*, 2, 69.
- Zhang, B., Fan, Y. Z., Dyks, J., et al. 2006, *ApJ*, 642, 354

Zheng, W. et al. 2018, GRB Coordinates Network, 22382, 1

Zhu, Z. P. et al. 2018, GRB Coordinates Network, 22395, 1